

**APPLIED  
COMPUTATIONAL  
ELECTROMAGNETICS  
SOCIETY  
JOURNAL**

May 2020  
Vol. 35 No. 5  
ISSN 1054-4887

**The ACES Journal is abstracted in INSPEC, in Engineering Index, DTIC, Science Citation Index Expanded, the Research Alert, and to Current Contents/Engineering, Computing & Technology.**

The illustrations on the front cover have been obtained from the research groups at the Department of Electrical Engineering, The University of Mississippi.

# THE APPLIED COMPUTATIONAL ELECTROMAGNETICS SOCIETY

<http://aces-society.org>

## EDITORS-IN-CHIEF

**Atef Elsherbeni**

Colorado School of Mines, EE Dept.  
Golden, CO 80401, USA

**Sami Barmada**

University of Pisa, ESE Dept.  
56122 Pisa, Italy

## ASSOCIATE EDITORS: REGULAR PAPERS

**Mohammed Hadi**

Kuwait University, EE Dept.  
Safat, Kuwait

**Alistair Duffy**

De Montfort University  
Leicester, UK

**Wenxing Li**

Harbin Engineering University  
Harbin 150001, China

**Maokun Li**

Tsinghua University  
Beijing 100084, China

**Mauro Parise**

University Campus Bio-Medico of Rome  
00128 Rome, Italy

**Yingsong Li**

Harbin Engineering University  
Harbin 150001, China

**Riyadh Mansoor**

Al-Muthanna University  
Samawa, Al-Muthanna, Iraq

**Antonio Musolino**

University of Pisa  
56126 Pisa, Italy

**Abdul A. Arkadan**

Colorado School of Mines, EE Dept.  
Golden, CO 80401, USA

**Salvatore Campione**

Sandia National Laboratories  
Albuquerque, NM 87185, USA

**Wei-Chung Weng**

National Chi Nan University, EE Dept.  
Puli, Nantou 54561, Taiwan

**Alessandro Formisano**

Seconda Università di Napoli  
81031 CE, Italy

**Piotr Gas**

AGH University of Science and Technology  
30-059 Krakow, Poland

**Long Li**

Xidian University  
Shaanxa, 710071, China

**Marco Arjona López**

La Laguna Institute of Technology  
Torreon, Coahuila 27266, Mexico

**Paolo Mezzanotte**

University of Perugia  
I-06125 Perugia, Italy

**Luca Di Rienzo**

Politecnico di Milano  
20133 Milano, Italy

**Lei Zhao**

Jiangsu Normal University  
Jiangsu 221116, China

**Sima Noghianian**

University of North Dakota  
Grand Forks, ND 58202, USA

**Qiang Ren**

Beihang University  
Beijing 100191, China

**Nunzia Fontana**

University of Pisa  
56122 Pisa, Italy

**Atif Shamim**

King Abdullah University of Science and Technology (KAUST)  
Thuwal 23955, Saudi Arabia

**Stefano Selleri**

DINFO – University of Florence  
50139 Florence, Italy

## ASSOCIATE EDITORS: EXPRESS PAPERS

**Lijun Jiang**

University of Hong Kong, EEE Dept.  
Hong, Kong

**Shinichiro Ohnuki**

Nihon University  
Tokyo, Japan

**Kubilay Sertel**

The Ohio State University  
Columbus, OH 43210, USA

**Steve J. Weiss**

US Army Research Laboratory  
Adelphi Laboratory Center (RDRL-SER-M)  
Adelphi, MD 20783, USA

**Jiming Song**

Iowa State University, ECE Dept.  
Ames, IA 50011, USA

**Amedeo Capozzoli**

Univerita di Napoli Federico II, DIETI  
I-80125 Napoli, Italy

**Yu Mao Wu**

Fudan University  
Shanghai 200433, China

**Maokun Li**

Tsinghua University, EE Dept.  
Beijing 100084, China

## EDITORIAL ASSISTANTS

**Matthew J. Inman**

University of Mississippi, EE Dept.  
University, MS 38677, USA

**Shanell Lopez**

Colorado School of Mines, EE Dept.  
Golden, CO 80401, USA

**Madison Le**

Colorado School of Mines, EE Dept.  
Golden, CO 80401, USA

**Allison Tanner**

Colorado School of Mines, EE Dept.  
Golden, CO 80401, USA

## EMERITUS EDITORS-IN-CHIEF

**Duncan C. Baker**

EE Dept. U. of Pretoria  
0002 Pretoria, South Africa

**Allen Glisson**

University of Mississippi, EE Dept.  
University, MS 38677, USA

**Ahmed Kishk**

Concordia University, ECS Dept.  
Montreal, QC H3G 1M8, Canada

**Robert M. Bevensee**

Box 812  
Alamo, CA 94507-0516, USA

**Ozlem Kilic**

Catholic University of America  
Washington, DC 20064, USA

**David E. Stein**

USAF Scientific Advisory Board  
Washington, DC 20330, USA

## EMERITUS ASSOCIATE EDITORS

**Yasushi Kanai**

Niigata Inst. of Technology  
Kashiwazaki, Japan

**Alexander Yakovlev**

University of Mississippi, EE Dept.  
University, MS 38677, USA

**Levent Gurel**

Bilkent University  
Ankara, Turkey

**Mohamed Abouzahra**

MIT Lincoln Laboratory  
Lexington, MA, USA

**Ozlem Kilic**

Catholic University of America  
Washington, DC 20064, USA

**Erdem Topsakal**

Mississippi State University, EE Dept.  
Mississippi State, MS 39762, USA

**Sami Barmada**

University of Pisa, ESE Dept.  
56122 Pisa, Italy

**Fan Yang**

Tsinghua University, EE Dept.  
Beijing 100084, China

**Rocco Rizzo**

University of Pisa  
56123 Pisa, Italy

**William O'Keefe Coburn**

US Army Research Laboratory  
Adelphi, MD 20783, USA

## EMERITUS EDITORIAL ASSISTANTS

**Khaled ElMaghoub**

Trimble Navigation/MIT  
Boston, MA 02125, USA

**Christina Bonnington**

University of Mississippi, EE Dept.  
University, MS 38677, USA

**Kyle Patel**

Colorado School of Mines, EE Dept.  
Golden, CO 80401, USA

**Anne Graham**

University of Mississippi, EE Dept.  
University, MS 38677, USA

**Mohamed Al Sharkawy**

Arab Academy for Science and Technology, ECE Dept.  
Alexandria, Egypt

**MAY 2020 REVIEWERS: REGULAR PAPERS**

**Kishore Balasubramanian**  
**Navid Barani Lonbani**  
**Cemile Bardak**  
**Istvan Bardi**  
**Subhradeep Chakraborty**  
**Thomas Ellis**  
**Alireza Ghaneizadeh**  
**Robert Ilgner**  
**Tianqi Jiao**  
**Ming Jin**  
**Lluis Jofre**  
**Kang Lan**  
**Ji Lei**  
**Long Li**  
**Weiwen Li**

**Yingsong Li**  
**Paolo Nepa**  
**Andrew Peterson**  
**Rachid Saadane**  
**Kanhaiya Sharma**  
**Ahalya Srikanth**  
**Ashok Kumar Srinivasan**  
**Candace Suriano**  
**Wei-Chung Weng**  
**Binbin Yang**  
**Guohui Yang**  
**Shihyuan Yeh**  
**Ferdows Zarrabi**  
**Lei Zhao**

TABLE OF CONTENTS – REGULAR PAPERS

Optimization of the Shape of Non-Planar Electronically Scanned Arrays for IFF Applications via Multi-Objective Invasive Weed Optimization Algorithm  
Stefano Maddio, Giuseppe Pelosi, Monica Righini, Stefano Selleri, and Irene Vecchi .....488

RCS Optimization Analysis Method for Sea-Skimming Unmanned Aerial Vehicle Based on Back Propagation Neural Network Algorithm  
Chengpan Yang, Wei Yan, Yang Zhao, Lu Geng, Shiliang Hou, and Jian Chen .....495

Design of Low RCS Vivaldi Antenna Based on Differential Evolution Algorithm  
Ge Zhao, Zi-Yu Pang, Xiao-Yu Ma, Guan-Long Huang, Luyu Zhao, Jia-Jun Liang, and Chow-Yen-Desmond Sim .....506

Research and Experiments on Anti-UAV Technology  
Hongbo Wei, Xinhui Wang, Xiaowei Shi, and Bo Liang .....511

Compact Multilayer Dual-mode Substrate Integrated Waveguide Filtering Crossover Based on Orthogonal Modes  
Zhigang Zhang and Yong Fan .....519

Design and Application of Coupled Line Cross-Shaped Resonator in Band-pass Filter  
Dong-Sheng La, Xin Guan, Hong-Cheng Li, Yu-Ying Li, and Jing-Wei Guo .....527

A Metal-Strip Integrated Filtering Waveguide  
Xiao-Yu Ma, Zi-Yu Pang, Ge Zhao, Jia-Jun Liang, Guan-Long Huang, Luyu Zhao, and Chow-Yen-Desmond Sim .....533

A 3D Printed Filtering Waveguide with Simple Metamaterial Construction  
Zi-Yu Pang, Xiao-Yu Ma, Ge Zhao, Jia-Jun Liang, Guan-Long Huang, Luyu Zhao, and Chow-Yen-Desmond Sim .....539

Three-Stacked Dielectric Ring Resonator Loaded Hybrid Monopole Antenna for Improved Ultrawide Bandwidth  
Ali A. Al-Azza, Nuhad A. Malalla, Mohamed M. Morsy, and Frances J. Harackiewicz .....545

Design of L-band Energy-Selective Surface with Circular Ring Gap  
Guohui Yang, Yong Li, Qun Wu, Yan Wang, and Yingsong Li .....551

Wideband MIMO Directional Antenna Array with a Simple Meta-material Decoupling Structure for X-Band Applications Jianfeng Jiang, Yingsong Li, Lei Zhao, and Xiaoguang Liu .....	556
A Dual-Polarized Sakura-Shaped Base Station Antenna for 5G Communications Peng Chen, Lihua Wang, and Tongyu Ding .....	567
Analysis on Crosstalk for Coplanar Irregular-placed Cables Based on Cascading Method and Cubic Spline Interpolation Algorithm Chong Ming Zhu, Wei Yan, Shi Cheng Liu, and Lu Geng.....	572
W-band Electronic Focus-Scanning by a Reconfigurable Transmitarray for Millimeter-Wave Imaging Applications Xiaotian Pan, Fan Yang, Shenheng Xu, and Maokun Li .....	580
Protective Role of Vitamin C in Wi-Fi Induced Oxidative Stress in MC3T3-E1 Cells in Vitro Mengxi Wang, Guohui Yang, Yu Li, Qun Wu, and Yingsong Li .....	587

# Optimization of the Shape of Non-Planar Electronically Scanned Arrays for IFF Applications via Multi-Objective Invasive Weed Optimization Algorithm

Stefano Maddio, Giuseppe Pelosi, Monica Righini, Stefano Selleri, and Irene Vecchi

Department of Information Engineering  
University of Florence

[stefano.maddio, giuseppe.pelosi, monica.righini, stefano.selleri]@unifi.it, irene.vecchi@stud.unifi.it

**Abstract** — The identify friend or foe antenna is a complement to many radar antennas which allows the discrimination between friendly and hostile targets by receiving identification data. Such antenna must synthesize both a sum and a difference pattern in azimuth to allow target discrimination and must point to the target being inquired, either by mechanical or electronic scanning in azimuth. In this paper, to attain optimal electronic scanning, an array of antennas lying on a generic planar curve is considered. A multi-objective optimization based on the invasive weed optimization algorithm is then applied to the shape of such curve, aimed at maximizing performances. Whereas a conventional linear array of 6 elements can effectively scan  $\pm 30^\circ$ , with respect to broadside, the proposed array, notwithstanding the same number of elements and overall length, can scan  $\pm 45^\circ$  and still synthesize effective sum and difference patterns.

**Index Terms** — Antenna arrays, conformal arrays, IFF antenna, optimization, phased arrays.

## I. INTRODUCTION

The identify friend or foe (IFF) system integrates military radar antenna. It allows the discrimination between friendly and hostile targets by receiving identification data. IFF systems relies on their own antenna, placed in proximity of the radar antenna [1]. IFF antennas are almost as old as radar itself and their design is a long running engineering problem [2]. Current IFF standard, Mark XII, states a transmitting frequency centered at 1030 MHz and a receiving frequency centered at 1090 MHz. Hence frequency much lower than those currently used on radars. Yet, the IFF antenna must have azimuth angular discrimination characteristics comparable to those of the matching radar and should not be larger than the radar antenna itself. These conflicting requirements are addressed by designing IFF antennas capable of generating at the same time a sum ( $\Sigma$ ) pattern for communication and a difference ( $\Delta$ ) pattern for target discrimination in a framework similar to that of monopulse radars [2-4]. The IFF is commonly a linear

array, seldom a planar array, of few elements which can of course be implemented on a flat surface [5,6] or made conformal to a curved surface [7].

If the radar is to be an electronically steering active array antenna, as it is the current state-of-the art, then also the IFF antenna should be electronically steerable in both sum and difference patterns, with steering performance comparable to that of the main antenna.

If the IFF antenna is to be of the same size of the main antenna, being requested to work at a much lower frequency, then its number of elements will be much smaller, and scanning capabilities would be impaired with respect to the main antenna [8]. In this contribution, a compact IFF array with few elements to keep its width minimal is designed, via a stochastic optimization procedure, to achieve maximum scanning capabilities.

Optimization is made on the curve, contained in the  $xy$ , horizontal, plane, on which radiating elements are placed and a multi-objective strategy is applied to the pattern as steering is performed on the  $xy$ -plane (azimuth) cut. The basic idea is that the array is not conformal to any given surface due to mechanical reasons but is rather of a shape designed so as to maximize scanning capabilities.

In this paper preliminary results are presented, attained on an ideal array comprising non-interacting elements with weakly directive patterns, optimized via an in-house multi-objective (MO) implementation of the invasive weed optimization (IWO) algorithm [9-10]. IWO has been chosen among many competing algorithms for its good performances in electromagnetic problems, both antenna ones [11-14] and circuit ones [15-16]. Its extension to MO is simple, as per any population based stochastic optimization method, as explained in [17]. In the present paper radiating elements are considered ideal sources, implementation with patch antennas and full wave simulations will be matter of future studies.

The paper is organized as follows: the following Section II describes the problem set up; Section III presents the optimization method; Section IV the optimization results. Finally, Section V draws some

conclusions.

## II. ARRAY GEOMETRY AND OPTIMIZATION VARIABLES

The reference for the analysis is a Cartesian reference with a vertical  $z$ -axis. Due to the IFF application only azimuth patterns will be considered, that is  $xy$  cuts of the radiation solid. The coordinate considered is  $\theta$ , measuring the angular distance between the  $x$ -axis and the direction of observation.

The problem geometry is sketched in Fig. 1: a spline, defined by  $N+2$  control points, the first  $(0,0)$  and last  $(L,0)$ , being fixed, is used as a baseline on which to deploy radiating elements. The internal  $N$  control points  $(x_i, y_i)$  with  $0 < x_1 < \dots < x_i < \dots < x_N < L$  are evenly spaced in  $x$ , while their coordinates  $0 < y_i < y_{\max}$  are the variables for the optimization procedure.

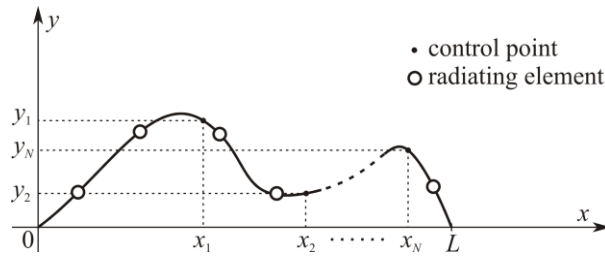


Fig. 1. A spline in the  $(x, y)$  plane defined by  $N+2$  control points and on which  $M$  radiating elements are uniformly spaced.

On the spline  $M$  equally spaced radiating elements are deployed. Since the spline length varies as the control points  $(x_i, y_i)$  are moved, physical feasibility constraints are enforced, i.e., the number of elements  $M$  is chosen so that the straight array along the segment of length  $L$  is realizable. That is, elements are further than half wavelength from each other in the straight array. Then, since any possible spline is longer than  $L$ , the spline-based array is realizable. First and last elements are placed at a distance from the end of the spline equal to half the inter element distance. This to ensure that, when this design will be used in practice, finite dimension patch antennas will have room within the spline.

Element pattern is assumed as either a cardioid or a cosine, both being a good approximation of a patch antenna pattern at least in the upper half-space:

$$P(\theta) = \begin{cases} \cos^n(\theta - \theta^{(b)}) & \text{if } \cos(\theta - \theta^{(b)}) > 0 & \text{cosine} \\ 0 & \text{otherwise} & \text{pattern} \end{cases} \quad (1)$$

$$P(\theta) = \frac{\cos(\theta - \theta^{(b)}) + 1}{2} \quad \text{cardioid pattern}$$

Being  $\theta^{(b)}$  the boresight direction (maximum radiation) of the pattern.

When elements are deployed onto the spline, the boresight direction  $\theta_i^{(b)}$  of the generic element  $i$  is set perpendicular to the spline as it is the standard in a conformal array (Fig. 2). By comparing boresight direction  $\theta_i^{(b)}$  with the desired scan angle  $\theta_0$  it is possible to switch off an element that would not contribute significantly to the pattern. In the following if  $|\theta_0 - \theta_i^{(b)}| > \theta_{\max}$  then, element  $i$  is turned off, being  $\theta_{\max}$  among the optimization parameters (Fig. 2).

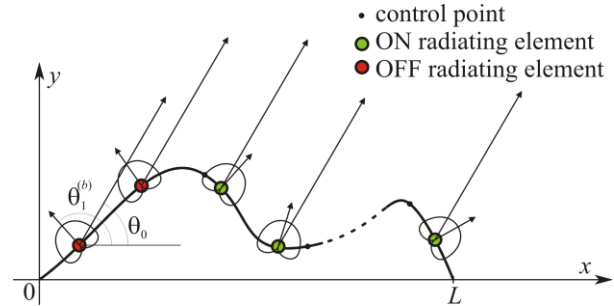


Fig. 2. On/off array elements selected on the basis of the beam steering. Angle  $\theta$  is measured from  $x$  axis.

## III. IWO ALGORITHM AND OPTIMIZATION SET-UP

The IWO algorithm searches for the best cost value by mimicking the behavior of invasive weed in a crop field. In its MO version (MO-IWO [14])  $P$  weed seeds are randomly scattered on the problem parameters domain, from each seed grows a plant, plants are then ranked according to a non-dominating sorting [17] on the basis of the various cost functions evaluated at their position. Plants in excess are discarded.

Plants ranking higher in the sorting are considered as growing in an area rich of resources and hence produce more seeds than plants with worse cost values. The number of seeds each plant can produce vary from 1 to  $M_s$ .

Newly produced seeds are then spread around the plant location according to a normal (Gaussian) distribution of standard deviation  $\sigma$ , and give rise to new plants in the population.  $\sigma$  is decreased at each iteration so as to refine solution. Basic algorithm details can be found in [9], where single objective IWO is discussed. Figure 3 shows the flow chart for the MO-IWO here implemented. Both the MO-IWO algorithm and the evaluation of the array costs detailed in the following have been implemented by the authors in Matlab.

For the present case  $N=3$  inner control points are chosen. The  $x_i$  are equally spaced in the  $[0, L]$  interval, and symmetry is enforced, i.e.,  $y_1 = y_3$ . Optimization variables are hence only two:  $y_1$  and  $y_2$ , with the additional choice of parameter  $y_{\max} = L$ .



Optimization parameters are then  $\theta_{\max}=\pi/3$ ,  $M=6$ ,  $L=2\lambda$ , being  $\lambda$  the free-space wavelength. Patterns are cosine type, with  $n=1$  (see eq. (1)).

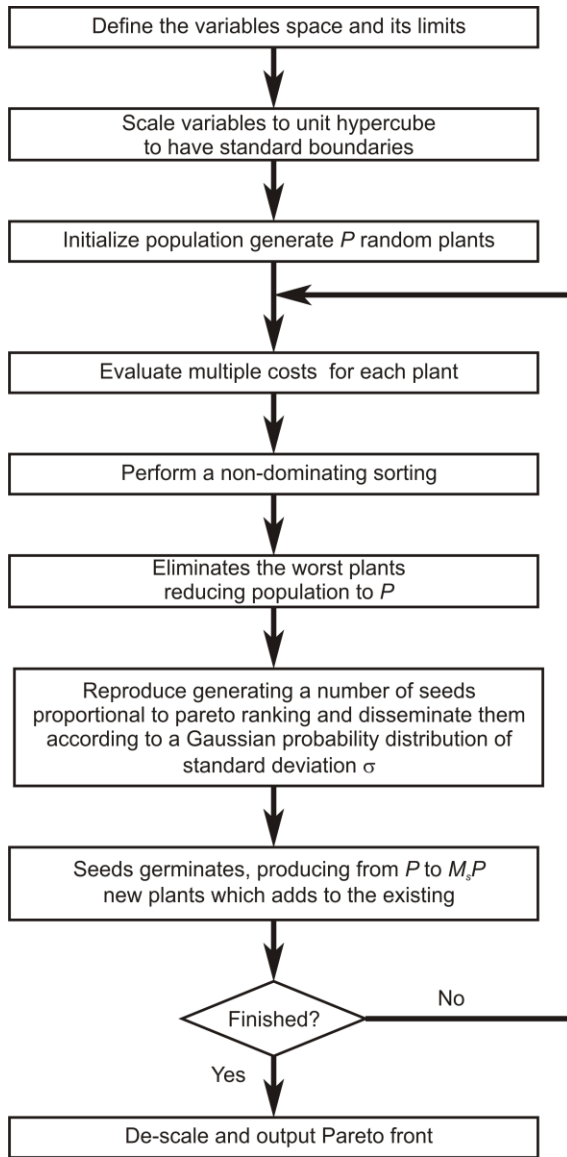


Fig. 3. MO-IWO Algorithm flowchart.

Costs are defined in terms of the following pattern quality parameters (Fig. 4):

- $\theta_0$  – desired scan angle; on the basis of this angle theoretical phases for the elements are computed;
- $\theta_{\Sigma}$  – scan angle effectively synthesized with theoretical phases on sum pattern ( $\Sigma$ ); this will differ from  $\theta_0$ , in general, due to the fact that element boresight directions are not aligned;
- $\theta_{\Delta}$  – scan angle effectively synthesized with theoretical phases on difference pattern ( $\Delta$ );

$\theta_{e-}$  – left crossing angle between sum and difference patterns;

$\theta_{e+}$  – right crossing angle between sum and difference patterns;

$ND$  – null depth, difference between normalized sum pattern maximum and normalized difference pattern minimum (computed in linear scale, not dB, i.e., in the [0,1] range).

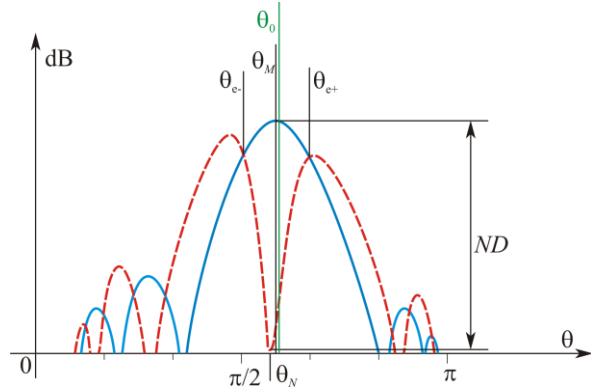


Fig. 4. Sum (blue, solid) and difference (red, dashed) and pattern parameters described in the text.

Based on these 6 quality factors, 5 costs are defined as the maximum values over the scan angle range of the following quantities:

$$c_1 = \max_{\theta_0 \in [\theta_-, \theta_+]} (ND), \quad (2)$$

$$c_2 = \max_{\theta_0 \in [\theta_-, \theta_+]} (|\theta_{\Sigma} - \theta_{\Delta}|), \quad (3)$$

$$c_3 = \max_{\theta_0 \in [\theta_-, \theta_+]} (\theta_{e+} - \theta_{e-}), \quad (4)$$

$$c_4 = \max_{\theta_0 \in [\theta_-, \theta_+]} (|\theta_{e+} - \theta_{\Sigma}|, |\theta_{e-} - \theta_{\Sigma}|), \quad (5)$$

$$c_5 = \max_{\theta_0 \in [\theta_-, \theta_+]} (|\theta_{e+} - \theta_{\Delta}|, |\theta_{e-} - \theta_{\Delta}|). \quad (6)$$

Being  $[\theta_-, \theta_+]$  the desired scan interval with respect to broadside. In our analysis  $\pm 45^\circ$ , that is, being the broadside direction  $\theta = 90^\circ$ :  $\theta_- = 45^\circ$ ,  $\theta_+ = 135^\circ$ .

A sixth cost,  $c_6$ , is given by the maximum  $y$  value of the spline, hence it accounts for the antenna overall size.

All costs ought to be minimized: Minimization of (2) leads to the deepest, hence sharper, null. Minimization of (3) leads to the best alignment between the sum maximum and the difference null. Minimization of (4); leads to the smallest effective angle, that is the smallest beamwidth for the sum/difference beam pair, which is a crucial parameter for target discrimination. Minimization of (5) and (6) leads to maximum symmetry between the effective angle and the maximum/null directions.

The IWO algorithm is run with  $P=25$ ,  $M_s=3$  for 200 generations. Standard deviation  $\sigma$  starts at 0.1 and linearly decreases to 0.001, at generation 200. Figure 5 shows the number of elements on the Pareto set. Note

that if all 25 plants are in the Pareto set, then each produces 3 seeds and the total number of plants, after ranking and before elimination of the worst, sums up to 100. If plants on the Pareto set must be discarded the crowding distance is employed to select those to discard [17]. At the end of the optimization procedure, a Pareto set containing 25 solutions is obtained. Run time over a relatively old i5-4590S PC with 16Gb ram was about 1h, with most of the time dedicated to the determination of the pattern quality parameters.

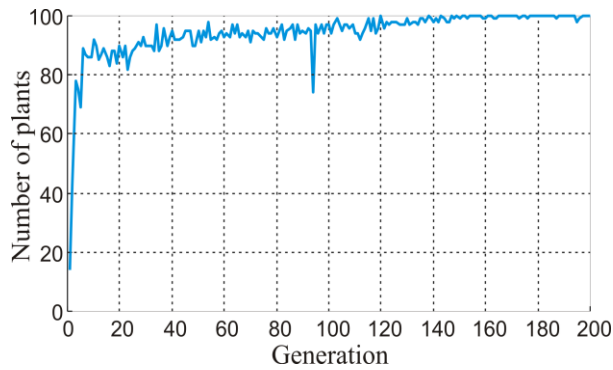


Fig. 5. Number of plants on the Pareto set as a function of generation.

#### IV. OPTIMIZATION RESULTS

The optimization run returned a Pareto set of 25 elements. A Pareto set is a set of non-dominated solutions in Pareto sense, that is, optimal solutions on which a trade-off must be done *a posteriori* [17]. Figure 6 shows six 2D projections of the 6D cost space. It is apparent how many different performances are attained. The chosen solution for showing patterns in detail in the following is number 24, highlighted by the green bullets in Fig. 6. Such a solution shows excellent cost values for the first four costs, an acceptable behavior on the fifth, and quite poor values for the sixth cost. Since  $c_6$  is bound to spline height, this means that the spline extends significantly in the  $y$  direction, but space occupation requirement is here considered less important than electromagnetic behavior.

The spline defining the optimal array chosen among the ones in the final Pareto set is defined by the control points reported in Table 1 and the shape sketched in Fig. 7. It is somewhat surprising at first that the array is not convex but a mix of convex and concave, the middle point being lower in  $y$  than the surrounding ones.

Table 1: Spline control points

	0	1	2	3	4
$x$	0	0.5	1	1.5	2
$y$	0	0.880	0.275	0.880	0

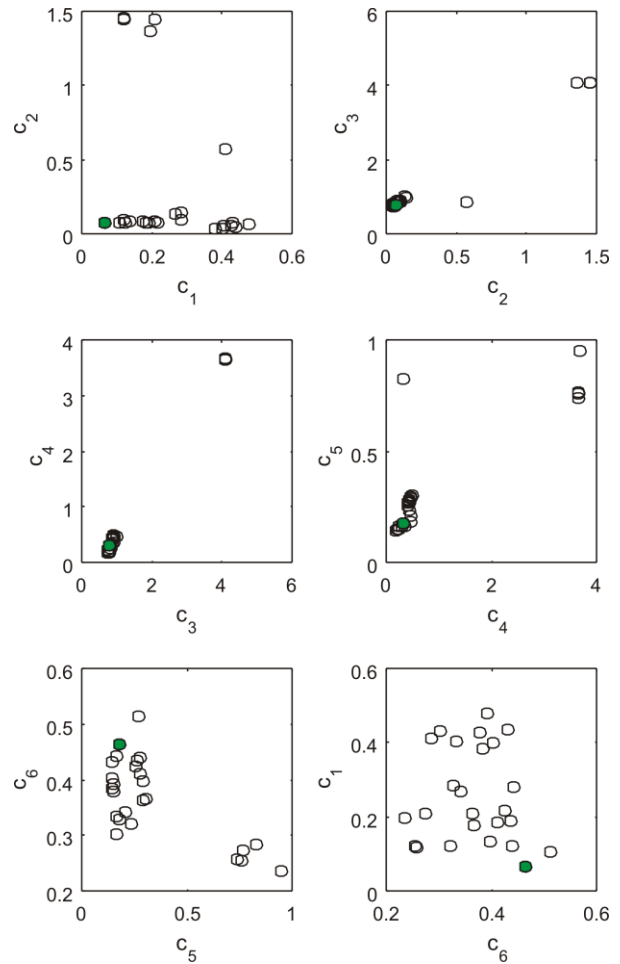


Fig. 6. 2D cuts of the 6D cost space showing the attained Pareto set. Empty circles: all solutions; filled bullet: solution selected. Costs are linear ( $c_1$ ), in radians ( $c_2$  to  $c_5$ ) or wavelengths ( $c_6$ ).

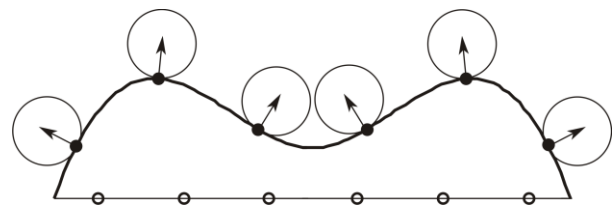


Fig. 7. Optimized geometry (bullets) with element factors and boresight directions highlighted, and equivalent linear array (empty circles).

This is indeed explained by the need of having a wide baseline for the array elements also while scanning. The optimized spline allows to have from 6 to 4 elements contributing to radiation for any scan angle, but, when four only are used, they may not be contiguous, especially at angles far from boresight, so effectively realizing a

larger baseline countering the baseline reduction due to scanning.

Figure 7 shows the optimized geometry and the equivalent linear array of the same baseline and number of elements used for comparison.

Figure 8 shows all the costs, as compared to the ones computed for the linear array with the same baseline. For a clearer understanding, null depth ( $c_1$ ) is reported in dB as a positive value while all the other costs are reported in degrees.

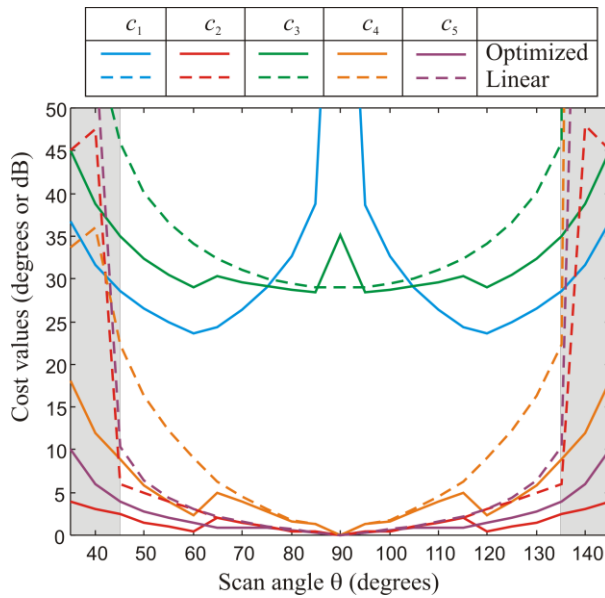


Fig. 8. Comparison between the five costs defined on patterns evaluated over the optimized array and over the corresponding linear array. Costs are in dB for null depth and degrees for the others.  $C_6$  is not shown since it is not angle dependent. Null depth for linear array is always better than 50dB and out of the graph.

It is apparent, as scan angle gets farther from broadside, how the linear array performs steadily worse, while the optimized array has a clear step down in costs when it passes from the configuration with all 6 elements turned on to one of those with just 4 elements on. It is worth noticing that better results could be achieved with amplitude modulation of the elements, but in this work it has been decided to use phase only synthesis so as to attain a simpler implementation of the real antenna in the future.

To have a better understanding of the performance comparison, Fig. 9 reports the sum and difference patterns for three scan angles, namely 45°, 60° and 90° (broadside).

It is clear from the patterns that the linear array is unusable at 45°, the difference pattern never gets higher than the sum pattern on the left of the main beam, meaning that the effective angle cannot even be defined.

Furthermore, the maximum and the null happen at quite different angles. On the other hand, the optimized array, even if presenting an asymmetry in the effective angle, has a much better behavior.

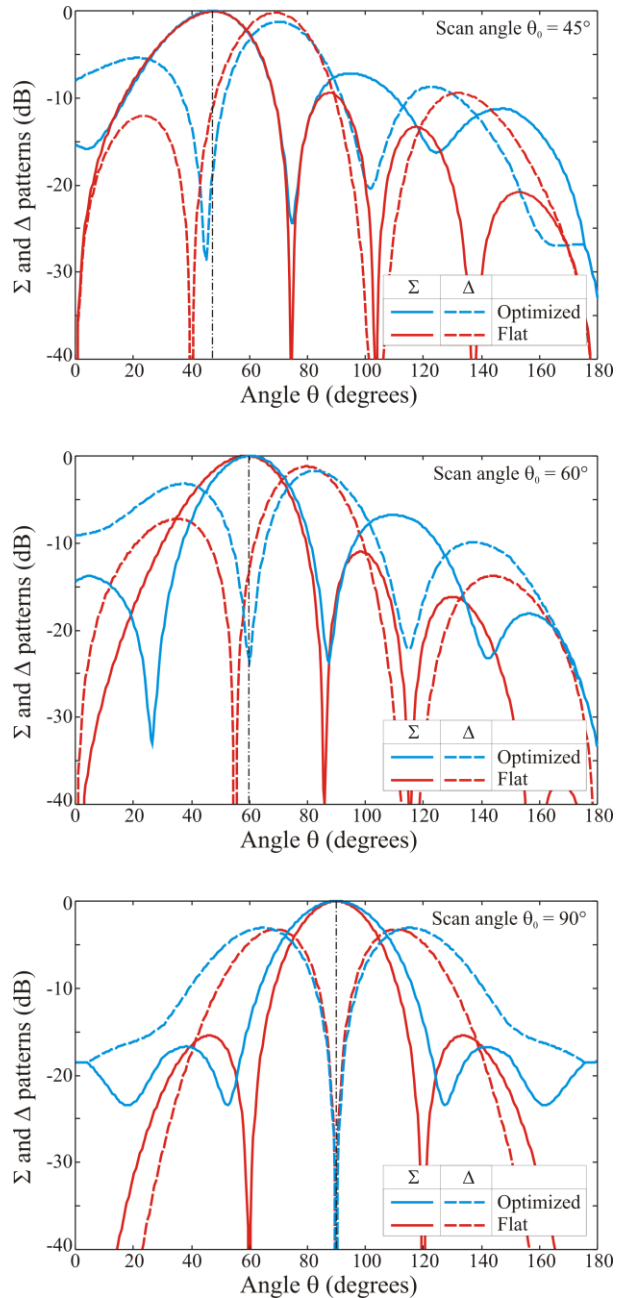


Fig. 9. Patterns for the optimized and linear array a three different scan angles.

The 60° case is less critical and the linear array can be used at that steering, yet the displacement of the null with respect to the maximum is much greater than for the optimized array. The 90° case is of course the best performing for both. It must be noted that, relying on

phase only synthesis, the linear array always has a very deep null thanks to the fact that all elements have the same orientation and hence perfect cancellation can be achieved. On the optimized array, due to different orientation, perfect cancellation is not attained by simply inverting half of the phases. Better null depth is hence possible via a minor optimization on the phase. This can be done via a further optimization, which also should take into account the real digital phase shifter to be used and hence their finite phase increment step.

## V. CONCLUSIONS

By allowing an automatic stochastic MO-IWO optimization on a spline-defined curved array for IFF applications superior scanning performances are attained. Elements are turned on/off on the basis of their boresight direction with respect to scan angle. The convex-concave curve, obtained by optimization, might seem counter-intuitive but *a posteriori* its superior performances can be justified by the increased baseline of the array when scanning. Further studies will be carried out in the future, with full wave simulations on a printed array in this shape to assess its electromagnetic performances also taking into account mutual coupling.

## REFERENCES

- [1] NCS - Federal Standard 1037C – Aug. 7, 1996.
- [2] A. Appelbaum and L. Kaplan, "Sidelobe suppression considerations in the design of an electronically steered IFF antenna," *IEEE Transactions on Antennas and Propagation*, vol. 24, no. 4, pp. 425-432, July 1976.
- [3] G. Giunta, L. Lucci, R. Nesti, G. Pelosi, S. Selleri, and F. Serrano, "A comparison between standard and crossfeed monopulse radars in presence of rough sea scattering and ship movements," *International Journal of Antennas and Propagation*, vol. 2010, p. 9, article ID 126757, 2010.
- [4] S. Maddio, "A circularly polarized switched beam antenna with pattern diversity for WiFi applications," *IEEE Antennas and Wireless Propagation Letters*, vol. 16, pp. 125-128, 2016.
- [5] A. Kreczkowski, T. Rutkowski, A. Buda, and S. Kostka, "The microstrip IFF antenna for the airborne radar," *14th International Conference on Microwaves, Radar and Wireless Communications, MIKON - 2002*, Gdansk, Poland, vol. 3, pp. 922-925, 2002.
- [6] S. Sanchez-Sevilleja, J. L. Masa-Campos, C. Dominguez-Grano-De-Oro, M. Sierra-Perez, and J. L. Fernandez-Jambrina, "Implementation and measurements of monopulse scanning beam planar array in L band for a IFF system," *The Second European Conference on Antennas and Propagation, EuCAP 2007*, Edinburgh, pp. 1-6, 2007.
- [7] S. P. Benham, T. J. Murphy, E. J. Totten, D. J. Knights, and M. Schick, "EM Modelling design of a conformal IFF system on an aircraft," *Proceedings of the Fourth European Conference on Antennas and Propagation*, Barcelona, pp. 1-4, 2010.
- [8] S. Maddio, G. Pelosi, M. Righini, S. Selleri, G. Giunta, and C. Novi, "A graphical method for the preliminary design of phased array antenna," *2018 IEEE Antennas and Propagation Society International Symposium and USNC/URSI National Radio Science Meeting*, Boston, MA, pp. 2105-2106, July 8-13, 2018.
- [9] A. R. Mehrabian and C. Lucas, "A novel numerical optimization algorithm inspired from weed colonization," *Ecol. Inform.*, vol. 1, pp. 355-366, Dec. 2006.
- [10] S. Karimkashi and A. Kishk, "Invasive weed optimization and its features in electromagnetics," *IEEE Trans. Antennas Propagat.*, vol. 58, no. 4, pp. 1269-1278, Apr. 2010.
- [11] S. Karimkashi and A. Kishk, "Antenna array synthesis using invasive weed optimization: A new optimization technique in electromagnetics," *2009 IEEE Antennas and Propagation Society International Symposium*, Charleston, SC, pp. 1-4 2009.
- [12] Y. Li, F. Yang, J. Ouyang, and P. Yang, "Synthesis of conical conformal array antenna using invasive weed optimization method," *ACES Journal*, vol. 28, pp. 1025-2013, 2013.
- [13] B. Bahreini, A. Mallahzadeh, and M. Soleimani, "Design of a meander-shaped MIMO antenna using IWO algorithm for wireless applications," *ACES Journal*, vol. 25, pp. 631-638, 2010.
- [14] S. Maddio, G. Pelosi, M. Righini, and S. Selleri, "A multiobjective invasive weed optimization for broad band sequential rotation networks," *2018 IEEE Antennas and Propagation Society International Symposium and USNC/URSI National Radio Science Meeting*, Boston, MA, pp. 955-956, July 8-13, 2018.
- [15] S. Maddio, G. Pelosi, M. Righini, and S. Selleri, "A comparison between grey wolf and invasive weed optimizations applied to microstrip filters," *2019 IEEE Antennas and Propagation Society International Symposium and USNC/URSI National Radio Science Meeting*, Atlanta, GA, pp. 1-2, 2019.
- [16] H. R. Khakzad, S. H. Sedighy, and M. K. Amirhosseini, "Design of compact SITLs low pass filter by using invasive weed optimization (IWO) technique," *ACES Journal*, vol. 28, pp. 228-233, 2013.
- [17] E. Agastra, G. Pelosi, S. Selleri, and R. Taddei, "Multiobjective optimization techniques," in *The Wiley Encyclopedia of Electrical and Electronics Engineering*, J. Webster, Ed. John Wiley & Sons,

New York (NY), pp. 1-29, 2014.



**Stefano Maddio** was born in Florence, Italy in 1978. He received the Electronic Engineering degree in 2005 and the Ph.D. degree in 2009 from University of Florence. He is currently a Research Fellow at the University of Florence. His current research interests include analysis and design of radiative systems for micro-electronics in the field of smart antenna technology for wireless applications with a particular emphasis on the issues of wireless localization and special-purpose antenna systems for dedicated short range communications, as well modeling of microwave, devices and circuits.



**Giuseppe Pelosi** was born in Pisa, Italy, in 1952. He received the Laurea (Doctor) degree in Physics (summa cum laude) from the University of Florence in 1976. He is currently with the Department of Information Engineering of the same university, where he is currently Full Professor of Electromagnetic Fields. His research activity is mainly focused on numerical techniques for applied electromagnetics (antennas, circuits, microwave and millimeter-wave devices, scattering problems). He was coauthor of several scientific publications on the aforementioned topics, appeared in international refereed journals. He is also coauthor of three books and several book chapters.

Pelosi was elected a Fellow of the IEEE for contributions to computational electromagnetics.



**Monica Righini** was born in Prato (Italy) in 1984. She received the Laurea degree (cum laude) in Telecommunication Engineering and the Ph.D. in Electronic Technologies for Information Engineering from the University of Florence (Italy) in 2011 and 2016, respectively. Her recent interests are mainly in multilayer planar technology radiating boards for space applications and in ultra-wideband electrically small antennas for direction finding on board of unmanned aerial vehicles.



**Stefano Selleri** was born in Viareggio, Italy, on December 9th, 1968. He obtained his degree (Laurea), cum laude, in Electronic Engineering and the Ph.D. in Computer Science and Telecommunications from the University of Florence in 1992 and 1997, respectively. He is author of over 100 papers on international referred journals and eight books or books chapters. He is currently an Assistant Professor at the University of Florence, where he conducts research on numerical modeling of microwave, devices and circuits with particular attention to numerical optimization.



**Irene Vecchi** was born in Montevarchi (AR), Italy in 1994. She received the bachelor in Electronic and Telecommunication Engineering and the master degree in Electronic Engineering, from the University of Florence in 2017 and 2019 respectively, with two thesis on active array antenna design.

# RCS Optimization Analysis Method for Sea-Skimming Unmanned Aerial Vehicle Based on Back Propagation Neural Network Algorithm

Chengpan Yang<sup>1</sup>, Wei Yan<sup>1,2\*</sup>, Yang Zhao<sup>1</sup>, Lu Geng<sup>3</sup>, Shiliang Hou<sup>1</sup>, and Jian Chen<sup>1</sup>

<sup>1</sup> School of Electrical and Automation Engineering  
Nanjing Normal University, Nanjing, Jiangsu, 210097, China  
61197@nynu.edu.cn

<sup>2</sup> Zhenjiang Institute for Innovation and Development  
Nanjing Normal University, Zhenjiang 212004, China

<sup>3</sup> China Energy Engineering Group, Nanjing, Jiangsu, 211102, China

**Abstract** — The radar cross section (RCS) of sea-skimming unmanned aerial vehicle (UAV) can be influenced by the sea surface scattering under different sea conditions. In this paper, a composite model of the rough sea surface and sea-skimming UAV is established. A hybrid algorithm based on the application of physical optics (PO) method and improved multilevel fast multipole algorithm (PO-IMLFMA) for solving the RCS of the composite model based on four-path model (FPM) is proposed. Compared with multilevel fast multipole algorithm (IMLFMA) and PO and method of moment (PO-MOM), PO-IMLFMA has the advantages of less memory consumption (about 295 MB) and faster solution speed (about 768 s) for solving the composite model. Furthermore, in view of the influence of sea surface on the RCS of sea-skimming UAV, a compensation scheme based on back propagation (BP) neural network for the RCS of UAV is proposed. The compensation scheme is analyzed for the monostatic RCS of sea-skimming UAV under different sea conditions. The compensation results show that the compensation errors under 1-scale, 3-scale and 5-scale sea conditions are less than 0.95 dBsm, 0.41 dBsm and 1.94 dBsm, respectively. In other words, the compensation scheme significantly reduces the influence of sea conditions.

**Index Terms** — back propagation (BP) neural network, four-path model (FPM), improved multilevel fast multipole algorithm (IMLFMA), physical optics (PO), Radar cross section (RCS), sea conditions, unmanned aerial vehicle (UAV).

## I. INTRODUCTION

With the rapid development of ocean construction in the world, sea-skimming aircraft has been widely used in quite a few aspects such as ocean reconnaissance and

disaster prevention. The sea-skimming unmanned aerial vehicle (UAV) can fly over the sea at extremely low altitudes when they perform various tasks [1]. The scattering of sea-skimming UAV can be hidden through the help of scattering of sea surface. Radar cross section (RCS) can be used to quantitatively characterize the stealth performance of targets. The electromagnetic scattering characteristics of sea-skimming UAV and the influence of sea clutter on the scattering characteristics of sea-skimming UAV can be analyzed by the study of RCS. The study of composite electromagnetic scattering characteristics of rough sea surface and target is widely used in radar detection, marine remote sensing and military confrontation, and becomes an effective means to solve the problem of radar detection and tracking of sea objects [2]. The RCS of UAV usually varies randomly with time or radar incident angle in the course of flight.

In [3-4], the RCS problem of UAV was considered from different angles. The RCS of three-dimensional (3-D) electrically large object can be calculated by the finite-difference time-domain (FDTD) algorithm [5], method of moments (MOM) [6-7], the multilevel fast multipole algorithm (MLFMA) [8-9], physical optics (PO) and the Kirchhoff Approximation (KA) methods [10-12]. The RCS of the UAV can be calculated accurately by the above numerical algorithms, but the influence of actual environment such as the rough sea surface on the electromagnetic scattering characteristics of targets is not considered.

Common models of the rough sea surface are Pierson-Moskowitz (PM) spectrum [13], Elfouhaily spectrum [14], and Philips spectrum [15]. Rayleigh was one of the first people to propose a mathematical model of rough sea surface [16]. Pino used the Monte Carlo method to construct a one-dimensional sea surface model and analyzed the electromagnetic scattering

characteristics of two-dimensional (2-D) objects above the sea surface by the generalized forward and backward iteration method (GFBM) [17]. In [18], the inhomogeneous fast plane wave algorithm is used to study the composite RCS characteristics of 2-D rough surface and 3-D complex objects above it. However, the RCS of sea-skimming UAV considering the sea conditions is not studied by above methods, and the RCS compensation method for the object under the influence of sea surface is not proposed. In this paper, the RCS of the composite model of the sea-skimming UAV and the 2-D rough sea surface is established based on four-path model (FPM). Then, the RCS of the composite model is calculated and analyzed by the new hybrid numerical method based on the application of the PO method and improved multilevel fast multipole algorithm (IMLFMA).

The RCS value of rough sea surface will affect the RCS value of UAV when solving or measuring the RCS of sea-skimming UAV. In order to eliminate this unnecessary influence, a strong non-linear fitting algorithm - back propagation (BP) neural network algorithm is introduced in this paper [19-20]. The relationship between different incident angles, azimuth angles, RCS values of the rough sea surface, RCS values of composite model and RCS values of sea-skimming UAV is obtained by the nonlinear mapping of BP neural network.

The structure of this paper is organized as follows. A model of rough sea and sea-skimming UAV is established in Section II. In Section III, the RCS of the sea-skimming UAV considering the sea conditions is analyzed by the IMLFMA based on the FPM. A RCS compensation method based on BP neural network for sea-skimming UAV is presented in Section IV. Section V validates and analyzes the algorithm proposed in this paper. Finally, a conclusion is presented in Section VI.

## II. MODELING FOR RCS CALCULATION OF ROUGH SEA SURFACE AND SEA-SKIMMING UAV

### A. Rough sea surface modeling based on Monte Carlo method

The sea conditions studied in this paper are the sea surfaces under different wind and wave scales. The basic parameters of the international sea conditions standard are shown in Table 1. Where W. h. stands for the wave height, W. v. represents the wind velocity. The sea surface model is generally considered to be rough surface within the scope of electromagnetic scattering calculation. Rough surface has strong randomness and can be represented by relevant statistical parameters, including power spectral density, root mean square deviation, correlation function, root mean square slope, and radius of curvature.

Table 1: Parameters of international sea conditions standard

Scale	Name	W. h. (m)	W. v. (m/s)
1	Tiny wave	0 - 0.30	0 - 3.08
2	Middle wave	0.91 - 1.52	6.17 - 7.71
3	Billow	2.44 - 3.66	10.28 - 12.85

The power spectrum, known as the wave spectrum, is the most important statistical parameter in rough sea surface modeling. It reflects the distribution of harmonic components in azimuth and spatial frequency, and is the result of Fourier transform of sea surface height fluctuation correlation function. In this paper, the rough sea surface is modeled based on the PM spectrum under different wind speeds. The PM spectrum is:

$$S(\omega) = \alpha \frac{g^2}{\omega^5} \exp\left\{-\beta \left(\frac{g}{U\omega}\right)^4\right\}, \quad (1)$$

where  $\alpha=8.1 \times 10^{-3}$  and  $\beta=0.74$  are dimensionless empirical constants,  $g$  is the gravitational acceleration,  $g = 9.81 \text{ m/s}^2$ ,  $U$  is the average wind speed at a height of 19.5 m above the sea surface and  $\omega$  is angular frequency.

The randomly rough sea surface model under different sea conditions is simulated by Monte Carlo method. The main principle is to filter the power spectrum in the frequency domain and then the inverse fast Fourier transform is performed to obtain the discrete height values of the rough surface.

A two-dimensional rough sea surface of size  $D_x \times D_y$  needs to generate  $N \times M$  grids in the  $x$  and  $y$  directions with  $\Delta x$  and  $\Delta y$  as the steps. The height  $z = f(x_n, y_m)$  of each point on the rough surface at  $(x_n = n\Delta x, y_m = m\Delta y)$ , ( $n = -N/2 + 1, \dots, N/2$ ;  $m = -M/2 + 1, \dots, M/2$ ) can be expressed as:

$$f(x_n, y_m) = \frac{1}{D_x D_y} \times \sum_{p=-\frac{N}{2}+1}^{\frac{N}{2}} \sum_{q=-\frac{M}{2}+1}^{\frac{M}{2}} F(k_{x,p}, k_{y,q}) e^{-jk_{x,p}x_n} e^{-jk_{y,q}y_m}, \quad (2)$$

where  $F$  is a coefficient, given by,

$$F(k_{x,p}, k_{y,q}) = 2\pi \sqrt{D_x D_y} W(k_{x,p}, k_{y,q}) \times \begin{cases} \frac{N(0,1) + iN(0,1)}{\sqrt{2}} & p=1, \dots, \frac{N}{2}-1; q=1, \dots, \frac{M}{2}-1, \\ N(0,1) & p=0, \frac{N}{2}; q=0, \frac{M}{2} \end{cases} \quad (3)$$

where  $k_{x,p}$  stands for the coefficient related to the  $x$  direction whereas  $k_{y,q}$  is the coefficient related to the  $y$  direction. Specifically  $k_{x,p} = 2\pi p/D_x$ ,  $k_{y,q} = 2\pi q/D_y$ .

In order to generate 2-D rough surfaces of real sequence,  $F(k_{x,p}, k_{y,q})$  must be conjugate symmetric with respect to the origin as shown in (4) and (5):

$$F(-k_{x,p}, -k_{y,q}) = F^*(k_{x,p}, k_{y,q}), \quad (4)$$

$$F(k_{x,p}, -k_{y,q}) = F^*(-k_{x,p}, k_{y,q}). \quad (5)$$

The PM spectrum is selected as the power spectrum and converted into polar coordinate form as:

$$W(k_{x,p}, k_{y,q}) = W_1(K, \phi), \quad (6)$$

where  $K = \sqrt{k_{x,p}^2 + k_{y,q}^2}$ ,  $\phi = \arctan(k_{y,q}/k_{x,p})$ .

The PM spectrum  $W_1(K, \phi)$  can be solved by:

$$W_1(K, \phi) = \Phi(K, \phi) \frac{\bar{W}(K)}{K}, \quad (7)$$

$$\bar{W}(K) = \begin{cases} S(\omega) \sqrt{g/K} / 2 & K > 0 \\ 0 & K < 0 \end{cases}, \quad (8)$$

where  $S(\omega)$  ( $\omega = \sqrt{gK}$ ) can be obtained by (1). If rough surface is approximately isotropic,  $\Phi(K, \phi) = 1/(2\pi)$ .

According to (2), sea surface models under different wind speeds can be simulated. Referring to the Table 1, the sea surface models under 1-scale sea condition with 1 m/s wind speed, 3-scale sea condition with 7 m/s wind speed and 5-scale sea condition with 12 m/s wind speed are established respectively, as shown in Fig. 1.

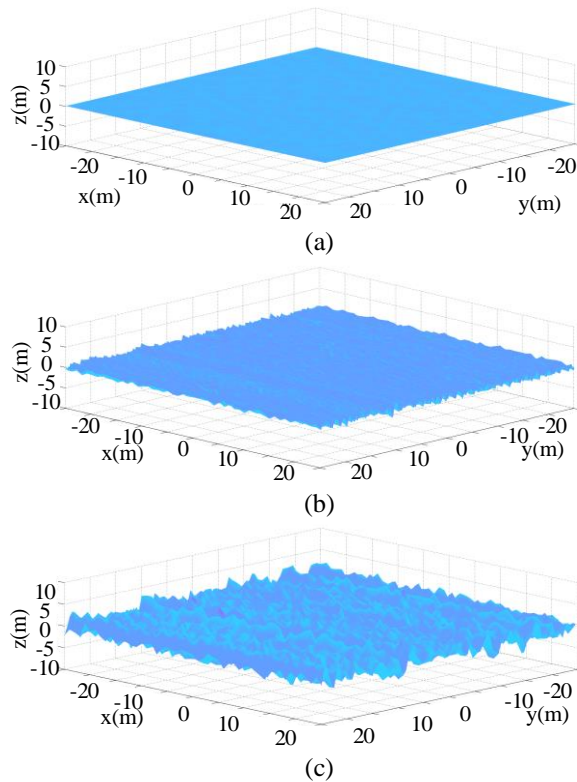


Fig. 1. Sea surface model under different sea conditions. (a) 1-scale Sea condition (wind speed 1 m/s). (b) 3-scale sea condition (wind speed 7 m/s). (c) 5-scale sea condition (wind speed 12 m/s).

## B. Construction of RCS calculation model for sea-skimming UAV

The RCS calculation model of sea-skimming UAV is established especially for the electromagnetic scattering problem. The electromagnetic scattering characteristics of each component of UAV have some degree impact on the RCS of the entire aircraft. Therefore, the scattering contribution of components is also considered in the structural design of UAV besides aerodynamic requirements. Compared with strong scattering components, some details of UAV have little contribution to the total scattering field, which can be neglected. So the RCS calculation model of sea-skimming UAV focuses on the components with strong scattering contribution. The following components are considered in UAV modeling:

1) Wing and tail. The wing is modeled with a twist-free wing, so the front and rear edges of the wing are not considered. The parameters of the tail are similar to those of the wing, but the angle between the flat tail and the vertical tail should be taken into account, because the incident electromagnetic waves will be reflected multiple times between the flat tail and the vertical tail.

2) Fuselage. The fuselage is the main part of the modeling. The position of the main axis and the shape parameters of the fuselage need to be considered. The shape structure of fuselage, the curve parameters of top, bottom, side and cross section must be considered in the process of modeling.

3) Inlet port. The inlet is a cavity, and its internal structure has a great influence on the scattering. The detailed geometry of the inlet should be taken into account when modeling. The main parameters include the lip curve, the top, bottom, side and cross section curve.

Referring to the parameters of a type of sea-skimming UAV, the model has a wingspan of 7.1 m, a fuselage length of 2.6 m and a height of 0.87 m. The surface material of the model is conventional metal conductor. The model is built in the FEKO software, as shown in Fig. 2. The  $\mathbf{k}_i$  and  $\mathbf{k}_s$  are the unit vectors of incident and scattering directions of the radar wave, respectively.  $\theta_i$  is the incident angle of the radar wave,  $\varphi_i$  is the azimuth angle of the radar wave,  $\theta_s$  is the scattering angle of the radar wave,  $\varphi_s$  is the azimuth angle of the scattering wave, and  $\gamma$  is the bistatic angle.  $\mathbf{h}_i$  and  $\mathbf{v}_i$  are unit vectors of horizontal and vertical polarization directions of incident electromagnetic waves, respectively.

The RCS  $\sigma$  is independent of  $R$  when the  $R$  is large enough to satisfy the far field condition.  $R$  is the distance between radar and UAV. The far field RCS of UAV is:

$$\sigma = \lim_{R \rightarrow \infty} 4\pi R^2 \frac{|\mathbf{E}_s|^2}{|\mathbf{E}_i|^2}, \quad (9)$$

where  $\mathbf{E}_s$  is the intensity of scattered electric field and  $\mathbf{E}_i$



is the intensity of incident electric field. The RCS of the UAV in HH polarization  $\sigma_{hh}$  and VV polarization  $\sigma_{vv}$  are:

$$\sigma_{hh} = \lim_{R \rightarrow \infty} 4\pi R^2 \frac{|E_s^h|^2}{|E_i^h|^2}, \quad (10)$$

$$\sigma_{vv} = \lim_{R \rightarrow \infty} 4\pi R^2 \frac{|E_s^v|^2}{|E_i^v|^2}, \quad (11)$$

where  $E_s^h$ ,  $E_s^v$ ,  $E_i^h$ , and  $E_i^v$  are the horizontal and vertical polarization components of  $E_s$  and  $E_i$ , respectively.

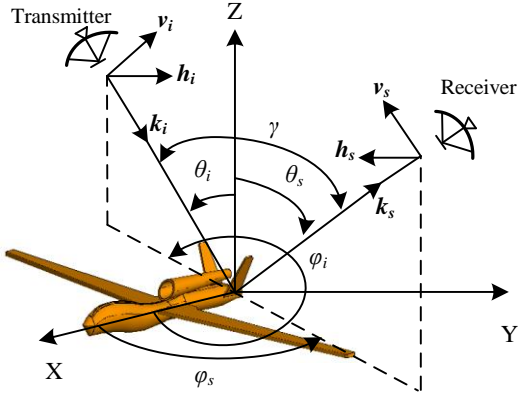


Fig. 2. Simulation model of sea-skimming UAV.

### III. RCS ANALYSIS OF SEA-SKIMMING UAV AND ROUGH SEA SURFACE

#### A. RCS analysis method of rough sea surface

The hardware requirement is high and the computing time is long when the numerical algorithm is used to accurately solve the scattered field of rough sea surface. Accordingly, the PO method based on high frequency approximation is applied to calculate the RCS of rough sea surface quickly. The scattering field of rough sea surface is calculated by the KA method. In the mode of long distance detection of high frequency radar wave, the radius of curvature of rough sea surface is larger than the wavelength and the far field condition is satisfied, so the calculation of scattering field of rough sea surface satisfies the application condition of the PO method.

The PO method uses the induced current on rough sea surface as the source of scattering field, and then integrates the surface current to obtain the scattering field. The scattering field is obtained by integrating the surface current. Figure 3 is a geometric schematic diagram of rough sea surface scattering. The  $\mathbf{r}'_{sea}$  is the position vector of scattering source point on rough sea surface and  $\mathbf{r}_{sea}$  is the position vector of receiving point. When the plane wave irradiates the rough sea surface, the magnetic vector potential at the receiving point  $P$

the scattered wave is:

$$\mathbf{A}_{sea}(\mathbf{r}_{sea}) = \frac{\mu_{sea}}{4\pi} \iint_{S_{sea}} \mathbf{J}_{sea}(\mathbf{r}'_{sea}) \frac{e^{-jkR_{sea}}}{R_{sea}} dS_{sea}, \quad (12)$$

where  $\mathbf{J}_{sea}(\mathbf{r}'_{sea})$  and  $dS_{sea}$  are the induced current density and element area at the scattering source point on the sea surface, respectively.  $\mu_{sea}$  is the sea surface permeability,  $\mathbf{k}$  is the wave vector,  $k = |\mathbf{k}| = 2\pi/\lambda$ ,  $\lambda$  is the wavelength,  $R_{sea}$  is the distance from the receiving point to the scattering source point,  $R_{sea} = |\mathbf{r}_{sea} - \mathbf{r}'_{sea}|$ .

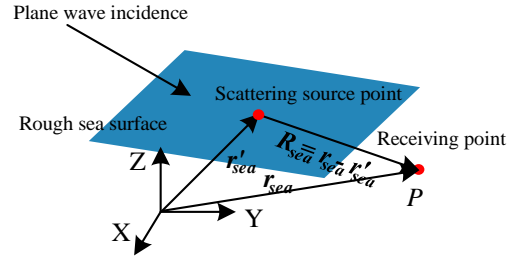


Fig. 3. Geometric schematic diagram of scattering from two-dimensional rough sea surface.

From (12) and far field condition  $|\mathbf{k}R| \gg 1$ , the scattering electric field of the sea surface is:

$$\mathbf{E}_{sea}(\mathbf{r}_{sea}) = \frac{-k^2}{j\omega\epsilon_{sea} \cdot 2\pi} \iint_{S_L} \mathbf{R}_{sea} \times [\mathbf{R}_{sea} \times (\mathbf{n}_{sea} \times \mathbf{H}_i)] \cdot \frac{e^{-jkR_{sea}}}{R} dS_L, \quad (13)$$

where  $S_L$  is the bright area of the scattering object,  $\epsilon_{sea}$  is the dielectric constant of the sea surface, and  $\mathbf{n}_{sea}$  is the bin normal unit vector of the scattering source point on the rough sea surface.

The expressions of the incident electric field  $\mathbf{E}_i$  and the incident magnetic field  $\mathbf{H}_i$  are:

$$\mathbf{E}_i(\mathbf{r}'_{sea}) = \mathbf{E}_0 e^{-jk\mathbf{r}'_{sea}}, \quad (14)$$

$$\mathbf{H}_i(\mathbf{r}'_{sea}) = \frac{1}{\eta} \mathbf{k}_0 \times \mathbf{E}_i(\mathbf{r}'_{sea}), \quad (15)$$

where  $\mathbf{k}_0$  is the unit vector of the direction of wave vector and  $\eta$  is the wave impedance. The RCS values of rough sea surface can be obtained by substituting (13) and (14) into (15).

#### B. Optimal method for RCS solution of sea-skimming UAV

Under the incident electric field  $\mathbf{E}_i$ , the scattering electric field generated by surface current of the UAV is as follows:

$$\mathbf{E}_{UAV}(\mathbf{r}_{UAV}) = -j\omega\mathbf{A}_{UAV}(\mathbf{r}_{UAV}) - \nabla\phi_{UAV}(\mathbf{r}_{UAV}), \quad (16)$$

where  $j$  stands for the imaginary symbol,  $\mathbf{r}_{UAV}$  is the field coordinate vector of receiving point,  $\mathbf{A}_{UAV}(\mathbf{r}_{UAV})$  is the magnetic vector potential of the UAV, and  $\phi_{UAV}(\mathbf{r}_{UAV})$  is the scalar potential of UAV.  $\mathbf{A}_{UAV}(\mathbf{r}_{UAV})$  and  $\phi_{UAV}(\mathbf{r}_{UAV})$

are as follows:

$$\mathbf{A}_{UAV}(\mathbf{r}_{UAV}) = \frac{\mu_{UAV}}{4\pi} \iint_{S_{UAV}} \mathbf{J}_{UAV}(\mathbf{r}'_{UAV}) \frac{e^{-jkR_{UAV}}}{R_{UAV}} dS_{UAV}, \quad (17)$$

$$\phi_{UAV}(\mathbf{r}_{UAV}) = \frac{-1}{4\pi j\omega\epsilon_{UAV}} \iint_{S_{UAV}} \nabla_S \mathbf{J}_{UAV}(\mathbf{r}'_{UAV}) \cdot \frac{e^{-jkR_{UAV}}}{R_{UAV}} dS_{UAV}, \quad (18)$$

where  $\mu_{UAV}$  and  $\epsilon_{UAV}$  are the permeability and dielectric constant of the UAV conductor,  $\mathbf{r}'_{UAV}$  is the coordinate vector of scattering source point,  $R_{UAV} = |\mathbf{r}_{UAV} - \mathbf{r}'_{UAV}|$  is the distance from the scattering source point to the receiving point, and  $\mathbf{J}_{UAV}(\mathbf{r}'_{UAV})$  denotes the current density at scattering source point of the UAV surface  $S_{UAV}$ ,  $\nabla_S$  is the divergence operator.

It can be seen from (16) that the RCS value of UAV can be obtained by calculating the surface current density. The approximately current distribution of the surface of the UAV can be obtained by the PO method. The difference between the unknown current and the PO current is closer to zero vector. The improvement of computational efficiency can be achieved by using the difference vector instead of the unknown vector.

The conventional MLFMA is an improvement of the MOM, but the initial value of iterative solution of the MLFMA is usually set to zero, which leads to a large gap with the actual target surface current distribution. Therefore, the IMLFMA based on the PO current distribution is proposed to solve the RCS of the UAV in this paper. The iteration times and the computing time are the focus of the proposed algorithm.

The PO surface current density of the UAV expanded by the Rao-Wilton-Glisson (RWG) basis functions can be expressed as:

$$\mathbf{J}_{UAV}(\mathbf{r}'_{UAV}) = \frac{1}{2} \mathbf{n}_{UAV} \times \mathbf{H}_i(\mathbf{r}_{UAV}) = \sum_{n=1}^{N_{PO}} a_n f_n(\mathbf{r}_{UAV}), \quad (19)$$

where  $a_n$  is the scalar coefficient to be calculated and  $f_n$  is the basis function of an orthogonal complete set,  $n = 1, 2, \dots, N_{PO}$ .  $\mathbf{n}_{UAV}$  is the normal unit vector of the surface of the UAV. The coefficient of the basis function can be obtained by:

$$\begin{aligned} & \int_{S_{UAV}} f_n(\mathbf{r}_{UAV}) \cdot \frac{1}{2} \mathbf{n}_{UAV} \times \mathbf{H}_i(\mathbf{r}_{UAV}) d\mathbf{r}_{UAV} \\ & = \sum_{n=1}^{N_{PO}} a_n \int_{S_{UAV}} f_n(\mathbf{r}_{UAV}) f_n(\mathbf{r}_{UAV}) d\mathbf{r}_{UAV} \end{aligned} \quad (20)$$

Assume that the impedance matrix equation is:

$$[\mathbf{Z}_{mn}][\mathbf{I}_n] = [\mathbf{V}_m], \quad (21)$$

where  $[\mathbf{Z}_{mn}]$  is a general impedance matrix of order  $M_{exc} \times N_{PO}$ ,  $[\mathbf{I}_n]$  is an unknown matrix of order  $N_{PO} \times 1$  and  $[\mathbf{V}_m]$  is an excitation matrix of order  $M_{exc} \times 1$ . The elements in the matrix are  $I_n = a_n$ ,  $Z_{mn}$  and  $V_m$  are inner product of  $Z_{mn} = \langle t_m, \mathbf{L}(f_n) \rangle$ ,  $V_m = \langle t_m, g_{exc} \rangle$ , respectively.

Where  $\mathbf{L}$  stands for a linear operator,  $g_{exc}$  denotes an excitation function and  $t_m$  ( $m = 1, 2, \dots, M_{exc}$ ) is a weight function. For iterative algorithms, the iteration times usually depends on the impedance matrix and the excitation vector. Different excitation vectors  $[V_m]$  need different iteration times when the impedance matrix  $[\mathbf{Z}_{mn}]$  is the same. For the same model, less step is needed to iterate if the surface current is relatively smooth. The iteration times of (21) is zero when there is no incident plane wave. The PO current is used as a correcting current to make  $[V_m]$  approach to zero, which can reduce the iteration times and improve the calculation efficiency.

The form of sparse matrix equation (20) is:

$$[\mathbf{Z}'_{nm}][\mathbf{I}'_0] = [\mathbf{V}'_m], \quad (22)$$

where

$$\mathbf{Z}'_{nm} = \int_{S_{UAV}} f_m(\mathbf{r}_{UAV}) f_n(\mathbf{r}_{UAV}) d\mathbf{r}_{UAV}, \quad (23)$$

$$\mathbf{V}'_m = \int_{S_{UAV}} f_m(\mathbf{r}_{UAV}) \cdot \frac{1}{2} \mathbf{n}_{UAV} \times \mathbf{H}_i(\mathbf{r}_{UAV}) d\mathbf{r}_{UAV}. \quad (24)$$

The local current vector  $[\mathbf{I}'_0]$  is extended to the overall current vector  $[\mathbf{I}_0]$ , and the  $[\mathbf{I}'_0]$  distribution of the original element is retained. Substituting  $[\mathbf{I}_n - \mathbf{I}_0]$  into (21):

$$[\mathbf{Z}_{nm}][\mathbf{I}_n - \mathbf{I}_0] = [\mathbf{V}_m] - [\mathbf{Z}_{nm}][\mathbf{I}_0]. \quad (25)$$

The right part of the equation can be expressed as:

$$[\mathbf{V}_0] = [\mathbf{Z}_{nm}][\mathbf{I}_0]. \quad (26)$$

Replace the initial vector with a zero vector:

$$[\mathbf{Z}_{nm}][\mathbf{I}_x] = [\mathbf{V}_m] - [\mathbf{V}_0]. \quad (27)$$

The iterative algorithm is used to solve the matrix equation of (27). After the iterative operation is finished, the calculation result is corrected by  $[\mathbf{I}_0]$ , and the final solution of the electromagnetic scattering problem is:

$$[\mathbf{I}_n] = [\mathbf{I}_x] + [\mathbf{I}_0]. \quad (28)$$

As can be seen from the above process that the PO current matrix is relatively easy to obtain and requires only a small storage space, so the process of solving the impedance matrix equation is also less time consuming. Although another matrix vector multiplication operation is required before the start of the iteration of (27), the total solution time is not significantly increased. After the improvement, the vector  $[\mathbf{V}_m] - [\mathbf{Z}_{nm}][\mathbf{I}_0]$  is closer to zero vector than the vector  $[\mathbf{V}_m]$ . Less iterative steps are required during the iterative process to obtain the results of the calculation. Consequently, the IMLFMA based on the PO current can be used to calculate the RCS of UAV quickly and accurately.

### C. RCS solution model of sea-skimming UAV and rough sea surface based on FPM

Strict iteration requires too much memory and computing time to solve the coupled electromagnetic scattering between rough sea surface and UAV. The FPM has become one of the most effective models for

solving the coupled scattering field [21]. The FPM has been verified to be able to correctly solve the main electromagnetic scattering between the target object and the sea surface. The FPM can be further simplified using the quasi-mirror method, as shown in Fig. 4.

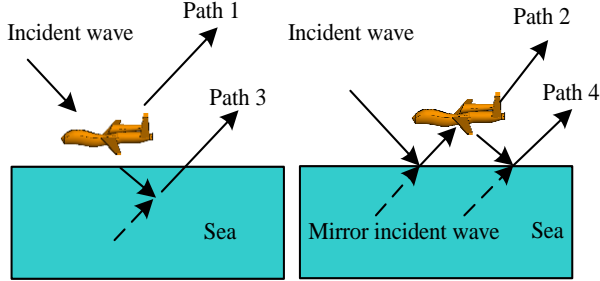


Fig. 4. Simplified four-path model.

According to the idea of the FPM, the composite scattering of rough sea surface and UAV includes the scattering electric field  $E_{UAV}$  of the UAV, the scattering electric field  $E_{sea}$  of the sea surface and the coupling scattering  $E_{co}$  between the sea surface and the UAV. The composite RCS  $\sigma_c$  of rough sea surface and UAV can be obtained by the hybrid algorithm of the PO method and the IMLFMA (PO-IMLFMA) based on the FPM, as shown in the following formula:

$$\sigma_c = 4\pi \lim_{R \rightarrow \infty} R^2 |E_{UAV} + E_{sea} + E_{co}|^2 / |E_i|^2, \quad (29)$$

where  $R$  is the distance from the receiving point to the scattering source point.  $E_{UAV}$  is obtained by the IMLFMA.  $E_{sea}$  is obtained by the PO method. It can be seen from Fig. 4 that the coupled scattering field contains the scattering contribution of the path 2 - 4. The coupling scattering between the sea surface and the UAV is:

$$E_{co} = E_{os}^{second} + E_{so}^{second} + E_{sos}^{third}, \quad (30)$$

where  $E_{os}^{second}$  is the secondary coupling scattering of ‘‘UAV-Sea Surface’’.  $E_{so}^{second}$  is the secondary coupling scattering of ‘‘Sea Surface-UAV’’.  $E_{sos}^{third}$  is the third coupling scattering of ‘‘Sea Surface-UAV-Sea Surface’’. As shown in Fig. 4, combined with the quasi-mirror method, the coupling scattering calculation between UAV and sea surface can be further simplified by using the mirror radar and mirror UAV instead of the reflection of rough sea surface. A correlation reflection coefficient  $E_{co}$  is defined to simulate the reflection of sea rough surface in the calculation:

$$E_{co} = rE_{UAV}^{i-s'} + rE_{UAV}^{i'-s} + r^2E_{UAV}^{i'-s'}, \quad (31)$$

where  $r$  is the position of the receiving point.  $E_{UAV}$  is the scattering electric field of the UAV, the superscripts  $i'$  and  $s'$  are the mirror directions of the incident direction  $i$  and scattering direction  $s$ , respectively.

#### IV. RCS COMPENSATION METHOD FOR SEA-SKIMMING UAV BASED ON BP NEURAL NETWORK

In practice, the RCS value of UAV that is not affected by any interference is what we really need. However, the RCS of sea-skimming UAV is seriously affected by the sea conditions. The RCS values measured directly cannot accurately reflect the actual situation of UAV. Therefore, a RCS compensation model of sea-skimming UAV based on BP neural network is presented in this paper. The relationship between the input factors and the RCS values of sea-skimming UAV can be mapped by BP neural network as shown in Fig. 5.

In actual RCS measurements, it is easy to obtain the direction of incident wave, the azimuth angle, the RCS value of sea surface and the composite RCS value of target object and sea surface. Therefore, the input factors  $X$  are expressed by:

$$X = (\theta_i, \varphi_i, \sigma_{sea}, \sigma_c)^T, \quad (32)$$

where  $\theta_i$  ( $^\circ$ ) represents the incident angle,  $\varphi_i$  ( $^\circ$ ) represents the azimuth angle of airborne detection radar,  $\sigma_{sea}$  (dBsm) represents the monostatic RCS value of sea surface and  $\sigma_c$  (dBsm) stands for composite monostatic RCS value of sea surface and UAV. The number of neurons in the input layer is 4. The output factor  $Y$  is represented by:

$$Y = \sigma_{UAV}, \quad (33)$$

where  $\sigma_{UAV}$  (dBsm) represents monostatic RCS value of sea-skimming UAV. The number of neurons in the output layer is 1. The number of neurons in the hidden layer is an empirical range integral value  $h$  affected by the number of neurons in the input and output layers. The detailed calculation of  $h$  is:

$$h = \sqrt{5} + c, \quad (34)$$

where  $c$  denotes a constant in the interval  $[0,10]$ , which the specific value depends on the actual situation.

The BP neural network of sea-skimming UAV is a small and middle neural network, so one hidden layer is adopted. The transfer function of the hidden layer is set to the sigmoid function. The output layer transfer function of the BP neural network of the sea-skimming UAV is taken as a linear function. In the process of forward propagation of BP neural network, the information is transmitted from the input layer to the output layer and processed by each layer. The output of the neural network is:

$$y_1 = \sum_{j=1}^h \frac{v_{j1}}{\exp\left[-\sum_{i=1}^4 (w_{ij}x_i + \theta_j)\right] + 1} + b_1, \quad (35)$$

where  $w_{ij}$  is the weight between the  $i$ -th neuron of the input layer and the  $j$ -th neuron of the hidden layer, and  $v_{jk}$  is the weight between the  $j$ -th neuron of the hidden layer and the  $k$ -th neuron of the output layer,  $\theta_j$  is the

threshold of the  $j$ -th neuron in the hidden layer, and  $b_1$  is the threshold of the output layer neuron.

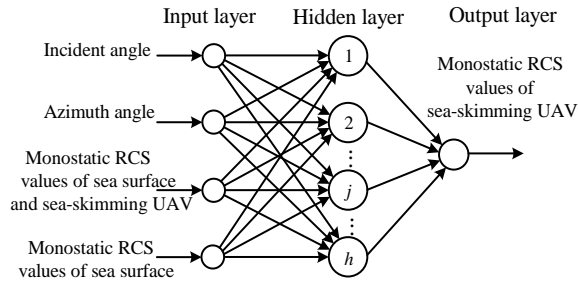


Fig. 5. Topological structure of RCS compensation model for sea-skimming UAV based on BP neural network.

When the results of output layer do not meet the requirements of the target, the information is transferred to the backpropagation state, and the error signal is returned back along the original path. In this process, the weights of the neurons in each layer will be modified sequentially, and the error signal can meet the mean square error accuracy requirement through repeated iterations.

The weights and thresholds of the hidden layer and the output layer are adjusted in a similar way, taking the output layer as an example here. Assuming that there are  $n$  training samples, and the mean square error of the  $i$ -th training sample is:

$$e = \frac{1}{2} (\sigma_{UAV0}^i - \sigma_{UAV}^i)^2, \quad (36)$$

where  $\sigma_{UAV0}^i$  and  $\sigma_{UAV}^i$  are the exact and actual output values of the neuron for the  $i$ -th RCS sample, respectively. The weights and thresholds of each layer are adjusted by the Levenberg-Marquardt (L-M) algorithm. The specific adjustment way of weights is:

$$w_{k+1} = w_k + \Delta w_k, \quad (37)$$

$$\Delta w_k = -[J^T(w_k)J(w_k) + \mu I]^{-1} J^T(w_k) \cdot e, \quad (38)$$

where  $w_k$  and  $w_{k+1}$  are the weights before and after the adjustment of each layer.  $J$  is a Jacobi matrix of the error  $e$  with respect to the weight  $w$ .  $\mu$  is a scalar factor, and  $I$  is an identity matrix. The L-M algorithm controls the iteration speed by changing the value of  $\mu$  in the iteration process of the sea-skimming UAV neural network, so as to ensure that the calculation speed can be improved under the condition that the accuracy requirement is met.

The neural network stops training and outputs weights and thresholds when the global error  $E$  of the trained network satisfies the target requirement or the training iteration number reaches the maximum iteration number. The global error  $E$  can be expressed as:

$$E = \frac{1}{2n} \sum_{i=1}^n (\sigma_{UAV0}^i - \sigma_{UAV}^i)^2. \quad (39)$$

## V. VERIFICATION AND ANALYSIS

The centimeter wave radar is often used to detect targets in the maritime and aerial field, so the calculation frequency is generally set above 2 GHz. In this paper, the incident frequency is set to 3 GHz, and the corresponding wavelength  $\lambda = 0.1$  m. The electric size of the UAV is about  $71 \lambda$ . This type of sea-skimming UAV is an electrically large size object. The excitation source is approximately plane wave. The azimuth angle of scattering wave is  $0^\circ$  at the head, and  $180^\circ$  at the tail of the UAV.

The composite RCS calculation model is obtained by combining the sea surface model and the sea-skimming UAV model in different sea conditions, as shown in Fig. 6. The reference model of the sea surface is located in the XOY plane, and the relative dielectric constant of seawater is 81.5. The size of sea surface is  $500 \lambda \times 500 \lambda$ .

This paper mainly studies an extremely low flying UAV over the very large size sea surface. The small range of variation of the flying height of the sea-skimming UAV has a weak influence on the coupling scattering, so the influence of a small range of variation in the flight height can be neglected. The vertical height  $h$  of the center point of the UAV from the sea surface is set to 15 m.

### A. Verification of RCS solution method for UAV and rough sea surface

In order to verify the solving accuracy, the operation efficiency and hardware memory requirements of the PO-IMLFMA method based on the FPM for the composite RCS of rough sea surface and sea-skimming UAV, this paper uses the PO-MOM method based on the FPM and the conventional MLFMA as contrast methods to solve and analyze the RCS of composite model. When using the PO-IMLFMA method, the RCS of sea surface is solved by the PO method and the RCS of UAV is solved by the IMLFMA. Similarly, the RCS of sea surface and UAV are solved respectively by the PO method and the MOM when using the PO-MOM algorithm. The MLFMA is an accurate method, which can provide high accuracy for solving RCS values [22]. The incident angle  $\theta_i$  is  $40^\circ$  and the azimuth angle  $\varphi_i$  of incident wave is  $90^\circ$ , the scattering azimuth angle  $\varphi_s$  is  $90^\circ$ , and the scattering angle  $\theta_s$  ranges from  $[-90^\circ, 90^\circ]$ .

The calculation results of the composite bistatic RCS of sea surface and sea-skimming UAV solved by three algorithms are shown in Fig. 7. The RCS calculation results of the three algorithms under the VV polarization and HH polarization are generally

consistent. The calculation results of the PO-IMLFMA method based on the FPM and the PO-MOM method based on the FPM are close, and the RCS values at some scattering angles are smaller than those of the conventional MLFMA, because the model of rough sea surface is solved approximately by the PO algorithm. The accuracy of the hybrid algorithm is limited in calculating the scattering field of some angles, but the error is small, and does not affect the overall composite RCS analysis.

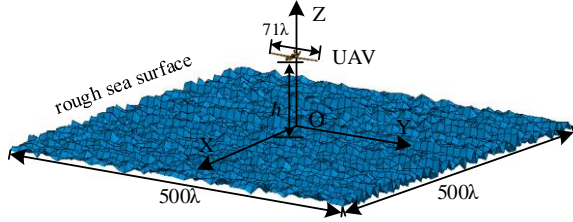


Fig. 6. Composite RCS calculation model of rough sea surface and sea-skimming UAV.

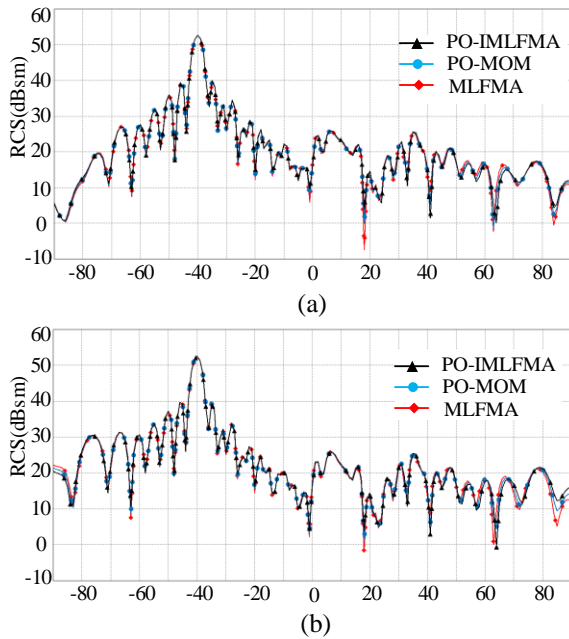


Fig. 7. Comparison of the bistatic RCS results for the composite model of rough sea surface and sea-skimming UAV calculated by different methods. (a) VV polarization. (b) HH polarization.

Table 2: Comparison between PO-IMLFMA, PO-MOM and MLFMA method (VV Polarization)

Method	Memory (MB)	Computing Time (s)
PO-IMLFMA	295	768
PO-MOM	751	2963
MLFMA	1765	5687

The memory requirement and computing time of the three methods in the VV polarization are compared as shown in Table 2. It is obvious from the data in the table that the memory required by the two hybrid algorithms is much less than that of the MLFMA, and the computational efficiency is much higher than the MLFMA. Compared with the PO-MOM method, the PO-IMLFMA method saves more memory space and less computation time. This is due to the fact that the memory consumption and computational complexity of the IMLFMA are lower than those of the MOM when calculating the composite model RCS for UAV area alone, which leads to lower memory consumption and higher computational efficiency when using the PO-IMLFMA hybrid algorithm. The results verify that the hybrid algorithm of the PO-IMLFMA method based on FPM can effectively and efficiently analyze the composite RCS of sea-skimming UAV under different sea conditions.

## B. RCS compensation of sea-skimming UAV under different sea conditions

The RCS compensation model topology of sea-skimming UAV in Fig. 5 is adopted. In order to ensure the generality of training samples and combine the actual situation of monostatic RCS of sea-skimming UAV, the range of incident angle  $\theta_i$  is  $[10^\circ, 80^\circ]$ , and the interval is  $10^\circ$ , the range of azimuth angle  $\phi_i$  is  $[0, 360^\circ]$ , and the interval is  $5^\circ$ . The composite monostatic RCS samples  $\sigma_c$  of BP neural network are obtained by PO-IMLFMA method proposed above. The monostatic RCS value  $\sigma_{sea}$  of sea surface and the monostatic RCS value  $\sigma_{UAV}$  of UAV are calculated by the PO method and the IMLFMA, respectively. The detailed relationships are shown in Fig. 8. The number of training samples under the 1-scale, 3-scale and 5-scale sea conditions is 1752 ( $3 \times 8 \times 73$ ) groups. The maximum number of iterations is set to 100. The data of some training samples is shown in Table 3. The number of the hidden layer  $h$  is 9. The RCS compensation model of sea-skimming UAV based on BP neural network can be obtained after training the sample data of sea-skimming UAV.

On the platform of VV polarized airborne radar, the RCS compensation model of sea-skimming UAV based on BP neural network is used to compensate the monostatic RCS under the 1-scale, 3-scale and 5-scale sea conditions. To verify the validity of the compensation model, the incident angle and azimuth angle data of the selected test samples are different from the training samples. The incident angles are  $65^\circ$ ,  $45^\circ$  and  $25^\circ$ . The range of azimuth angle is  $[0, 360^\circ]$ , and the interval is  $1^\circ$ . The RCS compensation results of sea-skimming UAV under the 1-scale, 3-scale and 5-scale sea conditions are shown in Fig. 9, Fig. 10 and Fig. 11, respectively. The uncompensated result stands for the monostatic RCS values of the sea-skimming UAV affected by sea

conditions. The expected value stand for the RCS of sea-skimming UAV under the same detection conditions. The compensated result stand for the monostatic RCS of sea-skimming UAV generated by the compensation network. It can be seen from Figs. 9-11 that the overlap ratio of compensation results and the expected values of different sea conditions is higher when the incident angle is  $65^\circ$  and  $45^\circ$ . However, the overlap ratio of curves decreases obviously when the incident angle is  $25^\circ$ . This is due to the fact that the detection radius of UAV detected by airborne radar at low incident angle is small at the same altitude, and the variation of RCS with the azimuth angle is not obvious. The smaller the incident angle is, the closer the detection direction is to vertical overlooking, and the contribution of sea surface scattering is stronger. The scattering characteristics of UAV are almost completely covered up by the sea surface when the incident angle is small.

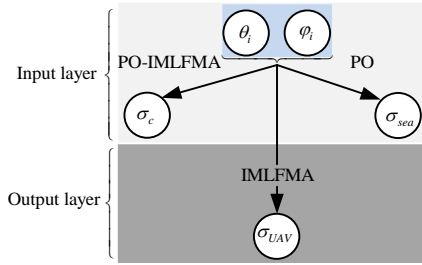


Fig. 8. Relation diagram of training samples and its solution algorithms.

Table 3: Part of the training samples

Number	$\theta_i$ ( $^\circ$ )	$\varphi_i$ ( $^\circ$ )	$\sigma_c$ (dBsm)	$\sigma_{sea}$ (dBsm)	$\sigma_{UAV}$ (dBsm)
1	10	0	24.59	19.88	19.06
2	10	0	19.69	18.32	19.06
3	10	0	28.25	26.18	19.06
4	10	5	23.22	17.52	9.75
5	10	10	15.16	13.73	10.29
6	10	15	12.33	14.67	2.17
7	10	20	21.16	18.50	-1.17
8	20	0	30.48	28.15	-8.99
9	30	0	18.27	-1.50	-0.27
10	40	0	20.25	20.01	-6.33
11	50	0	19.36	18.21	-3.79
12	60	0	13.47	14.90	0.37

The mean values of the three cases are shown in Table 4. The compensation error under the 1-scale sea condition is less than 0.95 dBsm, under the 3-scale sea condition is less than 0.41 dBsm, and under the 5-scale sea condition is less than 1.94 dBsm. The compensation error denotes the difference between expected value and compensated value. Compared with the uncompensated value, the mean error of the compensated result is

smaller, which verifies the effectiveness of the RCS compensation scheme of the sea-skimming UAV based on BP neural network.

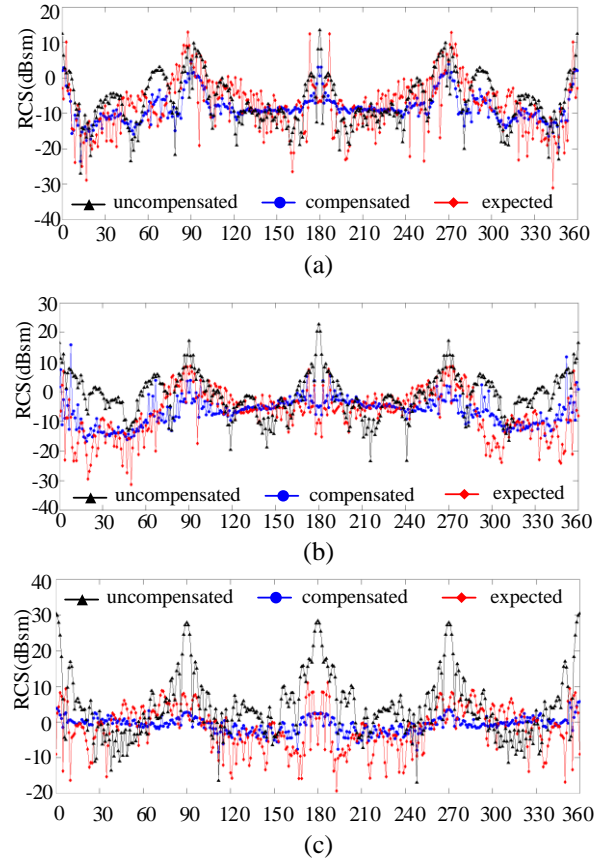


Fig. 9. Monostatic RCS compensation results of sea-skimming UAV under 1-scale sea condition. (a) Incident angle  $65^\circ$ . (b) Incident angle  $45^\circ$ . (c) Incident angle  $25^\circ$ .

The BP neural network compensation model can significantly reduce the impact of sea conditions on the overall RCS of the sea-skimming UAV, but it is difficult to accurately obtain the scattering characteristics of the sea-skimming UAV with the azimuth variation. Actually, the general airborne radar is far away from the sea-skimming UAV, and the radar wave has a large incident angle. Therefore, the compensation model can be employed to most cases, and the error after compensation is insignificant, which can effectively obtain the RCS indicating the electromagnetic scattering characteristics of sea-skimming UAV.

In the actual environment, the RCS value of the UAV can be obtained by compensation algorithm, which can help the relevant personnel directly and effectively analyze the detected characteristics of the flying object, such as aircraft type. This compensation algorithm has a broader application space in the field of military anti-reconnaissance.

Table 4: RCS compensation result of sea-skimming UAV considering sea conditions

Scale	Angle	Uncompensated (dBsm)	Compensated (dBsm)	Expected (dBsm)	Error (dBsm)
1	65°	-6.51	-8.45	-7.50	0.95
	45°	-0.94	-6.51	-7.14	-0.63
	25°	4.15	-0.85	-1.53	-0.68
3	65°	17.71	-7.91	-7.50	0.41
	45°	19.54	-6.74	-7.14	-0.4
	25°	20.84	-1.13	-1.53	-0.4
5	65°	10.81	-8.71	-7.50	1.21
	45°	15.07	-7.06	-7.14	-0.08
	25°	19.50	-3.47	-1.53	1.94

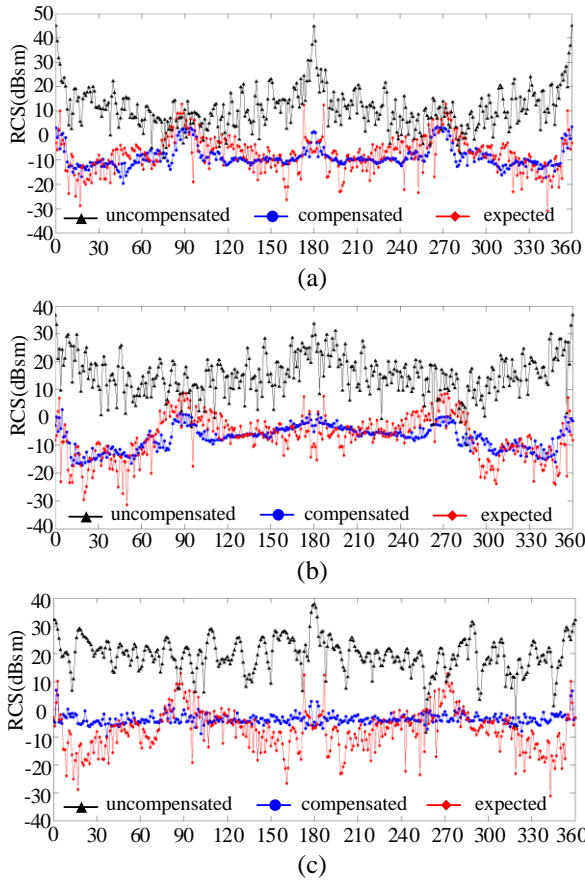


Fig. 10. Monostatic RCS compensation results of sea-skimming UAV under 3-scale sea condition. (a) Incident angle 65°. (b) Incident angle 45°. (c) Incident angle 25°.

**VI. CONCLUSION**

The far field RCS of the sea-skimming UAV and rough sea surface is studied in this paper. A rough sea surface model is established by using the PM spectrum and Monte Carlo method, and a fast algorithm for the sea surface RCS based on the PO method is applied. Then, a composite model of rough sea surface and the sea-skimming UAV is established, and a hybrid algorithm of

the PO-IMLFMA method based on the application of PO method and IMLFMA method for solving the RCS of the composite model based on the FPM is proposed. Compared with the IMLFMA and the PO-MOM, the PO-IMLFMA has the advantages of less memory consumption (about 295 MB) and faster solution speed (about 768 s) for solving the composite model.

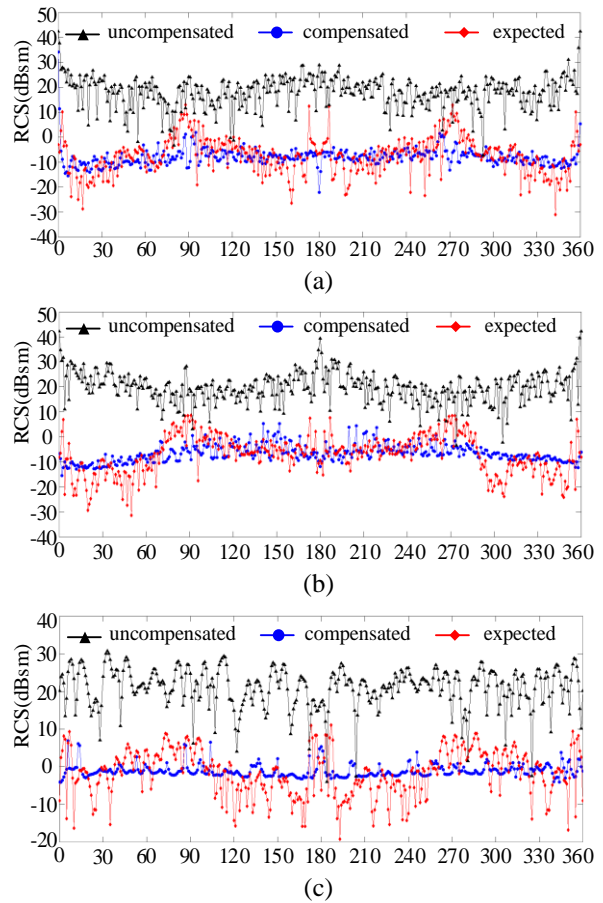


Fig. 11. Monostatic RCS compensation results of sea-skimming UAV under 5-scale condition. (a) Incident angle 65°. (b) Incident angle 45°. (c) Incident angle 25°.

In addition, in view of the influence of rough sea surface on the RCS values of UAV, the RCS compensation scheme of UAV based on BP neural network is proposed. Moreover, the efficiency of BP neural network compensation scheme is verified by an example analysis. The compensation results demonstrate that the compensation errors under the 1-scale, 3-scale and 5-scale sea conditions are less than 0.95 dBsm, 0.41 dBsm and 1.94 dBsm respectively, namely the compensation scheme significantly reduces the influence of sea conditions.

## REFERENCES

- [1] Y. Fu, M. Ding, C. Zhou, and H. Hu, "Route planning for unmanned aerial vehicle (UAV) on the sea using hybrid differential evolution and quantum-behaved particle swarm optimization," *IEEE Trans. Syst. Man Cybern. Syst.*, vol. 43, no. 6, pp. 1451-1465, Nov. 2013.
- [2] Y. Zhao, M. Zhang, H. Chen, and X. Yuan, "Radar scattering from the composite ship-ocean scene: Doppler spectrum analysis based on the motion of six degrees of freedom," *IEEE Trans. Antennas Propag.*, vol. 62, no. 8, pp. 4341-4347, Aug. 2014.
- [3] A. V. Khristenko, et al., "Magnitude and spectrum of electromagnetic wave scattered by small quadcopter in X-band," *IEEE Trans. Antennas Propag.*, vol. 66, no. 4, pp. 1977-1984, Apr. 2018.
- [4] M. Pieraccini, L. Miccinesi, and N. Rojhani, "RCS measurements and ISAR images of small UAVs," *IEEE Aero. El. Syst. Mag.*, vol. 32, no. 9, pp. 28-32, Sep. 2017.
- [5] A. V. Khristenko, et al., "Magnitude and spectrum of electromagnetic wave scattered by small quadcopter in X-band," *IEEE Trans. Antennas Propag.*, vol. 66, no. 4, pp. 1977-1984, Apr. 2018.
- [6] M. Pieraccini, L. Miccinesi, and N. Rojhani, "RCS measurements and ISAR images of small UAVs," *IEEE Aero. El. Syst. Mag.*, vol. 32, no. 9, pp. 28-32, Sep. 2017.
- [7] G. Çakir, M. Çakir, and L. Sevgi, "An FDTD-based parallel virtual tool for RCS calculations of complex targets," *IEEE Antennas Propag. Mag.*, vol. 56, no. 5, pp. 74-90, Oct. 2014.
- [8] A. Sefer, M. A. Uslu, and L. Sevgi, "MATLAB-based 3-D MoM and FDTD codes for the RCS analysis of realistic objects [Testing Ourselves]," *IEEE Antennas Propag. Mag.*, vol. 57, no. 4, pp. 122-148, Aug. 2015.
- [9] L. Zhang, N. Yuan, M. Zhang, L. Li, and Y. Gan, "RCS computation for a large array of waveguide slots with finite wall thickness using the MoM accelerated by P-FFT algorithm," *IEEE Trans. Antennas Propag.*, vol. 53, no. 9, pp. 3101-3105, Sep. 2005.
- [10] J. Lee, J. Zhang, and C.-C. Lu, "Sparse inverse preconditioning of multilevel fast multipole algorithm for hybrid Integral equations in electromagnetics," *IEEE Trans. Antennas Propag.*, vol. 52, no. 9, pp. 2277-2287, Sep. 2004.
- [11] Ö. Ergul and L. Gurel, "Efficient parallelization of the multilevel fast multipole algorithm for the solution of large-scale scattering problems," *IEEE Trans. Antennas Propag.*, vol. 56, no. 8, pp. 2335-2345, Aug. 2008.
- [12] F. T. Ulaby and C. Elachi, *Radar Polarimetry for Geoscience Application*. Boston, MA, USA: Artech House, 1990.
- [13] J. A. Ogilvy, *Theory of Wave Scattering From Random Rough Surfaces*. Bristol, U.K.: Inst. of Physics, 1991.
- [14] C. Corbel, C. Bourlier, N. Pinel, and J. Chauveau, "Rough surface RCS measurements and simulations using the physical optics approximation," *IEEE Trans. Antennas Propag.*, vol. 61, no. 10, pp. 5155-5165, Oct. 2013.
- [15] W. J. Pierson, Jr. and L. Moskowitz, "A proposed spectral form for fully developed wind seas based on the similarity theory of S. A. Kitaigorodskii," *J. Geophys. Res.*, vol. 69, no. 24, pp. 5181-5190, Jan. 1964.
- [16] T. Elfouhaily, B. Chapron, K. Katsaros, and D. Vandemark, "A unified directional spectrum for long and short wind-driven waves," *J. Geophys. Res.*, vol. 102, no. C7, pp. 15781-15796, Feb. 1997.
- [17] O. M. Phillips, "The equilibrium range in the spectrum of windgenerated waves," *J. Fluid Mech.*, vol. 4, no. 4, pp. 426-434, Aug. 1958.
- [18] J. W. S. Rayleigh, *The Theory of Sound*. Macmillan, London, 1877.
- [19] M. R. Pino, R. J. Burkholder, and F. Obelleiro, "Spectral acceleration of the generalized forward-backward method," *IEEE Trans. Antennas Propag.*, vol. 50, no. 6, pp. 785-797, June 2002.
- [20] B. Hu and W. C. Chew, "Fast inhomogeneous plane wave algorithm for scattering from objects above the multilayered medium," *IEEE Trans. Geosci. Remote Sens.*, vol. 39, no. 5, pp. 1028-1038, May 2001.
- [21] T. Rashid, *Make Your Own Neural Network*, Charleston. Create Space Independent Publishing Platform, Charleston, 2016.
- [22] M. Hassoun, *Fundamentals of Artificial Neural Networks*. Bradford Book, Cambridge, 2003.



# Design of Low RCS Vivaldi Antenna Based on Differential Evolution Algorithm

Ge Zhao<sup>1</sup>, Zi-Yu Pang<sup>1</sup>, Xiao-Yu Ma<sup>1</sup>, Guan-Long Huang<sup>1\*</sup>, Luyu Zhao<sup>2\*</sup>,  
Jia-Jun Liang<sup>3</sup>, and Chow-Yen-Desmond Sim<sup>4</sup>

<sup>1</sup> College of Electronics and Information Engineering, Shenzhen University, Shenzhen, Guangdong 518060, China  
\*guanlong.huang@ieee.org

<sup>2</sup> National Key Laboratory of Antennas and Microwave Technology,  
Xidian University, Xi'an, Shaanxi, 710071, P.R. China  
\*lyzhao@xidian.edu.cn

<sup>3</sup> School of Physics and Telecommunication Engineering, Yulin Normal University, Yulin, P.R. China

<sup>4</sup> Department of Electrical Engineering, Feng Chia University, Taichung 40724, Taiwan

**Abstract** — A novel method to reduce antenna radar cross section (RCS) is proposed in this paper. A wideband Vivaldi antenna is adopted for demonstration, the shape of which is optimized by the differential evolution algorithm (DEA) under Python and HFSS co-simulation environment. By utilizing this simple and efficient design approach, no additional structure is required for RCS reduction while other electromagnetic performance of the antenna can be well maintained. Results show that the designed Vivaldi antenna achieves a good RCS reduction from 4 GHz to 9 GHz, validating the possibility and feasibility of this method for further radar target application.

**Index Terms** — Differential evolution algorithm (DEA), radar cross section (RCS) reduction, Vivaldi antenna.

## I. INTRODUCTION

With the development of detection technology and stealth technology, the radar cross section (RCS) reduction of the antenna is undoubtedly of great military significance. RCS is a physical indicator that quantitatively describes the effective scattering area of the incident wave from a certain direction. Obviously, different kinds of antennas have different RCS response [1]-[7]. Vivaldi antenna, as a typical ultra-wideband (UWB) antenna, is often used in the military field due to its advantages of good directivity, wide frequency band and high gain. Therefore, to enhance its practical versatility in practical application, it is of significance to reduce the Vivaldi antenna's RCS.

The RCS reduction of Vivaldi antenna has been studied in many literatures. Basically, reducing the RCS

of Vivaldi antenna can be categorized to two groups. One is to load specially-designed structures on the Vivaldi antenna to achieve antenna RCS reduction. In [8], ultrathin microwave-absorbing materials (MAMs) are placed at the side edges of a Vivaldi antenna, which can absorb the reverse currents at the outer side edges so that the RCS can be reduced. A half-mode substrate integrated waveguide (SIW) structure proposed in [9] is used in antenna design for RCS reduction while a phase-switched screen (PSS) is designed for the same purpose in [10]. In addition, a photonic band gap (PBG) structure is applied to a bilateral Vivaldi antenna to realize antenna's RCS reduction [11].

The other group is to modify the shape of the Vivaldi antenna so as to achieve low RCS response. In [12], an antipodal Vivaldi antenna with low RCS characteristic is demonstrated, which is realized by removing a portion of the metal from the antenna and placing periodic slots near the edges of the radiating element. Vivaldi antennas are modified in [13] by three pairs of arcs to realize wideband RCS reduction. In [14], an approach to implement annular slot along with exponential curves in the antenna is proposed to achieve RCS reduction. Moreover, a flat corrugated slotline is designed in [15] to replace the exponential gradient curve of antenna, which results in RCS reduction when the incident wave is perpendicular to the antenna.

However, regarding to the approaches of either introducing extra structures or modifying the shape of the antennas, all of these above-mentioned design methods still have to take a long and customized simulation process, which is not a universal methodology for RCS reduction. Therefore, it is necessary to have a

new and highly efficient method so that researchers can specify design goals and then use an optimization tool to find and select the most reasonable result and obtain the desired performance. From the mathematical point of view, the optimization method should be a fast way to find extreme values, i.e., under the constraints of a set of equations or inequalities, the system's objective function reaches its extreme value of maximum or minimum.

In this paper, in order to alleviate the aforementioned problems, a low RCS Vivaldi antenna is designed by a highly efficient optimization method. The co-simulation of the commercial electromagnetic tool, HFSS, and Python program is adopted, and the differential evolution algorithm (DEA) is utilized to find the optimal antenna pattern that satisfies both radiation and scattering requirements.

## II. PRINCIPLE OF DEA METHOD

The DEA is a random parallel direct search algorithm proposed by Storm Rainer and Price Kenneth in 1995 [16]. It has the characteristics of simple operation and global search, which not only can avoid the shortcomings of classic and local optimization methods such as low convergence accuracy and easy convergence to local extreme values, but also has been successfully applied to complex electromagnetic optimization problems such as array synthesis and filter design. In this work, the DEA is applied to the RCS reduction of the antenna for the first time. Figure 1 shows the flowchart of optimizing the RCS of Vivaldi antenna with DEA method.

In this paper, Vivaldi antenna is separated into small rectangles, and low RCS Vivaldi antenna is obtained by controlling the presence or absence of the rectangles in each position. Each column of the Vivaldi antenna is considered as a variable. Before the optimization, the number of rectangles (denoted as  $N$ ) contained in each column of the Vivaldi antenna needs to be calculated. For each variable, the value ranges from 0 to  $2^N - 1$ . When the Vivaldi antenna is optimized by the DEA, the individuals of population number are randomly generated to form the first generation population, and then the HFSS software is called by Python script, where the antenna model is simulated by Finite Element Method (FEM) to realize the calculation of antenna radiation and scattering characteristics and then each individual fitness value can be obtained. The fitness function here is the RCS of the antenna. The fitness value will be compared with the target value afterwards. Once the fitness value is less than the target value, the optimal pattern of the low RCS Vivaldi antenna can be obtained. Otherwise, mutation and crossover operations are then performed to obtain crossover individual. Next, the target individual is compared with the crossover individual. If the fitness value calculated by the crossover individual is less than the fitness value calculated by the target individual, the crossover individual is inherited to the next generation.

Otherwise, the target individual will be given to the next generation. This is going to repeat until the fitness value is less than the target value or the number of iterations reaches the specified maximum number of iterations, the whole optimization process will be terminated.

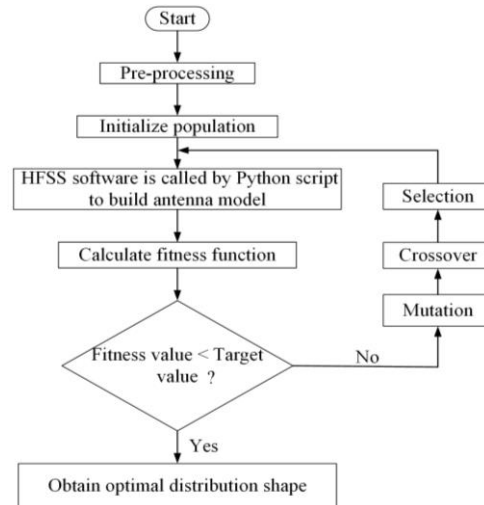


Fig. 1. Flowchart of DEA method for Vivaldi antenna RCS reduction.

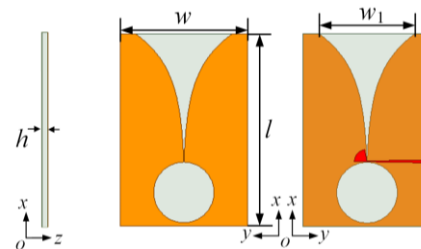


Fig. 2. Geometry of the reference Vivaldi antenna.

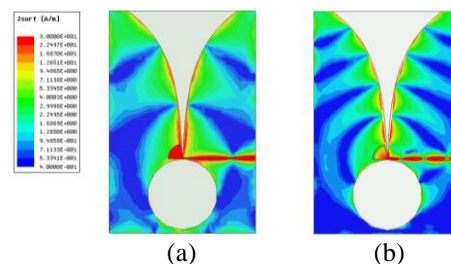


Fig. 3. Surface radiating current of the reference Vivaldi antenna at: (a) 4.5 GHz and (b) 8.5 GHz.

It is worth noting that for the design of low RCS Vivaldi antenna, both radiation and scattering characteristics must be taken into account. Therefore, as long as the reflection coefficient of the Vivaldi antenna is less than -10 dB, a series of subsequent steps such as the comparison between the fitness value and the target value would be performed.

### III. DESIGN AND DISCUSSION OF LOW RCS VIVALDI ANTENNA

#### A. Low RCS Vivaldi antenna design

In order to illustrate the RCS reduction effect, a conventional Vivaldi antenna is taken as the reference antenna, and its geometry is shown in Fig. 2. It can be known that the Vivaldi antenna is composed of a stepped microstrip feeding line and a radiating tapered slot.

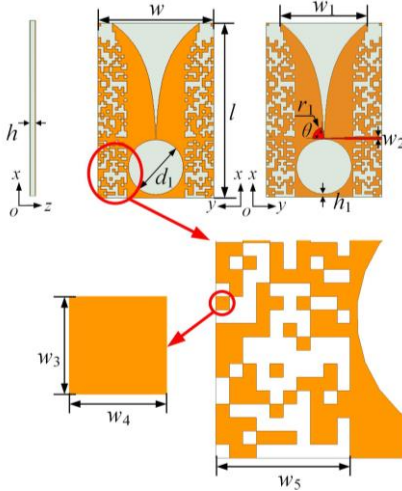


Fig. 4. Geometry of the proposed Vivaldi antenna.

The surface radiating current distributions of the reference antenna at 4.5 GHz and 8.5 GHz are shown in Fig. 3, which can be observed that the radiating current of the Vivaldi antenna is mainly concentrated on both sides of the tapered slot and the microstrip line, so DEA method can be applied to optimize the remaining part of the Vivaldi antenna with relatively weak radiating current, which can in turn help reduce the antenna's RCS. The proposed antenna optimized by DEA method is shown in Fig. 4. Both antennas are printed on Rogers 5880 substrate with dielectric constant of 2.2, loss tangent of 0.0009 and thickness of 0.508 mm. The detailed dimensions of the proposed antenna are shown in Table 1.

Table 1: Parameters of the proposed Vivaldi antenna

Parameter	Value	Parameter	Value
$w$	80 mm	$w_4$	2 mm
$l$	120 mm	$w_5$	20 mm
$h$	0.508 mm	$d_1$	38 mm
$w_1$	60 mm	$h_1$	2 mm
$w_2$	1.65 mm	$r_1$	7.8 mm
$w_3$	2 mm	$\theta$	$80^\circ$

#### B. Radiation performance

In order to verify the radiation characteristics of the proposed antenna, the VSWRs, maximum radiation gains, and radiation patterns of the reference antenna and the proposed antenna are discussed in this section.

The simulated VSWRs and gains are depicted in Fig. 5. It can be seen that the VSWR of the proposed antenna is less than 2 in the frequency range of 4~9 GHz, which is similar to that of the reference antenna. By observing the gain response in Fig. 5, it can be found that the gain of the proposed antenna is slightly lower than the reference antenna but within an acceptable range, the phenomenon of which can be understood that the effective radiation aperture of the proposed antenna is slightly smaller than the reference antenna.

The  $E$ -plane and  $H$ -plane normalized radiation patterns of the two antennas at 4.5 GHz and 8.5 GHz are plotted in Fig. 6, from which one can observe that the proposed antenna has comparable radiation performance as the reference one.

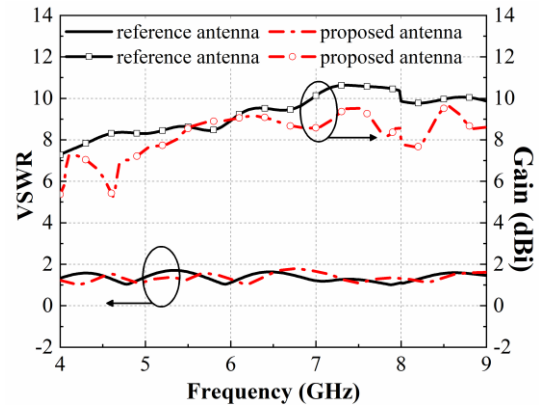


Fig. 5. Simulated VSWRs and gains of the reference and the proposed antennas.

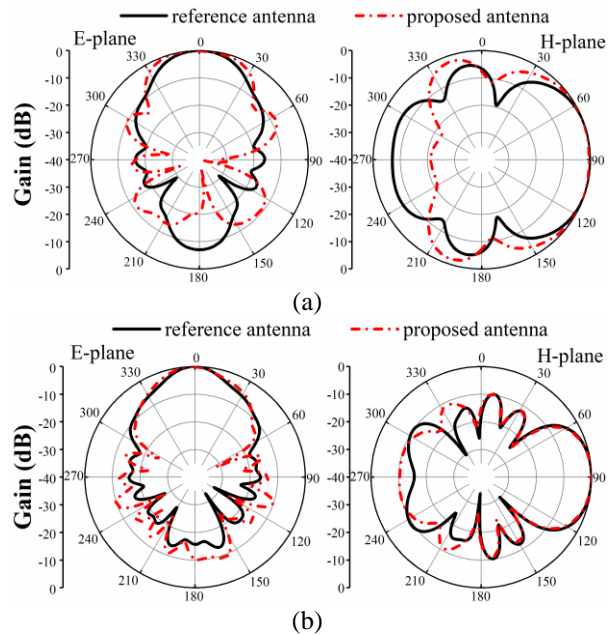


Fig. 6. Radiation patterns of the reference and the proposed antennas at: (a) 4.5 GHz and (b) 8.5 GHz.

### C. Scattering performance

In order to evaluate the scattering characteristics of the proposed antenna, planar incident wave is uniformly illuminated on the antenna surface, and the monostatic RCS at different incident angles can be calculated in HFSS when the incident wave is  $\theta$ -polarized. According to Fig. 7 (a), when the incident wave is perpendicular to the Vivaldi antenna, i.e.,  $\varphi = 0^\circ$  and  $\theta = 0^\circ$ , the monostatic RCS of the proposed antenna in the whole frequency band is significantly reduced compared with the reference antenna. In particular, the monostatic RCS of the proposed antenna is reduced by 5.24 dB at 5.5 GHz.

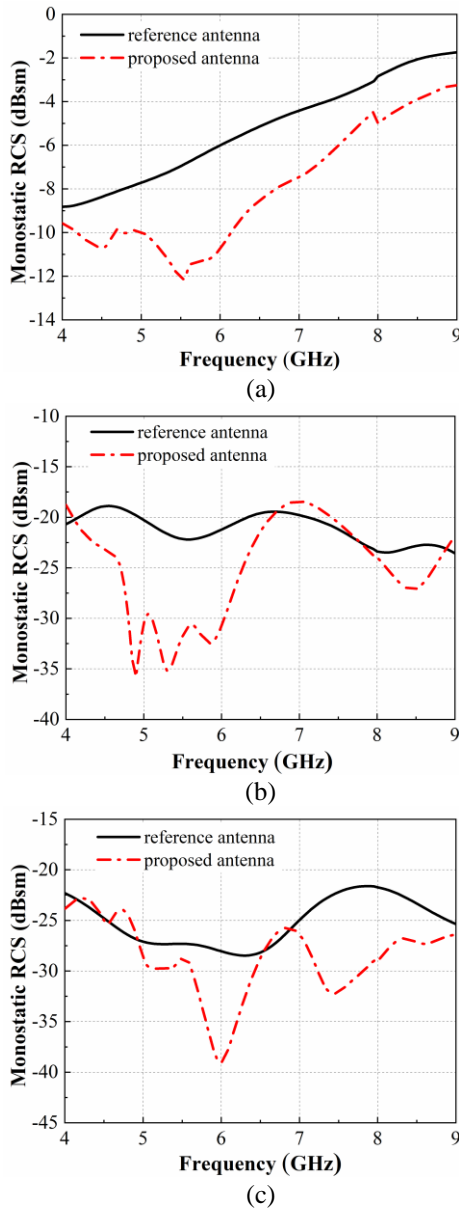


Fig. 7. Simulated monostatic RCS at different incident angles: (a)  $\varphi = 0^\circ, \theta = 0^\circ$ ; (b)  $\varphi = 0^\circ, \theta = 60^\circ$ ; (c)  $\varphi = 90^\circ, \theta = 60^\circ$ .

Figures 7 (b) and (c) show the monostatic RCS performance when the angle of incident wave  $\theta$  increases to  $60^\circ$ . It can be seen that, though the incident direction varies to a large angle, the monostatic RCS reduction of the proposed antenna can still maintain in a satisfactory range in most frequency bands of 4~9 GHz. Especially, when  $\varphi = 0^\circ$  and  $\theta = 60^\circ$ , the monostatic RCS of the proposed antenna can be reduced more than 6 dB in the band of 4.75~6.2 GHz; and at 4.85 GHz, 14.4 dB RCS reduction is achieved. At the case of  $\varphi = 90^\circ$  and  $\theta = 60^\circ$ , the proposed antenna obtains more than 6.5 dB RCS reduction in both 5.8~6.2 GHz and 7.25~8.05 GHz bands, particularly 11 dB RCS reduction is achieved at 6 GHz. Therefore, it can be concluded that the average monostatic RCS of the proposed antenna in the whole frequency band is much lower than that of the reference antenna while the proposed one still possesses other good radiation performance similar to the reference one.

### IV. CONCLUSION

A low RCS Vivaldi antenna for UWB communication system application is proposed in this paper. Numerical results show that satisfactory radiation performance of the proposed antenna has been obtained. Compared with the reference antenna, the operational bandwidth of the proposed antenna can cover a wide range from 4 GHz to 9 GHz with VSWR less than 2, while its radiation patterns still maintain directional performance. The scattering characteristics when the incident wave is  $\theta$ -polarized are also analyzed. Results show that when the incident wave is perpendicular to the antenna, the monostatic RCS of the proposed antenna has been reduced in the whole frequency band, particularly when the incident wave angle increases to  $60^\circ$ , the monostatic RCS still maintain a good reduction in most frequencies of 4~9 GHz.

### ACKNOWLEDGMENT

This work was supported partially by the National Taipei University of Technology-Shenzhen University Joint Research Program under Grant No. 2020011, the Fok Ying-Tong Education Foundation, China under Grant No. 171056, the National Natural Science Foundation of China under Grants 61801300 and 61701320, and the New Teacher Natural Science Research Project of Shenzhen University under Grant No. 860-000002110627.

### REFERENCES

- [1] J. Jiang, Y. Xia, and Y. Li, "High isolated X-band MIMO array using novel wheel-like metamaterial decoupling structure," *Applied Computational Electromagnetics Society Journal*, vol. 34, no. 12, pp. 1829-1836, 2019.
- [2] F. Liu, J. Guo, L. Zhao, G. L. Huang, Y. Li, and Y. Yin, "Dual-band metasurface-based decoupling method for two closely packed dual-band antennas,"

- IEEE Transactions on Antennas and Propagation*, vol. 68, no. 1, pp. 552-557, Jan. 2020.
- [3] G.-L. Huang, J. Liang, L. Zhao, D. He, and C.-Y.-D. Sim, "Package-in-dielectric liquid patch antenna based on liquid metal alloy," *IEEE Antennas and Wireless Propagation Letters*, vol. 18, no. 11, pp. 2360-2364, Nov. 2019.
- [4] J. Li, X. Zhang, Z. Wang, X. Chen, J. Chen, Y. Li and A. Zhang, "Dual-band eight-antenna array design for MIMO applications in 5G mobile terminals," *IEEE Access*, vol. 7, pp. 71636-71644, 2019.
- [5] F. Liu, J. Guo, L. Zhao, G. Huang, Y. Li, and Y. Yin, "Ceramic superstrate-based decoupling method for two closely packed antennas with cross-polarization suppression," *IEEE Transactions on Antennas and Propagation*, Submitted.
- [6] J. Guo, F. Liu, L. Zhao, Y. Yin, G. Huang, and Y. Li, "Meta-surface antenna array decoupling designs for two linear polarized antennas coupled in H-plane and E-plane," *IEEE Access*, vol. 7, pp. 100442-100452, 2019.
- [7] L. Zhao, G. Jing, G.-L. Huang, W. Lin, and Y. Li, "Low mutual coupling design for 5G MIMO antennas using multi-feed technology and its application on metal-rimmed mobile phones," *IEEE Transactions on Antennas and Propagation*, Submitted.
- [8] P. Zhang and J. Li, "Compact UWB and low-RCS Vivaldi antenna using ultrathin microwave-absorbing materials," *IEEE Antennas and Wireless Propagation Letters*, vol. 16, pp. 1965-1968, 2017.
- [9] Y. Jia, Y. Liu, Y. Hao, and S. Gong, "Vivaldi antenna with reduced RCS using half-mode substrate integrated waveguide," *Electronics Letters*, vol. 50, no. 5, pp. 345-346, Feb. 2014.
- [10] G. Zhang, L. Xu, and A. Chen, "RCS reduction of Vivaldi antenna array using a PSS boundary," *2008 8th International Symposium on Antennas, Propagation and EM Theory*, Kunming, China, pp. 345-347, 2008.
- [11] W. Jiang, Y. Li, S. Gong, and W. Wang, "Novel UWB vivaldi antenna with low RCS," *2014 Asia-Pacific Microwave Conference*, Sendai, Japan, pp. 1405-1407, 2014.
- [12] N. Rajesh, K. Malathi, S. Raju, V. Abhai Kumar, S. Deepak Ram Prasath, and M. G. N. Alsath, "Design of Vivaldi antenna with wideband radar cross section reduction," *IEEE Transactions on Antennas and Propagation*, vol. 65, no. 4, pp. 2102-2105, Apr. 2017.
- [13] Y. Jia, Y. Liu, S. Gong, T. Hong, and D. Yu, "Printed UWB end-fire Vivaldi antenna with low RCS," *Progress in Electromagnetics Research Letters*, vol. 37, 2013.
- [14] R. Natarajan, M. Kanagasabai, and J. V. George, "Design of an X-band Vivaldi antenna with low radar cross section," *IET Microwaves, Antennas & Propagation*, vol. 10, no. 6, pp. 651-655, 2016.
- [15] T. Luo and Z. Nie, "RCS reduction of antipodal Vivaldi antenna," *2015 Asia-Pacific Microwave Conference (APMC)*, Nanjing, pp. 1-3, 2015.
- [16] S. Rainer and P. Kenneth, "Differential evolution—a simple and efficient heuristic for global optimization over continuous spaces," *Journal of Global Optimization*, vol. 11, no. 4, pp. 341-359, 1997.

# Research and Experiments on Anti-UAV Technology

Hongbo Wei, Xinhuai Wang\*, Xiaowei Shi, and Bo Liang

National Key Laboratory of Science and Technology on Antennas and Microwave  
Xidian University, Xi'an, Shaanxi, 710071, China  
w5918666@vip.qq.com, \*xinhuaiwang@xidian.edu.cn,  
xwshi@mail.xidian.edu.cn, Seeker93@outlook.com

**Abstract** — Unregistered flight of Unmanned Aerial Vehicle (UAV) has been a severe challenge to the security of low-altitude airspace. Illegal elements may use UAV to carry dangerous goods or steal privacy. More and more conferences and large-scale activities pay attention to the security and privacy of the air defense. This paper focuses on two kinds of UAV interference solutions, traditional full-band suppression and targeted spectrum suppression. Experiments show that the target spectrum suppression scheme can reduce 4.61dB transmission power compared with traditional full-band suppression for a certain UAV at the same attack distance. The novelty of paper is that we use artificial intelligence method to analyze the spectrum of UAV signal and the new scheme can reduce power transmission by more than half at the same attack distance. This paper also carry out comparative experiments on different types of UAVs, demonstrating its excellent performance. In addition, for some WiFi UAVs, this paper can even steal their password to acquire the UAVs' control.

**Index Terms** — Control password, low transmission power, targeted spectrum suppression, traditional full-band suppression, Unmanned Aerial Vehicle (UAV).

## I. INTRODUCTION

The number of civilian UAVs had grown tremendously in the past years. There is a huge potential that UAV offers in as far as revolutionizing approaches to handling tasks that require precision, accuracy and risk are concerned. As a result, there is a growing application of UAV in running recreational and commercial tasks. "Aerial photography", for instance, has gradually become a trend in society. Policies and guidelines exist on the registration and operational conduct of UAV for commercial purposes. However, there is lack of complete and rigorous management practices for civilian UAV, and most consumers do not receive any professional training [1-2].

The security control of large-scale activities is becoming more and more strict. Therefore, the anti-UAV

technology is becoming more critical. UAV poses a threat to the security of society. Implementing mandatory dispersal ways is necessary. Based on the analysis of the existing UAV interference technology and its application status, this paper proposed traditional full-band suppression and targeted spectrum suppression methods. The full-band suppression interference is based on frequency sweeping. The targeted spectrum suppression interference is based on spectrum analysis. Both methods could suppress UAV communication signal by high-power noise signal. In this paper, a certain UAV is experimentally validated and the advantages and disadvantages are compared [3-4].

## II. OVERVIEW OF UAV JAMMING TECHNOLOGY

Given the difficulty in regulating the airspace for unregistered and unexpected UAV, the remaining approach is to jam the signal communication so as to disable pesky ones. To understand how unregistered UAV can be stopped from accessing the airspace, we first need to understand their functioning. UAVs are piloted via RF technology and two frequency bands exist which assist in their communications: the 2.4GHz and the 5.8 GHz. Devices such as UAV represent modem application of tight frequency reuse and adaptive modulation. Using their communications technology, some expensive UAVs can easily control from far away and perform video recording functions. Even some UAVs can carry light dangerous items and Fig. 1 shows the dangerous UAV captured by military [5-7]. The following will introduce the interference methods.

### A. Traditional full-band suppression interference

UAV suppression interference entails sending out noise interference signals on the target frequency band. Civilian UAV operates within known bands, if experimentally interrupted, the communication in this frequency band will interfere, and therefore the electronic device will not work correctly. In this design, the spectrum suppression signal is directly generated by frequency sweeping.



Fig. 1. Hazardous UAV.

Firstly, the traditional scheme is introduced. In the wide spectrum range, the signal jamming transmitter generates a periodic linear frequency sweep interference signal in a certain way. Therefore, the bit error rate of UAV communication receiver increases or even saturates directly. The UAV will disconnect with the remote controller and not able work properly. A communication breakdown between the device pilot and the device will make it impossible for the device to operate and to make any significant exploration of the airspace. This way, any targeted UAV can be eliminated from the airspace and only registered ones can operate.

### B. Targeted spectrum suppression interference

The previous method requires a lot of transmission power, but the targeted spectrum scheme is a new scheme which can reduce unnecessary energy loss. This scheme is also the core innovation of this paper. The targeted spectrum interference adopts an idea of "interception-analysis-interference". Above all, this project needs to intercept the UAV communication signal, then analyze and process the UAV communication signal to get the signal communication frequency point, and finally suppress the UAV by transmitting the targeted frequency signal. Targeted spectrum suppression can theoretically saturate the UAV receiver efficiently, thus reducing the ability of the receiver to process normal signals and ultimately cutting off the communication of the target UAV.

In the case of losing the control signal, the UAV will return, hover or make a forced landing according to the original program, and ultimately achieve the purpose of intercepting the UAV.

## III. DESIGN SCHEME

### A. Overall design

The ultimate goal of both UAV interference plans

is blocking the UAV receiver and paralyzing the coordination which would result in the successful piloting of the device illegally over an airspace. The Full-band suppression interference is based on the frequency sweeping method to spread the noise signal over a wider frequency band, and need not know the specific frequency. With the high-power interference transmitter, the interference can be performed within the communication band of the UAV. Targeted spectrum suppression interference takes the software radio technology as the core to form the frequency reconfigurable UAV interference platform. This platform can intercept the spectrum of the UAV communication signal, and analyze the communication frequency point to carry out targeted interference [8-10].

UAV communication signal includes control signal and image transmission signal, which can be in 2.4 GHz band or 5.8 GHz band. Due to the similarity between the 2.4 GHz band and the 5.8 GHz band, this paper takes the 2.4 GHz band as an example for specific analysis. Both plans block the UAV receiver by transmitting high-power suppression signals. The power amplifier and the antenna are the same except for the signal source. The whole system is shown in Fig. 2.

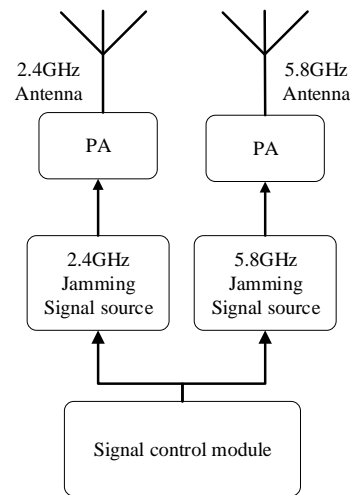


Fig. 2. The block diagram of whole system.

### B. Design of traditional full-band suppression interference

The full-band suppression interference design consists of a sawtooth signal source, a voltage-controlled oscillator (VCO), a driver amplifier, and a power amplifier. The sawtooth signal is provided by the Agilent 33600A waveform generator. A sawtooth/triangle signal also could be generated by either a microcontroller or two operational amplifiers circuitry. The waveform generator control VCO generates the frequency sweeping signal in the 2.4GHz~2.47GHz frequency band. VCO

selects chip MVE2400 and power amplifier selects chip SKY65135.

### C. Design of targeted spectrum suppression interference

Targeted spectrum suppression interference is based on software radio and select USRP platform to design. The USRP is consisted of a Xilinx Kintex-7 FPGA and the AD9361, whose transmit frequency up to 6 GHz. Based on the Linux system, the USRP is used as the RF signal sources. USRP analyzes the spectrum of the UAV to obtain the frequency hopping frequency of the UAV communication signal and generates targeted suppression signals for these frequencies. By controlling and adjusting the RF parameters of USRP on the Linux system, the noise signal is transmitted through the power amplifier to block the UAV communication receiver, causing the UAV to be disconnected from the remote controller.

## IV. EXPERIMENTAL RESULTS AND DISCUSSION

### A. Module signal generation

The full-band suppressed interference signal module is connected to the spectrum analyzer, and the interference signal is observed to be distributed from 2.4 GHz to 2.47 GHz, and the power is about -1.56 dBm. The test result is shown in Fig. 3.

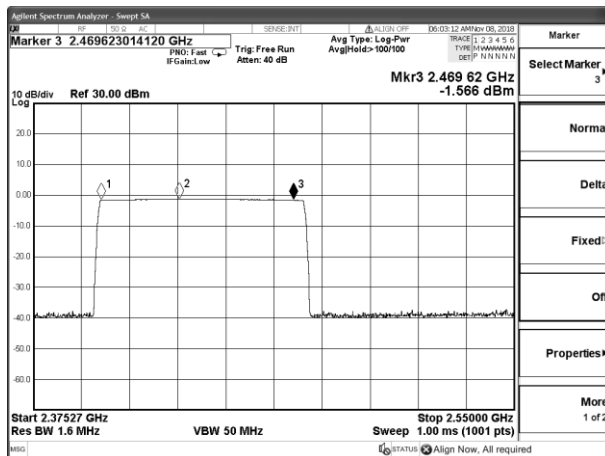


Fig. 3. Full-band suppressed spectrogram.

In this article, we chose DJI GO as the experimental object. DJI GO is a universal RF-controlled UAV that sells for about \$1,500 in online mall. The specific parameters of the specific UAV can be found on the official website. The picture of DJI GO is shown in Fig. 4.



Fig. 4. DJI GO.

DJI GO communicates based on OFDM, which is an orthogonal frequency division multiplexing technology and a Multi-carrier modulation (MCM) technology. The basic idea of MCM technology is to convert the serial data stream to parallel data stream by decomposition, and then modulate these parallel data stream to several carriers of different frequencies. The targeted spectrum suppression interference scheme needs to know the hopping frequency point of the UAV communication signal [11]. Above all, receive the transmission signal from the UAV remote controller and then the signal is connected to the USRP platform. The communication signal of a certain UAV is analyzed to obtain the spectrum data, as shown in Fig. 5. It can be seen from the figure that the communication frequencies of UAV are constantly changing.

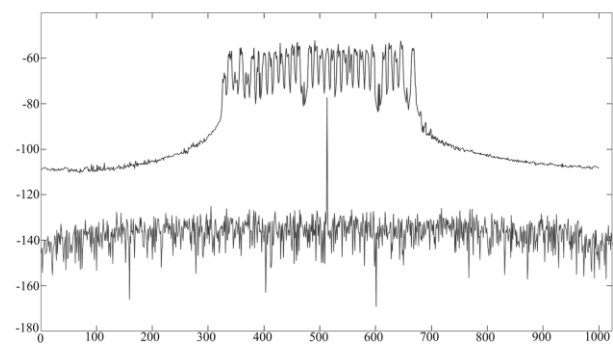


Fig. 5. Spectrum of UAV Communication Signal.

In this paper, we use the Long Short Term Memory model (LSTM) to recognize the frequency hopping sequence of UAV. The network structure schematic and network parameter model of long short term memory model are shown in Fig. 6.



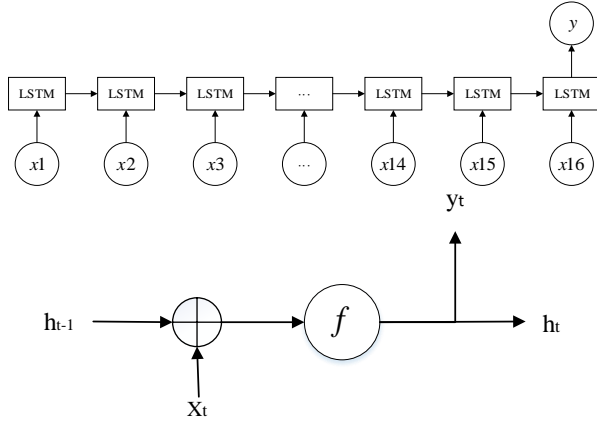


Fig. 6. LSTM model.

The spectrum difference of UAV communication signal is used as the feature of signal, so feature extraction is to transform the time domain data of UAV communication signal into frequency domain data. Formula transformation is expressed as (1):

$$X(k) = \sum_{n=0}^{N-1} x(n) e^{-j \frac{2\pi}{N} kn} \quad (k = 0, 1, 2, \dots, N-1), \quad (1)$$

The formula for calculating the neuron cell structure of LSTM neural network can be expressed as follows:

$$\begin{aligned} h_t &= f(W_{sh}x_t + W_{hh}x_{t-1} + b_h) \\ y_t &= W_{hy}h_t + b_y \end{aligned} \quad (2)$$

For the given time series  $x_t$ , using the RNN model, equations (1) can be used to calculate  $h_t$  and the output sequence  $y_t$ . In the formula,  $W$  represents the weight coefficient matrix,  $b$  represents the offset vector, and  $f$  represents the activation function.

Using the LSTM model to train the drone signal, the project can get the accuracy rate and loss value with the training rounds [12]. The loss function can be expressed as the formula (3):

$$\begin{aligned} loss &= \frac{1}{N} \sum_{i=1}^N DL(y^i || \bar{y}^i) = -\frac{1}{N} \sum_{i=1}^N \sum_{j=1}^C y_j^i \log \bar{y}_j^i \\ &= -\frac{1}{N} \sum_{i=1}^N \log \bar{y}_k^i \end{aligned} \quad (3)$$

The LSTM model originally used the gradient descent method to optimize the neural network, but if the amount of data is large or the structure of the network is more complicated, the operation will take more time. In order to accelerate the analysis of loss value, this paper finally adopted Stochastic Gradient Descent method. This method can quickly complete the processing of UAV signals, and the formula is shown in (4):

$$w^{r+1} = w^r + \eta(t_n - (w^r)^T x^{(n)})x^n. \quad (4)$$

The LSTM model test results are shown in Fig. 7. The accuracy rate increases with the number of training rounds, and the accuracy rate gradually approaches

100%. At the beginning, the loss value will slightly jitter up and down, but similar to the accuracy rate, the loss value eventually approaches 0. In addition, the project also uses different signal-to-noise ratio signals for artificial intelligence recognition, which can obtain the accuracy curve with different signal-to-noise ratio signals.

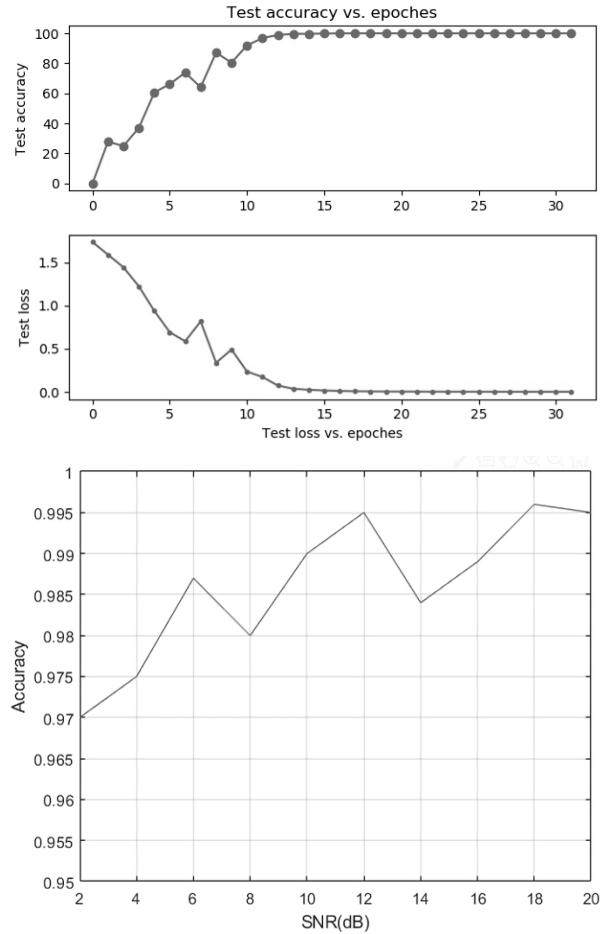


Fig. 7. LSTM training process.

The change of signal-to-noise ratio has a certain impact on the accuracy of UAV signal recognition. With the increase of signal-to-noise ratio, the accuracy has a trend to improve, but the improvement is actually small. It can be seen from the figure that the SNR increases from 2dB to 20dB, and the recognition rate increases by about 2.5%, so the recognizer has certain anti-interference ability Power.

By further analyzing the spectrum data of the UAV communication signal received once, the hopping frequency points of the signal spectrum can be obtained. The hopping frequency signal has 28 points, the hopping interval is 14ms, the frequency point bandwidth is 1.2MHz, and the spectrum range is 2404MHz~2470MHz.

USRP generates a targeted spectrum suppression signal with this data, the frequency hopping sequence and point is shown in Table 1 and Fig. 8.

Table 1: Frequency hopping point

Hopping Sequence	1	2	3	4	5	6
Frequency hopping point	2424	2470	2448	2425.8	2404	2456
Hopping Sequence	7	8	9	10	11	12
Frequency hopping point	2428	2405.8	2452	2430	2408	2454
Hopping Sequence	13	14	15	16	17	18
Frequency hopping point	2431.8	2412	2458	2436	2414	2460
Hopping Sequence	19	20	21	22	23	24
Frequency hopping point	2437.8	2416	2464	2442	2420	2466
Frequency hopping point	25	26	27	28		
Hopping Sequence	2444	2422	2468	2445.8		

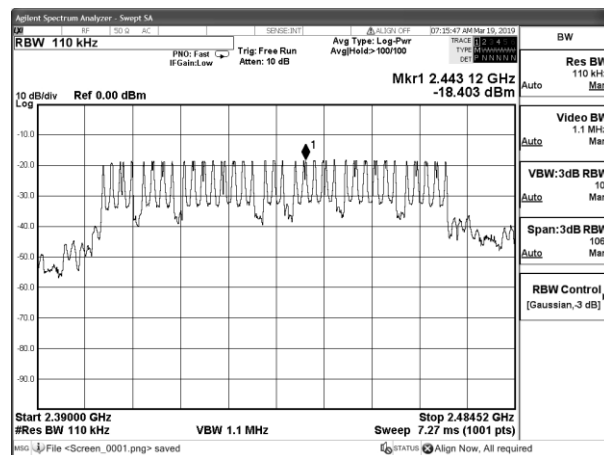


Fig. 8. Targeted Spectrogram.

**B. Experiment and comparison of jamming UAV**

The traditional full-band suppressed interference output signal is in the 2.4GHz~2.47GHz band and connect the signal source to the power meter to measure its average output power is -0.86dBm, as shown in Fig. 9.

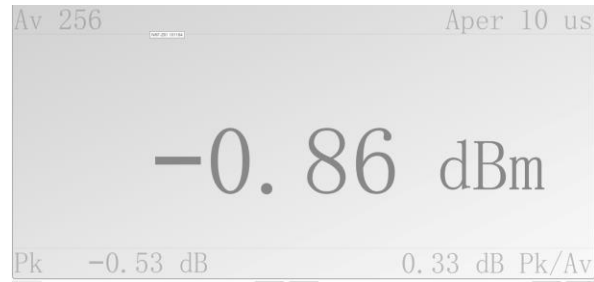


Fig. 9. Full-band suppressed output average power.

The full-band suppressed signal source is connected to the power amplifier, with an average output gain of 36dB. The antenna is a well-directed Yagi antenna with a gain of 15 dBi. What’s more, the remote controller is 50 meters away from the UAV and ensures that the remote controller is not affected by interference signals. The schematic diagram of the experimental test is shown in the Fig. 10.

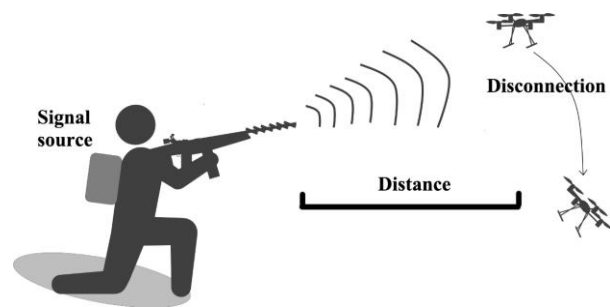


Fig. 10. Schematic diagram of the experiment.

Experiments show that the maximum distance of full-band suppression interference attack UAV can reach 380 meters. Replacing high power amplifier and high gain antenna can increase the attack distance.

Next, experiments are carried out on the targeted spectrum suppression jamming scheme. The average output power of the targeted spectrum interference signal source is set the same as the full-band suppression interference signal source, which is about -0.86 dBm.

When the transmit power is similar, targeted spectrum suppression interference scheme can attack UAV up to 670 meters. The critical point of test result is that the UAV remote controller changes from weak signal state to unconnected aircraft state. At this time, UAV communication receiver is blocked and cannot receive control and image transmission signals. The unconnected state of the aircraft is shown in Fig. 11.



Fig. 11. The state of UAV being disconnected.

The average output power of the targeted spectrum suppressed signal source is set as a variable and the standard is 0.86 dBm. The experiment measures when the average output power is reduced by 3 dB and the attack distances of the two schemes are the same. The test results is shown in Table 2.

Table 2: Experimental results of targeted spectrum suppression

Average Power of Signal Source/dBm	-0.86	-3.83	-5.47
Attack distance/m	670	500	380

What should be emphasized in this table is that the signal source does not include the power amplifier. The power amplifier and antenna uses the same modules and have the same gain as the previous experiment.

Free space loss describes the energy loss when electromagnetic waves propagate in air. The free space loss formula is expressed as follows:

$$L_s = 20\lg(F) + 20\lg(D) + 32.4 \quad (4)$$

$$P_r = P_t + G_t - L_s + G_r$$

F is the frequency, D is the distance,  $P_t$  is the transmit power,  $G_t$  is the transmit antenna gain,  $L_s$  is the free space loss, and  $G_r$  is the receive antenna gain. In this paper, the control variable only modifies P in the design process, and the other influences are the same.

According to the free transmission loss formula, when other factors are determined, the transmitting power is the most important factor affecting the attack distance of UAV [13-14]. On the basis of the test results, with the same power amplifier and Yagi antenna, the attack distance of the targeted spectrum suppression scheme is approximately 1.76 times that of the full-band suppression scheme. At the same attack distance, the average output power of the targeted spectrum suppression scheme is reduced by approximately 4.61 dB. The average output power is -5.47dBm, as shown in Fig. 12.

Through the above experimental tests, it is proved that the targeted spectrum suppression scheme has superior performance compared with the traditional full-band suppression scheme.

In addition, data acquisition and attack experiments of other types of UAVs are also carried out. For the DJI GO series UAVs, the power consumption can be saved to varying degrees by suppressing attacks. The following is a data acquisition chart of different series of UAVs, as shown in Fig. 13.



Fig. 12. Targeted spectrum suppression output average power.

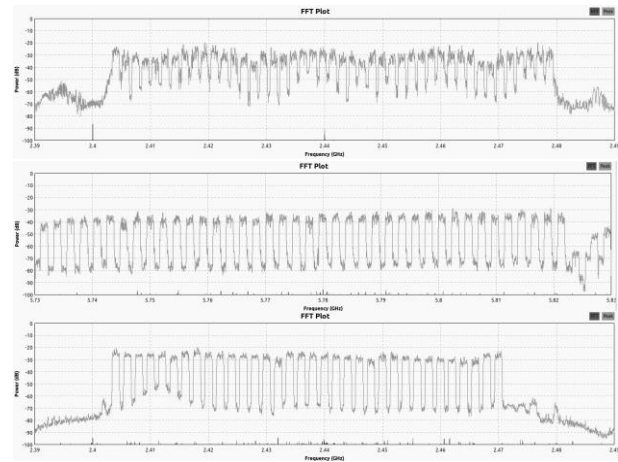


Fig. 13. DJI GO Series UAVs Signal Data.

The project carries out comparative experiments for different series of UAVs. By using neural network to analyze the UAV OFDM data signal and suppress the UAV OFDM signal in real time. In the experiments of different series of UAVs, the experimental results of the project are similar to the above table data. Under the same attack distance, the power consumption is saved about 4.6dB or the same transmit power, the attack distance is about 1.7 times.

In addition, the project also studies the WiFi-controlled UAV with the scheme of De-authentication Flood Attack. Some UAVs can even decipher WiFi passwords to gain control of the UAV. By sending forged cancellation authentication frames, De-authentication Flood attack makes the access point mistakenly think that the client wants to disconnect from it, and then the WiFi type UAV is out of control. Attack experiments for WiFi UAV are shown in Fig. 14.

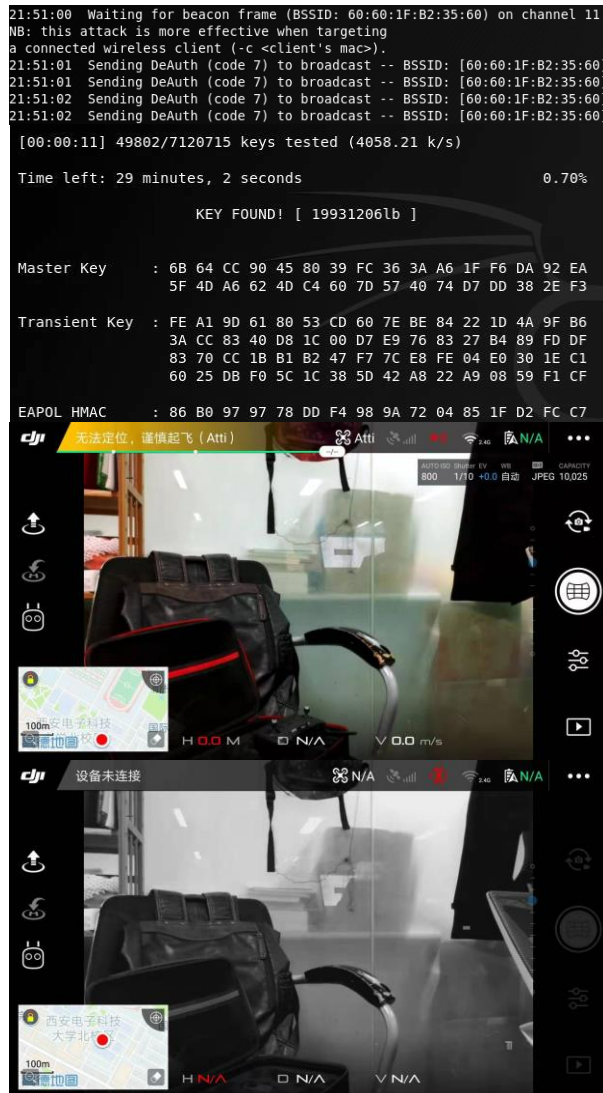


Fig. 14. Attack experiment process of WiFi UAV.

## V. CONCLUSION

The Unregistered flight of UAV poses a serious threat to the security work in large-scale events. Whereas there is widespread adoption of UAV in recreational activities, there is record of inappropriate use of UAV to access highly sensitive information areas. Besides their size, the fact that UAV are remotely piloted provides a certain anonymity that can breed insecurity and inappropriate use of airspace. This paper proposes two solutions to this problem, traditional full-band suppression and targeted spectrum suppression. The experiments show that traditional full-band suppression scheme consumes more energy and has a shorter attack distance. In order to solve this problem, this paper proposes a targeted spectrum suppression scheme, and the novelty of this scheme lies in that the targeted spectrum

suppression scheme can reduce the average output power by 4.61dB or can attack longer distances, which has a very good application prospect [15-18]. This experiment has tested other common UAVs on the market, and the experimental results are in line with expectations. For some WiFi UAVs, this experiment can even get their control passwords. This paper provides a new direction for the design of anti-UAV jammers and electromagnetic countermeasure system.

## ACKNOWLEDGMENT

This work is supported by the The National Key Laboratory of Antennas and Microwave Technology from Xidian University, the Fundamental Research Funds for the Central Universities, the Innovation Fund of Xidian University and the National Natural Science Foundation of China (61405152).

## REFERENCES

- [1] S. S. Guo, "Development status of anti-UAV technology and products," *Military Digest*, vol. 19, pp. 36-39, 2016.
- [2] D. Mei and L. Gao, "Application of directional energy weapon in anti-UAV operation," *China Plant Engineering*, vol. 7, pp. 40-42, 2017.
- [3] Y. Fan and W. M. Li, "The impact of UAV on future air defense operations and countermeasures," *Modern Defense Technology*, [D], 2003.
- [4] Y. Yang, C. Wang, and Y. Wu, "Current situation and development trend of anti-UAV strategy and weapon equipment," [J]. *Aerial Missile*, vol. 8, no. 8, pp. 27-31, 2013.
- [5] X. H. Pan and Z. Q. Qin, "Brief analysis of anti-UAV system," [J]. *Scientific Chinese*, vol. 2Z, p. 29, 2016.
- [6] M. Y. Xia, K. Zhao, and W. Ni, "Key technologies for the prevention and control of anti-UAV systems," [J]. *Command and Control and Simulation*, vol. 40, no. 2, pp. 53-60, 2018.
- [7] F. L. Hui, "Research on anti-UAV industry," [J]. *China's Strategic Emerging Industries*, vol. 16, p. 9, 2018.
- [8] L. Liu, Y. F. Wei, and Y. H. Zhang, "Analysis of the development of US anti-UAV technology and equipment," [J]. *Aerospace Electronic Countermeasure*, vol. 33, no. 1, p. 60, 2017.
- [9] Y. Zhi and S. Lan, "Development of non-destructive anti-UAV technology abroad," [J]. *Light Weapons*, vol. 2018, no. 07, pp. 18-23, 2018.
- [10] B. Luo, Y. C. Huang, and H. Zhou, "Overview of the development status of foreign anti-UAV systems," [J]. *Aerial Missiles*, vol. 2017, no. 09, pp. 24-28, 2017.
- [11] M. Saber, A. El Rharras, R. Saadane, et al., "Artificial neural networks, support vector

machine and energy detection for spectrum sensing based on real signals,” [J]. *International Journal of Communication Networks and Information Security*, vol. 11, no. 1, pp. 52-60, 2019.

- [12] M. Saber, A. El Rharras, R. Saadane, et al., “Transmit-power and interference control algorithm in cognitive radio network based on non-cooperative game theory, [C]. *The Proceedings of the Third International Conference on Smart City Applications*. Springer, Cham, pp. 647-662, 2019.
- [13] D. Me and L. Gao, “Application of directional energy weapons in anti-UAV operations,” [J]. *China Equipment Engineering*, 7:40, 2017.
- [14] Q. H. Zhu, *Technique of Communication Jamming and its Application in Spectrum Management*, Beijing: Posts & Telecom Press, 2010.
- [15] Y. W. Liu and X. B. Liao, “Construction of basic framework for anti UAV technology system,” *Journal of Weapon Industry*, 10:E926.3, 2015.
- [16] J. Chen and D. S. Chen, “Analysis of effectiveness index system of microwave weapon anti UAV,” *Journal of Guilin College of Aerospace Technology*, 2010.
- [17] C. Liang, “Research on UAV detection and jamming method based on wireless signal,” *Zhejiang University*, 2018.
- [18] H. Liu, “Development and application of anti aircraft system for security enterprises,” *China Security*, 2018.



**Hongbo Wei** was born in 1995 and received the B. S. degree in Electrical Engineering from Xidian University, Xi'an, China, in 2017. He is currently working toward the M.S. degree in Electromagnetic Field and Microwave Technology from Xidian University. His recent

research interests are mainly in the design of circuits and algorithms.



**Xinhui Wang** received the B. Eng. degree, M.Eng. and Ph.D. degrees in Electrical Engineering from Xidian University, Xi'an, China, in 2004, 2007, and 2011, respectively. Since 2011, he has been with Collaborative Innovation Center of Information Sensing and Understanding at Xidian University and Science and Technology on Antenna and Microwave Laboratory, Xidian University, as a Lecturer and Associate Professor. He has authored or coauthored over 60 international and regional refereed journal papers. His recent research interests are mainly in the design of microwave components system. He is a member of IEEE and senior member CIE.



**Xiaowei Shi** received the B.Eng. degree and Ph.D. degrees in Electrical Engineering from Xidian University, Xi'an, China, in 1982 and 1995, respectively. He has authored or coauthored over 200 international and regional refereed journal papers. He is IEEE Senior

Member and the Chairman of the IEEE Microwave Society Xi'an Chapter.



**Bo Liang** was born in 1993 and received the M.S. degree in Electromagnetic Field and Microwave Technology from Xidian University, Xi'an, China, in 2019. His field of expertise is related to drones, and research interests are mainly in the embedded system and algorithms.

# Compact Multilayer Dual-mode Substrate Integrated Waveguide Filtering Crossover Based on Orthogonal Modes

Zhigang Zhang and Yong Fan

Fundamental Science on Extreme High Frequency Key Laboratory  
University of Electronic Science and Technology of China, Chengdu 611731, China  
freemanzzg@163.com, yfan@uestc.edu.cn

**Abstract** — A novel multilayer substrate integrated waveguide (SIW) filtering crossover is proposed based on the orthogonal degenerate modes in SIW rectangular cavities (SIRCs). The degeneracy of dual-mode in multilayer SIRCs is used to realize the cross transmission and the orthogonality of the two modes is utilized to achieve the isolation relying on the four coupling slots located on metal layers. E-field distributions of the SIW cavities at  $TE_{102}$  and  $TE_{201}$  modes are studied for guiding the circuit realization. And then input/output and isolated ports can share the same resonator, which reduces the number of resonators by two. By adjusting the position of the coupling slots located between layers, the bandwidth can be controlled independently in a certain range without affecting the isolation effect. The detailed analysis and the design method based on coupling matrix have been first introduced to realize a third-order multilayer filtering crossover. Compared with other filtering crossovers, the proposed design exhibits good filtering responses, better isolation, lower loss, as well as compact size.

**Index Terms** — Dual-mode, filtering crossover, multilayer, and substrate integrated waveguide (SIW).

## I. INTRODUCTION

Crossovers are essential components in various microwave and millimeter-wave circuits, which allow different signals to cross each other without mutual interferences. It can be applied in the Butler matrix which has been widely used to construct modern beam-forming technology. However, most of these crossovers are implemented by microstrip technology, which would always suffer from high losses in high frequency-band.

To meet the need of higher frequency operation, the emerging substrate-integrated waveguide (SIW) technology [1-8] has been successfully applied to the design of various crossovers with high isolation, low insertion, and easy integration with other planar circuits. Moreover, a variety of microwave filters [1,5-6], power dividers [2,7], couplers, and antennas [3] are well

designed based on SIW structures.

Since the conventional SIW circuits are still too large for high-density microwave/millimeter wave systems, miniaturization design is becoming one of the primary trends for SIW components. The use of multilayered topologies [4-6] is known to provide more freedom to design coupling paths between waveguided structures while maintaining a compact circuit size. A compact multilayer dual-mode filter based on the substrate integrated waveguide circular cavity (SICC) is developed in [5]. A novel out-of-phase power divider based on a two-layer SIW is presented in [8].

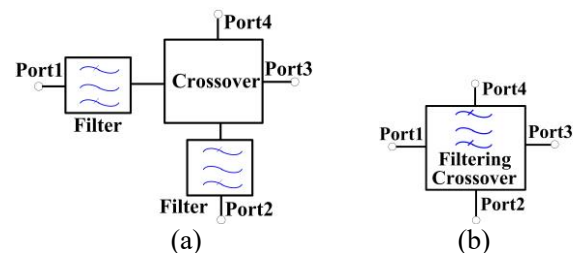


Fig. 1. Schematic of the crossover cascaded with BPFs and the filtering crossover: (a) traditional crossover; (b) filtering crossover.

As shown in Fig. 1, two filters are needed to integrate bandpass responses to one crossover, occupying large circuit areas. To further reduce size, a single device integrated with different functionalities, such as filtering crossover [9-16] has been attracting increasing attention. It also recommends an effective method to avoid the interstage mismatch and performance degradation due to a cascade connection of two individual components. A wideband filtering crossover using dual-mode ring resonator is proposed in [9]. In [12], a compact crossover with bandpass responses is presented by using a stub-loaded ring structures. In [16], a SIW filtering crossover is proposed based on degenerate modes in SIW cavities. Nevertheless, the footprint of this crossover is a little large due to the employment of five oversized square

cavities. As for aforementioned filtering crossover [13-16], the bandwidth can be adjusted only by changing the size of coupling aperture, which will also affect isolation level at the same time.

In this paper, a compact multilayer dual-mode SIW filtering crossover is presented based on the orthogonal degenerate modes in SIW rectangular cavities (SIRCs). The main design concept of this crossover is to make full use of the dual-modes in multilayer SIW rectangular cavities (SIRCs) to realize the cross transmission and the orthogonality of the two modes to achieve the isolation relying on the four coupling slots located between substrate layers. Unlike other filtering crossovers [9-12, 16] (each port need to be loaded a resonator), by utilizing the isolation property of the orthogonal degenerate modes, input/output and isolated ports can share the same resonator, which reduces the number of resonators by two. Moreover, with multilayer dual-mode technology, a third-order filtering crossover with flexibly controlled bandwidth can be realized by occupying only one resonator area. Comparatively speaking, both the bandwidth and isolation level of planar filtering crossover [12-16] depends on the width of the coupling aperture. By adjusting the position of the four coupling slots located between layers, the bandwidth of proposed design can be controlled independently in a certain range without affecting the isolation effect. What's unique about the analysis process of crossover is that the filtering crossover is divided into two band-pass filters (BPFs), and then the coupling matrix method is used to evaluate the initial value of design parameters accurately according to the specifications, which is beneficial to accelerate the later optimization design process. It's a good combination of multilayered topologies, dual-mode SIW cavities and multifunctional components [18-24], which realize the miniaturization design of the device while keeping good performance.

**II. ANALYSIS AND DESIGN**

**A. Filtering crossover structure**

As shown in Fig. 2, the proposed filtering crossover consists of three SIW rectangular cavities (SIRCs), which are coupled with each other by the four rectangular coupling slots located in different layers for miniaturization. Based on the isolation property of the orthogonal degenerate modes, Port1, Port2, and Port3, Port4 share the same Cavity I and III, which save the number of resonators by two. There are two paths for signal transmission (Port1 to 3 and Port2 to 4). When Port1 is the input port, Port3 is the through port, whereas Ports 2 and 4 are isolation port. Since the structure is completely symmetrical, it can be inferred that the signal will only be transmitted from Port 2 to 4 when Port 2 is excited. The coupling slots have variable lengths ( $L_{slot}$ ), widths ( $W_{slot}$ ) and offsets, and are arranged with respect to bandwidth and isolation level. In these figures,  $W_c$  is

the width of the external coupling aperture and  $L_{gap}$  is the length of feeding slot.  $L_{c1}$  and  $W_{c1}$  are length and width of Cavity I and III. The length and width of Cavity II are denoted as  $L_{c2}$  and  $W_{c2}$ , respectively.

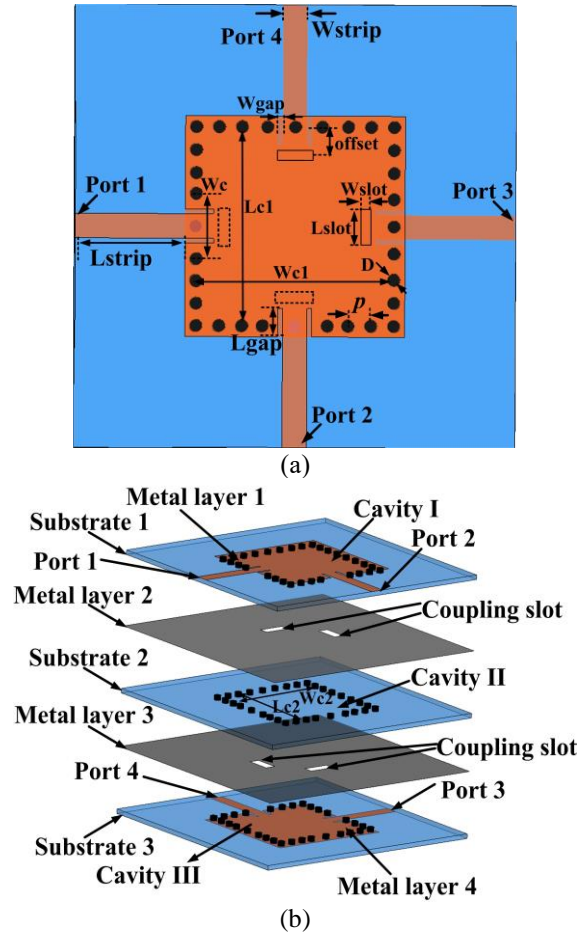


Fig. 2. The proposed multilayer dual-mode SIW filtering crossover: (a) top view; (b) anatomy view.

**B. Dual-mode theory**

A dual-mode SIW cavity[25-28] can support two degenerate modes within one resonant unite, which not only reduces the circuit size more than half but also adds the design flexibility.

By using the electromagnetic simulation software, the E-field distributions of the square cavity at the orthogonal degenerate modes can be analyzed. Figure 3 depicts the electric field magnitude distributions of  $TE_{102}$  and  $TE_{201}$  modes in a SIRC. As seen in Fig. 3 (a), the electric field within the SIW cavity is divided into two regions, which are represented as region A and region B. As can be seen, the electric field of  $TE_{102}$  mode is the strongest in region A, but the weakest in region B. Compared to the  $TE_{102}$  mode, it can be observed the electric field of  $TE_{201}$  mode is the weakest in region A, but the strongest in region B, as shown in Fig. 3 (b).

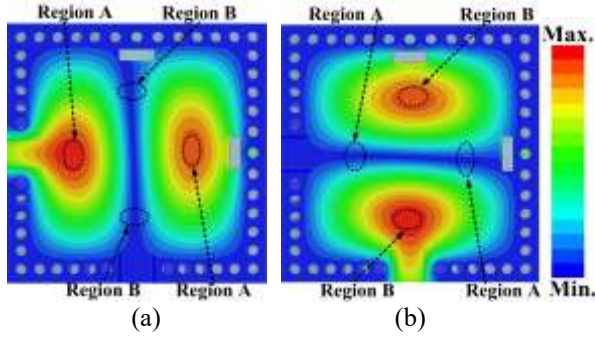


Fig. 3. E-field distributions of the dual-mode SIW cavity at: (a)  $TE_{102}$  mode; (b)  $TE_{201}$  mode in SIRC.

Therefore,  $TE_{102}$  and  $TE_{201}$  modes are orthogonal degenerate modes, which mean that the  $TE_{102}$  mode will be driven without the excitation of  $TE_{201}$  if the two ports are placed in region A, and vice versa in region B. Given this characteristic, input/output and isolated ports can share the same cavity, which helps to save the number of resonators by two. On the other hand, the resonant frequency of the  $TE_{m0n}$  mode for rectangular cavity is decided by [31]:

$$f_{m0n} = \frac{c}{2\sqrt{\mu_r \epsilon_r}} \sqrt{\left(\frac{m}{a_{eff}}\right)^2 + \left(\frac{n}{b_{eff}}\right)^2}, \quad (1)$$

$$a_{eff} = a - \frac{D^2}{0.95p}, \quad b_{eff} = b - \frac{D^2}{0.95p}. \quad (2)$$

Where,  $a_{eff}$  and  $b_{eff}$  are the SIRC's equivalent length, width, respectively.  $a$  and  $b$  are physical length and width of SIW cavity,  $D$  and  $p$  are the diameter of metallized via-holes and center-to-center pitch between two adjacent via-holes.

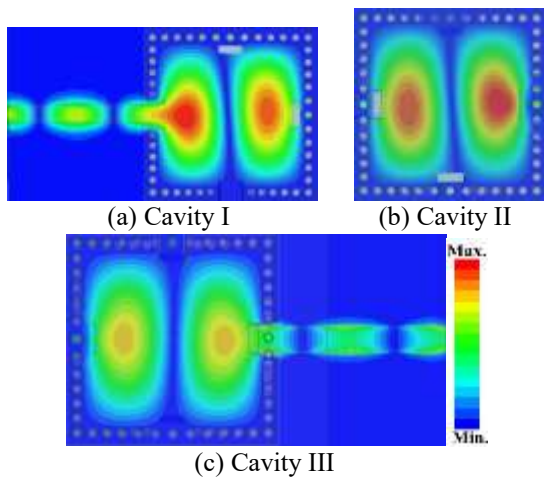


Fig. 4. E-field distributions in the multilayer SIW filtering crossover when Port 1 is excited.

Figure 4 illustrates the electric field magnitude distributions at 18 GHz in the multilayer SIW filtering crossover when Port 1 is driven. As can be seen,  $TE_{102}$  modes in cavities I~III have been excited to transmit the signal from Port 1 to 3 with the isolation of energy to Ports 2 and 4.

### C. Analysis of crossover

The topology of the filtering crossover is shown in Fig. 5 (a). Resonator 1, 4, resonator 2, 5 and resonator 3, 6 represent two degenerate modes exist in the same cavity. Since these two modes are perpendicular to each other, there is no coupling between them ( $M_{14}=M_{25}=M_{36}=0$ ).

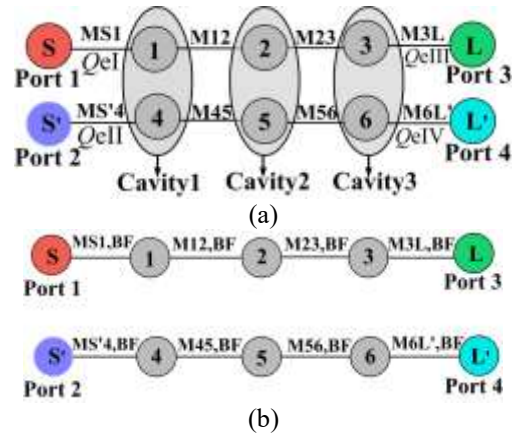


Fig. 5. (a) Topology of the third-order filtering crossover; (b) schematic topology of two third-order filters.

Obviously, there are two paths for signal transmission (Port1 to 3 and Port2 to 4). As depicted in Fig. 5 (b), in these two working states, the filtering crossover is equivalent to two third-order bandpass filters (BPFs) which have the same operating frequency and passband characteristics. The coupling matrix of third-order coupled-resonator BPFs is expressed as:

$$m_{N+2} = \begin{matrix} S & 1 & 2 & 3 & L \\ \begin{matrix} S \\ 1 \\ 2 \\ 3 \\ L \end{matrix} & \begin{bmatrix} 0 & m_{S1,BF} & 0 & 0 & 0 \\ m_{1S,BF} & 0 & m_{12,BF} & 0 & 0 \\ 0 & m_{21,BF} & 0 & m_{23,BF} & 0 \\ 0 & 0 & m_{32,BF} & 0 & m_{3L,BF} \\ 0 & 0 & 0 & m_{L3,BF} & 0 \end{bmatrix} & \end{matrix} \quad (3)$$

And the normalized input impedance of the filtering crossover in Fig. 5 (a) is required to be the same as matrix (3). Thus, the coupling coefficients for the filtering crossover topology in Fig. 5 (a) are determined as:

$$M_{S1,BF} = M_{S1}, \quad M_{S'4,BF} = M_{S'4}, \quad (4a)$$

$$M_{3L,BF} = M_{3L}, \quad M_{6L',BF} = M_{6L'}, \quad (4b)$$

$$M_{12,BF} = M_{45,BF} = M_{12} = M_{45}, \quad (4c)$$

$$M_{23,BF} = M_{56,BF} = M_{23} = M_{56}, \quad (4d)$$



The required normalized coupling coefficient ( $m$ ) and external quality factors ( $Q_e$ ) for the filtering crossover can be calculated by:

$$m_{12} = \frac{M_{12}}{FBW} = \frac{M_{45}}{FBW} = m_{12,BF}, \quad (5)$$

$$m_{23} = \frac{M_{23}}{FBW} = \frac{M_{56}}{FBW} = m_{23,BF}, \quad (6)$$

$$Q_e = \frac{FBW}{M_{S1}^2} = \frac{FBW}{M_{3L}^2} = \frac{1}{FBW \times m_{S1}^2} = \frac{1}{FBW \times m_{3L}^2}. \quad (7)$$

Generally, external quality factor ( $Q_e$ ) is related to the length of feeding slot ( $L_{gap}$ ) and the width of external coupling aperture ( $W_c$ ). It should be noted that  $L_{gap}$  can be used to control the bandwidth, which also have decisive impact on isolation levels. This is mainly because the degenerate mode in another channel will be excited easily for larger  $L_{gap}$ , so the isolation level will decrease with the increase of bandwidth.

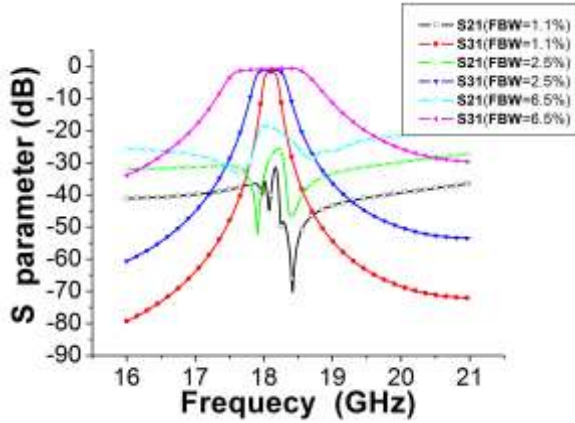


Fig. 6. Simulated S21 and S31 of the proposed third-order multilayer SIW filtering crossover with 25-dB RL and different FBWs

Figure 6 shows the simulated results of the proposed multilayer SIW filtering crossover with the same 25-dB return loss ( $RL$ ) and different fractional bandwidths ( $FBWs$ ). It can be seen that the isolation level degrades from  $-33$  to  $-20$  dB when the 3-dB  $FBW$  increases from 1.1% to 6.5%.

As for traditional filtering crossover, the bandwidth can be adjusted only by changing the size of coupling aperture, which will also affect isolation level at the same time. Thanks to the multilayer coupling structure, the bandwidth of proposed design can be adjusted independently in a certain range by controlling the position of the coupling slots ( $offset$ ), without affecting the isolation effect.

Figure 7 depicts the simulated S-parameter of the proposed multilayer SIW filtering crossover with the same 25-dB isolation level and different fractional bandwidths ( $FBWs$ ). Obviously, for different  $FBWs$ , the

isolation level remains unchanged, so the bandwidth of proposed filtering crossover can be adjusted independently. The main reason is that the change of the coupling slots offset only affect the strength of the magnetic coupling, but not stimulate the degenerate mode in another channel.

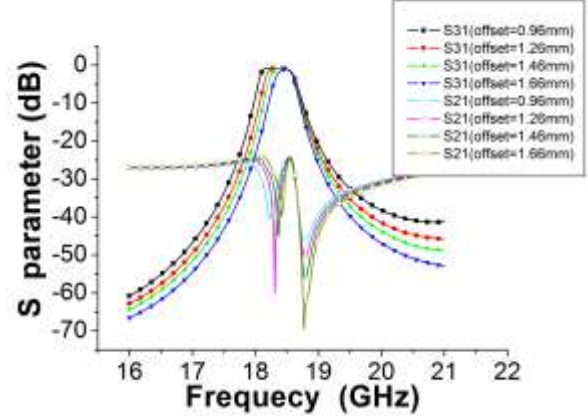


Fig. 7. Simulated S21 and S31 of the proposed third-order SIW filtering crossover with 25-dB isolation level and different FBWs

### E. Design example

In our design, the desired passband is centered at 18.2 GHz with the 1.3% fractional bandwidth ( $FBW$ ) of 25-dB equal-ripple return loss. Based on the advanced coupling matrix synthesis method in [30], the initial normalized coupling matrix of corresponding BPF can be synthesized as:

$$m_{N+2} = \begin{matrix} S \\ 1 \\ 2 \\ 3 \\ L \end{matrix} \begin{bmatrix} S & 1 & 2 & 3 & L \\ 0 & 1.2214 & 0 & 0 & 0 \\ 1.2214 & 0 & 1.2197 & 0 & 0 \\ 0 & 1.2197 & 0 & 1.2197 & 0 \\ 0 & 0 & 1.2197 & 0 & 1.2214 \\ 0 & 0 & 0 & 1.2214 & 0 \end{bmatrix}. \quad (8)$$

From (3)–(8) the desired parameters of the filtering crossover can be calculated as follows:

$$M_{12} = M_{23} = M_{45} = M_{56} = 0.015856, \quad Q_{e,S1} = 51.5645, \\ Q_{e,S3L} = Q_{e,S6L} = 51.5645.$$

To extract  $Q_e$ , full-wave simulations using ANSYS HFSS are carried out for the singly loaded SIRC excited by a 50- $\Omega$  microstrip line. The coupling strengths are controlled by the feeding slot length  $L_{gap}$  with fixed slot width  $W_{gap} = 0.3$  mm and coupling window width  $W_c = 3.28$  mm.  $Q_e$  can be extracted from the phase and the group delay response of S11 using [29]:

$$Q_e = \frac{f_0}{\Delta f_{\pm 90^\circ}}. \quad (9)$$

Where,  $f_0$  denotes the frequency at which the group delay

of S11 reaches the maximum,  $\Delta f_{\pm 90^\circ}$  indicates the ABW (absolute bandwidth) between  $\pm 90^\circ$  points with respect to the absolute phase of S11 at  $f_0$ .

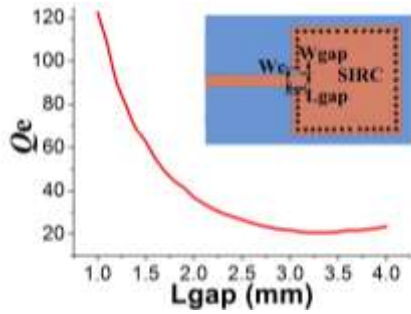


Fig. 8. Simulated external quality factor  $Q_e$  change with  $L_{gap}$ .

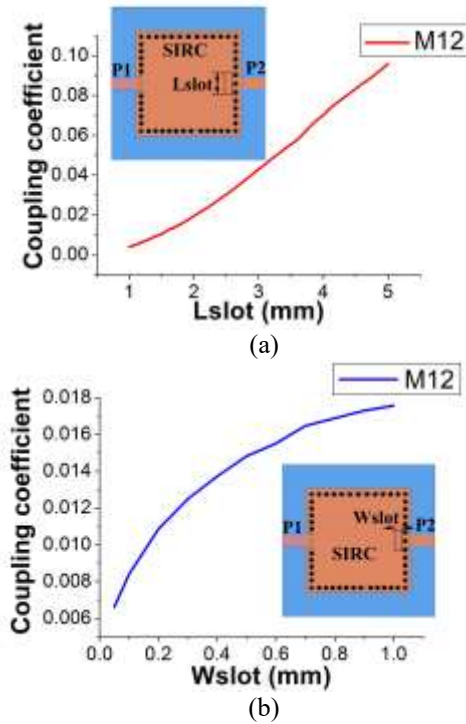


Fig. 9. Coupling coefficients versus the coupling slot: (a)  $M_{12}$  versus  $L_{slot}$ ,  $W_{slot}=0.6\text{mm}$ ; (b)  $M_{12}$  versus  $W_{slot}$ ,  $L_{slot}=1.8\text{mm}$ .

Figure 8 shows the external quality factor  $Q_e$  versus the length of feeding slot  $L_{gap}$ . It can be seen that the larger the feeding slot length, the smaller the external quality factor. Based on the previous analysis, the filtering crossover can be divided into two bandpass filters. The adjustment of external quality factor is realized by changing the value of  $L_{gap}$ , as depicted in Fig. 8. Then, the desired  $Q_e$  ( $Q_{eI} = Q_{eII} = Q_e$ ) can be achieved and then the initial value of  $L_{gap}$  can also be determined.

In general, the coupling coefficient of two coupled

resonators can be extracted by full-wave simulations. For two synchronously tuned coupled resonators weakly coupled by input and output ports, two split resonant frequencies can easily be identified by two resonance peaks, the coupling coefficient can then be evaluated using the formula [29]:

$$M_{ij} = \frac{f_{p2}^2 - f_{p1}^2}{f_{p2}^2 + f_{p1}^2}, \quad (10)$$

where  $f_{p1}$  and  $f_{p2}$  are the lower and higher resonant frequencies, respectively.

Figure 9 illustrates the extracted curves of  $M_{21}$ , which versus the length ( $L_{slot}$ ) and width ( $W_{slot}$ ) of coupling slot, respectively. As can be seen, when the length and width of the coupling slot increases, coupling coefficients also increases accordingly. Obviously, larger  $L_{slot}$  and  $W_{slot}$  correspond to the wider bandwidth.

In summary, the design procedure of the proposed filtering crossover is listed as follows. Firstly, the resonant frequency of the SIRC is calculated by formula (1) ~ (2), to meet the required center frequency  $f_0$ . Secondly, a coupling matrix of a third-order BPF is synthesized according to the desired center frequency  $f_0$  and the fractional bandwidth (FBW). Thirdly, according to formula (3) ~ (8), the coupling matrix and  $Q_e$  of the corresponding filtering crossover are obtained. Moreover, internal coupling parameters ( $L_{slot}$ ,  $W_{slot}$ , offset) and external coupling parameters ( $W_c$ ,  $L_{gap}$ ) are tuned to meet desired values of coupling coefficients and external quality factor, respectively. Finally, fine tuning of the entire structure is performed to realize good filtering crossover performance.

### III. SIMULATED AND MEASURED RESULTS

After optimization implemented by HFSS, the geometry parameters of the proposed filtering crossover are chosen as follows (all in mm):  $D=0.6$ ,  $p=1$ ,  $Lc1=Wc1=12.48$ ,  $Lc2=Wc2=12.61$ ,  $Lgap=1.55$ ,  $Lslot=1.75$ ,  $Wslot=0.6$ ,  $Wgap=0.3$ ,  $Wstrip=1.55$ ,  $Lstrip=11$ ,  $Wc=3.28$ ,  $offset=0.95$ .

To verify the above method, the proposed crossover was designed and fabricated on a substrate with thickness of 0.508 mm, relative dielectric constant of 2.2 and dielectric loss tangent 0.0009 (at 10 GHz). The measurement is accomplished by using the Agilent N5244A network analyzer.

Figure 10 shows the simulated and measured S-parameters of the multilayer filtering crossover. The measured passband is centered at 18.16 GHz with the 3-dB FBW of 2.35%. The in-band return loss (RL) is better than 19.56dB. The minimum insertion loss (IL) measured in the passband is 1.85 dB, while the isolation is better than 24.5 dB over the band of interest. It could be observed that the measured results are in excellent agreement with the simulation results.

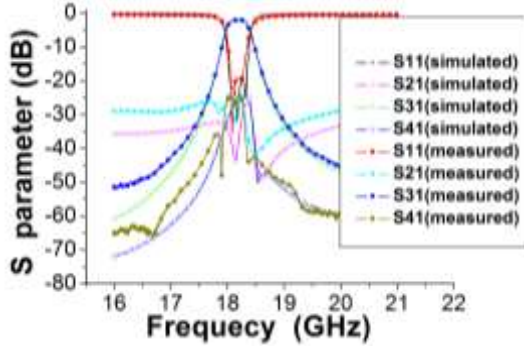


Fig. 10. Simulated and measured results of the fabricated multilayer SIW filtering crossover.

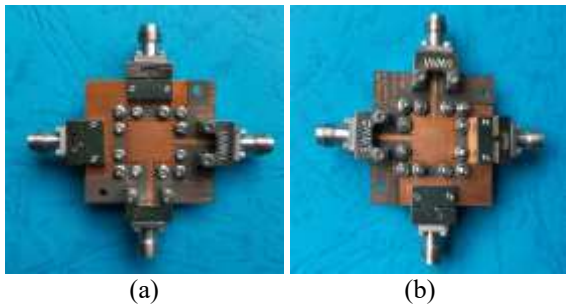


Fig. 11. Photograph of the fabricated multilayer dual-mode filtering crossover: (a) front view; (b) back view.

Table 1: Performance comparison of various crossovers

Ref.	$f_0(\text{GHz})/\text{FBW}(\%)$	Size( $\lambda_g^2$ )/ Isolation(dB)/ IL(dB)	Techniques/ Resonators*/ RL(dB)/ $\epsilon_r$
[12]	2/9.5	0.18/20/1.7	Microstrip/ 5/13/3.38
[13]	60/5	1.44/20/0.85	SIW/-/13/9.8
[14]	35/16.6	17.76/17/0.95	SIW/-/17/2.94
[15]	30/2.4	1.44/17/2.2	SIW/5/13/2.2
[16]	20/ 6.6	4.06/20/1.63	SIW/5/18/2.2
[17]	30/16.7	1.44/18/2.1	SIW/5/14/2.2
<b>This work</b>	18.16/2.35	0.69/24.5/1.85	SIW/3/20/2.2

Where  $\lambda_g$  is the guided wavelength on the substrate at the center frequency  $f_0$ , FBW represents the fractional bandwidth. Resonators\* represents the number of resonators.

The photograph of the fabricated filtering crossover based on multilayer dual-mode SIRC is displayed in Fig. 11. A detailed performance comparison with crossovers in recent years is shown in Table 1, which demonstrates the advantages of the proposed crossover clearly. Compared with [12], the proposed design has much higher  $Q$  factor and self-consistent electromagnetic shielding structure, which is suitable for higher frequency operation. Moreover, the proposed third-order

filtering crossover with flexibly controlled bandwidth can be realized by occupying only one resonator area.

Compared with the works in [13-17], the presented filtering crossover has featured better isolation and RL, flexibly controlled bandwidth, lower loss, minimum number of resonators, as well as more compact size.

#### IV. CONCLUSION

In this paper, a compact multilayer dual-mode SIW filtering crossover is proposed based on the orthogonal modes in SIRC. By properly arranging the feeding ports and the four coupling slots in multilayer dual-mode SIRC, excellent transmission and isolation responses have been successfully achieved. Moreover, input/output and isolated ports can share the same cavity, which save the number of resonators by two. The bandwidth of proposed design can be controlled independently in a certain range without affecting the isolation effect. What's unique about the analysis process of crossover is that the filtering crossover is divided into two band-pass filters (BPFs), and then the coupling matrix method is introduced to evaluate the initial value of design parameters accurately. With the acceptable isolation levels ( $>20\text{dB}$ ), the controllable bandwidth range is from 1.1% to 6.5%. A third-order multilayer filtering crossover operating at 18.2 GHz with a FBW of 2.4% was designed and fabricated. Good circuit performance in the experimental results has verified the proposed ideas. The presented multilayer filtering crossover with dual-mode SIW cavities could be more suitable for the development of high density and miniaturized RF/microwave system.

#### ACKNOWLEDGMENT

This work was supported in part by the Ministry of Science and Technology of the People's Republic of China under Grant 2013YQ200503 and in part by the National Natural Science Foundation of China (NSFC) under Grant 61001028.

#### REFERENCES

- [1] X.-P. Chen and K. Wu, "Substrate integrated waveguide cross-coupled filter with negative coupling structure," *IEEE Trans. Microw. Theory Tech.*, vol. 56, no. 1, pp. 142-149, Jan. 2008.
- [2] K. Song and Q. Xue, "Novel ultra-wideband (UWB) multilayer slotline power divider with bandpass response," *IEEE Microw. Wirel. Compon. Lett.*, vol. 20, no. 1, pp. 13-15, Jan. 2010.
- [3] Y. J. Cheng, W. Hong, and K. Wu, "94 GHz substrate integrated monopulse antenna array," *IEEE Trans. Antennas Propag.*, vol. 60, no. 1, pp. 121-128, Jan. 2012.
- [4] Y. J. Cheng, W. Hong, K. Wu, and Y. Fan, "A hybrid guided-wave structure of half mode substrate integrated waveguide and conductor-backed slotline and its application in directional

- couplers,” *IEEE Microw Wireless Compon Lett.* vol. 21, no. 2, pp. 65-67, Feb. 2011.
- [5] Z.-G. Zhang, Y. Fan, Y. J. Cheng, and Y.-H. Zhang “A compact multilayer dual-mode substrate integrated circular cavity (SICC) filter for X-band application,” *Prog. Electromagn. Res.*, vol. 122, no. 1, pp. 453-465, Jan. 2012.
- [6] Z.-G. Zhang, Y. Fan, and Y.-H. Zhang, “Compact 3-D multilayer substrate integrated circular and elliptic cavities (SICCs and SIECs) dual-mode filter with high selectivity,” *Appl. Comp. Electro. Society (ACES) Journal*, vol. 28, no. 4, pp. 333-340, Apr. 2013.
- [7] M.-K. Li, C. Chen, and W. Chen, “Miniaturized dual-band filter using dual-capacitively loaded SIW cavities,” *IEEE Microw. Wireless Compon. Lett.*, vol. 27, no. 4, pp. 344-346, Apr. 2017.
- [8] Q. Chen and J. Xu, “Out-of-phase power divider based on two-layer SIW,” *Electron Lett.*, vol. 50, no. 14, pp. 1005-1007, July 2014.
- [9] W. J. Feng, Y. Zhang, and W. Q. Che, “Wideband filtering crossover using dual-mode ring resonator,” *Electron Lett.*, vol. 52, no. 7, pp. 541-542, Apr. 2016.
- [10] M. Luo, X.-H. Tang, D. Lu, and Y.-H. Zhang, “Approach for filtering crossover design using mixed electric and magnetic coupling,” *Electron Lett.*, vol. 54, no. 9, pp. 5760-578, May 2018.
- [11] Q.-Y. Guo, X. Y. Zhang, and L. Gao, “Novel compact planar crossover with bandpass response based on cross-shaped resonator,” *IEEE Trans. Compon., Packag., Manuf. Technol.*, vol. 7, no. 12, pp. 2018-2026, Dec. 2017.
- [12] X. Y. Zhang, Q.-Y. Guo, K.-X. Wang, B.-J. Hu, and H. L. Zhang, “Compact filtering crossover using stub-loaded ring resonator,” *IEEE Microw. Wireless Compon. Lett.*, vol. 24, no. 5, pp. 327-329, May 2014.
- [13] T. Djerafi and K. Wu, “60 GHz substrate integrated waveguide crossover structure,” in *Proc. 39th Eur. Microw. Conf.*, Rome, Italy, pp. 1014-1017, 2009.
- [14] A. B. Guntupalli, T. Djerafi, and K. Wu, “Ultra-compact millimeter wave substrate integrated waveguide crossover structure utilizing simultaneous electric and magnetic coupling,” in *IEEE MTT-S Int. Microw. Symp. Dig.*, Montreal, QC, Canada, pp. 1-3, Mar. 2012.
- [15] X.-F. Ye, S.-Y. Zheng, and J.-H. Deng, “A compact patch crossover for millimeter-wave applications,” in *Proc. IEEE Int. Workshop Electromagn.*, Hsinchu, pp. 1-2, 2015.
- [16] Y. L. Zhou, K. Zhou, J. D. Zhang, C. X. Zhou, and W. Wu, “Miniaturized substrate integrated waveguide filtering crossover,” *2017 IEEE Electrical Design of Advanced Packaging and Systems Symposium*, Dec. 2017.
- [17] S. Y. Zheng and X. F. Ye, “Ultra-compact wideband millimeter-wave crossover using slotted SIW structure,” in *Proc. IEEE Int. Workshop Electromagn.*, Nanjing, China, pp. 1-2, May 2016.
- [18] P. Li, H. Chu, and R. S. Chen, “SIW magic-T with bandpass response,” *Electron Lett.*, vol. 51, no. 14, pp. 1078-1080, July 2015.
- [19] C.-K. Lin and S.-J. Chung, “A compact filtering 180° hybrid,” *IEEE Trans. Microw. Theory Tech.*, vol. 59, no. 12, pp. 3030-3036, Dec. 2011.
- [20] J.-X. Xu, X.-Y. Zhang, and H.-Y. Li, “Compact narrowband filtering rat-race coupler using quad-mode dielectric resonator,” *IEEE Trans. Microw. Theory Tech.*, vol. 66, no. 9, pp. 4029-4039, Sep. 2018.
- [21] Z.-G. Zhang, Y. Fan, and Y.-H. Zhang, “Multilayer half-mode substrate integrated waveguide wide-band coupler with high selectivity,” *Appl. Comp. Electro. Society (ACES) Journal*, vol. 34, no. 9, pp. 1418-1425, Sep. 2019.
- [22] S.-Q. Han, K. Zhou, J.-D. Zhang, C.-X. Zhou, and W. Wu, “Novel substrate integrated waveguide filtering crossover using orthogonal degenerate modes,” *IEEE Microw. Wireless Compon. Lett.*, vol. 27, no. 9, pp. 803-805, Sep. 2017.
- [23] Y.-J. Cheng and Y. Fan, “Compact substrate-integrated waveguide bandpass rat-race coupler and its microwave applications,” *IET Microw., Antennas Propag.*, vol. 6, no. 9, pp. 1000-1006, June 2012.
- [24] H.-Y. Li, J.-X. Xu, and X.-Y. Zhang, “Substrate integrated waveguide filtering rat-race Coupler based on orthogonal degenerate modes,” *IEEE Trans. Microw. Theory Techn.*, vol. 67, no. 1, pp. 140-150, Jan. 2019.
- [25] S. Zhang, J.-Y. Rao, J.-S. Hong, and F.-L. Liu, “A novel dual-band controllable bandpass filter based on fan-shaped substrate integrated waveguide,” *IEEE Microw. Wireless Compon. Lett.*, vol. 28, no. 4, pp. 308-310, Apr. 2018.
- [26] Y.-D. Dong and T. Itoh, “Miniaturized substrate integrated waveguide slot antennas based on negative order resonance,” *IEEE Trans. Antennas Propag.*, vol. 58, no. 12, pp. 3856-3864, Dec. 2010.
- [27] R. Rezaiesarlak, M. Salehi, and E. Mehrshahi, “Hybrid of moment method and mode matching technique for full-wave analysis of SIW circuits,” *Appl. Comp. Electro. Society (ACES) Journal*, vol. 26, no. 8, pp. 688-695, Aug. 2011.
- [28] Z. J. Zhu, L. Cao, and C. L. Wei, “Novel compact microstrip dual-Mode filters with two controllable transmission zeros,” *Appl. Comp. Electro. Society (ACES) Journal*, vol. 33, no. 1, pp. 43-48, Jan. 2018.
- [29] J.-S. Hong and M.-J. Lancaster, *Microstrip Filter for RF/Microwave Applications*. New York, NY,

USA: Wiley; 2001.

- [30] R.-J. Cameron, "Advanced coupling matrix synthesis techniques for microwave filters," *IEEE Trans. Microw. Theory Tech.*, vol. 51, no. 1, pp. 1-10, Jan. 2003
- [31] D.-M. Pozar, *Microwave Engineering*. Second edition, New York: Wiley; 1998.



**Zhigang Zhang** was born in Shanxi Province, China. He received the B.S. degree in Electronic Information Engineering and M.S. degree in Wireless Physics from Sichuan University and is currently working toward the Ph.D. degree in Electromagnetic Field and Micro-wave

Technology from The University of Electronic Science and Technology of China (UESTC), Chengdu, Sichuan, China. His current research interests include SIW technology and its application, microwave and millimeter-wave filters and couplers, electromagnetic theory.



**Yong Fan** received the B.E. degree from the Nanjing University of Science and Technology, Nanjing, Jiangsu, China, in 1985, and the M.S. degree from the University of Electronic Science and Technology of China (UESTC), Chengdu, Sichuan, China, in 1992.

He is currently with the School of Electronic Engineering, UESTC. He has authored or coauthored over 60 papers. From 1985 to 1989, he was interested in microwave integrated circuits. Since 1989, his research interests include millimeter-wave communication, electromagnetic theory, millimeter-wave technology, and millimeter-wave systems. Fan is a Senior Member of the Chinese Institute of Electronics (CIE).

# Design and Application of Coupled Line Cross-Shaped Resonator in Band-pass Filter

Dong-Sheng La<sup>1,2</sup>, Xin Guan<sup>1</sup>, Hong-Cheng Li<sup>1</sup>, Yu-Ying Li<sup>1</sup>, and Jing-Wei Guo<sup>3</sup>

<sup>1</sup> School of Computer and Communication Engineering  
Northeastern University at Qinhuangdao, Qinhuangdao, 066004, China  
ladongsheng@163.com, guanxinww@163.com, redorangel@163.com, believeerr@163.com

<sup>2</sup> Guangxi Key Laboratory of Wireless Wideband Communication and Signal Processing  
Guilin, 541004, China

<sup>3</sup> School of Information Science and Engineering  
Yanshan University, Qinhuangdao, 066004, China  
jingweigu@ysu.edu.cn

**Abstract** — A coupled line cross-shaped resonator (CLCSR) is proposed, which consists of four parallel coupled lines. By using even- and odd-mode approach, this resonator is characterized and designed to build up a wide band-pass filter. There are three transmission poles in the pass-band and two transmission zeros out of the pass-band. The positions of the transmission zeros are fixed. The transmission poles are determined and adjusted by the parameters:  $z_1$ ,  $z_2$ ,  $k_1$ , and  $k_2$ . Then two coupled line cross-shaped resonators are cascaded to realize a wide band-pass filter. The sharper selectivity and better performance can be obtained by cascading two CLCSRs. Good S-parameters are achieved as demonstrated in both simulated and measured results.

**Index Terms** — Band-pass filter, coupled line cross-shaped resonator, transmission pole, transmission zero.

## I. INTRODUCTION

The multi-mode resonator wide band-pass filter (BPF) design has become a research hotspot due to its simple filter topology, compact physical size and simple design process. In Ref. [1], an ultra-wideband BPF is designed with a cross-shaped resonator. An ultra-wideband BPF with the capacitively coupled stub-loaded resonator is introduced in Ref. [2]. Reference [3] proposes a differential wideband BPF which consists of slot-line multimode resonators. Cheng proposes a wideband BPF with reconfigurable bandwidth function [4]. The wideband BPF is composed of a parallel-coupled line structure and a cross-shaped resonator. In Refs. [5-11], some structures are added to the cross-shaped resonator, such as coupled lines, short stubs. Those band-pass filters provide better ideas for this

study. There are many studies based on cross-shaped resonators. However, the performance of the ordinary cross-shaped resonators is poor, and the frequency selectivity of the filters needs to be improved.

In this paper, a new coupled line cross-shaped resonator filter is proposed. The input impedance of its equivalent circuit can be calculated through the odd-even mode method. The proposed filter is miniaturized by bending parallel coupled lines. In order to increase the bandwidth and improve the out-of-band performance, two CLCSRs are cascaded in the wideband BPF design. The simulated results are basically consistent with the measured ones. Compared with single cross-shaped resonator, the frequency selectivity of the cascaded CLCSR BPF is improved.

## II. BAND-PASS FILTER DESIGN

Figure 1 (a) shows the proposed BPF which is composed of single CLCSR. The CLCSR consists of four parallel coupled lines. They are connected at the middle node position. The proposed BPF circuit is a symmetric structure. The odd mode characteristic impedance and even mode characteristic impedance of the parallel coupled lines are denoted as  $z_{ce1} = z_1 \sqrt{1+k_1} / \sqrt{1-k_1}$ ,  $z_{co1} = z_1 \sqrt{1-k_1} / \sqrt{1+k_1}$ . The odd mode characteristic impedance and even mode characteristic impedance of the other two coupled lines are denoted as  $z_{ce2} = z_2 \sqrt{1+k_2} / \sqrt{1-k_2}$ ,  $z_{co2} = z_2 \sqrt{1-k_2} / \sqrt{1+k_2}$ . The electrical length of all coupled lines is  $\theta$ .

The odd mode circuit is shown in Fig. 1 (b) and the even mode circuit is shown in Fig. (c). The normalized impedance parameters  $z_1 = Z_1 / Z_0$  and  $z_2 = Z_2 / Z_0$  are

used in the even-odd mode circuit. The input impedances  $z_{ine(o)}$  can be derived from formula (1) and (2) in Ref [12]. According to the odd-even mode circuit, the even mode load impedance is in formula (2) and the odd mode load impedance is in formula (3):

$$z_{ine(o)} = \frac{z_{Le(o)}z_1(1-k_1^2) - (1-k_1^2)\tan\theta z_{Le(o)}z_1 + jz_1^2\tan\theta\sqrt{1-k_1^2}}{(2j\tan\theta z_{Le(o)}\sqrt{1-k_1^2} + z_1(1+k_1))(1-k_1)}, \quad (1)$$

$$z_{Le} = \frac{z_2\sqrt{1-k_2^2}}{2j\tan(\theta)(1-k_2)}, \quad (2)$$

$$z_{Lo} = 0. \quad (3)$$

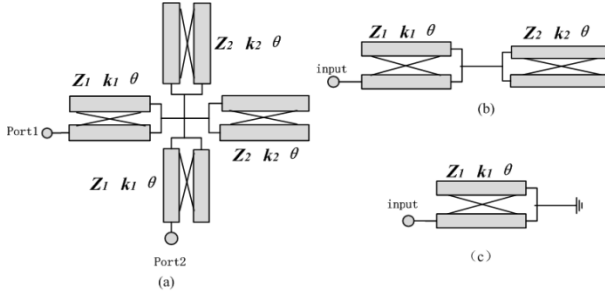


Fig. 1. (a) Ideal circuit of the CLCSR BPF, (b) odd-mode equivalent circuit, and (c) even-mode equivalent circuit.

In a symmetric two-port network, the normalized frequency response is

$$s_{11} = s_{22} = \frac{z_{ine}z_{ino} - 1}{(z_{ine} - 1)(z_{ino} - 1)}, \quad (4)$$

$$s_{12} = s_{21} = \frac{z_{ine} - z_{ino}}{(z_{ine} - 1)(z_{ino} - 1)}. \quad (5)$$

When  $\theta$  is equal to  $\pi$ , the corresponding frequency is  $f_0$ , as shown in formula (6). When  $|s_{21}|$  is equal to zero, the transmission zeros of the CLCSR BPF can be obtained. The transmission zeros  $f_{z1}$  and  $f_{z2}$  are shown in formula (7a) and (7b). The positions of the CLCSR BPF's transmission zeros can be adjusted through the  $f_0$ :

$$\theta = \pi = \frac{2\pi f_0 l}{v}, \quad (6)$$

$$f_{z1} = \frac{1}{2}f_0, \quad (7a)$$

$$f_{z2} = \frac{3}{2}f_0. \quad (7b)$$

When  $|s_{11}|$  is equal to zero, the transmission poles of the CLCSR BPF can be obtained. The calculated results of the transmission poles are as shown in formula (8) and (9):

$$f_{p1} = \frac{2f_0 \arctan(\sqrt{u_p})}{\pi}, \quad (8)$$

$$f_{p2} = f_0, \quad (9)$$

$$f_{p3} = \frac{2f_0(\pi - \arctan(\sqrt{u_p}))}{\pi}, \quad (10)$$

$$u_p = \frac{(-\sqrt{1-k_1^2}z_2(-\frac{1}{2}z_1^2 + k_1 - 1)\sqrt{1-k_2^2} + z_1(k_1 - 1)(k_2 - 1)(1+k_1))}{z_1^2(-\frac{1}{2}z_2(-1+k_1)\sqrt{1-k_2^2}\sqrt{1-k_1^2} - z_1(1+k_1)(k_2 - 1))}. \quad (11)$$

The transmission poles  $f_{p1}$  and  $f_{p3}$  are symmetric about the  $f_0$ . There are two transmission zeros out of the pass-band and three transmission poles in the pass-band. The zero-pole distribution of the ideal CLCSR BPF is shown in Fig. 2.

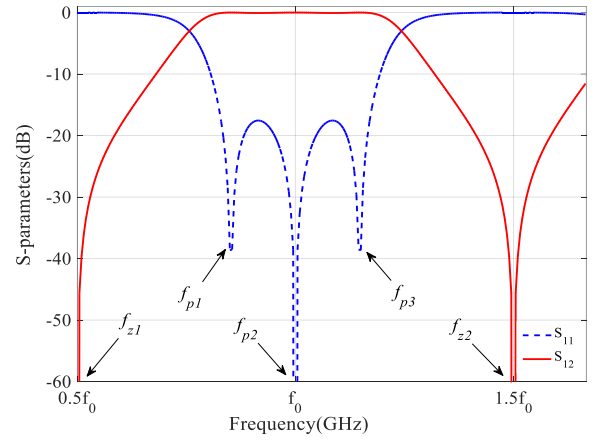


Fig. 2. Zero-pole distribution of the CLCSR BPF's circuit.

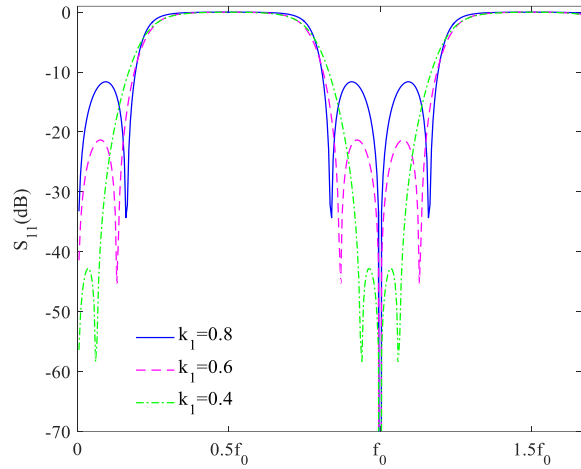
In Fig. 2, the relationship between the transmission poles and the transmission zeros in the frequency range is:

$$f_{z1} < f_{p1} < f_{p2} < f_{p3} < f_{z2}. \quad (12)$$

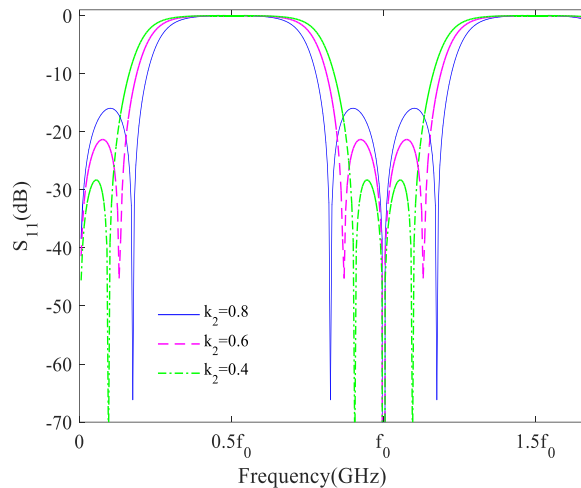
The influence of the design parameters on the return loss of the CLCSR BPF is given in Fig. 3. When one parameter changes, the other parameters remain unchanged. The transmission poles  $f_{p1}$  and  $f_{p3}$  are far away from each other when one parameter increases. In Fig. 3 (a), with the increases of  $k_1$ , the return loss decreases and the frequency selectivity is improved. The bandwidth increases and the return loss decreases with the increases of  $k_2$  in Fig. 3 (b). In Fig. 3 (c), the frequency selectivity is improved and the return loss decreases with the increase of  $z_1$ . In Fig. 3 (d), the bandwidth increases and the return loss decreases with the increase of  $z_2$ .

The physical structure parameters of the coupled lines

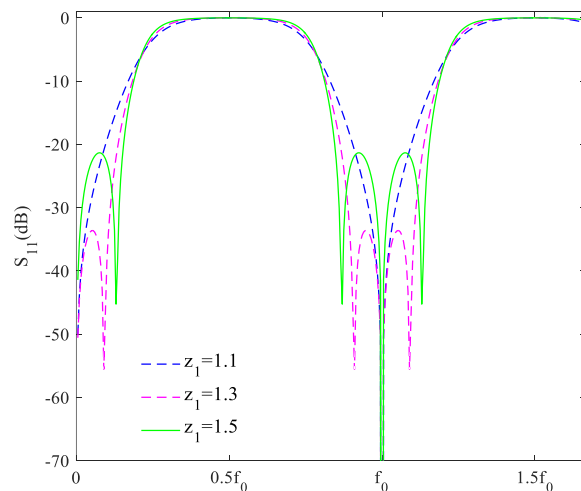
can be calculated based on  $Z$  and  $k$ . The characteristic impedance  $Z$  is smaller when the width of the coupled line is wider. When the gap between the coupled lines is wider, the value of  $k$  is usually smaller. Thus, the design parameters are selected as  $k_1 = k_2 = 0.6$ ,  $z_1 = z_2 = 1.5$ .



(a) Frequency(GHz)



Frequency(GHz)



(c) Frequency(GHz)

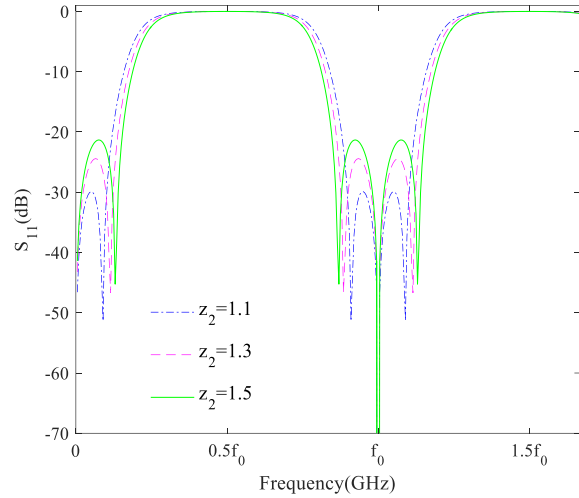


Fig. 3. The influence of  $z_1$ ,  $z_2$ ,  $k_1$ , and  $k_2$  on the return loss of the CLCSR BPF: (a)  $z_1$ ; (b)  $z_2$ ; (c)  $k_1$ ; (d)  $k_2$ .

### III. RESULT AND DISCUSSION

The final size of the CLCSR BPF is shown in Fig. 4 (a) and the photograph of the CLCSR BPF is shown in Fig. 4 (b). The coupled lines are bended for filter miniaturization. The resonant frequencies of the CLCSR BPF are simulated by using ANSYS HFSS. The EM method in simulation is finite element method. The CLCSR BPF is designed on Rogers RT5880 microwave dielectric board ( $h = 0.508$  mm,  $\epsilon_{re} = 2.2$ ,  $\tan \delta = 0.0009$ ). The line width  $g = 1.54$  mm is chosen for the characteristic impedance of  $50\Omega$  for the input/output microstrip line. The characteristic impedance of SMA connector is  $50\Omega$  which matches the microstrip line.

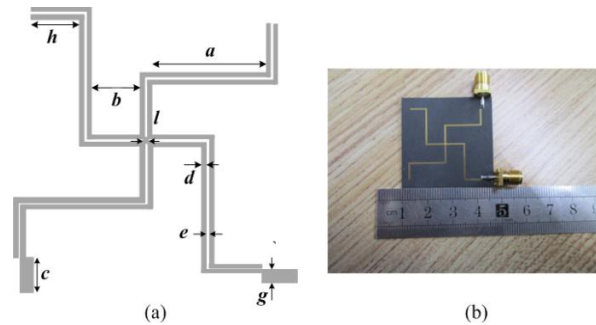


Fig. 4. (a) The CLCSR BPF structure parameters ( $a=14.1$ ,  $b=7.19$ ,  $c=5$ ,  $d=0.255$ ,  $e=0.15$ ,  $g=1.54$ ,  $h=6.58$ ,  $l=0.2$ , Unit: mm), (b) photograph of the CLCSR BPF.

Figure 5 shows the simulated and measured results of the CLCSR BPF. The measured results are obtained with Agilent N5230C vector network analyzer. As shown in Fig. 5, the measured results almost agree well with the simulation ones. The absolute bandwidth of the CLCSR BPF is 1.6 GHz, which is from 3.2 to 4.8 GHz. The return



loss is bigger than 12dB in the whole pass-band. In addition, the stop-band rejection is better than 14dB from 2 to 3.2 GHz. Moreover the stop-band rejection is better than 12 dB from 4.8 to 7 GHz.

In order to improve the out-of-band performance and expand the pass-band frequency range, two CLCSRs are cascaded in wide-band BPF design. Figure 6 (a) shows the equivalent circuit of the cascaded CLCSR BPF. The cascaded CLCSR BPF structure parameters are slightly different from the CLCSR BPF in Fig. 1. The cascaded CLCSR BPF layout is shown in Fig. 6 (b) and the photograph of the cascaded CLCSR BPF is shown in Fig. 6 (c).

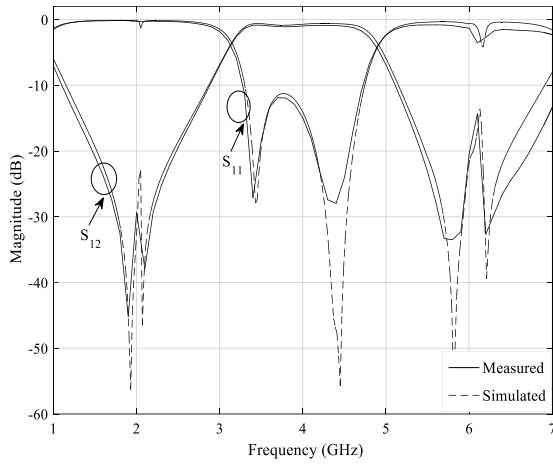


Fig. 5. Simulated and measured results of the CLCSR BPF.

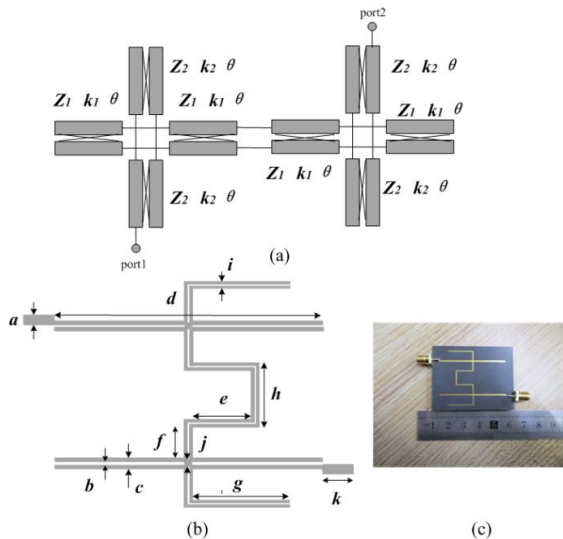


Fig. 6. (a) Ideal circuit diagram for the cascaded CLCSR BPF, (b) actual size of the cascaded CLCSR BPF circuit ( $a=1.54$ ,  $b=0.15$ ,  $c=1.05$ ,  $d=43.12$ ,  $e=10.78$ ,  $f=5.92$ ,  $g=16.66$ ,  $h=4.9$ ,  $i=0.7$ ,  $j=0.2$ ,  $k=4.5$ , Unit: mm), (c) photograph of the cascaded CLCSR BPF.

The simulated and measured results of the cascaded CLCSR BPF are shown in Fig. 7. The absolute bandwidth of the cascaded CLCSR BPF is 2 GHz from 4.2 to 6.2 GHz. The return loss is bigger than 12dB in the pass-band. The out-of-band rejection levels are greater than 20 dB. The simulated results are basically consistent with the measured ones. The frequency discrepancy between the simulated and measured results is due to the machining error and the material parameters difference. The material parameters include the dielectric constant and the thickness of dielectric plate. The discrepancy of the return loss and the insertion loss is due to the conductor loss, the dielectric loss and the radiation loss. There are a few errors in the simulated and measured results, which also makes the simulated results different from the measured ones.

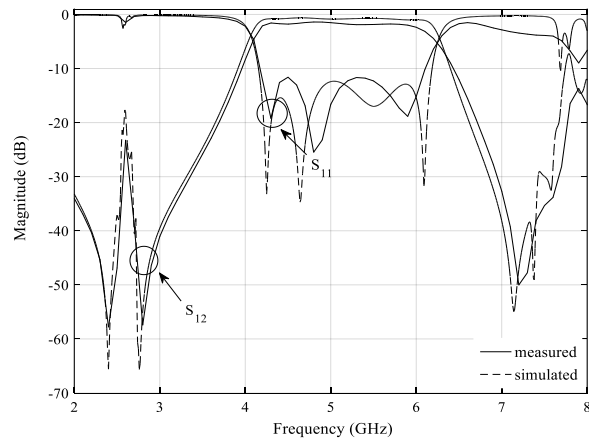


Fig. 7. Simulated and measured results of the cascaded CLCSR BPF.

Table 1 compares the proposed works with some previous works. Obviously, the proposed filters have some advantages, such as wide bandwidth, compact size and high performance.

#### IV. CONCLUSION

In this paper, a CLCSR is proposed, which consists of four parallel coupled lines. By using the odd-even mode method, the CLCSR is analyzed and designed to construct a wide-band BPF. The cascaded CLCSR BPF is designed by cascading CLCSRs. Finally, the CLCSR BPF and the cascaded CLCSR BPF are simulated, fabricated and measured. The simulated and measured results for two proposed wide-band BPFs are basically the same.

#### ACKNOWLEDGMENT

This work is supported by National Natural Science Foundation of China under Grant 61501100, Natural Science Foundation of Hebei Province under Grant F2019203012, the Fundamental Research Funds for the

Central Universities under Grant N2023017, and the Open Project of Guangxi Key Laboratory of Wireless

Wideband Communication and Signal Processing under Grant GXKL06180201.

Table 1: Compares the proposed works with some previous works

Reference	Center Frequency	TZs/TPs	Insertion Loss	Return Loss	Size ( $\lambda_g * \lambda_g$ )
Ref. [1]	6.65	2/4	0.35	>20	0.5*0.79
Ref. [2]	6.85	4/5	0.6	>14	0.38*1.14
Ref. [3]	2.6	Not give	0.5	>10	1.4*1.4
Ref. [4]	5.7	2/3	1.4	>10	0.18*0.18
Ref. [5]	1.75	Not give	1.5	Not give	0.38*0.17
CLCSR BPF	4	2/3	0.4	>12	0.15*0.15
Cascaded CLCSR BPF	5.2	2/5	1.1	>12	0.19*0.15

## REFERENCES

- [1] H. Wang, G. Yang, and W. Kang, "Application of cross-shaped resonator to the ultra wideband bandpass filter design," *IEEE Microwave and Wireless Components Letters*, vol. 17, no. 12, pp. 667-669, Dec. 2011.
- [2] T. H. Duong and I. S. Kim, "Steeply sloped UWB band-pass filter based on stub-loaded resonator," *IEEE Microwave and Wireless Components Letters*, vol. 20, no. 8, pp. 441-443, Aug. 2010.
- [3] D. Chen, H. Z. Bu, L. Zhu, et al., "A differential-mode wideband band-pass filter on slot-line multimode resonator with controllable bandwidth," *IEEE Microwave and Wireless Components Letters*, vol. 25, no. 1, pp. 28-30, Jan. 2015.
- [4] T. Cheng and K. W. Tam, "A wideband band-pass filter with reconfigurable bandwidth based on cross-shaped resonator," *IEEE Microwave and Wireless Components Letters*, vol. 27, no. 10, pp. 909-911, Oct. 2017.
- [5] A. Zakharov and M. Ilchenko, "Trisection microstrip delay line filter with mixed cross-coupling," *IEEE Microwave and Wireless Components Letters*, vol. 27, no. 12, pp. 1083-1085, Dec. 2017.
- [6] X. K. Bi, C. Teng, P. Cheong, et al., "Wideband band-pass filters with reconfigurable bandwidth and fixed notch bands based on terminated cross-shaped resonator," *IET Microwaves, Antennas & Propagation*, vol. 13 no. 6, pp. 796-803, May 2019.
- [7] Z. C. Guo, L. Zhu, and S. W. Wong, "A quantitative approach for direct synthesis of band-pass filters composed of transversal resonators," *IEEE Transactions on Circuits and Systems—II: Express Briefs*, vol. 66, no. 4, pp.577-581, Apr. 2019.
- [8] D. Chen, H. Z. Bu, L. Zhu, et al., "A differential-mode wideband band-pass filter on slot-line multimode resonator with controllable bandwidth," *IEEE Microwave and Wireless Components Letters*, vol. 25, no. 1, pp. 28-30, Jan. 2015.
- [9] L. X. Zhou, Y. Z. Yin, W. Hu, et al., "Compact band-pass filter with sharp out-of-band rejection and its application," *ACES Journal*, vol. 32, no. 3, pp. 249-255, Mar. 2017.
- [10] M. Y. Fu, Q. Y. Xiang, and Q. Y. Feng, "A tunable trisection bandpass filter with constant fractional bandwidth based on magnetic coupling," *ACES Journal*, vol. 34, no. 12, pp. 1888-1896, Dec. 2019.
- [11] D. Y. Tian, Q. Y. Feng, and Q. Y. Xiang, "Design of high order cross-coupled constant absolute bandwidth frequency-agile bandpass filters," *ACES Journal*, vol. 34, no. 9, pp. 1373-1378, Sep. 2019.
- [12] I. Z. George and A. K. Johnson, "Coupled transmission line networks in an inhomogeneous dielectric medium," *IEEE Transactions on Microwave Theory and Techniques*, vol. 17, no. 10, pp. 753~759, Oct. 1969.



**Dong-Sheng La** was born in Hebei, P.R. China. He has received his Masters degrees from Xinjiang Astronomical Observatory, Chinese Academy of Sciences in 2008, and his Ph.D. degrees from Beijing University of Posts and Telecommunications in 2011. He is currently an Associate Professor in the School of Computer and Communication Engineering, Northeastern University at Qinhuangdao in China. His recent research interests include passive RF components, patch antennas and electromagnetic compatibility. He has authored or coauthored over 20 journal and conference papers.



**Xin Guan** received B.S. degree in Information Warfare Technology from Shenyang Ligong University, Shenyang, China, in 2018. Since 2018, she is now working toward the Master degree in Northeastern University at Qinhuangdao, Qinhuangdao, China, where she

studied the content of electromagnetic waves, microstrip transmission lines, and microstrip filters. Her research interests include microwave filter, electromagnetic compatibility.



**Hong-Cheng Li** received the Bachelor's degree in Communications Engineering from Northeastern University at Qinhuangdao, Qinhuangdao, China, in 2019. He is now working toward the Master degree in Northeastern University, Qinhuangdao, China. His research interests include synthesis and design of microwave filters, electromagnetic compatibility.



**Yu-Ying Li** received the Bachelor's degree in Electronic Information Engineering from Shenyang University of Technology, Shenyang, China, in 2019. She is now working toward the Master degree in Northeastern University at Qinhuangdao, Qinhuangdao, China. Her research interests include antenna and antenna array.



**Jing-Wei Guo** was born in Hebei, China, in 1982. He received his Ph.D. degree in Electromagnetic Field and Microwave Technology from Beijing University of Posts and Telecommunications in 2011. He is engaging in the research of metamaterials, semiconductor technology and optoelectronic field recently, as an Associate Professor of Yanshan University, China.

## A Metal-Strip Integrated Filtering Waveguide

Xiao-Yu Ma<sup>1</sup>, Zi-Yu Pang<sup>1</sup>, Ge Zhao<sup>1</sup>, Jia-Jun Liang<sup>2\*</sup>, Guan-Long Huang<sup>1\*</sup>  
Luyu Zhao<sup>3</sup>, and Chow-Yen-Desmond Sim<sup>4</sup>

<sup>1</sup> College of Electronics and Information Engineering  
Shenzhen University, Shenzhen, Guangdong 518060, China  
\*guanlong.huang@ieee.org

<sup>2</sup> School of Physics and Telecommunication Engineering  
Yulin Normal University, Yulin, P. R. China  
\*shuigpjd@163.com

<sup>3</sup> National Key Laboratory of Antennas and Microwave Technology  
Xidian University, Xi'an, Shanxi, 710071, P.R. China

<sup>4</sup> Department of Electrical Engineering, Feng Chia University, Taichung 40724, Taiwan

**Abstract** — In this paper, a metal-strip integrated filtering waveguide is proposed. The overall structure consists of a traditional rectangular waveguide and a metal-strip surface which is loaded at the bottom wall of the waveguide. The customized surface can be considered as a meta-surface, the working property of which can be transformed between perfect electric conductor (PEC) and perfect magnetic conductor (PMC) depending on its operational frequency. When the surface acts as a PEC, the filtering waveguide works at pass-band and electromagnetic waves can freely travel inside the waveguide like a conventional one. When the surface plays a role as a PMC outside the interested frequency band, a stop-band can be created where the propagation of electromagnetic waves could be effectively prevented. By integrating the band-pass and band-stop functions into the same waveguide, a compact filtering waveguide structure can be obtained. The proposed filtering waveguide operates in Ku-band with pass-band of 12 GHz~15.1 GHz and stopband of 15.8 GHz~17.4 GHz. Experimental results show a favorable consistency with the simulation results and verify the proposed concept. Moreover, the proposed structure also possesses a compact size and characterizes for easy-fabrication, having a promising practicability in advanced satellite communication system applications.

**Index Terms** — Filtering waveguide, metal-strip surface, meta-surface, PEC, PMC.

### I. INTRODUCTION

Satellite communication (Satcom) technology is of great significance for global ocean, land and

meteorology monitoring and surveillance. As an important front-end device for the Satcom wireless communication systems, antenna is responsible for transmitting and receiving radio frequency (RF) signals. However, most of the antennas are “passive” and receive signals without any distinction [1]-[7]. Therefore, these signals may cause certain interference to the RF transmitting and receiving systems. Waveguide-based components are frequently adopted in Satcom communication due to its excellent resistance to cosmic radiation and great electrical and structural performance. Traditionally waveguide-based antenna and filters are bridged via waveguide channels, which usually causes a bulky size of the RF front-end. Hence, it is always a requirement that if the signal propagation and filtering function can be properly integrated into a waveguide, not only the loss caused by the waveguide cascade topology can be avoided, but also the size of the overall RF front-end can be greatly reduced.

In recent years, various integrated filtering waveguide have been proposed [8]-[10]. A waveguide band-pass filter is introduced in [11], which is built on a dielectric substrate and applies a new type of microstrip to waveguide transition. In [12], an end-coupled band-pass filter based on the micro-bandgap waveguide technology is demonstrated. The designed filter has a planar structure and is therefore suitable for integration with active and passive components. A rectangular waveguide band-pass filter designed in [13] is made by deep reactive ion etching micromachining on a silicon wafer. On the other hand, an idea of integrating a metamaterial-based surface in a waveguide antenna is presented in [14] to achieve a filtering slotted antenna.

As the height of its internal metal nails is about a quarter wavelength at the center frequency of the stop-band, a perfect ideal magnetic conductor characteristic can be obtained. By utilizing this feature, the antenna can possess better attenuation characteristic in the stop-band, thereby the filtering function can be realized. This surface is usually integrated on the bottom layer of the waveguide to implement the filtering function of the antenna. However, loading such metallic metamaterial surface can be considered as adding a “thick” plate below the bottom of the waveguide which would increase the profile of the whole structure.

In this paper, a metal-strip surface is integrated in a rectangular waveguide for Ku-band communication application. Its operational frequency band is around 12-15.1 GHz with a stop-band of around 15.8-17.4 GHz so as to achieve good anti-interference characteristic. The proposed design adopts the metal-strip meta-surface to be realized by low-cost printed circuit board (PCB) technique. By changing the structural configuration of the metal-strip surface, the stop-band and pass-band characteristics of the filtering waveguide can be customized. The paper consists of the following parts: Section II introduces the structure of the proposed filtering waveguide. The design details and analysis are discussed in Section III. Section IV demonstrates the simulation and the measurement results with favorable comparison. A conclusion of the work is drawn in Section V.

## II. WAVEGUIDE STRUCTURE

The configuration of the filtering waveguide proposed in this work is shown in Fig. 1. Unlike a conventional rectangular waveguide, a metal-strip layer is integrated at the bottom wall of the waveguide. In this design, the metal-strip meta-surface is composed of 22 rectangular metallic strips and shorted to the bottom metal plane through vias. The shorted metal-strip surface is finally realized on a RO4003C substrate with dielectric constant of 3.55 and thickness of 0.813 mm. In order to facilitate the measurement, the meta-surface consisting of the metal-strips is fixed to the bottom wall of the waveguide with conductive adhesive, and two WR-62 standard coaxial-to-waveguide adaptors are mounted to the two ports of the filtering waveguide. The overall dimensions of the proposed waveguide are tabulated in Table 1.

## III. DESIGN AND ANALYSIS OF FILTERING WAVEGUIDE

### A. Design fundamental

According to waveguide theory, when two parallel plates are perfect electric conductors (PECs), the vertical electric field can be freely propagated between the plates. However, when one PEC plate is replaced by

a perfect magnetic conductor (PMC) plate, the propagation of the electric field is highly relevant to the distance between the two parallel plates. If the distance is less than  $\lambda/4$ , the vertical electric field cannot propagate successfully, where  $\lambda$  corresponds to the wavelength at the operating frequency [15], [16]. The abovementioned propagation characteristics are shown in Fig. 2. It can be seen that once the spacing between the PEC and PMC plates is less than  $\lambda/4$ , neither the electric field nor the magnetic field is able to propagate through the waveguide, therefore a stop-band can be generated in this structure.

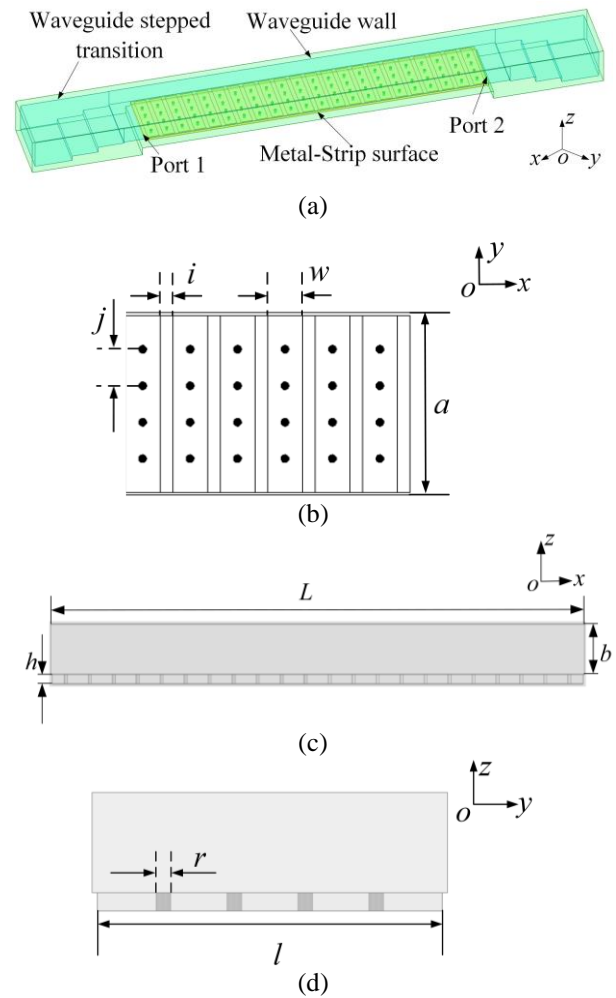


Fig. 1. Configuration of the proposed filtering waveguide. (a) 3-D perspective view of the complete filtering waveguide. (b) Top-view of the metal-strip surface. (c) Front-view of the filtering waveguide. (d) Side-view of the filtering waveguide.

### B. Design of filtering waveguide

According to the fundamental mentioned in last section, it is key to construct a meta-surface to perform a

frequency-dependent PEC/PMC layer in the waveguide. In this design, a metal-strip layer is adopted as the PEC/PMC meta-surface, which is able to generate a pass-band characteristic in the bandwidth of 12~15.1 GHz while a stop-band in the frequency range of 15.8~17.4 GHz. The proposed metal-strip surface is printed on a PCB board with size of  $L \times a \times h$ , where the length and width of the metal-strip is  $a$  and  $w$  respectively. The distance between the adjacent metal-strips is  $i$ . A ground plane is designed at the bottom of the PCB, shorted with the metal-strips at the top layer by vias. The radius of the vias is  $r$ . The PCB layer is finally embedded in the bottom wall of the waveguide to achieve filtering performance.

Table 1: Parameters of the filtering waveguide

Parameter	Value
$a$	16 mm
$b$	4.5 mm
$h$	0.813 mm
$L$	93.5 mm
$w$	3.1 mm
$i$	1.1 mm
$j$	2.5 mm
$r$	0.35 mm
$l$	15.7 mm

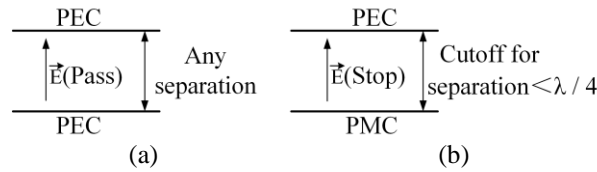


Fig. 2. Electric field propagation inside two parallel plates: (a) model with two PEC plates, and (b) model with a PEC plate and a PMC plate.

### C. Analysis of filter waveguide

The reflection and transmission coefficients of the proposed filtering waveguide is shown in Fig. 3, characterized by  $S_{11}$  and  $S_{21}$  respectively. It can be seen that the  $S_{11}$  coefficient is less than -20 dB in the band of 12~15.1 GHz, indicating the metal-strip surface can be used as a PEC layer for electromagnetic (EM) wave propagation in this bandwidth. While in the frequency range of 15.8~17.4 GHz,  $S_{11}$  is close to 0 dB and  $S_{21}$  is below -60 dB, which shows that the EM wave in this frequency band is almost totally reflected. In this case, the metal-strip surface acts as a PMC layer to prevent signal propagation. Therefore, the proposed filtering waveguide can generate a pass-band of 12~15.1 GHz for target signal propagation, while there is a stop-band

existing in 15.8~17.4 GHz for interference signal rejection. Note that when the metal-strip layer acts as PMC, the cut-off frequency appears at around 15.8 GHz as the spacing ( $b$ ) between the top and bottom plate of the waveguide is close to a quarter wavelength at this frequency. All the signal below 15.8 GHz under this condition will be rejected.

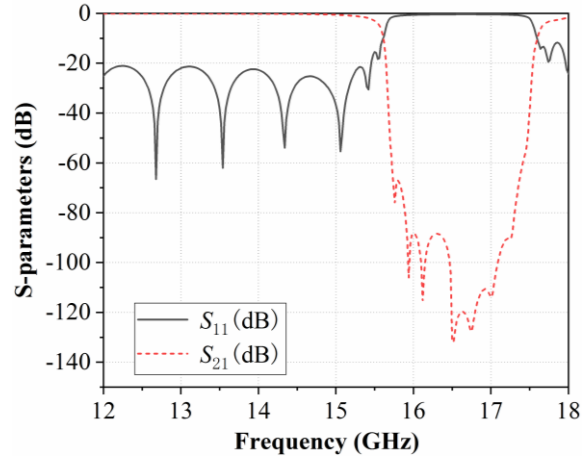


Fig. 3. S-parameter results of the proposed filtering waveguide.

### D. Parametric analysis

The frequency response of the metal-strip surface can be changed by some key structural parameters, which could make it easily customize to different anti-interference requirements with specified pass-band and stop-band.

Two typical parameters are studied in this work. Figure 4 shows the effect of the vias' height ( $h$ ) on the frequency response of the stop-band. As the height increases, the stop-band shifts to lower frequencies and the corresponding bandwidth is also affected. Figure 5 shows the influence of the via spacing of metal strips ( $j$ ) on the waveguide stop-band performance. As the spacing increases, the stop-band has similar response as the vias' height that shifts to lower frequency band while the bandwidth of the stop-band is also affected. Figure 6 shows the effect of the width ( $w$ ) of the metal-strip on the stopband performance, from which it can be seen that as the width increases, the stopband slightly shifts to a lower frequency band. Parametric studies on other parameters are not necessary to present as similar effect can be expected. Based on the above analysis, it can be seen that the filtering response could be easily adjusted by changing the corresponding parameters of the metal-strip layer, and therefore the proposed filtering waveguide can be flexibly designed for various applications.

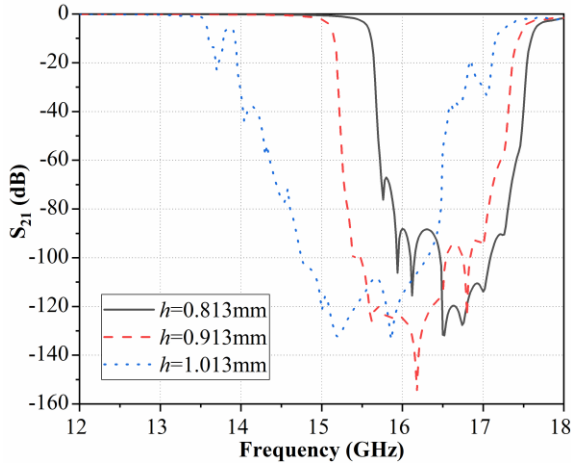


Fig. 4. Transmission coefficient of the proposed filtering waveguide with different heights ( $h$ ) of the vias.

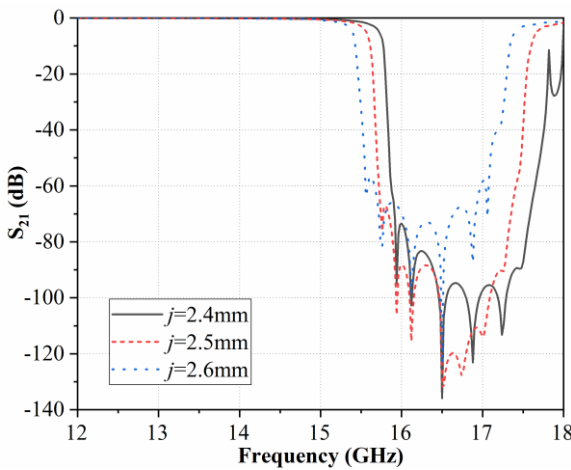


Fig. 5. Transmission coefficient of the proposed filtering waveguide with different vias' spacing ( $j$ ).

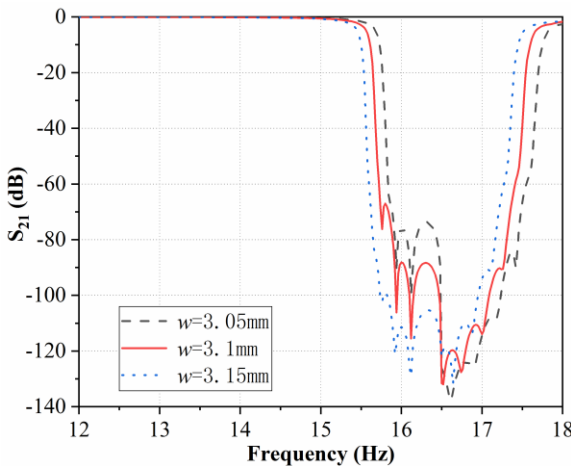


Fig. 6. Transmission coefficient of the proposed filtering waveguide with different width of metal-strip ( $w$ ).

#### IV. RESULT ANALYSIS

As shown in Fig. 7, the waveguide consists of two parts: a cover and a cavity. The cavity includes a waveguide step transition and an embedded metal-strip surface. The waveguide is assembled by fixing the cover on the top of the cavity with screws.

In order to verify the transmission characteristics of the proposed filtering waveguide, a prototype manufactured by machining technique has been tested with vector network analyzer (VNA). The reflection coefficient (represented by  $S_{11}$  in units of dB) and the transmission coefficient (represented by  $S_{21}$  in units of dB) of the prototype are shown in Fig. 8 with comparison of simulation results. The experimental results are somehow consistent with the overall trend of the simulation results. The reflection coefficient ( $S_{11}$ ) of the pass-band is close to -20 dB though the frequency response at lower frequencies deteriorates, and the ability of stop-band to suppress interference signals is better than 30 dB. It is also noticed that the stop-band shifts to higher frequency by about 1.3 GHz and the corresponding bandwidth becomes narrower.

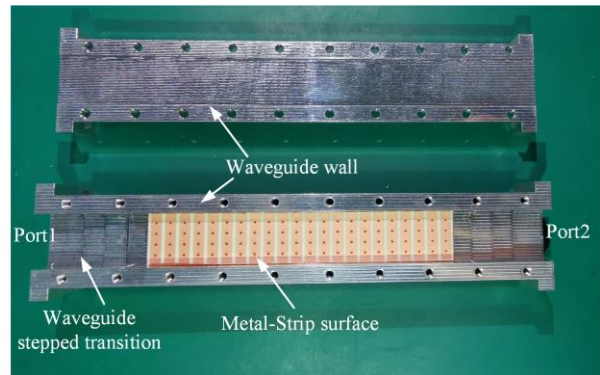


Fig. 7. Photograph of the proposed waveguide.

After a careful inspection, there are several reasons causing the difference between the measured and simulated results: (1) The actual thickness of the dielectric substrate becomes smaller after copper coated on both sides of the substrate. According to the previous parametric analysis, this error would cause a frequency-shift to higher frequency in the stop-band and also changing the bandwidth; (2) In addition, the dielectric constant of the substrate is around 3.38 instead of the dielectric constant 3.55 set in the simulation; (3) All the metallic materials of the filtering waveguide are set to PEC in the simulation environment without considering the actual conductive loss. After reducing the thickness and dielectric constant in the design model, the simulation is re-run to investigate the change and the result is shown in Fig. 9. Now the experimental results are basically consistent with the simulation ones though the bandwidth of the stop-band still has deviation.

Furthermore, it should be noted that as the WR-62 standard coaxial-to-waveguide adapter operates from 12.4 GHz up to 18.0 GHz, it might affect the reflection coefficient of the filtering waveguide at lower frequency during the measurement.

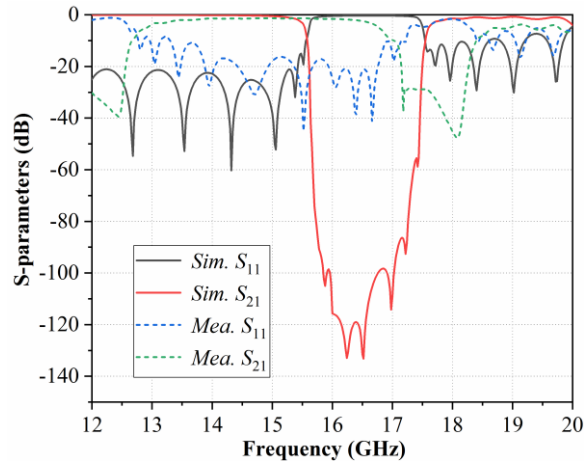


Fig. 8. Simulated and measured S-parameters of the filtering waveguide.

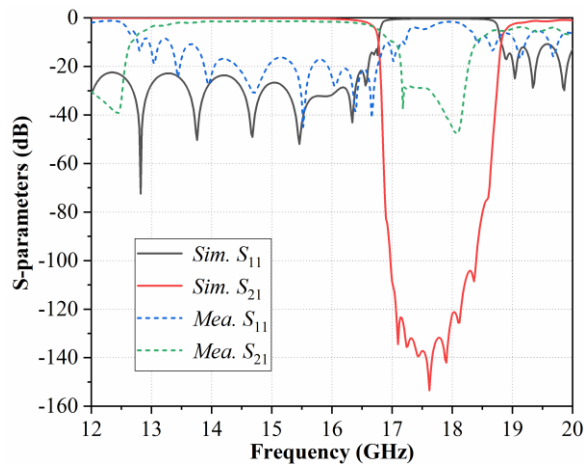


Fig. 9. Simulated and measured S-parameters of the filtering waveguide.

## V. CONCLUSION

A new metal-strip integrated filtering waveguide is investigated in this paper. The structure simply consists of a traditional waveguide and a metal-strip meta-surface embedded at the bottom of the waveguide. The meta-surface can act as a PEC layer in the pass-band while exhibit PMC characteristic in the stop-band. After simulation analysis and experimental verification, the filtering waveguide is able to meet different design requirements. The metal-strip surface is realized on the PCB, the design process of which is relatively simple and convenient for practical implementation and easy for

size miniaturization.

## ACKNOWLEDGMENT

This work was supported partially by the Foundation for Distinguished Young Talents in Higher Education of Guangdong Province, China, under Grant 2017KQNCX173, the Academic Cooperation Project between Shenzhen University and National Taipei University of Technology under Grant No. 2020011, the Fok Ying-Tong Education Foundation, China under Grant No. 171056, the National Natural Science Foundation of China under Grants 61801300 and 61701320, and the New Teacher Natural Science Research Project of Shenzhen University under Grant No. 860-000002110627. The authors would like to express our sincere thanks to Dr. Vincent Zhang for his valuable suggestion during the research progress of the work.

## REFERENCES

- [1] J. Jiang, Y. Xia, and Y. Li, "High isolated X-band MIMO array using novel wheel-like metamaterial decoupling structure," *Applied Computational Electromagnetics Society Journal*, vol. 34, no. 12, pp. 1829-1836, 2019.
- [2] F. Liu, J. Guo, L. Zhao, G. L. Huang, Y. Li, and Y. Yin, "Dual-band metasurface-based decoupling method for two closely packed dual-band antennas," *IEEE Transactions on Antennas and Propagation*, vol. 68, no. 1, pp. 552-557, Jan. 2020.
- [3] G.-L. Huang, J. Liang, L. Zhao, D. He, and C.-Y.-D. Sim, "Package-in-dielectric liquid patch antenna Based on Liquid Metal Alloy," *IEEE Antennas and Wireless Propagation Letters*, vol. 18, no. 11, pp. 2360-2364, Nov. 2019.
- [4] F. Liu, J. Guo, L. Zhao, G. Huang, Y. Li, and Y. Yin, "Ceramic superstrate-based decoupling method for two closely packed antennas with cross-polarization suppression," *IEEE Transactions on Antennas and Propagation*, Submitted.
- [5] J. Guo, F. Liu, L. Zhao, Y. Yin, G. Huang, and Y. Li, "Meta-surface antenna array decoupling designs for two linear polarized antennas coupled in H-plane and E-plane," *IEEE Access*, vol. 7, pp. 100442-100452, 2019.
- [6] L. Zhao, G. Jing, G.-L. Huang, W. Lin, and Y. Li, "Low mutual coupling design for 5G MIMO antennas using multi-feed technology and its application on metal-rimmed mobile phones," *IEEE Transactions on Antennas and Propagation*, Submitted.
- [7] J. Li, X. Zhang, Z. Wang, X. Chen, J. Chen, Y. Li, and A. Zhang, "Dual-band eight-antenna array design for MIMO applications in 5G mobile terminals," *IEEE Access*, vol. 7, pp. 71636-71644, 2019.
- [8] C.-K. Lin and S.-J. Chung, "A filtering microstrip



- antenna array,” *IEEE Trans. Microw. Theory Techn.*, vol. 59, no. 11, pp. 2856-2863, Nov. 2011.
- [9] X. Chen, F. Zhao, L. Yan, and W. Zhang, “A compact filtering antenna with flat gain response within the passband,” *IEEE Antennas Wireless Propag. Lett.*, vol. 12, pp. 857-860, 2013.
- [10] W. Wang, et al., “A waveguide slot filtering antenna with an embedded metamaterial structure,” *IEEE Transactions on Antennas and Propagation*, vol. 67, no. 5, pp. 2953-2960, May 2019.
- [11] L. Murphy, M. Yazdani, D. Bates, J. Mautz, E. Arvas, and S. Tozin, “Design of V-band dielectric filled waveguide filters with improved loss and suppression of parasitic waves,” *2014 44th European Microwave Conference*, Rome, Italy, pp. 1115-1117, 2014.
- [12] S. T. Choi, K. S. Yang, K. Tokuda, and Y. H. Kim, “A V-band planar narrow bandpass filter using a new type integrated waveguide transition,” *IEEE Microwave and Wireless Components Letters*, vol. 14, no. 12, pp. 545-547, Dec. 2004.
- [13] D. Lei, et al., “A micromachined 805 GHz rectangular waveguide filter on silicon wafers,” *2014 IEEE International Conference on Communication Problem-solving*, Beijing, pp. 653-655, 2014.
- [14] W. Wang, et al., “A waveguide slot filtering antenna with an embedded metamaterial structure,” *IEEE Transactions on Antennas and Propagation*, vol. 67, no. 5, pp. 2953-2960, May 2019.
- [15] P.-S. Kildal, E. Alfonso, A. Valero-Nogueira, and E. Rajo-Iglesias, “Local metamaterial-based waveguides in gaps between parallel metal plates,” *IEEE Antennas Wireless Propag. Lett.*, vol. 8, pp. 84-87, 2009.
- [16] P.-S. Kildal, “Three metamaterial-based gap waveguides between parallel metal plates for mm/submm waves,” *Proc. 3rd Eur. Conf. Antennas Propag.*, pp. 28-32, Mar. 2009.

# A 3D Printed Filtering Waveguide with Simple Metamaterial Construction

Zi-Yu Pang<sup>1</sup>, Xiao-Yu Ma<sup>1</sup>, Ge Zhao<sup>1</sup>, Jia-Jun Liang<sup>4\*</sup>, Guan-Long Huang<sup>1,2,3\*</sup>,  
Luyu Zhao<sup>5</sup>, and Chow-Yen-Desmond Sim<sup>6</sup>

<sup>1</sup> College of Electronics and Information Engineering  
Shenzhen University, Shenzhen, Guangdong 518060, China  
\*guanlong.huang@ieee.org

<sup>2</sup> State Key Laboratory of Millimeter Waves, Nanjing, Jiangsu 210096, P.R. China

<sup>3</sup> Peng Cheng Laboratory, No.2 Xingke 1st Street, Nanshan, Shenzhen, Guangdong 518052, China

<sup>4</sup> School of Physics and Telecommunication Engineering  
Yulin Normal University, Yulin, P.R. China  
\*shuigpjd@163.com

<sup>5</sup> National Key Laboratory of Antennas and Microwave Technology  
Xidian University, Xi'an, Shaanxi, 710071, P.R. China

<sup>6</sup> Department of Electrical Engineering  
Feng Chia University, Taichung 40724, Taiwan

**Abstract** — A novel filtering waveguide with bandwidth controllable characteristic is proposed in this work. The filtering waveguide consists of a common rectangular waveguide and metamaterial-based metallic bars. The proposed waveguide is designed for Ku-band application. Inside the operational frequency band, the metallic bars forming a metamaterial surface can behave as perfect electric conductor (PEC), which generates a pass-band for signal transmission, while outside the band of interest, the metallic bars act as perfect magnetic conductor (PMC) and block the transmission of undesired signals, where a stop-band is formed. After integrating the pass-band and stop-band features into the waveguide, a customized waveguide with filtering response is realized. A prototype of the proposed filtering waveguide is fabricated with the advanced metallic 3D printing technique, and experimental results well verify the desired performance. Moreover, the pass-band and stop-band of the filtering waveguide can be flexibly and easily adjusted to meet different requirements with low insertion loss.

**Index Terms** — Bandwidth controllable, filtering waveguide, low loss, metamaterial.

## I. INTRODUCTION

With the development of wireless communication, high-frequency devices are always desired to be highly

integrated and versatile with compact size and lightweight. As two important microwave components, waveguide-based antennas and filters are frequently employed in advanced wireless systems like radar and satellite [1]-[7], where the filters are usually cascaded behind the antennas via waveguide connection. However, such traditional ways for cascading different components with waveguides result in a bulky size of the hardware system, which fails to meet the current wireless development requirements. Therefore, it is necessary to investigate multi-functional devices in a high-integration level. Waveguides integrated with filtering function are one of these devices and continually playing an important role in modern communication systems due to their unique radio-frequency (RF) advantages such as low insertion loss and high-power handling capabilities [8]. However, it is always challenging to realize such versatile three-dimensional components in a simple way.

Metamaterial is an artificial material proposed decades ago. It typically consists of a series of periodic electromagnetic (EM) structures or unit cells that can change the characteristics of incident electromagnetic waves, such as the direction of propagation, wave number and phase [9]. In recent years, the application of metamaterial structures to achieve filtering response in various microwave devices becomes a hot topic. Different methods for designing filtering structures with metamaterial have also been widely studied. For

example, a magnetic wall made of mushroom-shaped metamaterial was added into rectangular waveguide [10], [11], the analysis of which shows that the critical frequency of such a waveguide depends on the metamaterial resonance frequency and is close to 4 GHz, where the considered structure acts as waveguide filter and provides 500 MHz stop-band with rejection level of 21~24 dB. Although it could perform filtering function in a waveguide, this structure is too complicated to realize and had a relatively large insertion loss. Recently, a design approach of a waveguide slot filtering antenna array was proposed [12]. In this design, a metamaterial surface with numbers of metal nails are embedded into the bottom of the waveguide cavity to achieve the filtering response, where slots are opened on the waveguide broad-wall to realize frequency resonance and energy radiation of the antenna array. Such structure has the advantages of simple structure, easy manufacturing and large stop-band range. However, several amounts of energy is easily retained in the gaps among the large number of metal nails, which has been verified a large insertion loss exists in this structure and finally results in a poor transmission performance.

In this paper, in order to alleviate the above-mentioned technical problems, a new type of filtering waveguide is proposed and realized with the help of 3D printing technique. Unlike the structures of the previous works, the presented design has a much simpler structure and lower loss, and the pass-band and stop-band can be easily adjusted to meet different application requirements.

## II. CONSTRUCTION OF FILTERING WAVEGUIDE

The construction of the proposed filtering waveguide is shown in Fig. 1. As different from a conventional waveguide with complete solid metallic walls, the designed structure possesses a metamaterial-based surface to take place of one of the broad-walls. The metamaterial-based surface is composed of periodic metallic bars. By employing such surface into the waveguide, the model is able to transmit a desired bandwidth of signal (pass-band) in the Ku-band while generating an out-of-band rejection (stop-band). In order to facilitate the experimental setup and test, two waveguide stepped transitions are designed to connect the two filtering waveguide ports with commercial coaxial-to-waveguide adapters. The structural parameters of the filtering waveguide shown in Fig. 1 are tabulated in Table 1, where  $a$  and  $b$  are the length and width of the rectangular waveguide respectively;  $w$  and  $h$  are the width and height of the metallic bars respectively;  $i$  is the interval among the metallic bars. Note that the length of the periodic bars is identical to the length of the waveguide broad-wall. In addition, I structure of the waveguide stepped transition is shown in Fig. 2. The

transition is composed of four steps. Its structural parameters are tabulated in Table 1, where  $(b, b_1, b_2$  and  $b_3)$  and  $(c_0, c_1, c_2,$  and  $c_3)$  are the heights and widths of the four steps respectively.

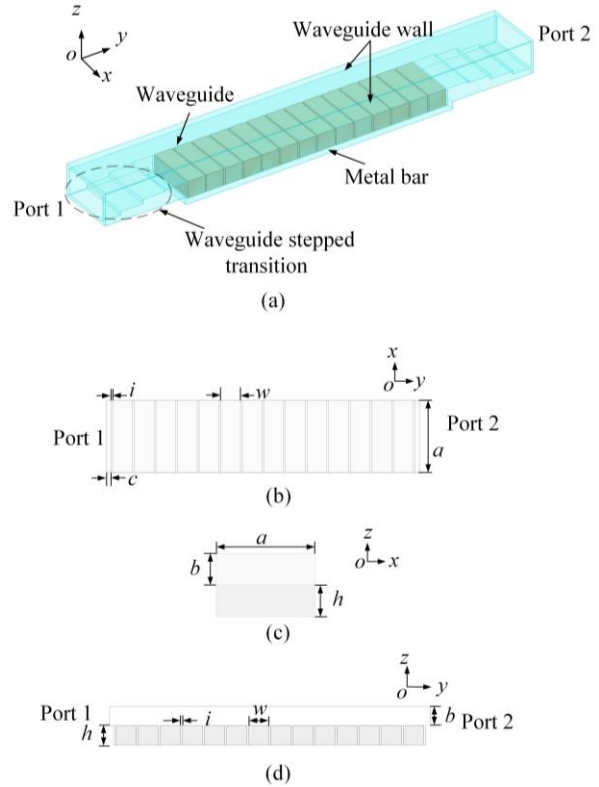


Fig. 1. Structure of the designed filtering waveguide. (a) 3D-view of the whole filtering waveguide. (b) Top-view of the filtering waveguide. (c) Front-view of the filtering waveguide. (d) Side-view of the filtering waveguide.

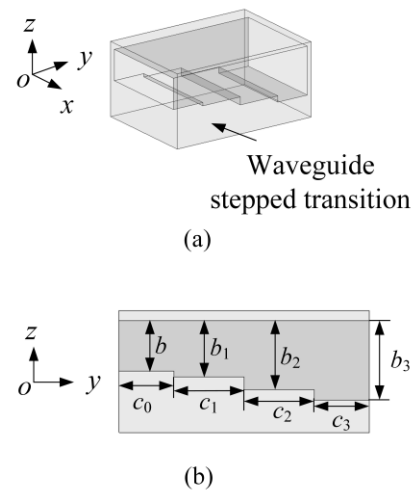


Fig. 2. Structure of the waveguide stepped transition. (a) 3D-view of the waveguide stepped transition. (b) Front-view of the waveguide stepped transition.

Table 1: Parameters of the filtering waveguide

Parameter	Value	Parameter	Value
$a$	15.79 mm	$b_1$	5.6 mm
$b$	5.06 mm	$b_2$	6.9 mm
$c$	1.2 mm	$b_3$	7.89 mm
$w$	5.5 mm	$c_0$	5.5 mm
$h$	4.8 mm	$c_1$	7.0 mm
$i$	0.7 mm	$c_2$	7.0 mm
-	-	$c_3$	5.5 mm

### III. DESIGN AND ANALYSIS OF THE FILTERING WAVEGUIDE

#### A. Operational principle

According to EM theory, the electric-field ( $E$ -field) propagates vertically between two parallel perfect electric conductors (PECs) at any spacing. However, when one of the two parallel PECs is replaced by a perfect magnetic conductor (PMC), the EM wave propagation property would be changed. Once the distance between the two conductors (PEC and PMC) is less than quarter wavelength of the operating frequency, propagation of the  $E$ -field no longer exists, i.e., its cut-off frequency is higher than that of all propagation modes [13]. The periodic surface can create a cut-off band, which is realized theoretically by providing high surface impedance on the periodic structure, i.e., rendering it as an artificial magnetic conductor [13].

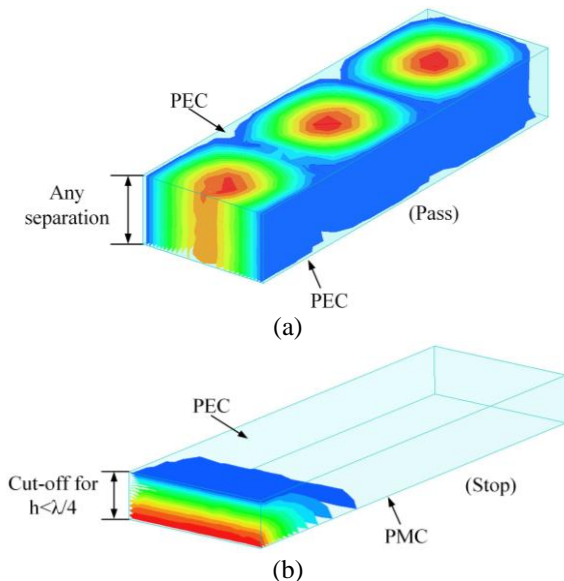


Fig. 3.  $E$ -field propagation of a waveguide with different constructions on the top and bottom surfaces. (a) A PEC top surface and a PEC bottom surface. (b) A PEC top surface and a PMC bottom surface.

According to the principle mentioned above, a metamaterial-based surface with a customized structure

can be designed so that it can appear as a PEC surface in the interested frequency band where signals can be transmitted freely, while at the same time, it can also perform as a PMC surface in a specific frequency band where undesired signals will be blocked, as shown in Fig. 3. Therefore, a filtering function with pass-band and stop-band characteristics simultaneously is possible to be realized in a single waveguide.

#### B. Analysis of the filtering waveguide

According to the principle described in last subsection, the filtering waveguide can be established in the form of the configuration as shown in Fig. 1. To properly realize the PEC and PMC functional transformation in desired and undesired frequency bands, a metamaterial-based surface consisting of periodic metallic bars is adopted and integrated to replace one of the waveguide broad-wall. The proposed filtering waveguide is designed in Ku-band operation. The EM model is analyzed and optimized in CST Microwave Studio® [14]. The transmission coefficient (characterized by  $S_{21}$ ) of the designed filtering waveguide is shown in Fig. 4, from which one can observe that the  $S_{21}$  response of the waveguide in the bandwidth of 12.0 GHz~15.5 GHz, is almost the same as that of a traditional waveguide, i.e.,  $S_{21}$  is close to 0 dB due to the low insertion loss of the waveguide structure. More specifically, the insertion loss is less than 0.1 dB from 12.0 GHz to 14.5 GHz with reflection coefficient (characterized by  $S_{11}$ ) lower than -15 dB, which demonstrates good wave-propagation performance in the pass-band.

On the other hand, there is a large attenuation appearing in the bandwidth from 16.2 GHz to 17 GHz in the designed filtering waveguide, as shown in Fig. 4. The reason is traced to the phenomenon that the proposed metamaterial-based surface operates as a PMC layer at the bottom of the waveguide in this frequency band, so a stop-band is obtained.

To further illustrate the pass-band and stop-band performance of the proposed filtering waveguide, the  $E$ -field distribution at different frequencies inside the waveguide is shown in Fig. 5. In addition, the operating pass-band and stop-band of the filtering waveguide can be easily adjusted via properly choosing the parameters of the metamaterial-based surface. For instance, the height ( $h$ ) and the width ( $w$ ) of the metallic bars can be tuned to meet different requirements. As shown in Fig. 6, the stop-band moves to lower frequency band as the height of the metallic bar becomes larger while the other parameters are kept unchanged. Similarly, as the width of the metallic bar increases, the stop-band becomes wider and shifts slightly to the lower frequency band at the same time. All of the above analysis verifies the proposed structure is a simple but efficient approach to function a desired filtering response in a waveguide.

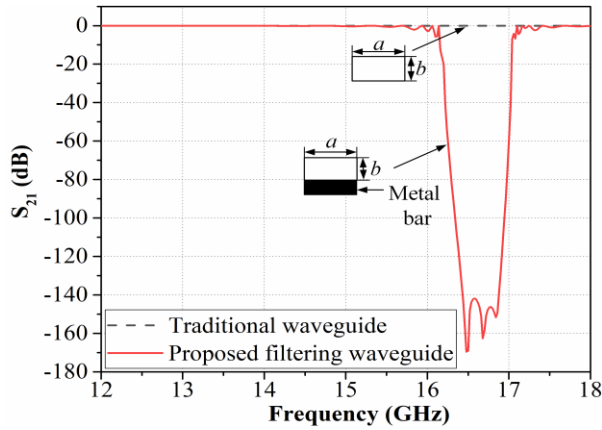


Fig. 4. Simulated  $S_{21}$  of the filtering waveguide and traditional waveguide.

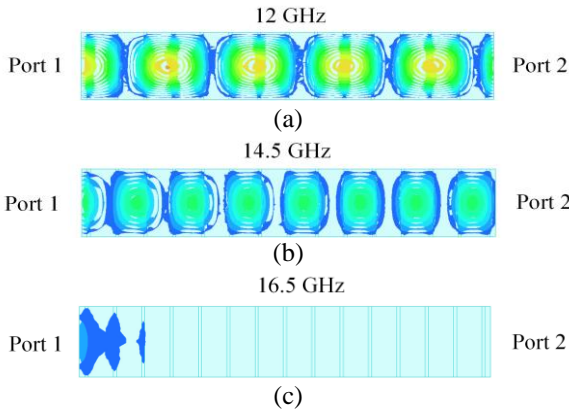


Fig. 5. Top-views of the electric-field distribution in the proposed filtering waveguide at different frequencies.

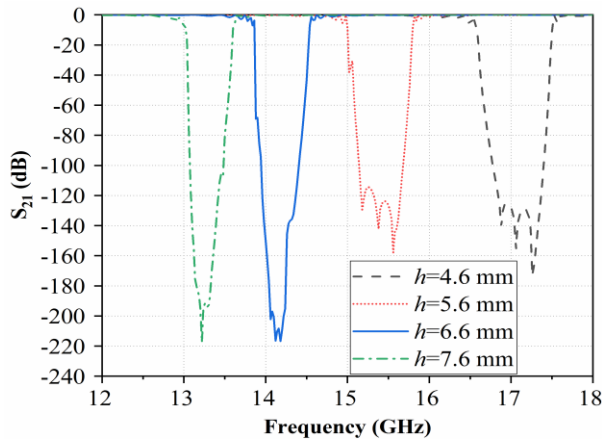


Fig. 6. Effect of various metallic bars' heights on the filtering waveguide.

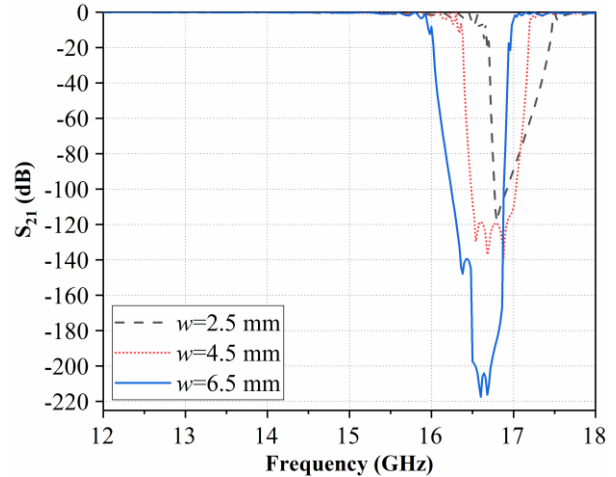


Fig. 7. Effect of various metallic bars' widths on the filtering waveguide.

#### IV. EXPERIMENTAL RESULTS

To prove the feasibility of the proposed filtering waveguide, a prototype waveguide has been fabricated by using 3D printing technology and tested with vector network analyzer (VNA) in laboratory. The prototype is 3D printed in aluminum via the metal printing process called direct-metal-laser-sintering (DMLS) [15], [16], which can greatly reduce or even eliminate any assembly and alignment errors from traditional machining process. The final test model is assembled by the proposed waveguide and two standard WR-62 coaxial-to-waveguide adaptors at both ends of the waveguide, as shown in Fig. 8. The measured S-parameters results of the filtering waveguide is presented in Fig. 9. As can be seen from the figure, the measured results are in good agreement with the simulated ones obtained from simulation environment. The pass-band and stop-band are roughly locating at the same range as the simulation, indicating that the designed filtering waveguide is indeed feasible in a compact waveguide volume. In addition, from the test results, it is observed that the stop-band is slightly narrower than the simulated one, which is mainly caused by minor tolerances on certain key structural parameters of the metallic bars during the DMLS manufacturing process. At the same time, as the internal surface and structure of the prototype are hard to polish while a planar surface with PEC surface is set in simulation, some uneven places can be observed in the waveguide, which introduces several amount of insertion loss into the filtering performance. Further fine post-processing on the surface roughness of the prototype will help improve the filtering response.

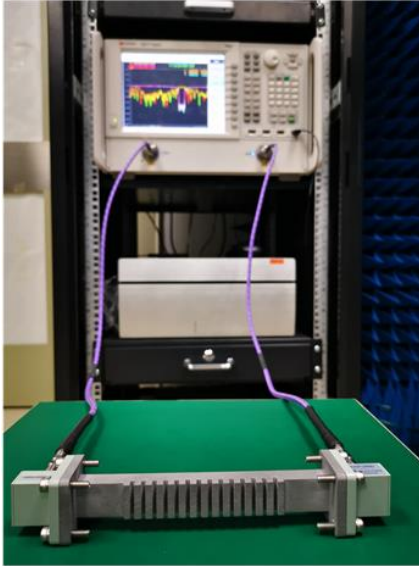


Fig. 8. The prototype waveguide in test environment.

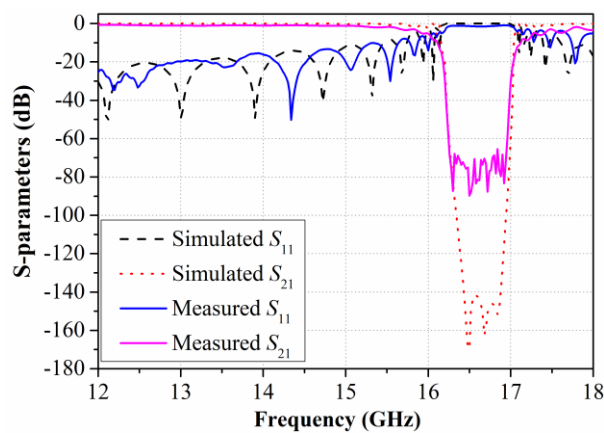


Fig. 9. Simulated and measured S-parameters of the filtering waveguide.

## V. CONCLUSION

A new type of filtering waveguide is proposed in this work. The filtering waveguide is configured by a conventional rectangular waveguide and periodic metallic bars as the metamaterial-based surface, functioning as a PEC in pass-band while PMC in stop-band. The operating principle and design process have been illustrated. A 3D printed prototype was tested and the overall test results well agree with the simulated ones. The proposed design is also easily for customizing to different frequency bands' application by adjusting certain structural parameters, which makes it more applicable to various advanced communication systems.

## ACKNOWLEDGMENT

This work was supported partially by the State Key Laboratory of Millimeter Waves under Grant No.

K201932, the National Taipei University of Technology-Shenzhen University Joint Research Program under Grant No. 2020011, the Fok Ying-Tong Education Foundation, China under Grant No. 171056, the National Natural Science Foundation of China under Grants 61801300 and 61701320, and the New Teacher Natural Science Research Project of Shenzhen University under Grant No. 860-000002110627. The authors would like to express our sincere thanks to Dr. Vincent Zhang for his valuable suggestion during the research progress of the work.

## REFERENCES

- [1] J. Jiang, Y. Xia, and Y. Li, "High isolated X-band MIMO array using novel wheel-like metamaterial decoupling structure," *Applied Computational Electromagnetics Society Journal*, Accepted, vol. 34, no. 12, pp. 1829-1836, 2019.
- [2] F. Liu, J. Guo, L. Zhao, G. L. Huang, Y. Li, and Y. Yin, "Dual-band metasurface-based decoupling method for two closely packed dual-band antennas," *IEEE Transactions on Antennas and Propagation*, vol. 68, no. 1, pp. 552-557, Jan. 2020.
- [3] G.-L. Huang, J. Liang, L. Zhao, D. He, and C.-Y.-D. Sim, "Package-in-dielectric liquid patch antenna based on liquid metal alloy," *IEEE Antennas and Wireless Propagation Letters*, vol. 18, no. 11, pp. 2360-2364, Nov. 2019.
- [4] J. Li, X. Zhang, Z. Wang, X. Chen, J. Chen, Y. Li, and A. Zhang, "Dual-band eight-antenna array design for MIMO applications in 5G mobile terminals," *IEEE Access*, vol. 7, pp. 71636-71644, 2019.
- [5] F. Liu, J. Guo, L. Zhao, G. Huang, Y. Li, and Y. Yin, "Ceramic superstrate-based decoupling method for two closely packed antennas with cross-polarization suppression," *IEEE Transactions on Antennas and Propagation*, Submitted.
- [6] J. Guo, F. Liu, L. Zhao, Y. Yin, G. Huang, and Y. Li, "Meta-surface antenna array decoupling designs for two linear polarized antennas coupled in H-plane and E-plane," *IEEE Access*, vol. 7, pp. 100442-100452, 2019.
- [7] L. Zhao, G. Jing, G.-L. Huang, W. Lin, and Y. Li, "Low mutual coupling design for 5G MIMO antennas using multi-feed technology and its application on metal-rimmed mobile phones," *IEEE Transactions on Antennas and Propagation*, Submitted.
- [8] Q. Wu, F. Zhu, Y. Yang, and X. Shi, "An effective approach to suppressing the spurious mode in rectangular waveguide filters," *IEEE Microwave and Wireless Components Letters*, vol. 29, no. 11, pp. 703-705, Nov. 2019.
- [9] V. G. Veselago, "The electrodynamics of substances with simultaneously negative values of  $\epsilon$  and  $\mu$ ,"

- Sov. Phys.-Usp.*, vol. 10, no. 4, pp. 509-514, Jan.-Feb. 1968.
- [10] A. Yelizarov, I. Nazarov, A. Skuridin, and A. Kukharevko, "Investigation of a rectangular waveguide with a magnetic wall made of mushroom-shaped metamaterial," *2017 Eighteenth International Vacuum Electronics Conference (IVEC)*, London, pp. 1-3, 2017.
- [11] A. A. Yelizarov, I. V. Nazarov, T. V. Sidorova, O. E. Malinova, and V. N. Karavashkina, "Modeling of a waveguide stop-band filter with a mushroom-shaped metamaterial wall and dielectric substrates," *2018 Systems of Signal Synchronization, Generating and Processing in Telecommunications (SYNCHROINFO)*, Minsk, pp. 1-3, 2018.
- [12] W. Wang, *et al.*, "A waveguide slot filtering antenna with an embedded metamaterial structure," *IEEE Transactions on Antennas and Propagation*, vol. 67, no. 5, pp. 2953-2960, May 2019.
- [13] P.-S. Kildal, A. U. Zaman, E. Rajo-Iglesias, E. Alfonso, and A. Valero-Nogueira, "Design and experimental verification of ridge gap waveguide in bed of nails for parallel-plate mode suppression," *IET Microwaves, Antennas & Propagation*, vol. 5, no. 3, pp. 262-270, Feb. 21, 2011.
- [14] CST Microwave Studio, Dec. 2019. [Online] Available: <https://www.cst.com/>
- [15] G.-L. Huang, C.-Z. Han, W. Xu, T. Yuan, and X. Zhang, "A compact 16-way high-power combiner implemented via 3-D metal printing technique for advanced radio-frequency electronics system applications," *IEEE Transactions on Industrial Electronics*, vol. 66, no. 6, pp. 4767-4776, Jun. 2019.
- [16] G.-L. Huang, S.-G. Zhou, and T. Yuan, "Design of a compact wideband feed cluster with dual-polarized sum- and difference-patterns implemented via 3-D metal printing," *IEEE Transactions on Industrial Electronics*, vol. 65, no. 9, pp. 7353-7362, Sept. 2018.

# Three-Stacked Dielectric Ring Resonator Loaded Hybrid Monopole Antenna for Improved Ultrawide Bandwidth

Ali A. Al-Azza<sup>1</sup>, Nuhad A. Malalla<sup>2</sup>, Mohamed M. Morsy<sup>3</sup>, and Frances J. Harackiewicz<sup>4</sup>

<sup>1</sup>Department of Electrical Engineering, College of Engineering  
University of Basrah, Basra, Iraq  
alieng@siu.edu

<sup>2</sup>Department of Chemical and Petroleum Refining Engineering, College of Oil and Gas Engineering  
Basra University for Oil and Gas, Basra, Iraq  
nuheng@siu.edu

<sup>3</sup>Electrical Engineering Department  
Texas A&M University-Texarkana, Texarkana, TX 75503, USA  
mmorsy@tamut.edu

<sup>4</sup>Department of Electrical and Computer Engineering  
Southern Illinois University Carbondale, Carbondale, IL 62901 USA  
franl@siu.edu

**Abstract** — In this paper, a new wideband and compact three-segment composite dielectric ring resonator (DRR) antenna excited by an axi-symmetric coaxial monopole has been introduced. The proposed antenna has been investigated numerically and experimentally for enhanced impedance bandwidth. At the lowest operating frequency, the presented antenna has a footprint area of just  $0.16\lambda_0 \times 0.16\lambda_0$ . According to the measurement results, the antenna offers a fractional impedance bandwidth equal to 159% with 8dBi peak gain. The antenna provides symmetrical and stable monopole like radiation pattern over the entire impedance bandwidth. With such performance, the suggested antenna can be usefully employed in different wideband applications such as electromagnetic interference (EMI) and defense applications.

**Index Terms** — Dielectric resonator, hybrid monopole antenna, wideband antenna.

## I. INTRODUCTION

Designing an ultra-wideband monopole antenna with stable radiation patterns by using an electric monopole (MP) with dielectric ring resonator (DRR) has received great interest from researchers. The first research study in this field was made in 2002 by researchers from Canada by experimentally studying a configuration of a MP loaded by an annular DRR [1] which showed a simulated impedance bandwidth of 100% [2]. Such wideband behavior was due to the

excitation of three resonant modes. The lowest and highest resonance frequencies are generated by the MP and the excitation of the  $TM_{01\delta}$  mode of the DRR, respectively. While the coupling between the MP and DRR is responsible for generation of the intermediate resonance. A useful design guideline for the wideband MP-DRR antenna was developed by Guha et al. [3]. After that, many research groups developed several hybrid configurations of an electric monopole and a DRRs over a period of time [4-10]. The impedance bandwidth was enhanced to 110% in [4] by using inverted cone-shaped DRR. Similar impedance bandwidth in [4] was reported in [5] but by using a MP with a configuration of ‘T’-like shape. In [6], a pawn-like shape DRR has been explored by stacking a conical and hemispherical ring. Impedance bandwidth of about 122% was obtained by using such configuration. Table 1 summarizes the chronology of bandwidth enhancement of hybrid monopole antenna. Till the date, the maximum reported impedance bandwidth being 137-140% [8-10].

In this paper, three-segment composite dielectric ring resonator are stacked and excited by a coax-fed cylindrical monopole. The proposed antenna exhibits an ultra-wide impedance bandwidth compared to earlier studies in the literature as listed in Table 1. About 159% (8.6:1) fractional bandwidth is experimentally obtained with a constant monopole like radiation over the entire frequency range. The simulation study of antenna has been performed through Computer Simulation Technology (CST) which is a 3D electromagnetic



simulation software. Details of the proposed antenna design and simulated current distributions are discussed. The prototype of the antenna has been fabricated and

tested. The measured results are compared with the simulated ones and a good agreement is revealed.

Table 1: Reported bandwidth enhancement techniques of hybrid monopole antenna

Structure Investigated	Year	DRR Unit	No. of Resonances	Ratio (Percent BW)
Annular ring DR excited by electric monopole [2]	2005	1	3	3:1 (100%)
Inverted conical DRA loaded monopole [4]	2008	1	4	3.5:1 (111%)
Annular DRA excited by T-shaped monopole [5]	2008	1	4	3.5:1 (112%)
Pawn shaped DRA loaded monopole [6]	2009	2	4	4:1 (122%)
Hemispherical/conical DR loaded monopole [7]	2012	1	4	4.2:1 (126%)
Stacked conical ring DR loaded monopole [8]	2013	2	5	5.4:1 (138%)
Stacked annular ring DR [9]	2014	2	6	5.6:1 (140%)
Three-segment composite DR [10]	2017	3	6	5.4:1 (137%)
Proposed design	-	3	9	8.6:1 (159%)

## II. ANTENNA GEOMETRY AND DESIGN

The design clue of the proposed composite antenna has been extracted from the earlier studies [3], [8] as depicted in Fig. 1. By placing an annular ring on the top of two stacked conical DRs, the operating bandwidth is enhanced as a result of increased number of resonance modes. The proposed antenna introduces nine monopole-like resonances, which is four additional resonances above those provided by [8]. The details of the antenna configuration are given in Fig. 2. The probe of the Pasternack's PE4434 commercial SMA connector is used as a cylindrical MP with a radius ( $r$ ) equal to 0.65 mm. The coaxial feed and the MP share the same rotational axis of symmetry (the  $z$ -axis). The value of MP length ( $\ell$ ) can be determined as  $\ell = \lambda_1/4$ , where  $\lambda_1$  is the wavelength at the corresponding dominant mode of the monopole. The MP is loaded by three vertically stacked annular dielectric elements. All DRs are made up by using Eccostock ceramic based dielectric material with permittivity equal to 10. Selecting a material with higher dielectric constant could degrade the bandwidth and the radiation of the antenna as discussed in [7]. A cylindrical hole of radius  $R_h$  is drilled through the center of the three DRs. The value of the coupling between the MP and the stacked DR elements is determined by the spacing distance of the air gap between the MP surface and the internal face of DRR structure. Spacing parameter can be determined as  $s = R_h - r$ . The overall performance of the antenna can be deteriorated with higher values of  $s$ . The best choice for the parameter  $s$  is selected according to  $r < s < 2r$ .

A copper plate with dimensions of  $40 \times 40$  mm<sup>2</sup> and a thickness of 3 mm is used to place the designed antenna.

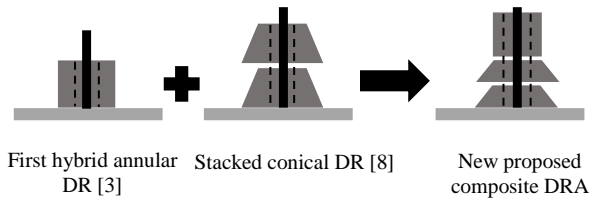


Fig. 1. Proposed antenna configuration as a combination of other design shapes.

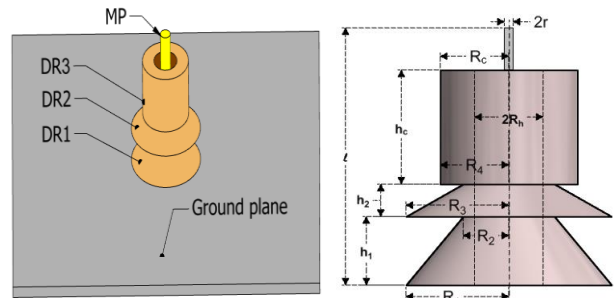


Fig. 2. Proposed antenna configuration.

The base radius of conical dielectric resonator is selected according to:

$$R_1 = 47.713 \times \text{Re}\{K_0 a\} / f_r, \quad (1)$$

where  $R_1$  is in millimeter, and  $f_r$  is in GHz which is the mid frequency between the fundamental resonant frequency of quarter wave MP and the first higher resonant mode of MP due to the conical DR.  $\text{Re}\{K_0 a\}$  is the real part of the  $K_0 a$ , and its value depends upon the permittivity of the DR [7] as shown in Table 2.

Table 2:  $Re(k_0 a)$  of the dr resonant mode with respect to permittivity

$\epsilon_r$	$Re(k_0 a)$	$\epsilon_r$	$Re(k_0 a)$	$\epsilon_r$	$Re(k_0 a)$
2	3.182	25	0.842	60	0.567
4	2.246	30	0.779	65	0.546
6	1.834	35	0.728	70	0.527
8	1.588	40	0.685	75	0.510
10	1.420	45	0.649	80	0.494
15	1.160	50	0.618	85	0.480
20	0.922	55	0.591	90	0.467

By using the hemispherical counterpart of the conical DR, its height can be calculated as  $h = \sqrt{R_1^2 - R_h^2}$ .

The height and radius of the cylindrical DR can be estimated as [3]:

$$\begin{aligned} 0.4\ell_t &\leq h_c \leq 0.5\ell_t \\ R_c &= R_h / 0.3, \end{aligned} \quad (2)$$

where  $\ell_t$  is the value of the MP length starting from the base of the cylinder to the top end of MP.

To improve the impedance bandwidth, an extensive parametric study is performed to select and tune the parameters of the antenna. Table 3 lists the finally optimized dimensions of the proposed antenna.

Table 3: Geometry details in millimeters of the proposed antenna

Physical Dimension	Value
Cone1 (Base radius $R_1$ , Top radius $R_2$ , height $h_1$ )	(4.5, 2, 3)
Cone2 (Base radius $R_3$ , Top radius $R_4$ , height $h_2$ )	(4.5, 2, 1.42)
Cylinder (radius $R_c$ , height $h_c$ )	(3, 5)
Inner radius of DRs ( $R_h$ )	1.5
Monopole radius ( $r$ )	0.65
Monopole length ( $\ell$ )	12

### III. SIMULATIONS AND MEASUREMENTS

All nine distinct resonances of the antenna are individually studied to investigate the operation principle of the antenna. Figure 3 shows the magnitude of the reflection coefficient characteristics of MP alone, DRR alone, and the suggested antenna. The MP loading effect with different dielectric elements is also studied and depicted in Fig. 4. The fundamental and the first higher order mode resonances of the monopole occur at 5.7 GHz ( $\ell = \lambda/4$ ) and 16 GHz ( $\ell = 3\lambda/4$ ), respectively as shown in Fig. 3. The intermediate resonances which occurs at around 10.3 GHz and 13 GHz are due to the loading effect of the cylindrical DR as it is clearly observed in

Fig. 4. The dielectric configuration loads the MP in such a way that the MP has effective length ( $\ell_{eff}$ ) less than the actual length at these two frequencies. Additional two resonances are identified at 24 GHz and 35 GHz. The fundamental  $TM_{018}$  resonance of the DR is clearly observed at 24 GHz. While a higher order mode is present in the DR configuration at 35 GHz. Third and fourth higher modes of the MP are observed at 30 GHz ( $\ell = 5\lambda/4$ ) and 38 GHz ( $\ell = 7\lambda/4$ ), respectively. Finally, an extra resonance is obtained at 43 GHz where the MP height is approximately a complete wavelength.

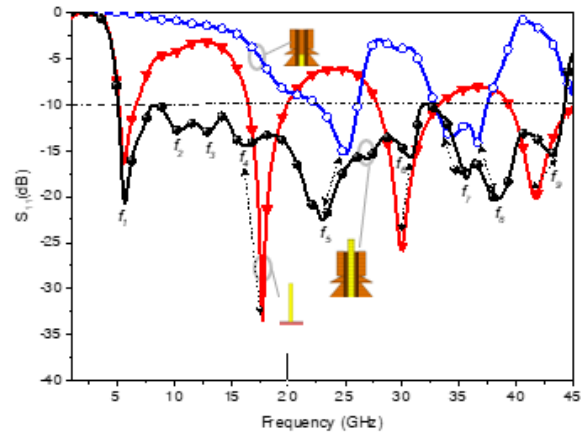


Fig. 3. Magnitude of the reflection coefficient of: MP, DRs excitation only, and proposed antennas.

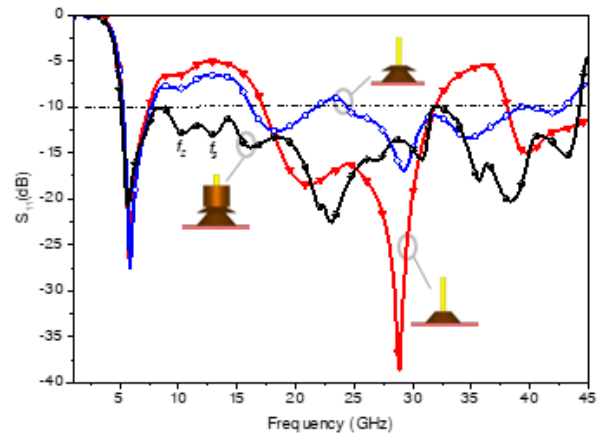

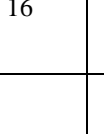
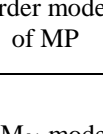
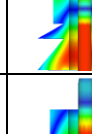
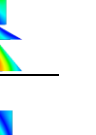
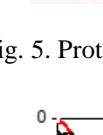
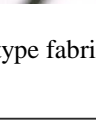
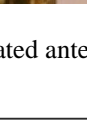
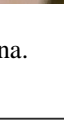


Fig. 4. MP loading effect with different blocks of DR.

Table 4 lists the observations of the magnetic field distributions for all nine resonant frequencies which clearly support the explanations that concluded from the magnitude of the reflection coefficient response of the antenna.

Table 4: Identification the nature of resonant modes in the proposed antenna

Resonances	Frequency (GHz)	Observations	Magnetic Field Distributions
1 <sup>st</sup> ( $f_1$ )	5.7	Excitation of a quarter wave MP	
2 <sup>nd</sup> ( $f_2$ )	10.3	Excitation of a quarter wave MP with $\ell_{eff} = 0.8\ell$	
3 <sup>rd</sup> ( $f_3$ )	13	Excitation of a quarter wave MP with $\ell_{eff} = 0.6\ell$	
4 <sup>th</sup> ( $f_4$ )	16	1 <sup>st</sup> higher order mode of MP	
5 <sup>th</sup> ( $f_5$ )	24	TM <sub>01</sub> mode in DRs	
6 <sup>th</sup> ( $f_6$ )	30	2 <sup>nd</sup> higher order mode of MP	
7 <sup>th</sup> ( $f_7$ )	35	1 <sup>st</sup> higher order mode of DRs	
8 <sup>th</sup> ( $f_8$ )	38	Weak 2 <sup>nd</sup> higher order mode TM <sub>02δ</sub> of DRs	
9 <sup>th</sup> ( $f_9$ )	43	3 <sup>rd</sup> higher order mode of MP	

The proposed antenna was fabricated to corroborate the simulated results. Figure 5 shows the photograph of fabricated antenna. To measure the fabricated antenna, HP 8510C vector network analyzer has been calibrated over the frequency range from 4 GHz to 45 GHz to observe the impedance bandwidth response of the antenna. Synthetic adhesive is used to fasten the DR

structure on the metal plane. Figure 6 shows the measured and simulated magnitude of the reflection coefficient characteristics of the antenna indicating a close agreement between them. About 159% measured bandwidth centered at 24 GHz is achieved, indicating more than 8.6:1 ratio bandwidth. Compared to all previous published works that mentioned in Table 1, the presented antenna offers the widest impedance bandwidth.

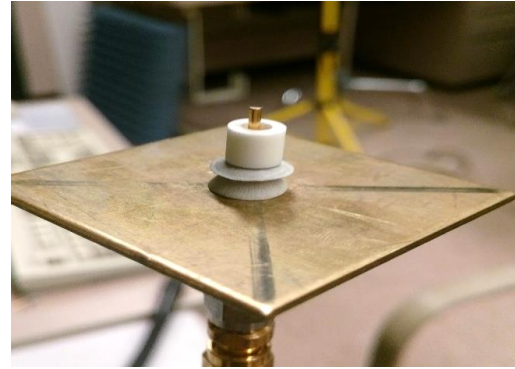


Fig. 5. Prototype fabricated antenna.

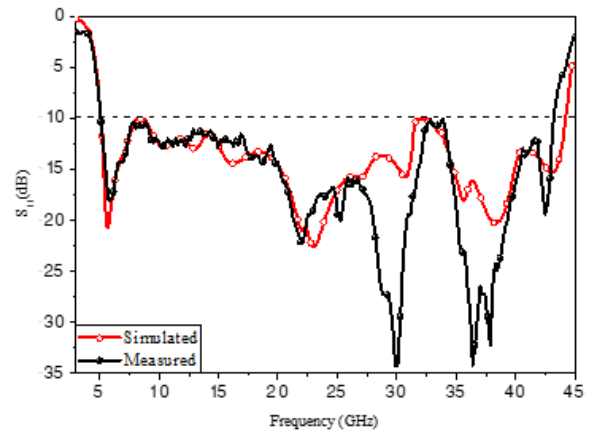


Fig. 6. Simulated and the measured magnitude of the reflection coefficient for the proposed antenna.

The radiation patterns of the antenna at different resonant frequencies covering the entire band are shown in Fig. 7. A single vertical plane ( $xz$ -plane) is used to investigate the radiation characteristics of the antenna since the antenna has vertical symmetrical configuration. Generally, radiation patterns of wideband antennas are varying with the operating frequency. However, and as it can be noticed in Fig. 7, the monopole-type radiation pattern is evident over the entire impedance bandwidth with a maximum gain of 7.8 dBi. The radiation patterns are measured at 5.7 GHz and 10.3 GHz and compared with the simulated ones as shown in Fig. 8, and a good

mutual agreement is revealed.

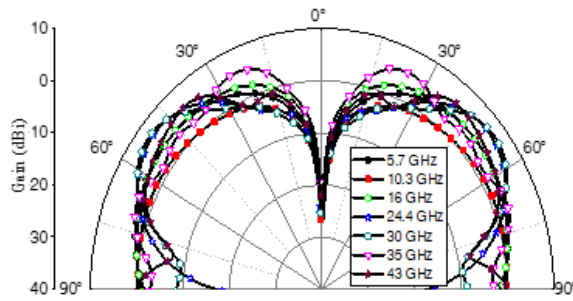


Fig. 7. Gain patterns of the proposed antenna along the xz-plane at different frequency points.

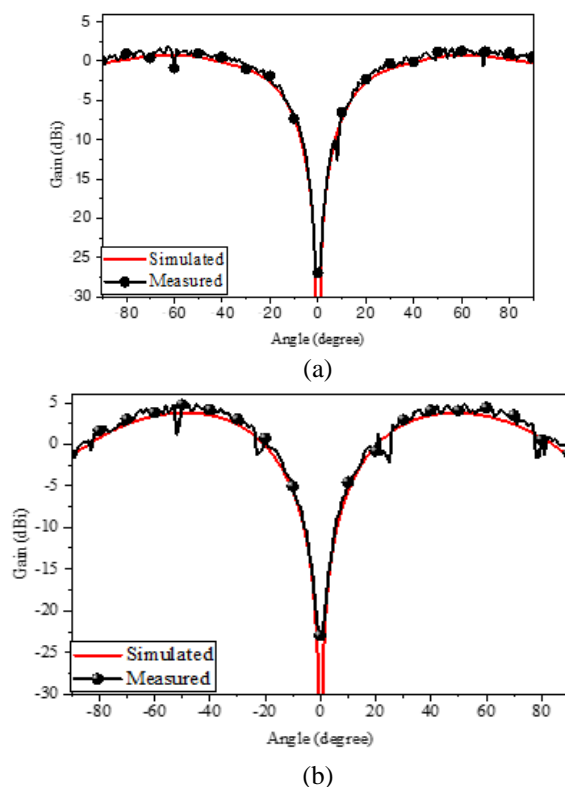


Fig. 8. Radiation field pattern for the antenna under test obtained at: (a) 5.7 GHz and (b) 10.3 GHz.

#### IV. CONCLUSION

A wideband hybrid monopole antenna has been proposed and investigated. The operational concept of the antenna was described, and its performance for ultra-wideband wireless applications was examined. The antenna has been fabricated and tested to validate its computed performance. The measured results indicate that the proposed antenna recorded the highest bandwidth value achieved so far of about 159%, covering a frequency

from 5 to 43 GHz along with consistent radiation pattern and peak gain of 7.8 dBi. With such performance, the proposed antenna can be utilized for wide range of applications such as ultra-wideband communications and EM wideband sensor.

#### REFERENCES

- [1] A. P. A. Ittipiboon and S. Thirakoune, "Bandwidth enhancement of a monopole using dielectric antenna resonator loading," in *Proc. ANTEM Conf.*, pp. 387-390, 2002.
- [2] M. Lapierre, Y. M. M. Antar, A. Ittipiboon, and A. Petosa, "Ultra wideband monopole/dielectric resonator antenna," *IEEE Microwave and Wireless Components Letters*, vol. 15, pp. 7-9, 2005.
- [3] D. Guha, Y. M. M. Antar, A. Ittipiboon, A. Petosa, and D. Lee, "Improved design guidelines for the ultra wideband monopole-dielectric resonator antenna," *IEEE Antennas and Wireless Propagation Letters*, vol. 5, pp. 373-376, 2006.
- [4] M. N. Jazi and T. A. Denidni, "A new hybrid skirt monopole dielectric resonator antenna," in *2008 IEEE Antennas and Propagation Society International Symposium*, pp. 1-4, 2008.
- [5] S. Ghosh and A. Chakrabarty, "Ultrawideband performance of dielectric loaded T-shaped monopole transmit and receive antenna/EMI sensor," *IEEE Antennas and Wireless Propagation Letters*, vol. 7, pp. 358-361, 2008.
- [6] D. Guha, B. Gupta, and Y. M. M. Antar, "New pawn-shaped dielectric ring resonator loaded hybrid monopole antenna for improved ultrawide bandwidth," *IEEE Antennas and Wireless Propagation Letters*, vol. 8, pp. 1178-1181, 2009.
- [7] D. Guha, B. Gupta, and Y. M. M. Antar, "Hybrid monopole-DRA's using hemispherical/conical-shaped dielectric ring resonators: Improved ultrawideband designs," *IEEE Transactions on Antennas and Propagation*, vol. 60, pp. 393-398, 2012.
- [8] C. Ozzaim, F. Ustuner, and N. Tarim, "Stacked conical ring dielectric resonator antenna excited by a monopole for improved ultrawide bandwidth," *IEEE Transactions on Antennas and Propagation*, vol. 61, pp. 1435-1438, 2013.
- [9] C. Ozzaim, "Monopole antenna loaded by stacked annular ring dielectric resonators for ultrawide bandwidth," *Microwave and Optical Technology Letters*, vol. 56, pp. 2395-2398, 2014.
- [10] D. Guha, D. Ganguly, S. George, C. Kumar, M. Sebastian, and Y. M. M. Antar, "A new design approach for a hybrid monopole to achieve increased ultrawide bandwidth [Antenna Designer's Notebook]," *IEEE Antennas and Propagation Magazine*, vol. 59, pp. 139-144, 2017.



**Ali A. Al-Azza** received the B.S. and M.S. degrees in Electrical Engineering from Basrah University, Iraq in 2005 and 2008, respectively. In 2016, he received Ph.D. degree in Electrical and Computer Engineering from Southern Illinois University, Carbondale, IL. Since 2017, he has been an Instructor with the Electrical Engineering Department, Basrah University, Basra, Iraq. He is the author of more than 18 peer-review research papers. His research interests include electromagnetic devices, antennas, RF filters, and dielectric resonators (DR), evolutionary optimization techniques.



**Nuhad A. Malalla** received the B.S. and M.S. degrees in Electrical Engineering from Basrah University, Iraq in 2005 and 2008, respectively. In 2016, she received Ph.D. degree in Electrical and Computer Engineering from Southern Illinois University, Carbondale, IL. Since 2018, she has been an Instructor with the Department of Chemical Engineering and Petroleum Refining Engineering, College of Oil and Gas Engineering, Basrah University for Oil and Gas. Her research interests include electromagnetic devices, imaging techniques, antennas, control methods, and dielectric resonators (DR), and optimization.



**Mohamed Morsy** received the B.S. degree in Electrical Engineering from Alexandria University, Egypt in 2004 and the M.S. and Ph.D. degrees in Electrical and Computer Engineering from Southern Illinois University, Carbondale, IL, in 2006 and 2010; respectively. Since 2018, he has been an Associate Professor with the Electrical Engineering Department, Texas A&M University-Texarkana, Texarkana, TX. He is the author of more than 20 peer-review articles. His research interests include electromagnetic devices, antennas, RF filters, and dielectric resonators (DR). Other subjects of research are on designing antennas for the 4/5G- mobile terminals, and phased array antennas. Morsy is an IEEE senior member and an IDEAL (Institute for the Development of Excellence in Assessment Leadership) scholar.



**Frances J. Harackiewicz** received B.S., M.S., and Ph.D. degrees in Electrical Engineering from University of Massachusetts Amherst, in 1984, 1986, and 1990, respectively. She has more than 30 peer-review papers. Her research interests include electromagnetics, antenna theory and design, microwaves, microstrip phased arrays and anisotropic materials, small multiband and broadband antennas, PIFAs, loops, printed and dielectric antennas.

Harackiewicz is senior, IEEE (Institute of Electrical and Electronics Engineers, Inc.). She is also member, WEPAN (Women in Engineering Programs & Advocates Network). She is Counselor of SIUC Student Branch of the IEEE Advisor, SIUC Student Chapter of Engineering Honor Society Tau Beta Pi.

## Design of L-band Energy-Selective Surface with Circular Ring Gap

Guohui Yang<sup>1</sup>, Yong Li<sup>1</sup>, Qun Wu<sup>1</sup>, Yan Wang<sup>2</sup>, and Yingsong Li<sup>3,\*</sup>

<sup>1</sup>School of Electronic and Information Engineering, Harbin Institute of Technology, Harbin 150001, China

<sup>2</sup>Shenyang Aircraft Design and Research Institute, AVIC, Shenyang 110000, China

<sup>3</sup>College of Information and Communication Engineering, Harbin Engineering University, Harbin 150001, China  
gh.yang@hit.edu.cn, liyingsong@ieee.org\*

**Abstract** — An narrow-band energy-selective surface (ESS) in L-band is presented for airborne GPS antenna protection. Periodic square metal inlaid with circular ring gap is designed and loaded with pin diodes to obtain the energy selection characteristics. The parameters of unit structure are determined with optimization. By simulation, we know that the insertion loss is less than 3dB and the shielding efficiency is more than 30dB. Using the method of equivalent test, we experimentation verified that the proposed ESS structure can be used for airborne GPS antenna protection

**Index Terms** — Circular ring gap, energy selective surface, pin diodes, self-actuated protection.

### I. INTRODUCTION

Around 1960, EMP began to receive the attention of the military. EMP weapons have been developing rapidly [1]. At the same time, the electromagnetic protection structure based on frequency selective surface has been developed, such as hybrid radome, band stop filter, etc. [2]. FSS is widely used, such as antenna array decoupling and beamforming [3-6]. However, although FSS can effectively reduce the electromagnetic pulse outside the passband, it can't protect the pulse inside the passband. This led to the emergence of ESS. ESS is a kind of self-adaptive protection structure which using the structure of FSS controlled by the electric field sensitive device, it can pass the low-power signal and shield the high-power signal in the same frequency band.

At present, using diode as the energy selective surface design of electronic control device is the mainstream practice. Corresponding to the on state and off state of diode under the excitation of induced voltage, ESS also have two states of high-power state and small signal state. As the name suggests, high power state is to use the band stop characteristic of FSS to protect the strong electromagnetic pulse, and small

signal state is to use the band-pass characteristic of FSS to ensure that the small signal can pass normally. In fact, ESS is FSS which can adaptively switch the above two states. When ESS is irradiated by the high power electromagnetic pulse, the electronic characteristic structure of ESS will be changed from the band-pass structure (small signal state) to the band stop structure (high power state) in the most ideal situation. There are two main design ideas in ESS using diode. One design idea is based on band stop frequency selection surface. When ESS is in small signal state, resonance frequency should be far away from working frequency band to ensure normal passing of small signal. When ESS is in high power state, resonance frequency should be consistent with working frequency band to shield large signal pulse. The cross strip structure designed by this design idea has been proved to have good performance in [7]. However, this design idea also has disadvantage, in order to keep the resonant frequency as far away from the working frequency band as possible, it is necessary to make the unit very small, which will make the diode number of the whole ESS become a lot, resulting in processing difficulties and high costs. Another design idea can effectively avoid this problem that is based on a band pass frequency selection surface. When ESS is in small signal state, resonance frequency should work in working frequency band to ensure normal passing of small signal. When ESS is in high power state, resonance frequency should far away from working frequency band to shield large signal pulse. Because the working frequency of the antenna is in the L-band, the size of the unit is generally large, and the diodes used in each unit will not increase too much, so the diodes used in the whole ESS are greatly reduced. The structure proposed in this paper is designed according to the second design idea, and its advantages of low cost and easy processing will be seen below.

In this paper, an ESS in L-band is designed and optimized. Electromagnetic simulations are carried out by CST Microwave Studio and the results show that the

presented ESS structure has good performance in 1.5-1.57GHz. The proposed structure has small size and simple structure, which is easy to applied.

## II. ESS UNIT AND ANALYSIS

### A. Structure introduction

The unit of ESS designed in this paper is shown in Fig. 1 and Fig. 2. It consists of a square metal surface inlaid with a circular ring gap. The ring gap structure has band-pass characteristics. The resonance frequency is determined by choosing the appropriate unit size. Connect 4 diodes across the gap. In this way, when it is not enough to trigger the small signal of diode conduction to pass through, it can be ensured to pass normally by the same characteristics. When a large signal is incident, the diode turns on and the ESS switches to the high power state.

As is shown in Fig. 1 and Fig. 2, the parameters are side length equals to 46.6 mm,  $r = 21$  mm, patch = 46.4 mm,  $h = 0.7$  mm and gap = 1.5 mm. The dielectric board material is FR4, the dielectric constant is 4.3, the patch metal is pure copper. Based on the principle of small transmission coefficient in forward bias and large transmission coefficient in reverse bias, by comparing the S parameter of diodes, we finally choose BAP70-03.

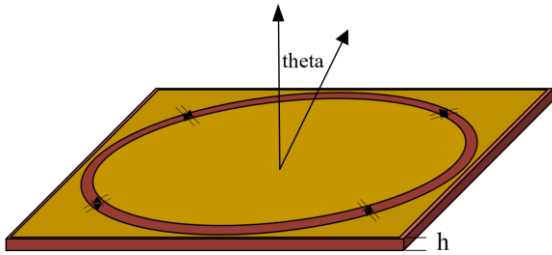


Fig. 1. Structure of ESS unit.

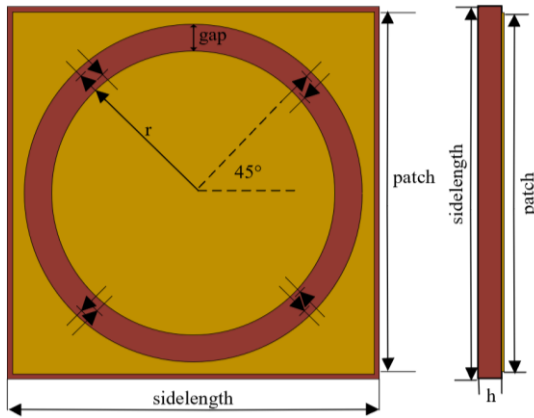


Fig. 2. ESS unit front view and side view.

### B. Simulation results of CST software

For the convenience of simulating diode in CST, we choose the diode equivalent model in [8-12] which is shown in Fig. 3, where the boundary is unit cell.

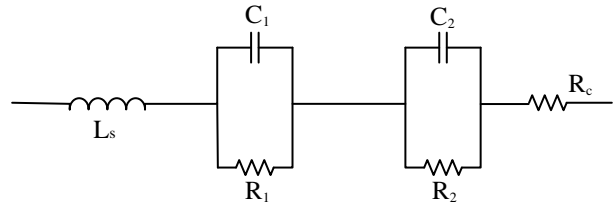


Fig. 3. Diode equivalent circuit.

And then, the S-parameter data of the selected diode is imported into ADS, confirming that it is consistent with the datasheet. Then, we establish the diode equivalent circuit model. By using the optimization function of ADS software, the equivalent circuit of the diode in the reverse and forward biases is obtained in Fig. 4 and Fig. 5.

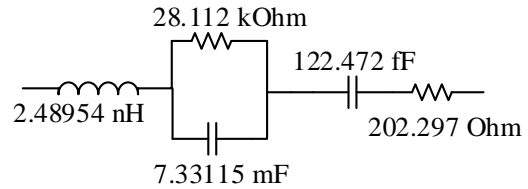


Fig. 4. Disconnected state equivalent circuit.

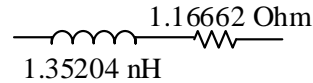


Fig. 5. Conduction state equivalent circuit.

Take the equivalent model into CST, and get the Transmission coefficient and shielding effectiveness curve as shown in the Fig. 6. In the simulation, we found that the number of the diodes will affect the performance of the ESS. If many diodes are used in the ESS, the transmission performance will get worse, while the shielding behaviour will get better, and vice versa. Thus, we give an example in Fig. 2 to discuss the design of the ESS.

The incident angle has an effect on the bandwidth, resonance frequency, transmission performance, shielding performance and other indicators of ESS. In practical application, the incident direction cannot always be vertical, so to study the stability of ESS performance at large angle of incidence, the incident angle was set from 0° to 45°. The results are shown in Fig. 7 and Fig. 8.

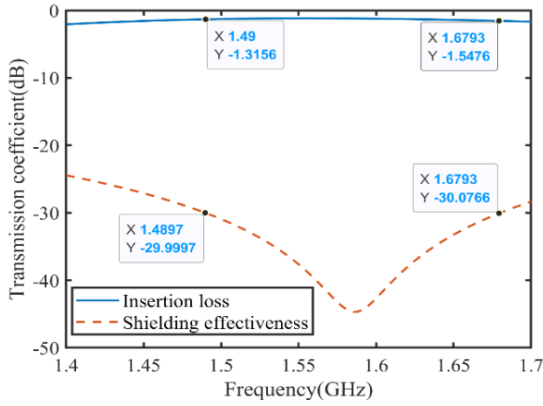


Fig. 6. Insertion loss and shielding effectiveness at normal incidence.

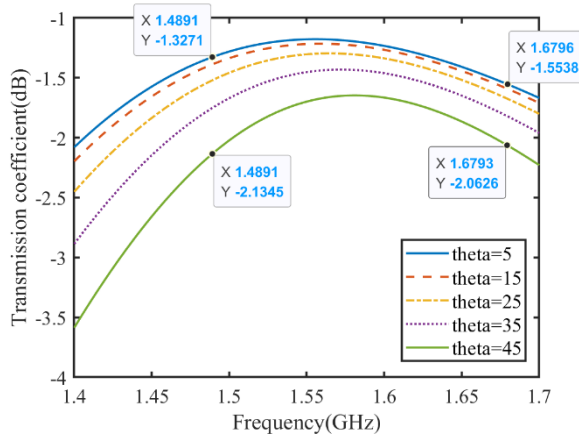


Fig. 7. Transmission coefficient varies with the incident angle.

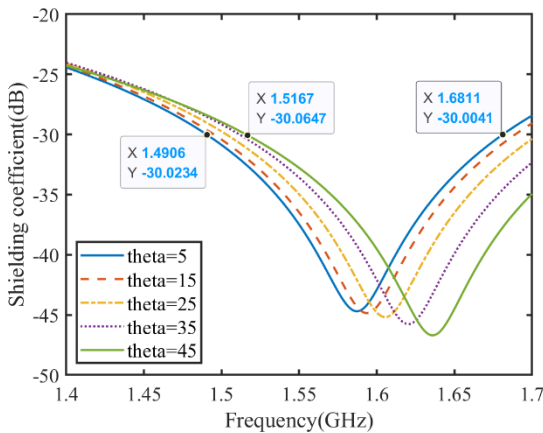


Fig. 8. Shielding effectiveness varies with the incident angle.

As shown in Fig. 6, it can be seen that the bandwidth of 30 dB shielding coefficient is about 210 MHz. the insertion loss is less than 2dB. From Fig. 7

and Fig. 8, with the increase of incident angle, the insertion loss and shielding coefficient increase slightly, but the consistency is wonderful. So far, after simulation and optimization, we have determined that the size of the cell is  $46.6\text{mm} \approx 0.215\lambda$ , and each cell uses four diodes. The design of ESS has been completed.

### III. EXPERIMENTAL VALIDATION

#### A. Fabrication and experiment

To verify the performance of ESS, a prototype including  $7 \times 7$  cells is fabricated as shown in Fig. 9, and a 15mm space is reserved around the patch to fix the printed circuit.

#### B. Test Result

According to the shielding effectiveness measurement method of electromagnetic shielding materials mentioned in military standard GJB6190-2008, build the test block diagram as shown in Fig. 10 and the test environment as shown in Fig. 11 and Fig. 12.

Because it is very difficult to produce EMP, the proposed test method is to use two test boards that have been processed, manually change their working conditions, and then use the low-power incident wave for testing. The diode on one test board does not do any processing, which is considered to work in the wave transmission state. The other uses solder instead of diode to simulate the shielding state. The test results are as shown in Fig. 13.

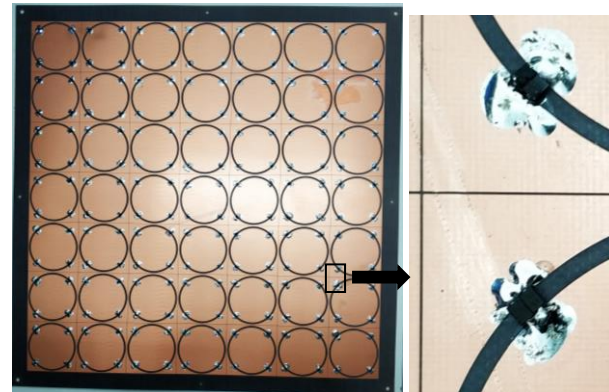


Fig. 9. Photograph of the ESS prototype

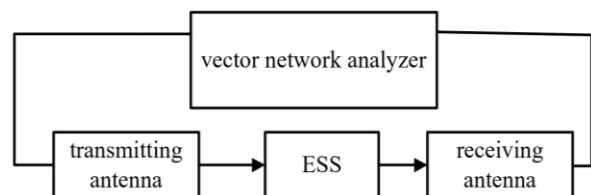


Fig. 10. Test diagram.



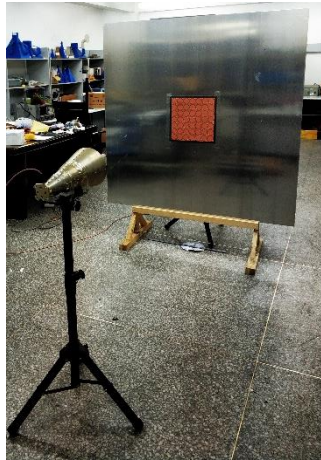


Fig. 11. Test environment (front side).



Fig. 12. Test environment (back side).

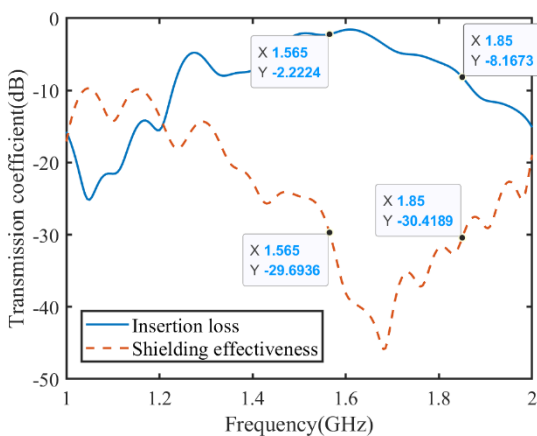


Fig. 13. Insertion loss and shielding effectiveness at normal incidence.

From Fig. 13, it can be seen that the shielding curve reaches 29.69 dB at 1.565 GHz. At this time, the

insertion loss is about 2.2 dB, which generally meets the design requirements. Comparing the simulation Fig 6 with the test result Fig. 13, it can be found that the center frequency of the shielding effectiveness stopband is shifted about 200 MHz to the high frequency direction. This is because the diode will have an impact on the resonant frequency point. Replacing the diode with solder will cause the resonant frequency point to move.

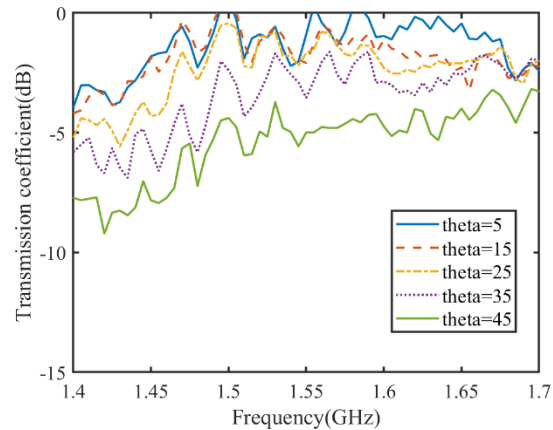


Fig. 14. Transmission coefficient varies with the incident angle.

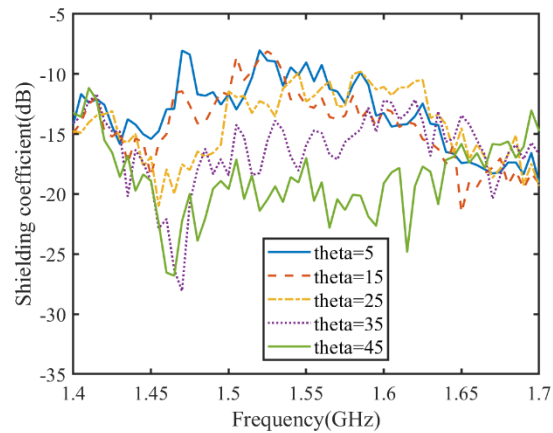


Fig. 15. Shielding effectiveness varies with the incident angle.

Next, verify the stability of ESS at large angle of incidence, and the test results are shown in Fig. 14 and Fig. 15. From the test results, it can be seen that at the working frequency of 1.565 GHz of the Airborne GPS antenna, the insertion loss slightly increases with the incident angle increasing, but it still does not exceed 3 dB, and the shielding efficiency is not less than 30 dB, which is in line with the expected effect, which proves that the designed unit structure has practical value and theoretical guidance significance.

#### IV. CONCLUSION

A narrow-band ESS in L-band is presented in this paper. The proposed ESS has an operating frequency at 1.565 GHz and operating band from 1.49 GHz to 1.68 GHz. Diode equivalent circuit model was used for simulation. On this basis, we verify the stability of large angle incident. Both simulation and experiments result show that the insertion loss of the structure is less than 3 dB at 1.565 GHz, and the shielding efficiency is more than 30 dB, which meets the design requirements. It can be used for high power microwave protection of Airborne GPS antenna. In the future, we will consider the application for circular polarization antennas [13] and use the adaptive method to control the diodes [14-15] for array applications [16].

#### ACKNOWLEDGMENT

This work was supported in the Fundamental Research Funds for the Central Universities (3072020CFT0802) and the Key Research and Development Program of Heilongjiang (GX17A016) and Open Project of State Key Laboratory of Millimeter Waves (K202017).

#### REFERENCES

- [1] C. E. Baum, "Reminiscences of high-power electromagnetics," *IEEE Transactions on Electromagnetic Compatibility*, vol. 49, no. 2, pp. 211-218, 2007.
- [2] B. A. Munk, *Frequency Selective Surface, Theory and Design*. Wiley, 2000.
- [3] F. Liu, J. Guo, L. Zhao, G. Huang, Y. Li, and Y. Yin, "Dual-band metasurface-based decoupling method for two closely packed dual-band antennas," *IEEE Transactions on Antennas and Propagation*, vol. 68, no. 1, pp. 552-557, Jan. 2020.
- [4] K. Yu, Y. Li, and X. Liu, "Mutual coupling reduction of a MIMO antenna array using 3-D novel meta-material structures," *Appl. Comput. Electromagn. Soc. J.*, vol. 33, no. 7, pp. 758-763, 2018.
- [5] J. Jiang, Y. Xia, and Y. Li, "High isolated X-band MIMO array using novel wheel-like metamaterial decoupling structure," *Appl. Comput. Electromagn. Soc. J.*, vol. 34, no. 12, pp. 1829-1836, 2019.
- [6] S. Luo, Y. Li, Y. Xia, et al., "Mutual coupling reduction of a dual-band antenna array using dual-frequency metamaterial structure," *Applied Computational Electromagnetics Society Journal*, vol. 34, no. 3, pp. 403-410, 2019.
- [7] C. Yang, P. Liu, and X. Huang, "A novel method of energy selective surface for adaptive HPM/EMP protection," *IEEE Antennas and Wireless Propagation Letters*, vol. 12, pp. 112-115, 2013.
- [8] R. F. Harrington, *Time-Harmonic Electromagnetic Fields*. McGraw-Hill, New York, 1961.
- [9] S. Shin and S. Kanamaluru, "Diplexer design using EM and circuit simulation techniques," *IEEE Microwave Magazine*, vol. 8, no. 2, pp. 77-82, Apr. 2007.
- [10] V. Rizzoli, A. Costanzo, D. Masotti, and P. Spadoni, "Circuit-level nonlinear electromagnetic co-simulation of an entire microwave link," *IEEE MTT-S Int. Microwave Symp. Dig.*, Long Beach, CA, pp. 813-816, June 2005.
- [11] Ansoft High Frequency Structure Simulation (HFSS), ver. 10, Ansoft Corporation, Pittsburgh, PA, 2005.
- [12] W. Rufe, Z. Haiying, Y. Junjian, et al., "A novel equivalent circuit model of GaAs PIN diodes," *Journal of Semiconductors*, vol. 29, no. 4, pp. 672-676, 2008.
- [13] K. L. Chuang, X. Yan, Y. Li, and Y. Li, "A Jia-shaped artistic patch antenna for dual-band circular polarization," *AEU - International Journal of Electronics and Communications*, 10.1016/j.aeue.2020.153207.
- [14] Y. Li, Z. Jiang, O. M. Omer-Osman, et al., "Mixed norm constrained sparse APA algorithm for satellite and network echo channel estimation," *IEEE Access*, vol. 6, pp. 65901-65908, 2018.
- [15] Y. Li, Y. Wang, and T. Jiang, "Sparse-aware set-membership NLMS algorithms and their application for sparse channel estimation and echo cancellation," *AEU - International Journal of Electronics and Communications*, vol. 70, no. 7, pp. 895-902, 2016.
- [16] X. Zhang, T. Jiang, and Y. Li, "A novel block sparse reconstruction method for DOA estimation with unknown mutual coupling," *IEEE Communications Letters*, vol. 23, no. 10, pp. 1845-1848, 2019.

# Wideband MIMO Directional Antenna Array with a Simple Meta-material Decoupling Structure for X-Band Applications

Jianfeng Jiang<sup>1</sup>, Yingsong Li<sup>1,2,\*</sup>, Lei Zhao<sup>3</sup>, and Xiaoguang Liu<sup>4</sup>

<sup>1</sup> College of Information and Communication Engineering  
Harbin Engineering University, Harbin, 150001, China  
\*liyingsong@ieee.org

<sup>2</sup> Key Laboratory of Microwave Remote Sensing  
Chinese Academy of Sciences, Beijing, 100190, China

<sup>3</sup> School of Information and Control Engineering  
China University of Mining and Technology, Xuzhou, 221116, China

<sup>4</sup> Department of Electrical and Computer Engineering  
University of California, Davis, 95618, China

**Abstract** — In this paper, a compact wideband MIMO directional antenna array with a single-layered meta-material is proposed to realize high isolation. The meta-material decoupling structure, which is composed of a modified split-rings and a square loop structure, is suspended over the two antenna elements to reduce the mutual coupling. The achieved results show that the proposed antenna array owns a  $-10$  dB impedance bandwidth ranging from 8.5 GHz to 11.5 GHz. Furthermore, by loading the proposed meta-material superstrate over the two-element MIMO antenna, the designed MIMO antenna array not only has good performance but also enhances the isolation to be more  $-15$  dB within the operating frequency band. In addition, the performances of the proposed antenna array are also tested by radiation pattern, gain, envelope correlation coefficient, diversity gain, total active reflection coefficient and so on. Therefore, these simulation results prove that the proposed wideband MIMO directional antenna array is a suitable candidate for X-band communication.

**Index Terms** — Directional, high isolation, low mutual coupling, low mutual coupling, meta-material, MIMO antenna, wideband, X-band.

## I. INTRODUCTION

The X-band (8–12 GHz) of the radio spectrum is used in many applications including satellite communications, and radar [1-3]. To improve the link quality at X-band, it is often desirable to use directional antennas for their higher gain, narrower beam width, and better interference tolerance [4]. Meanwhile,

wideband technologies have also received extensive attention for their ability to support higher data transmission and multi-channel connectivity [5]. When the channel bandwidth is large, however, multipath fading can degrade of channel capacity [6]. Multiple-input multiple-output (MIMO) technology has been proposed to overcome some of these problems. Because multiple data signals can be transmitted simultaneously, MIMO technology can enable high-capacity communications without increasing the bandwidth or signal-to-noise ratio (SNR) [7,8]. Thus, combining wideband technology with MIMO technology has become a research focus, and will play an important role in the future wireless communications [9–11].

In addition, owing to the increasing demand for miniaturization and portability of modern wireless communication devices and the increased number of antennas in MIMO systems, the antenna array structure is becoming more and more compact. However, the close proximity of antenna elements will cause strong mutual coupling between the antenna elements. Mutual coupling in an MIMO antenna array is mainly due to three factors: (1) surface wave, (2) coupling between the adjacent feeding lines, (3) coupling caused by space electromagnetic field [12, 13]. If the mutual coupling effect is not considered in the MIMO wireless communication system, it may cause antenna performance deterioration [14, 15]. Therefore, it is essential to give a solution to reduce the mutual coupling effect.

Several techniques have been proposed to mitigate mutual coupling in arrays. These techniques can be broadly categorized as the following:

(1) The neutralization line techniques: in this method, the two antenna elements are connected by a microstrip line, and the phase of current passing through this microstrip is opposite to the phase of equivalent current of the mutual coupling, thereby achieving the decoupling effect [16–18].

(2) The defected ground structure (DGS) techniques: in [19–21], the DGS is etched in the ground plane between microstrip patch antennas to change the distribution of effective substrate permittivity and the distributed inductance and capacitance of microstrip line to reduce mutual coupling.

(3) The parasitic element decoupling techniques: in [22–24], the researchers use the indirect coupled field generated by the parasitic element to cancel the direct coupling field to weaken the mutual coupling.

(4) The pattern and space diversity techniques: in [25–27], the antennas are placed in an orthogonal fashion to reduce the mutual coupling by taking advantage of the polarization orthogonality.

(5) The meta-material decoupling techniques: in [28–30], the electromagnetic band gap (EBG) structures are placed between two antenna elements to increase the isolation. In [32–33], meta-surface walls are inserted between the two antennas to reduce the mutual coupling.

A disadvantage of these methods is that they invariably occupy a large space between the two antenna elements, which is contrary to the trend of miniaturization.

Placing a meta-material superstrate above the antennas presents a viable solution to reduce the coupling between the two antenna elements while ensuring the miniaturization of antenna [34, 35]. As a two-dimensional periodic artificial structure, the meta-material is a structure in which plurality of slot cells or ideal conductor patches are distributed in a plane with a specific arrangement [36]. The meta-material superstrate has been used in many antenna applications, such as gain enhancement [37], radar cross section (RCS) reduction [38], radar radome [39], polarization converter [40], and microwave absorber [41]. Thus, various configurations such as patch, square loop, circular ring and slot shapes have been used to design the meta-material superstrate. However, most of the meta-materials are utilized in the field of narrowband antenna developments because the bandwidth of meta-material is limited [42]. Traditionally, the bandwidth of meta-material can be broadened by cascading multiple substrate layers [43, 44]. But this method increases the overall thickness, complexity and cost of fabrication.

In this paper, a meta-material based mutual coupling reduction structure is proposed and demonstrated. As a proof-of-concept example, a single-layered meta-material superstrate is suspended over a two-element patch antenna array working in the frequency of 8.5–11.5 GHz. We demonstrate that the

proposed meta-material structure can enhance the isolation between the two patch elements, resulting in a low mutual coupling of less than -15 dB.

The organization of the rest of the paper is as follows: In Section II, the evolution process and the final optimized configuration of MIMO wideband directional antenna array and meta-material superstrate are proposed. Section III demonstrates the simulated results and analyzes the characteristics of optimized wideband MIMO directional antenna array. Finally, a conclusion is made in the last section.

## II. DESIGN OF THE PROPOSED ANTENNA ARRAY

Figure 1 shows the proposed antenna array which is composed of two layers including the radiating patch antenna array and the meta-material superstrate.

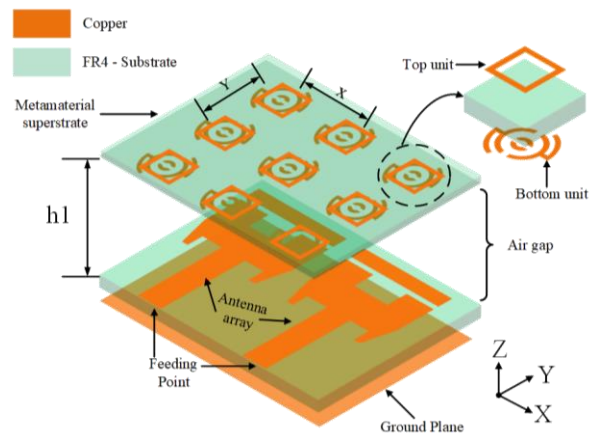


Fig. 1. Proposed MIMO antenna array with meta-material superstrate.

### A. Design process of the antenna array

Microstrip patch antennas are widely used because of their low profile and ease of fabrication. However, a significant disadvantage of patch antennas is their narrow bandwidth. In order to improve the bandwidth, regular microstrip patch monopole antennas have been modified and optimized in this work. Figure 2 shows the evolution of the designs (denoted by antenna 1, 2, and 3, where antenna 3 is the final design used in this work). Figure 3 shows their respective  $S_{11}$ . The design starts from Antenna 1 with two identical monopole antennas, which have only two resonant frequency at 8 GHz and 13 GHz. In order to obtain a wider bandwidth, two rectangular parasitic patches are added as shown in Antenna 2. It can be seen that the higher resonant mode moved from 13 GHz to 12 GHz and impedance matching has been significantly improved over 10.5–12.5 GHz. However, the reflection coefficient of Antenna 2 over 8.5–10.5 GHz is still higher than -10

dB. Then, slot and beveled edge are added into the patch element to improve the impedance match over 8.5–10.5 GHz as shown as Antenna 3. Figure 3 shows that the lower resonant frequency shift to 9 GHz and the bandwidth range from 8.5 GHz to the 12.5 GHz.

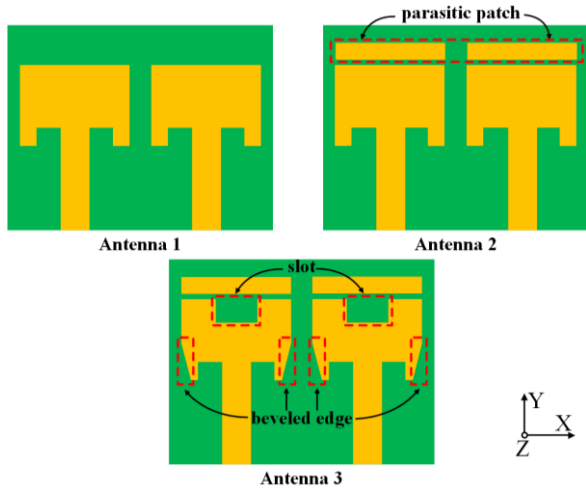


Fig. 2. Design process of the proposed wideband MIMO directional antenna array.

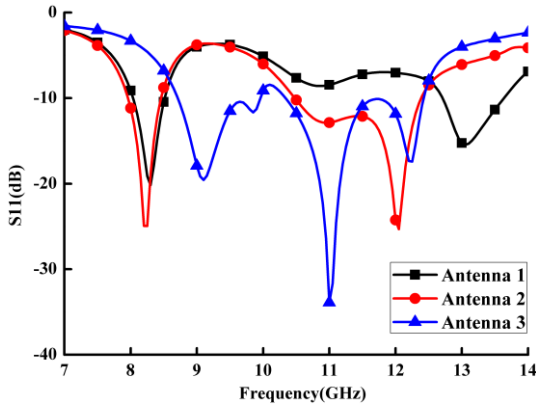


Fig. 3. The simulated  $S_{11}$  with evolution from antenna 1 to 3.

Figure 4 shows the top view and bottom view of the final design and the critical dimensions of the two-element patch antenna are presented in Table 1. The two-element antenna array is integrated on the top of a FR4 substrate with a thickness of 1.6 mm, a relative permittivity of 4.4 and a loss tangent of 0.02. The ground plane acts as a reflector covering almost the entire bottom surface. The proposed two-element radiating patch has an overall dimension of  $30 \times 22 \times 1.6 \text{ mm}^3$ . Besides, as can be seen from the figure, the edge-to-edge distance between the two radiating antenna elements is only 2.3 mm ( $0.076 \lambda_0$ , where  $\lambda_0$  refers to the wavelength of 10 GHz in vacuum), which is very

compact and suitable for use in miniaturized devices.

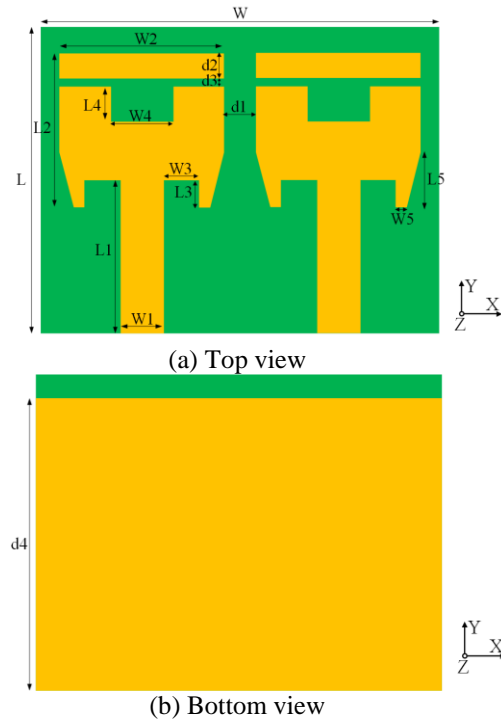


Fig. 4. Geometry of the proposed MIMO antenna array.

**B. Design of the meta-material unit**

It is well known that natural materials do not have negative dielectric constant ( $\epsilon < 0$ ) and negative magnetic permeability ( $\mu < 0$ ), but the proper design of metamaterials allows it to meet both of above these conditions within the required bandwidth. As we know, the response of a meta-material structure entirely depends on the proper design of its periodic cell. Figure 5 shows the proposed single-layered meta-material cell which consists of two different meta-material structures, a modified double split-rings and a square loop structure. The two structures are printed on the two sides of a FR4 substrate with a thickness ( $h_2$ ) of 0.6 mm. To maintain good isolation over the wide bandwidth, the proposed meta-material cell is further optimized and the finalized parameters of periodic cell are presented in Table 2.

In order to obtain the electromagnetic characteristics of proposed meta-material unit, the meta-material unit is simulated in HFSS Fig. 6 shows the simulation setup; the meta-material unit is placed between two floquet ports and proper boundary conditions including perfectly electric conducting (PEC) and perfectly magnetic conducting (PMC) in the x- and y-direction, respectively. The real and imaginary parts of the S-parameters can be calculated. In [45], the equivalent permittivity can be calculated by the S-parameters, which is presented in formula (1) - (4):

$$z = \pm \sqrt{\frac{(1+S_{11})^2 - S_{21}^2}{(1-S_{11})^2 - S_{21}^2}}, \quad (1)$$

$$e^{jnk d} = \frac{S_{21}}{1 - S_{11} \frac{z-1}{z+1}}, \quad (2)$$

$$\epsilon = \frac{n}{z}, \quad (3)$$

$$\mu = n \cdot z, \quad (4)$$

where  $k$  is the wave number of free space,  $d$  is the thickness of meta-material unit,  $n$  is the refractive index,  $z$  is the wave impedance,  $\epsilon$  is the equivalent permittivity and  $\mu$  is the equivalent permeability.

Table 1: The parameters of antenna (Unit: mm)

Parameters	W	W1	W2	W3	W4	W5
Values	30	3	11.7	2.6	4.4	0.75
Parameters	L	L1	L2	L3	L4	L5
Values	22	10.8	11	2	2	2.5
Parameters	h	d1	d2	d3	d4	
Values	1.6	2.3	1.8	0.6	20	

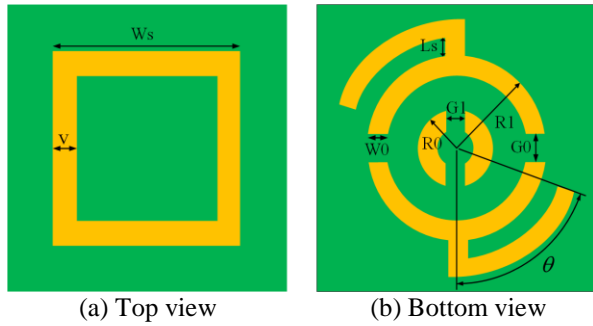


Fig. 5. Configuration of the meta-material cell.

Table 2: The parameters of meta-material cell (Unit: mm)

Parameters	R0	R1	W0	G0	G1
Values	0.8	2	0.4	0.4	0.4
Parameters	Ws	Ls	v	$\theta$	
Values	4	0.4	0.6	40°	

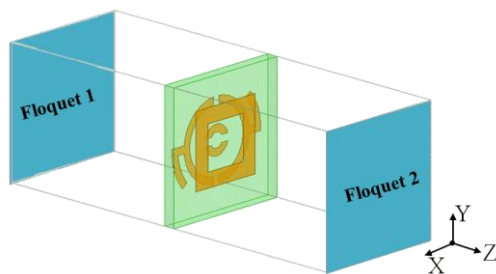


Fig. 6. The electromagnetic model to extract design parameters.

Figure 7 shows the extracted equivalent permittivity and permeability. It is noticed that the unit cell has both a negative permittivity and a negative equivalent permeability in entire X-band.

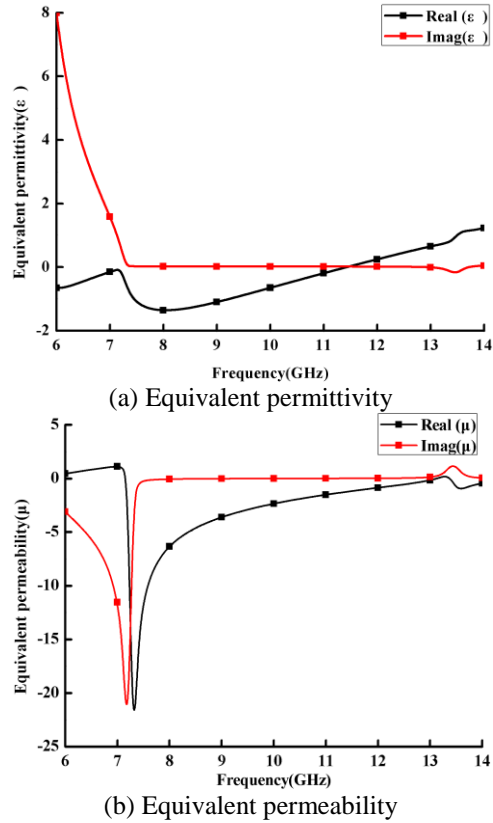


Fig. 7. The equivalent permittivity and permeability of proposed meta-material unit.

### C. Analysis of mutual coupling reduction performance

The meta-material superstrate contains  $3 \times 3$  unit cells in the x-axis and y-axis, respectively (Fig. 1). The distance between the centers of each identical periodic cells along the x-axis is 7.5 mm, and the distance along the y-axis is 7 mm. The gap ( $h_1$ ) between the radiating patch and the meta-material layer is 2.1 mm.

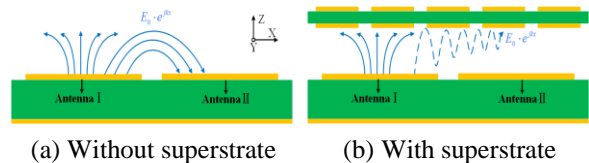


Fig. 8. The radiated field distribution of proposed MIMO antenna array.

Figure 8 illustrates the working principles of the proposed mutual coupling scheme. When the antenna I

is excited, a lateral wave  $E_0 e^{jkx}$  propagates along the x-axis can cause an induced current on antenna II, thereby generating mutual coupling between the two antennas. As shown in Fig. 8 (b), a suspended meta-material on the antenna array creates a region of negative magnetic permittivity and permeability:

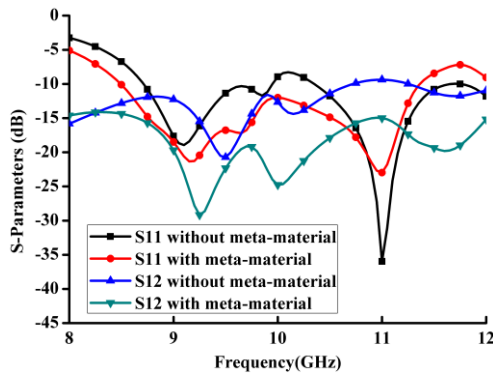
$$k^2 = \omega^2 \mu \varepsilon, \quad (5)$$

$$\vec{S} = \frac{1}{2} \vec{E} \times \vec{H} = \frac{1}{2} \frac{\vec{k}}{\omega \varepsilon} |\vec{E}|^2 = \frac{1}{2} \frac{\vec{k}}{\omega \mu} |\vec{H}|^2, \quad (6)$$

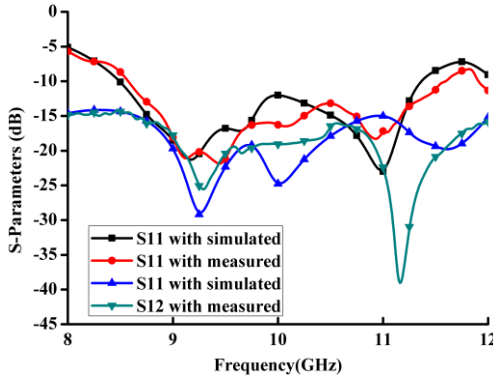
$$\vec{k} \cdot \vec{S} = \frac{1}{2} \omega \varepsilon |\vec{E}|^2 = \frac{1}{2} \omega \mu |\vec{H}|^2 < 0, \quad (7)$$

where  $k$  is the propagation constant of electromagnetic waves,  $\vec{S}$  is poynting vector,  $\varepsilon$  is the permittivity and  $\mu$  is the permeability.

According to (5) and (7), it can be concluded that the propagation direction of electromagnetic waves is opposite to the energy direction, so the electromagnetic waves propagating along the x-axis direction are gradually attenuated, thereby reducing the coupling of two antennas.



(a) With/without the meta-material superstrate

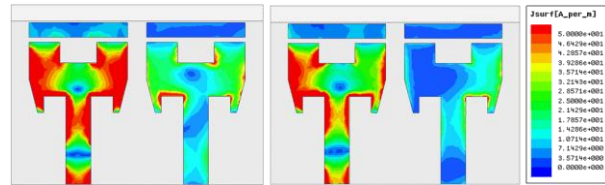


(b) With simulated and measured

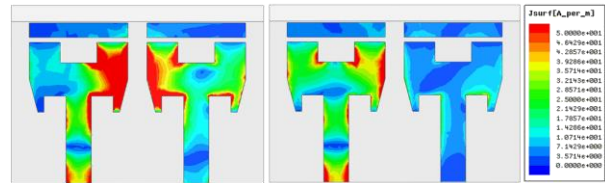
Fig. 9.  $S_{11}$  and  $S_{12}$  of the wideband MIMO directional antenna array.

Figure 9 (a) shows the simulated S-parameters of MIMO directional antenna with and without the meta-material superstrate. It is observed that the meta-material

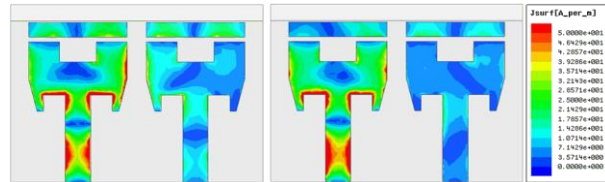
superstrate not only reduces the coupling between the two antennas but also improves the impedance matching of the proposed antenna array. Two resonant frequencies at 9.2 GHz and 11 GHz can be observed. This allows the antenna to cover almost the entire X-band from 8.5 GHz. The mutual coupling is reduced by 6 dB and the resulting leakage between the antennas are better than -15 dB. The measured values of S-parameters are shown in Fig. 9 (b) for a comparison with the simulated values. There is a good agreement between the measurement and the simulation. The small difference between the measurement and the simulation may be attributed to the fabrication tolerances.



(a) Without/with the decoupling structure at 9 GHz



(b) Without/with the decoupling structure at 10 GHz



(c) Without/with the decoupling structure at 11 GHz

Fig. 10. Surface current distribution on the proposed MIMO antenna array.

To better understand the working principles of the proposed meta-material superstrate, Fig. 10 plot the current distribution on the antennas with three selected frequencies:  $f_1 = 9$  GHz,  $f_2 = 10$  GHz,  $f_3 = 11$  GHz. In this case, one antenna element is fed, while the other one is terminated. As shown in the left of Figs. 10 (a), (b) and (c), the current distributions on the proposed MIMO antenna without meta-material superstrate is stronger can creates stronger coupling to the adjacent antenna element. After placing the proposed meta-material superstrate above the two antenna elements, it can be observed in the right of Figs. 10 (a), (b) and (c) that the surface current on the right antenna is significantly reduced. Therefore, it is concluded that the proposed meta-material superstrate can isolate the coupling between the two antennas.

### III. EXPERIMENTAL VALIDATION

To validate the proposed concept, a prototype antenna array is fabricated and measured. Figure 11 shows a photo the proposed antenna as fabricated according to the aforementioned parameters. The measured results are obtained by the vector network analyzer (VNA) E5063A.

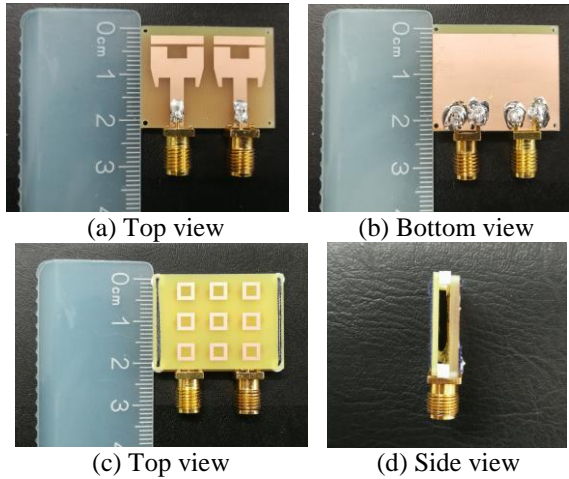


Fig. 11. Photograph of the fabricated wideband MIMO antenna.

Figure 12 shows the simulated 2D radiation patterns of proposed MIMO directional antenna array with specific frequencies:  $f_1 = 9$  GHz,  $f_2 = 10$  GHz,  $f_3 = 11$  GHz. Because of symmetry, one antenna element is excited, while the other one is terminated with a  $50 \Omega$  load. In Fig. 12, although the patterns of antenna fluctuate, the measured data and the simulated data are generally consistent within the allowable errors which are attributed to imperfections in the measurement setup. The proposed antenna array exhibits directional mode of wideband MIMO directional antenna array on the xoz-plane and the yoz-plane and the maximum radiation direction is the z-axis direction. It can be observed that the 3 dB beam-width of xoz-plane are  $64^\circ$ ,  $62^\circ$ ,  $62^\circ$  and the 3 dB beam-width of yoz-plane are  $64^\circ$ ,  $64^\circ$ ,  $58^\circ$ , at 9 GHz, 10 GHz, 11 GHz respectively.

In Fig. 13, the gain and efficiency of the proposed wideband MIMO directional antenna are presented with meta-material loading. It can be seen that, from 8.5 GHz to 11.5 GHz, the value of peak gain ranges from 5 dBi to 7.2 dBi and the value of radiation efficiency ranges from 66% to 79%. The maximum gain is 7.2 dBi at 10.1 GHz, and the minimum gain is 5 dBi at 11.5 GHz. Similarly, the maximum efficiency is 79% at 10.35 GHz, and the minimum gain is 66% at 11.5 GHz. Moreover, the variation in the gain values is found to be less than 1.5 dBi and the radiation efficiency is above 70% in the frequency band of 8.5 GHz–11.3GHz. However, the gain and efficiency deteriorate rapidly

after 11.3 GHz, and the reason may be that the impedance does not match, resulting in part of the energy to be reflected back on the feedline and not to be effectively radiated from the antenna.

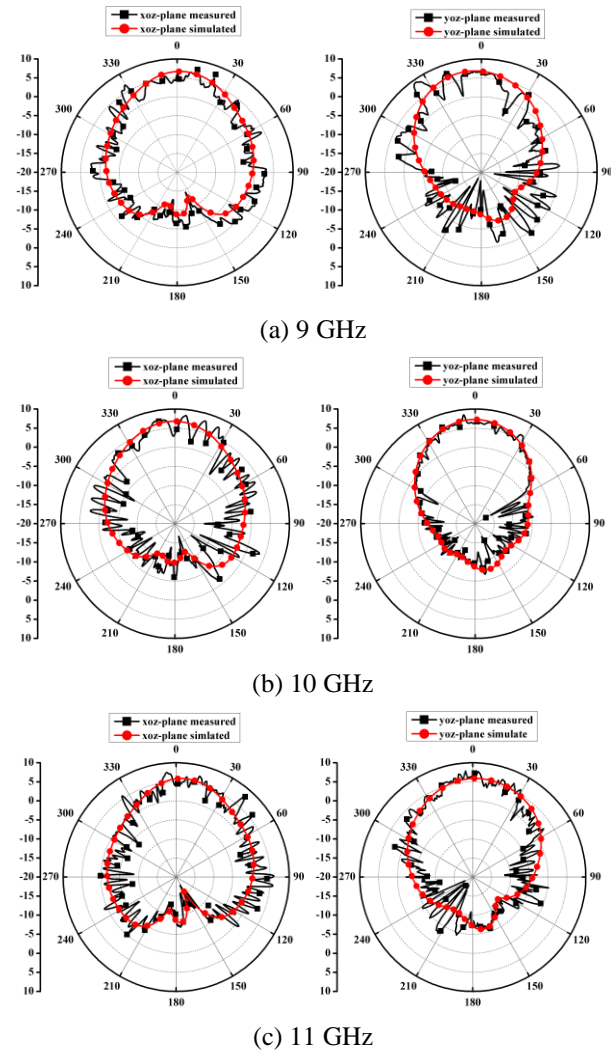


Fig. 12. The simulated and measured radiation patterns.

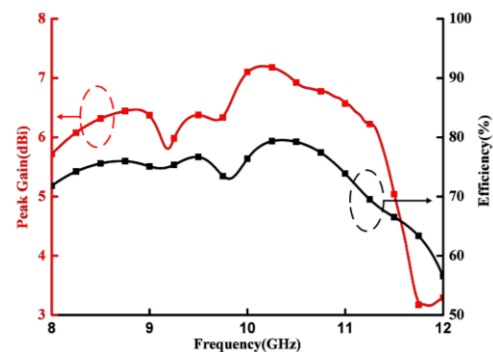


Fig. 13. The Gain and efficiency of the wideband MIMO antenna array.



To further verify the diversity performance of proposed wideband MIMO directional antenna array, the envelope correlation coefficient (ECC), diversity gain (DG) and total effective reflection coefficient (TARC) of the proposed design have been calculated and analyzed.

ECC is defined as a parameter of the level of correlation between antenna elements, and its value takes into account the radiation pattern, the polarization, and the relative phase of fields between them. For the two-element MIMO antenna system, ECC can be given as [46]:

$$\text{ECC} = \frac{|S_{11}^* S_{12} + S_{21}^* S_{22}|^2}{(1 - |S_{11}|^2 - |S_{21}|^2)(1 - |S_{22}|^2 - |S_{12}|^2)}. \quad (8)$$

Using the (8), we know that the ECC should be zero in an ideal situation, which is not possible in a real propagation world, even in line of site communication. Theoretically, for good diversity performance, the value of ECC must be less than 0.5 for mobile communication devices. In Fig. 14, the obtained value of ECC is less than 0.01 within the operating frequency band, which indicates that there is very small correlation among the antenna elements.

Another important diversity performance parameter of MIMO communication system is the diversity gain, which is calculated as [47]:

$$\text{DG} = 10 \times \sqrt{1 - |\text{ECC}|^2}. \quad (9)$$

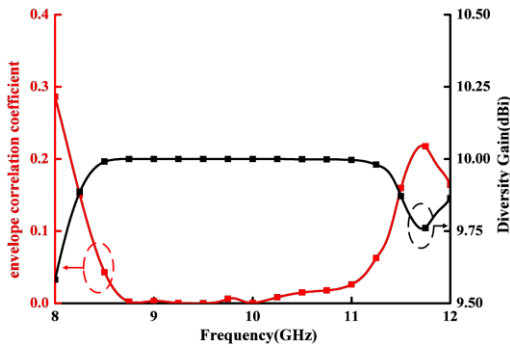


Fig. 14. The ECC and diversity Gain of proposed wideband MIMO directional antenna array.

Therefore, it can be seen from the (9) that the lower ECC, the higher diversity gain and vice versa. As shown in Fig. 14, the diversity gain is approximately 10 dBi from 8.5 GHz to 11.5 GHz.

Similarly, the TARC can be more accurately defined as the actual return loss of the entire MIMO antenna array because it depends on the reflection coefficients, transmission coefficients and the different excitation phase angles. For the two-element MIMO antenna system, the formula for TARC is as follows [48]:

$$\text{TARC} = \frac{\sqrt{(|S_{11} + S_{12}e^{j\theta}|^2 + |S_{21} + S_{22}e^{j\theta}|^2)}}{\sqrt{2}}. \quad (10)$$

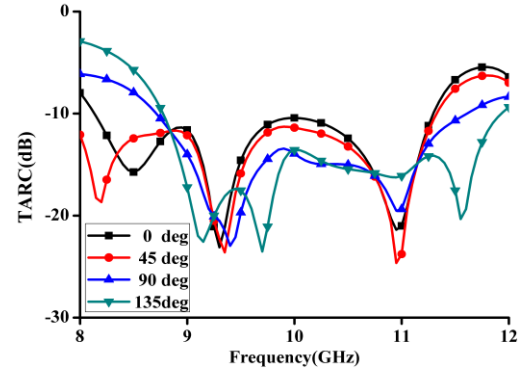


Fig. 15. The TARC of wideband MIMO directional antenna array.

Figure 15 shows the TARC of wideband MIMO directional antenna with four different phase angles:  $0^\circ$ ,  $45^\circ$ ,  $90^\circ$ ,  $135^\circ$ . As can be seen from this figure, the TARC is below -10 dB from 8.5 GHz to 11.5 GHz at any angle, which can explain that the excitation phase angle and the mutual coupling has less influence on the bandwidth of proposed wideband MIMO directional antenna array.

Table 3: Compared to other antennas

Ref.	The Distance between the Two Patches (mm)	Bandwidth (GHz)	Isolation (dB)	The Gap between the Two Layers (mm)
[49]	2.8 ( $0.034 \lambda_0$ )	Narrow band (3.7 and 4.1)	< -26	18 ( $0.219 \lambda_0$ )
[50]	5 ( $0.095 \lambda_0$ )	7.6% (5.6-6.05)	< -24	9 ( $0.171 \lambda_0$ )
[51]	1 ( $0.019 \lambda_0$ )	13.3% (5.6-6.4)	< -15	4.8 ( $0.086 \lambda_0$ )
[52]	18 ( $0.15 \lambda_0$ )	15.6% (2.3-2.69)	< -25	15 ( $0.219 \lambda_0$ )
[53]	4.5 ( $0.052 \lambda_0$ )	11.4% (3.3-3.7)	< -25	15 ( $0.125 \lambda_0$ )
This work	2.3 ( $0.076 \lambda_0$ )	30% (8.5-11.5)	< -15	2.1 ( $0.070 \lambda_0$ )

Finally, the performance of the proposed MIMO antenna array is compared with the other MIMO antenna array using the same techniques of mutual coupling reduction in Table 3. In [49], although this technique can make the coupling further reduced, the bandwidth is narrow. Furthermore, compare to [50-53], the proposed MIMO antenna array has a significantly higher bandwidth than before. In addition, adding dielectric plate above the antenna will inevitably

increase the overall profile thickness. In order to further reduce the thickness, the gap between the two dielectric plates is only 2.1 mm in this design. In summary, the proposed antenna has few advantages, such as compact size, wideband, high isolation and low profile. Additionally, the MIMO antenna can be minimized like [54-57] and designed to be circular polarization antenna [58] or array based on signal processing algorithms [59-65].

#### IV. CONCLUSION

In this paper, a novel single-layered meta-material superstrate is applied for suppressing mutual coupling of wideband MIMO directional antenna array, where the two antenna elements are in extremely close vicinity. The proposed antenna is designed, optimized, simulated to enhance the performance of antenna. In the entire operating band spanning from 8.5 GHz to 11.5 GHz, the mutual coupling is reduced to be -15 dB. Besides, it can be seen from the radiation pattern that the antenna has good directivity. Meanwhile, the value of peak gain ranges from 5 dBi to 7.2 dBi and the value of radiation efficiency ranges from 66% to 79%. Finally, by analyzing some parameters such as ECC, DG, TARC, it can be concluded that the proposed antenna has good diversity performance. Therefore, the proposed MIMO antenna array using single-layered meta-material decoupling structure would be an attractive candidate for wideband miniaturized wireless communication systems in the future.

#### ACKNOWLEDGMENT

This work was supported in the Fundamental Research Funds for the Central Universities (3072020CFT0802) and the Key Research and Development Program of Heilongjiang (GX17A016) and Open Project of State Key Laboratory of Millimeter Waves (K202017).

#### REFERENCES

- [1] C. Mao, S. Gao, Y. Wang, Q. Chu, and X. Yang, "Dual-band circularly polarized shared-aperture array for C-/X-band satellite communications," *IEEE Transactions on Antennas and Propagation*, vol. 65, no. 10, pp. 5171-5178, 2017.
- [2] J. Kumar, B. Basu, and F. A. Talukdar, "X-band antenna printed on a multilayered substrate," *IET Microwave Antennas & Propagation*, vol. 11, no. 11, pp. 1504-1509, 2017.
- [3] B. Mishra, "An ultra compact triple band antenna for X/Ku/K band applications," *Microwave and Optical Technology Letters*, vol. 61, no. 7, pp. 1857-1862, 2019.
- [4] X. Zhao, J. Geng, R. Jin, Y. Jin, X. Liu, and W. Yin, "Topological design of planar circularly polarized directional antenna with low profile using particle swarm optimization," *International Journal of Antennas and Propagation*, vol. 2017, pp. 1-12, 2017.
- [5] T. Kaiser, F. Zheng, and E. Dimitrov, "An overview of ultra-wide-band systems with MIMO," *Proceedings of the IEEE*, vol. 97, no. 2, pp. 285-312, 2009.
- [6] L. Nie, X. Lin, Z. Yang, J. Zhang, and B. Wang, "Structure-shared planar UWB MIMO antenna with high isolation for mobile platform," *IEEE Transactions on Antennas and Propagation*, vol. 67, no. 4, pp. 2735-2738, 2019.
- [7] S. Pahadsingh and S. Sahu, "An integrated MIMO filtenna with wide band-narrow band functionality," *AEU - International Journal of Electronics and Communications*, vol. 110, 2019.
- [8] H. H. Tran, N. Hussain, and T. T. Le, "Low-profile wideband circularly polarized MIMO antenna with polarization diversity for WLAN applications," *AEU - International Journal of Electronics and Communications*, vol. 108, pp. 172-180, 2019.
- [9] Y. Li, W. Li, and W. Yu, "A multi-band/UWB MIMO/diversity antenna with an enhance isolation using radial stub loaded resonator," *Applied Computational Electromagnetics Society Journal*, vol. 28, no. 1, pp. 8-20, 2013.
- [10] Y. Kong, Y. Li, and W. Yu, "A minimized MIMO-UWB antenna with high isolation and triple band-notched functions," *Frequenz*, vol. 70, no. 11-12, pp. 463-471, 2016.
- [11] A. Iqbal, O. A. Saraereh, A. W. Ahmad, and S. Bashir, "Mutual coupling reduction using F-shaped stubs in UWB-MIMO antenna," *IEEE Access*, vol. 6, pp. 2755-2759, 2018.
- [12] X. Chen, S. Zhang, and Q. Li, "A review of mutual coupling in MIMO systems," *IEEE Access*, vol. 6, pp. 24706-24719, 2018.
- [13] I. Nadeem and D. Choi, "Study on mutual coupling reduction technique for MIMO antenna," *IEEE Access*, vol. 7, pp. 563-586, 2019.
- [14] B. Pan, W. Tang, M. Qi, H. Ma, Z. Tao, and T. Cui, "Reduction of the spatially mutual coupling between dual-polarized patch antennas using coupled metamaterial slabs," *Scientific Reports*, vol. 6, 2016.
- [15] K. Yu, Y. Li, and X. Liu, "Mutual coupling reduction of a MIMO antenna array using 3-D novel meta-material structures," *Applied Computational Electromagnetics Society Journal*, vol. 33, no. 7, pp. 758-763, 2018.
- [16] Y. Wang and Z. Du, "A wideband printed dual-antenna with three neutralization lines for mobile terminals," *IEEE Transactions on Antennas and Propagation*, vol. 62, no. 3, pp. 1495-1500, 2014.
- [17] S. Zhang and G. F. Pedersen, "Mutual coupling

- reduction for UWB MIMO antennas with a wideband neutralization line,” *IEEE Antennas and Wireless Propagation Letters*, vol. 15, pp. 166-169, 2016.
- [18] S. Luo, Y. Li, Y. Xia, and L. Zhang, “A low mutual coupling antenna array with gain enhancement using metamaterial loading and neutralization line structure,” *Applied Computational Electromagnetics Society Journal*, vol. 34, no. 3, pp. 411-418, 2019.
- [19] R. Anitha, V. P. Sarin, P. Mohanan, and K. Vasudevan, “Enhanced isolation with defected ground structure in MIMO antenna,” *Electronics Letters*, vol. 50, no. 24, pp. 1784-1786, 2014.
- [20] C. Luo, J. Hong, and L. Zhong, “Isolation enhancement of a very compact UWB-MIMO slot antenna with two defected ground structures,” *IEEE Antennas and Wireless Propagation Letters*, vol. 14, pp. 1766-1769, 2015.
- [21] K. Wei, J. Li, L. Wang, Z. Xing, and R. Xu, “Mutual coupling reduction by novel fractal defected ground structure bandgap filter,” *IEEE Transactions on Antennas and Propagation*, vol. 64, no. 10, pp. 4328-4335, 2016.
- [22] Z. Li, Z. Du, M. Takahashi, K. Saito, and K. Ito, “Reducing mutual coupling of MIMO antennas with parasitic elements for mobile terminals,” *IEEE Transactions on Antennas and Propagation*, vol. 60, no. 2, pp. 473-481, 2012.
- [23] L. Zhao and K. Wu, “A decoupling technique for four-element symmetric arrays with reactively loaded dummy elements,” *IEEE Transactions on Antennas and Propagation*, vol. 62, no. 8, pp. 4416-4421, 2014.
- [24] J. Deng, J. Li, and L. Guo, “Decoupling of a three-port MIMO antenna with different impedances using reactively loaded dummy elements,” *IEEE Antennas and Wireless Propagation Letters*, vol. 17, no. 3, pp. 430-433, 2018.
- [25] J. Ren, W. Hu, Y. Yin, and R. Fan, “Compact printed MIMO antenna for UWB applications,” *IEEE Antennas and Wireless Propagation Letters*, vol. 13, pp. 1517-1520, 2014.
- [26] S. Rajkumar, K. T. Selvan, P. H. Rao, “Compact 4 element Sierpinski Knopp fractal UWB MIMO antenna with dual band notch,” *Microwave and Optical Technology Letters*, vol. 60, no. 4, pp. 1023-1030, 2018.
- [27] H. Singh and S. Tripathi, “Compact UWB MIMO antenna with cross-shaped unconnected ground stub using characteristic mode analysis,” *Microwave and Optical Technology Letters*, vol. 61, no. 7, pp. 1874-1881, 2019.
- [28] J. Lee, S. Kim, and J. Jang, “Reduction of mutual coupling in planar multiple antenna by using 1-D EBG and SRR structures,” *IEEE Transactions on Antennas and Propagation*, vol. 63, no. 9, pp. 4194-4198, 2015.
- [29] T. Jiang, T. Jiao, and Y. Li, “Array mutual coupling reduction using L-loading E-shaped electromagnetic band gap structures,” *International Journal of Antennas and Propagation*, vol. 2016, pp. 1-9, 2016.
- [30] T. Jiang, T. Jiao, and Y. Li, “A low mutual coupling MIMO antenna using periodic multi-layered electromagnetic band gap structures,” *Applied Computational Electromagnetics Society Journal*, vol. 33, no. 3, 2018.
- [31] A. Dadgarpour, B. Zarghooni, B. S. Virdee, T. A. Denidni, and A. A. Kishk, “Mutual coupling reduction in dielectric resonator antennas using metasurface shield for 60-GHz MIMO systems,” *IEEE Antennas and Wireless Propagation Letters*, vol. 16, pp. 477-480, 2017.
- [32] R. Karimian, A. Kesavan, M. Nedil, and T. A. Denidni, “Low-mutual-coupling 60-GHz MIMO antenna system with frequency selective surface wall,” *IEEE Antennas and Wireless Propagation Letters*, vol. 16, pp. 373-376, 2017.
- [33] Y. Zhao, Y. Li, W. Shi, and W. Yu, “Mutual coupling reduction between patch antenna and microstrip transmission line by using defected isolation wall,” *Applied Computational Electromagnetics Society Journal*, vol. 34, no. 1, pp. 100-106, 2019.
- [34] M. Akbari, M. M. Ali, M. Farahani, A. R. Sebak, and T. Denidni, “Spatially mutual coupling reduction between CP-MIMO antennas using FSS superstrate,” *Electronics Letters*, vol. 53, no. 8, pp. 516-518, 2017.
- [35] G. V. Eleftheriades and N. Engheta, “Metamaterials: Fundamentals and applications in the microwave and optical regimes,” *Proceedings of the IEEE*, vol. 99, no. 10, pp. 1618-1621, 2011.
- [36] S. Bukhari, J. Vardaxoglou, and W. Whittow, “A metasurfaces review: Definitions and applications,” *Applied Sciences-Basel*, vol. 9, no. 13, 2019.
- [37] F. Qin, S. Gao, Q. Luo, et al., “A simple low-cost shared-aperture dual-band dual-polarized high-gain antenna for synthetic aperture radars,” *IEEE Transactions on Antennas and Propagation*, vol. 64, no. 7, pp. 2914-2922, 2016.
- [38] Y. Liu, K. Li, Y. Jia, Y. Hao, S. Gong, and Y. J. Guo, “Wideband RCS reduction of a slot array antenna using polarization conversion metasurfaces,” *IEEE Transactions on Antennas and Propagation*, vol. 64, no. 1, pp. 326-331, 2016.
- [39] H. Baskey and M. Akhtar, “Design of flexible hybrid nanocomposite structure based on frequency selective surface for wideband radar cross section reduction,” *IEEE Transactions on Microwave Theory and Techniques*, vol. 65, no. 6,

- pp. 2019-2029, 2017.
- [40] F. Samadi, M. Akbari, S. Zarbakhsh, R. Chaharmir, and A. Sebak, "High efficient linear polariser using FSS structure," *IET Microwaves, Antennas & Propagation*, vol. 13, no. 1, pp. 88-91, 2019.
- [41] J. Zhang, J. Li, and J. Chen, "Mutual coupling reduction of a circularly polarized four-element antenna array using metamaterial absorber for unmanned vehicles," *IEEE Access*, vol. 7, pp. 57469-57475, 2019.
- [42] T. Hassan, M. U. Khan, H. Attia, and M. S. Sharawi, "An FSS based correlation reduction technique for MIMO antennas," *IEEE Transactions on Antennas and Propagation*, vol. 66, no. 9, pp. 4900-4905, 2018.
- [43] Y. Ranga, L. Matekovits, K. P. Esselle, and A. R. Weily, "Multioctave frequency selective surface reflector for ultrawideband antennas," *IEEE Antennas and Wireless Propagation Letters*, vol. 10, pp. 219-222, 2011.
- [44] Y. Cheng, X. Ding, X. Xu, X. Zhong, and C. Liao, "Design and analysis of a bow-tie slot-coupled wideband metasurface antenna," *IEEE Antennas and Wireless Propagation Letters*, vol. 18, no. 7, pp. 1342-1346, 2019.
- [45] X. Chen, T. M. Grzegorzczak, B. Wu, J. Pacheco, and J. Kong, "Robust method to retrieve the constitutive effective parameters of metamaterials," *Physical Review E*, vol. 70, no. 1, 2004.
- [46] R. G. Vaughan and J. B. Andersen, "Antenna diversity in mobile communications," *IEEE Transactions on Vehicular Technology*, vol. 36, no. 4, pp. 149-172, 1987.
- [47] L. Malviya, R. K. Panigrahi, and M. V. Kartikeyan, "MIMO antennas with diversity and mutual coupling reduction techniques: a review," *International Journal of Microwave and Wireless Technologies*, vol. 9, no. 8, pp. 1763-1780, 2017.
- [48] S. H. Chae, S. Oh, and S. Park, "Analysis of mutual coupling, correlations, and TARC in WiBro MIMO array antenna," *IEEE Antennas and Wireless Propagation Letters*, vol. 6, pp. 122-125, 2007.
- [49] Z. Niu, H. Zhang, Q. Chen, and T. Zhong, "Isolation enhancement in closely coupled dual-band MIMO patch antennas," *IEEE Antennas and Wireless Propagation Letters*, vol. 18, no. 8, pp. 1686-1690, 2019.
- [50] R. Mark, N. Rajak, K. Mandal, and S. Das, "Metamaterial based superstrate towards the isolation and gain enhancement of MIMO antenna for WLAN application," *AEU - International Journal of Electronics and Communications*, vol. 100, pp. 144-152, 2018.
- [51] Z. Wang, L. Zhao, Y. Cai, S. Zheng, and Y. Yin, "A meta-surface antenna array decoupling (MAAD) method for mutual coupling reduction in a mimo antenna system," *Scientific Reports*, vol. 8, 2018.
- [52] L. Zhao, F. Liu, X. Shen, et al., "A high-pass antenna interference cancellation chip for mutual coupling reduction of antennas in contiguous frequency bands," *IEEE Access*, vol. 6, pp. 38097-38105, 2018.
- [53] Y. Li, W. Li, and W. Yu, "A multi-band/UWB MIMO/diversity antenna with an enhanced isolation using radial stub loaded resonator," *Applied Computational Electromagnetics Society Journal*, vol. 28, no. 1, pp. 8-20, 2013.
- [54] J. Jiang, Y. Xia, and Y. Li, "High isolated X-band MIMO array using novel wheel-like metamaterial decoupling structure," *Applied Computational Electromagnetics Society Journal*, vol. 34, no. 12, pp. 1829-1836, 2019.
- [55] P. Xu, S. Luo, Y. Xia, et al., "A low mutual coupling two-element MIMO antenna with a meta-material matrix loading," *Applied Computational Electromagnetics Society Journal*, vol. 34, no. 12, pp. 1851-1856, 2019.
- [56] S. Luo, Y. Li, and Y. Xia, "Mutual coupling reduction of a dual-band antenna array using dual-frequency metamaterial structure," *Applied Computational Electromagnetics Society Journal*, vol. 34, no. 3, pp. 403-410, 2019.
- [57] J. Li, X. Zhang, X. Chen, et al., "Dual-band eight-antenna array design for MIMO applications in 5G mobile terminals," *IEEE Access*, vol. 7, pp. 71636-71644, 2019.
- [58] K. L. Chuang, X. Yan, Y. Li, et al., "A Jia-shaped artistic patch antenna for dual-band circular polarization," *AEÜ- International Journal of Electronics and Communications*, 10.1016/j.aeue.2020.153207.
- [59] Y. Li, Z. Jiang, O. M. Omer-Osman, et al., "Mixed norm constrained sparse APA algorithm for satellite and network echo channel estimation," *IEEE Access*, vol. 6, pp. 65901-65908, 2018.
- [60] Y. Li, Y. Wang, and T. Jiang, "Sparse-aware set-membership NLMS algorithms and their application for sparse channel estimation and echo cancelation," *AEU - International Journal of Electronics and Communications*, vol. 70, no. 7, pp. 895-902, 2016.
- [61] W. Shi, Y. Li, and B. Chen, "A separable maximum correntropy adaptive algorithm," *IEEE Transactions on Circuits and Systems II: Express Briefs*, 10.1109/TCSII.2020.2977608.
- [62] B. Chen, Z. Li, Y. Li, and P. Ren, "Asymmetric correntropy for robust adaptive filtering," *IEEE*

- Signal Processing Letters*, arXiv preprint arXiv:1911.11855.
- [63] Q. Wu, Y. Li, Y. V. Zakharov, et al., "A kernel affine projection-like algorithm in reproducing kernel hilbert space," *IEEE Transactions on Circuits and Systems II: Express Briefs*, 10.1109/TCSII.2019.2947317.
- [64] W. Shi, Y. Li, L. Zhao, et al., "Controllable sparse antenna array for adaptive beamforming," *IEEE Access*, vol. 7, pp. 6412-6423, 2019.
- [65] X. Zhang, T. Jiang, and Y. Li, "A novel block sparse reconstruction method for DOA estimation with unknown mutual coupling," *IEEE Communications Letters*, vol. 23, no. 10, pp. 1845-1848, 2019.

# A Dual-Polarized Sakura-Shaped Base Station Antenna for 5G Communications

Peng Chen, Lihua Wang, and Tongyu Ding

Information Engineering College  
Jimei University, Xiamen, Fujian, China  
chenpeng@jmu.edu.cn, wang15115565627@163.com, tyding@jmu.edu.cn

**Abstract** – In this paper, a dual-polarized sakura-shaped base station antenna for the fifth generation (5G) communication is designed and optimized. The antenna is mainly composed of four parts: main radiator, feed structures, bedframe and reflector. By fabricating and testing of the prototype of the antenna, the results show that the bandwidth (return loss  $>10\text{dB}$ ) of antenna port 1 and port 2 are 9.2% (3.3-3.62GHz) and 16.5% (3.12-3.68GHz), respectively. In the entire working frequency band, the isolation is greater than 23.5dB. Moreover, the proposed antenna has a stable radiation pattern, and the horizontal half-power beam width (HPBW) and gain of the antenna vary within  $65\pm 4^\circ$  and 5.25-6.31dBi, respectively. The antenna adopts PCB printed structure and has a compact structure  $70\times 70\times 28\text{mm}^3$ . The designed antenna has the advantages of low cost, light weight and good consistency of direction pattern.

**Index Terms** – 5G, Base station antenna, dual-polarized, low cost, printed-dipole.

## I. INTRODUCTION

With the rapid development of modern communication technologies, the channel will be contaminated by various noises that has been suppressed using channel estimations [1-4], which is realized on algorithms. For the antenna design, the MIMO antenna and dual-polarized antenna has been widely concerned by scholars [5-10] to combat multipath fading and improve the capacity of mobile communication system in complex environment. Considering the actual wireless communications [11-12], the  $45^\circ$  oblique polarization omnidirectional antenna [11-21] has been widely studied for base station applications. Not only does the  $45^\circ$  oblique polarization antenna receive electromagnetic waves from more directions, but also have higher diversity gain. Thus, the design of base station antenna has gradually adopts the form of dual-polarized. For example, in [12], a wideband dual-polarized antenna with anti-interference capability has been studied. The antenna obtained 52.6% (VSWR $<1.5$ ) bandwidth at the

operating frequency band of 2.27-2.53 GHz and peak notch bandwidth from 1.68 to 2.68GHz. In literature [11-12], dual-polarized antennas with simple structure and wide bandwidth are also developed. From the processing technology of base station antenna, metal [11-12] and PCB [12, 18, 21] are commonly used in the design procedure. Printed antenna has been widely used in base station because it is simpler and cheaper than metal fabrication. For example, in [15], two orthogonal placed dipoles and  $\pm 45^\circ$  dual-polarized feeding structures are adopted to realize broadband operation. The bandwidth reaches 38% in the working band ranging from 3.3 GHz to 4.2GHz, and its bandwidth is better than that in the literature [18, 20]. In [14], the ME dipole antenna not only embeds the metamaterials of the broadside coupled E-shaped unit cells into the magnetic dipole, but also adds two U-shaped patch together with a rectangular patch to the E-dipole, which can reduce the height of magnetic dipole and improve the anti-interference effect, respectively. In the range of 3.32-3.64GHz, the bandwidth is only 9.2%, which is far less than the literature [16-17,19]. Thus, the bandwidth is too narrow to cover the entire sub-6GHz band for 5G applications. In literature [17,19], the working frequency band of 5G base station antenna designed can well cover the entire sub-6GHz frequency band, which are 3.3-3.8GHz, 4.8-5.0GHz and 3.14-5.04GHz, respectively.

In this paper, a dual-polarized sakura-shaped base station antenna is developed, principally covering the frequency band required for 5G (3.3-3.6GHz). The measurement results of the prototype are consistent with the simulated results. The designed antenna achieves a bandwidth of 16.5% over 3.12-3.64GHz, which is wider than that of the antennas in the literatures [19,21]. The size of antenna is  $0.91\lambda_0\times 0.91\lambda_0\times 0.33\lambda_0$  ( $\lambda_0$  being the wavelength in free space at center operating frequency). Compared with literatures [15, 20], the designed antenna is smaller and cheaper. Herein, the antenna is well simulated, optimized, fabricated and measured to verify the performance for the practical application of 5G communication systems.

## II. ANTENNA STRUCTURE

The structure of the dual-polarized dipole-like base station antenna designed in this paper is shown in Fig. 1. The antenna is mainly composed of a pair of cross dipoles with  $\pm 45^\circ$ , two microstrip Balun printed with coupling feedings of height  $H_1$ , ground plane and a metal reflector. Two of them are placed vertically and a  $164\text{mm} \times 164\text{mm} \times 8\text{mm}$  reflector with side wall is placed, mainly to enhance the stability and the directivity of the antenna.

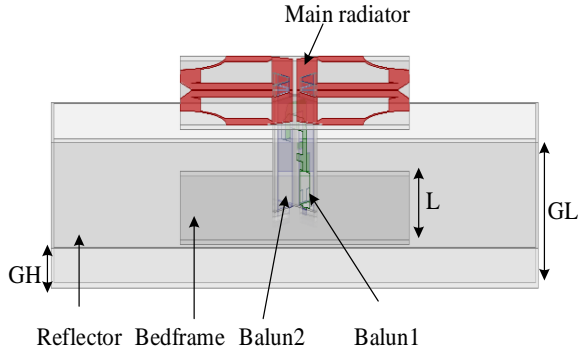


Fig. 1. Configuration of the proposed antenna.

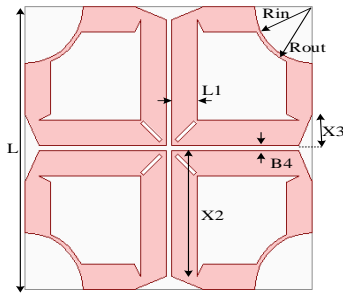


Fig. 2. Configuration of the main radiator.

As shown in Fig. 2, the main radiator of the antenna is sakura-shaped orthogonal dipoles printed on a 1mm thick FR-4 substrate with a relative dielectric constant of 4.4. Gaps in the dipole arm can be used as capacitive loads for good impedance matching. In Fig. 3, Two crossed substrates are distributed between the main radiator and reflector, which have  $\Gamma$ -shaped feeding lines on the front side and rectangle patches on the back side. Two slit orthogonal placement Baluns can not only make the coupling between the microstrip coupling feeder small, but also can make the structure stable and easy to process.

To get the good performance of the antenna, the antenna was simulated by electromagnetic (EM) simulation software Ansoft HFSS 15. By reasonably choosing the geometric parameters, the designed antenna is able to exhibit good performance. Geometric parameters of the antenna are displayed in Fig. 1-Fig. 3

and optimized values listed as follows (unit: mm):  $L=90$ ,  $L1=6.9$ ,  $X2=34$ ,  $X3=8.5$ ,  $B4=1.5$ ,  $Rin=15.5$ ,  $Rout=16.5$ ,  $BW=3$ ,  $H1=28$ ,  $w7=1.8$ ,  $d8=2.52$ ,  $d4=d6=7$ ,  $w4=4.6$ ,  $d7=11$ ,  $d3=7.7$ ,  $w5=1.3$ ,  $w2=w6=2.4$ ,  $d2=5.9$ ,  $d1=5.5$ ,  $w1=4.3$ ,  $GL=164$ ,  $GH=8$ ,  $w3=d5=2.8$ ,  $L5=20$ .

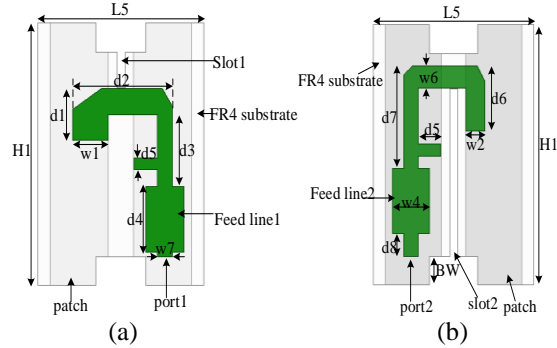


Fig. 3. Configuration of the Baluns: (a) Balun 1 and (b) Balun 2.

## III. RESULTS AND DISCUSSION

In order to validate the designed antenna, a prototype of the antenna is fabricated in Fig. 4. The network analyzer and chamber are used to measure the developed antenna. The return losses with different shapes are studied in Fig. 5. Ants.1, 2 and the proposed antenna are the evolution of the main radiators. We can see from the figure, the impedance matching of Ant.1 and Ant.2 is not good. By using the slots on the dipole arms as capacitive loading, the impedance match of the proposed antenna is improved, and it can cover the entire frequency band.

Figure 6 shows the simulated and measured S-parameters results for port1 and port2. Owing to the slight discrepancy in the two Balun structures, the operating frequency bands for port1 and port2 are not exactly same. The working bandwidth for port1 and port2 are 9.2% (3.3-3.62GHz) and 16.5% (3.12-3.68GHz). Since the measurement of the S-parameters is not obtained in the chamber, the simulated  $S_{12}$  is quite different from measured. The simulation efficiency of the antenna is about 0.857. However, the measured and simulated isolations are greater than 23.5dB over the entire operating frequency band.

Figure 7 shows the peak realized gain of the fabricated antenna and simulated  $S_{11}$  for different  $Rin$  and  $Rout$ . Measured peak realized gain varies from 5.25dBi to 6.31dBi, and beam width of the radiation pattern is  $65 \pm 4^\circ$  over 3.3-3.6GHz. Since there is a slight difference between the simulated reflector and the actual reflector, the gain varies is about 0.6dBi. We can see from this figure, when the value of the  $Rin$  increases, the frequency moves towards the high frequency. When the value of  $Rout$  is 17.5mm, the return loss is best. The measured and simulated radiation patterns are shown for

koz-plane and yoz-plane at 3.3, 3.45 and 3.6GHz in Fig. 8. Owing to the symmetry of the antenna, only the simulated and measured radiation patterns for port1 are presented in the figure. The measured radiation patterns agree well with the simulated ones.

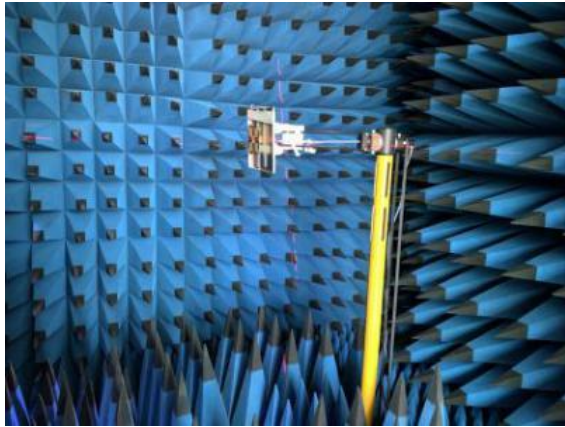


Fig. 4. Photograph of the designed antenna.

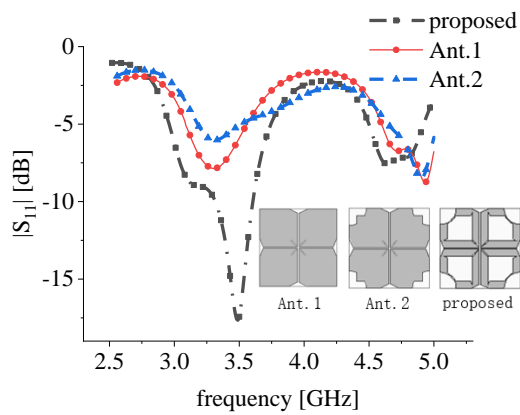


Fig. 5. Simulated  $S_{11}$  for Ant.1, Ant.2 and proposed antenna.

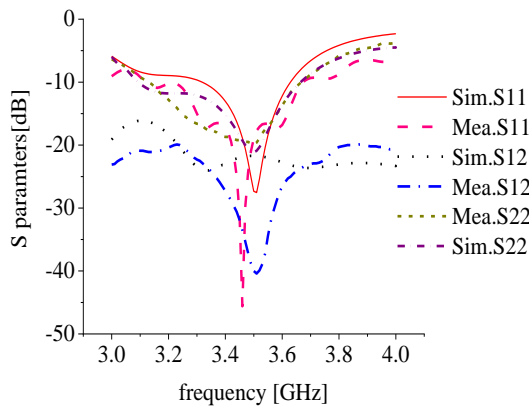


Fig. 6. Simulated and measured S-parameters of the proposed antenna.

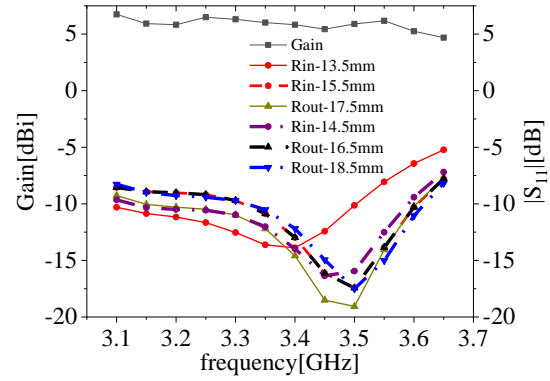


Fig. 7. Realized peak gain of the fabricated antenna and simulated  $S_{11}$  for different Rin and Rout.

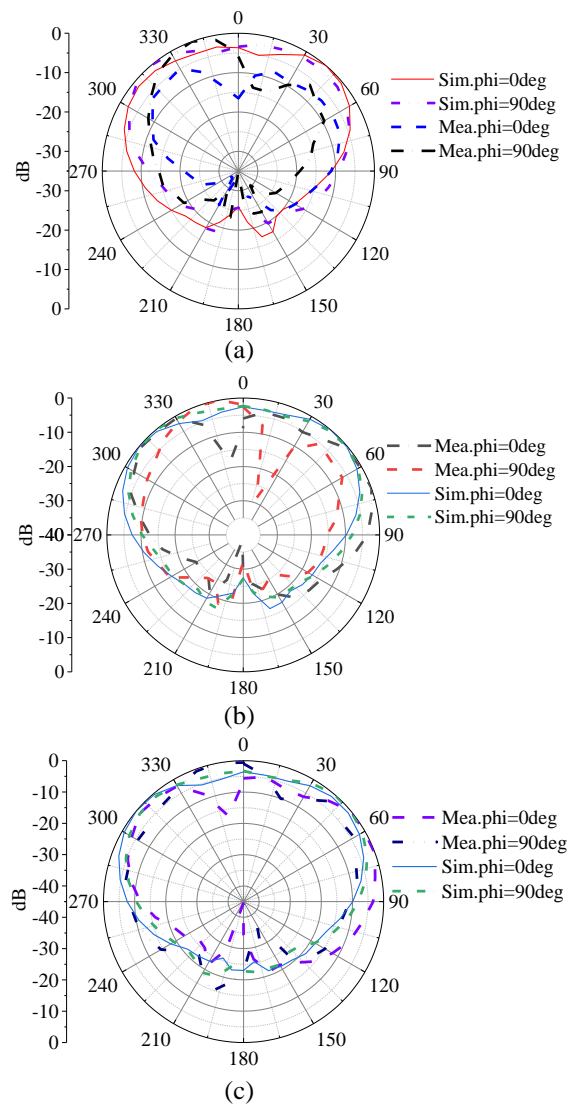


Fig. 8. Simulated and measured radiation patterns of the fabricated antenna at: (a) 3.3GHz, (b) 3.45GHz, and (c) 3.6 GHz.



The performance comparison between the designed antenna and the relevant 5G antenna are summarized in Table 1. To sum up, the antenna is an ideal choice for 5G base station antenna because of its advantages of strong structure, low cost, light weight and good consistency of direction pattern.

Table 1: Performance comparison of 5G base station antennas with the proposed antenna

Ref.	Bandwidth (GHz)	G (dBi)	Size ( $\lambda_0^3$ )	Isolation (dB)	Cost
[13]	3.3-4.2 (38%)	7	2×2×0.42	<-25	H
[16]	3.2-3.5 (8.9%)	5.61	0.91×0.63×0.58	-	L
[18]	3.25-3.81 (4.3%)	10.5	1×1×0.04	<-31	H
Proposed	3.12-3.68 (16.5%)	6.31	0.91×0.91×0.33	<-23.5	L

Note: "-" means not provided;  $\lambda_0$  is the wavelength in free space at center operating frequency.

#### IV. CONCLUSION

A novel dual-polarized sakura-shaped antenna is designed, fabricated and measured. According to the measured results, the proposed antenna achieves a reflection coefficient lower than -10dB and a minimum port-to-port isolation higher than -23.5dB over 3.3-3.62GHz. Furthermore, the antenna shows very stable radiation patterns with HPBWs varying in  $65\pm 4^\circ$  and average gain of around 5.84dBi. It has some advantages that low cost, light weight, strong structure and good consistency of direction pattern.

#### ACKNOWLEDGMENT

This work was supported in the Youth Natural Science Foundation of Fujian Province under Grant No. 2018J05109.

#### REFERENCES

- [1] W. Shi, Y. Li, B. Chen, "A separable maximum correntropy adaptive algorithm," *IEEE Transactions on Circuits and Systems II: Express Briefs*, 10.1109/TCSII.2020.2977608.
- [2] Y. Li, Z. Jiang, O. M. Omer, et al., "Mixed norm constrained sparse APA algorithm for satellite and network echo channel estimation," *IEEE Access*, vol. 6, pp. 65901-65908, 2018.
- [3] Y. Li, Y. Wang, and T. Jiang, "Sparse-aware set-membership NLMS algorithms and their application for sparse channel estimation and echo cancelation," *AEÜ-International Journal of Electronics and Communications*, vol. 70, no. 7, pp. 895-902, 2016.
- [4] X. Zhang, T. Jiang, Y. Li, and Y. Zakharov, "A novel block sparse reconstruction method for DOA estimation with unknown mutual coupling," *IEEE Communications Letters*, vol. 23, no. 10, pp. 1845-1848, 2019.
- [5] J. Jiang, Y. Xia, and Y. Li, "High isolated X-band MIMO array using novel wheel-like meta-material decoupling structure," *Applied Computational Electromagnetics Society Journal*, vol. 34, no. 12, pp. 1829-1836, 2019.
- [6] T. Jiang, T. Jiao, and Y. Li, "A low mutual coupling MIMO antenna using periodic multi-layered electromagnetic band gap structures," *Applied Computational Electromagnetics Society Journal*, vol. 33, no. 3, pp. 305-311, 2018.
- [7] K. Yu, Y. Li, and X. Liu, "Mutual coupling reduction of a MIMO antenna array using 3-D novel meta-material structures," *Applied Computational Electromagnetics Society Journal*, vol. 33, no. 7, pp. 758-763, 2018.
- [8] S. Luo, Y. Li, Y. Xia, G. Yang, L. Sun, and L. Zhao, "Mutual coupling reduction of a dual-band antenna array using dual-frequency metamaterial structure," *Applied Computational Electromagnetics Society Journal*, vol. 34, no. 3, pp. 403-410, 2019.
- [9] S. Luo, Y. Li, Y. Xia, and L. Zhang, "A low mutual coupling antenna array with gain enhancement using metamaterial loading and neutralization line structure," *Applied Computational Electromagnetics Society Journal*, vol. 34, no. 3, pp. 411-418, 2019.
- [10] K. L. Chuang, X. Yan, Y. Li, et al., "A Jia-shaped artistic patch antenna for dual-band circular polarization," *AEÜ-International Journal of Electronics and Communications*, 10.1016/j.aecue.2020.153207.
- [11] D. Su, J. J. Qian, Y. Hua, and D. Fu, "A novel broadband polarization diversity antenna using a cross-pair of folded dipoles," *IEEE Antennas and Wireless Propagation Letters*, vol. 4, pp. 433-435, 2005.
- [12] H. Huang, Y. Liu, and S. Gong, "A broadband dual-polarized base station antenna with anti-interference capability," *IEEE Antennas and Propag. Lett.*, vol. 16, pp. 613-616, 2016.
- [13] C.-W. Hsiao and W.-S. Chen, "Broadband dual-polarized base station antenna for LTE/5G C-band applications," presented at the *2018 Cross Strait Quad-Regional Radio Science and Wireless Technology Conference (CSQRWC)*, Xuzhou, China, 2018.
- [14] B. Feng, and K. L. Kwok, "A conformal magneto-electric dipole antenna with wide H-plane and band-notch radiation characteristics for sub-6-GHz 5G base-station," *IEEE Access*, vol. 7, pp. 17469-17479, 2019.
- [15] Q. Wu, P. Liang, and X. Chen, "A broadband  $\pm 45^\circ$  dual-polarized multiple-input multiple-output antenna for 5G base stations with extra decoupling

- elements,” *J. Commun. Inf. Netw.*, vol. 3, no. 1, pp. 31-37, 2018.
- [16] M. Li and X. Chen, “Dual-polarized broadband base station antenna backed with dielectric cavity for 5G communications,” *IEEE Antennas Wirel. Propag. Lett.*, vol. 18, no. 10, pp. 2051-2055, 2019.
- [17] Q. Hua, et al., “A novel compact quadruple-band indoor base station antenna for 2G/3G/4G/5G systems,” *IEEE Access*, vol. 7, pp. 151350-151358, 2019.
- [18] T. T. Pham, V. Group, and M. T. Le, “Novel dual-polarized 5G base station antenna,” presented at the *2019 26th International Conference on Telecommunications (ICT)*, Hanoi, Vietnam, Vietnam, 2019.
- [19] H. Tang, X. Zong, and Z. Nie, “Broadband dual-polarized base station antenna for fifth-generation (5G) applications,” *Sensors*, vol. 18, no. 8, p. 2701, Aug. 2018.
- [20] Y. Gao, R. Ma, Y. Wang, Q. Zhang, and C. Parini, “Stacked patch antenna with dual-polarization and low mutual coupling for massive MIMO,” *IEEE Trans. Antennas Propag.*, vol. 64, no. 10, pp. 4544-4549, 2016.
- [21] H. He, L. Ying, and S. Gong, “A broadband dual-polarized base station antenna with sturdy construction,” *IEEE Antennas Wirel. Propag. Lett.*, vol. PP, no. 99, pp. 1-1, 2016.

# Analysis on Crosstalk for Coplanar Irregular-placed Cables Based on Cascading Method and Cubic Spline Interpolation Algorithm

Chong Ming Zhu<sup>1,3</sup>, Wei Yan<sup>2\*</sup>, Shi Cheng Liu<sup>2</sup>, and Lu Geng<sup>4</sup>

<sup>1</sup>Nari Group Corporation, Nanjing 211000, Jiangsu, China  
danny08003123@126.com

<sup>2</sup>Department of Electrical and Automation Engineering  
Nanjing Normal University, Nanjing 210046, China  
\*61197@njnu.edu.cn, 875567351@qq.com

<sup>3</sup>State Key Laboratory of Smart Grid Protection and Operation Control, Nanjing 211000, Jiangsu, China

<sup>4</sup>China Energy Engineering Group, Nanjing 211102, China  
1046339056@qq.com

**Abstract** — The research on cable crosstalk is an important part of electromagnetic compatibility. The conventional research on cable crosstalk is mostly for parallel cables. However, most of the actual transmission line models are in a non-parallel state. A new method for the crosstalk prediction of coplanar irregular-placed cables is proposed in this paper. The method derives the integral form of the transmission line equation based on the cascade method. Combined with the cubic spline interpolation method for the processing of the per unit length parameter matrix, the crosstalk of the coplanar irregular-placed cables is predicted. The orthogonal experiment method is used to find that the distance between transmission lines has the greatest influence on crosstalk, followed by height from the current return plane, frequency, load and length. In order to verify the accuracy of the new method for crosstalk, the full wave method is introduced as a comparison method, and the experiment is introduced as a reference method. The verification results show that the new method has higher accuracy for the crosstalk prediction of coplanar irregular-placed cables, especially in the frequency band less than 100MHz.

**Index Terms** — Cascade method, crosstalk, cubic spline interpolation method, multi-conductor transmission line (MTL), orthogonal experiment method.

## I. INTRODUCTION

In modern electronic systems such as drones, ships and vehicles, the narrowness of the installation space and the high speed of the signal lead to the increasingly serious damage to signal integrity caused by crosstalk [1]. Therefore, crosstalk suppression of cables is a non-

negligible component of electromagnetic compatibility (EMC) [2]. It is of great theoretical and engineering significance for efficient operation of electrical equipment to explore the generation and transmission mechanism of cable electromagnetic crosstalk, and to predict the crosstalk of the transmission lines [3].

At present, the academic research on cable crosstalk is mainly based on the coupling of parallel cables. As early as the 1960s, the coupling formula and the famous BLT (Baum-Liu-Tesche) equations of three conductors under different port conditions were proposed [4]. The analysis methods of the structure of multi-conductor transmission line (MTL) mainly include full-wave method and transverse electromagnetic (TEM) field method [5]. In the crosstalk prediction of cables, it is further divided into prediction in the time domain and the frequency domain. Prediction in the time domain includes finite difference time domain (FDTD) method, time domain BLT equation method, cascade method [6-8], and prediction in the frequency domain mainly includes the moment of method (MOM) [9], modulus decoupling method [10].

Actually, the type of transmission line also includes coaxial cable [11], twisted pair cable [12], non-uniform cable and bundle cable [13-15]. Engineering applications are divided into optical fiber [16], aviation cable metal wire [17], vehicle cable [18]. The parameter matrix extraction method of the MTL includes theoretical calculation method and experimental method. The theoretical calculation method includes analytical method and numerical method [10]. The experimental method includes the scattering parameter method [19] and the separation network method [20].

However, most of the actual MTL models are in

an irregular state. Coplanar irregular-placed cables are difficult to analyze through the conventional method. Artificial intelligence algorithm prediction is often used now, like the BP neural network algorithm [21-22]. The neural network algorithm requires a large number of data samples of crosstalk experiments measured at different frequencies. It is unrealistic to measure the crosstalk of connected and used cables in most cases. It is highly probable that the original spatial relative position of the cable will change during the experiment, causing the crosstalk characteristics to change again.

The previous research did not make detailed theoretical derivation and calculation of coplanar irregular-placed cables crosstalk. Therefore, the method of crosstalk prediction for coplanar irregular-placed cables still needs further research.

The rest of the paper is presented as follows. In Section II, the model of coplanar irregular cables is studied based on the theory of cascaded transmission line, and the theoretical integral calculation formula of the crosstalk is derived. In Section III, the elements of the inductance parameter matrix are calculated by the analytic method and the elements of the capacitance parameter matrix are solved by the finite element method (FEM) combined with the cubic spline interpolation method. And the orthogonal experiment method is used to compare and analyze the factors affecting the crosstalk of transmission lines. In Section IV, a specific coplanar irregular-placed cables model is analyzed by using the new method, full wave method, and the experimental method. The conclusions of this paper are given in Section V.

## II. CROSSTALK SOLUTION OF COPLANAR IRREGULAR-PLACED CABLES MODEL

### A. Regular-placed cable model

The regular-placed cable model in this paper refers to the parallel MTL model. The per unit length (p.u.l.) equivalent circuit of the parallel MTL is shown in Fig. 1, where  $dz$  is expressed as an infinitely short transmission line. The entries  $l_{ii}$  and  $l_{jj}$  represent the p.u.l. self-inductances, the entries  $l_{ij}$  and  $l_{ji}$  represent the p.u.l. mutual inductances. The entries  $r_{ii}$  and  $r_{jj}$  represent the p.u.l. resistances. The entries  $c_{ii}$  and  $c_{jj}$  stand for the p.u.l. self-capacitances, the entries  $c_{ij}$  and  $c_{ji}$  stand for the p.u.l. mutual capacitances. The entries  $g_{ij}$  and  $g_{ji}$  denote the p.u.l. conductances. The coupling effect of the MTL can be fully characterized by the model with high precision.

The matrix differential equation of the MTL is [10]:

$$\begin{cases} d\bar{U}(z)/dz = -\mathbf{Z}\bar{I}(z) \\ d\bar{I}(z)/dz = -\mathbf{Y}\bar{U}(z) \end{cases}, \quad (1)$$

$$\begin{cases} \mathbf{Z} = \mathbf{R} + j\omega\mathbf{L} \\ \mathbf{Y} = \mathbf{G} + j\omega\mathbf{C} \end{cases}, \quad (2)$$

where  $\bar{U}(z)$  and  $\bar{I}(z)$  are the voltage and current on the MTL, respectively. The p.u.l. impedance and the p.u.l. admittance matrix are represented by  $\mathbf{Z}$  and  $\mathbf{Y}$ , respectively. The impedance matrix  $\mathbf{Z}$  is composed of the p.u.l. resistance matrix  $\mathbf{R}$  and the p.u.l. inductance matrix  $\mathbf{L}$ . The admittance matrix  $\mathbf{Y}$  is composed of the p.u.l. conductance matrix  $\mathbf{G}$  and the p.u.l. capacitance matrix  $\mathbf{C}$ . The p.u.l. parameter matrix  $\mathbf{R}$ ,  $\mathbf{L}$ ,  $\mathbf{C}$  and  $\mathbf{G}$  are symmetric matrices.

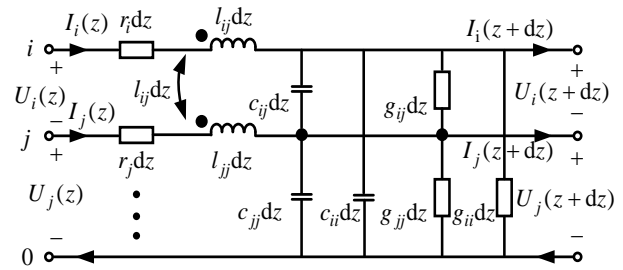


Fig. 1. Single spiral model.

### B. Coplanar irregular-placed cables model based on the theory of cascade transmission line

For the purposes of research, the coplanar irregular placed cables model must satisfy the situation of no twisting or crossing between the wires. Cable differentiated into  $m$  segments is shown in Fig. 2. When  $m$  is large enough, the transmission lines between each segment are considered to be parallel, and each segment of the cable meets the parallel MTL theory.

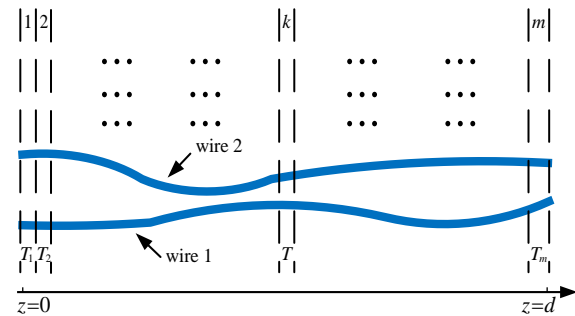


Fig. 2. The differential model of coplanar irregular-placed cables.

Similar to a regular-placed cable, each segment of the coplanar irregular-placed cables has a corresponding coupling matrix formula, and each segment has a parameter matrix  $\mathbf{Z}$ ,  $\mathbf{Y}$ . For the  $k$ -th segment, the equation is:

$$\begin{cases} d\bar{U}(k)/dz = -\mathbf{Z}_k\bar{I}(k) \\ d\bar{I}(k)/dz = -\mathbf{Y}_k\bar{U}(k) \end{cases}, \quad (3)$$

where  $\bar{U}(k)$  and  $\bar{I}(k)$  are the voltage and current on the  $k$ -th segment.  $Z_k$  and  $Y_k$  are the p.u.l. impedance matrix and the p.u.l. admittance matrix on the  $k$ -th segment, respectively.

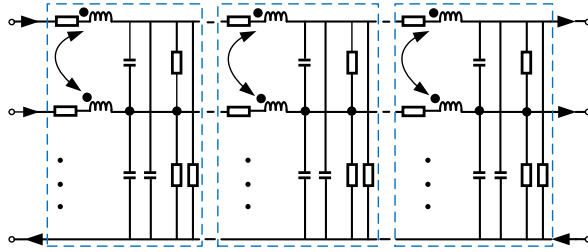


Fig. 3. Coplanar irregular-placed cables equivalent circuit model.

Assuming that the height of the cable is a constant, the equivalent circuit diagram is shown in Fig. 4. Coplanar irregular-placed cables are divided into  $m$  segment ( $m$  is large enough).

For the  $k$ -th segment of the differentiated cable, (3) is also acceptable. (3) is further simplified to:

$$\frac{d}{dz}\bar{F}(k) = T_k \bar{F}(k), \quad (4)$$

$$\text{where } \bar{F}(k) = \begin{bmatrix} \bar{U}(k) \\ \bar{I}(k) \end{bmatrix}, T_k = \begin{bmatrix} 0 & -Z_k \\ -Y_k & 0 \end{bmatrix}.$$

The matrix  $\bar{F}(z)$  on the  $k$ -th segment is left multiplied by  $e^{-T_k z}$  and differentiated by the length  $z$ :

$$\frac{d}{dz} e^{-T_k z} \bar{F}(z) = 0. \quad (5)$$

So the integral at  $[k, k + \Delta z]$  is:

$$\int_k^{k+\Delta z} \frac{d}{dz} e^{-T_k z} \bar{F}(z) = 0. \quad (6)$$

Then,

$$e^{-T_k(\Delta z+k)} \bar{F}(k+\Delta z) - e^{-T_k k} \bar{F}(k) = 0. \quad (7)$$

The solution of the first-order differential equations in the  $k$ -th segment is:

$$\bar{F}(k+\Delta z) = e^{-T_k \Delta z} \bar{F}(k). \quad (8)$$

Since the length of each segment is extremely short and the  $z$  is extremely small after the cable is differentiated, then  $T_k$  can be considered equal to  $T_{k+1}$ , so there is:

$$\bar{F}(d) = e^{-\sum_{i=1}^m T_i} \bar{F}(0) = e^{-\int_0^d T(z) dz} \bar{F}(0). \quad (9)$$

Therefore, the solution of the first-order cable crosstalk can be expressed as:

$$\begin{bmatrix} \bar{V}(d) \\ \bar{I}(d) \end{bmatrix} = \exp \left\{ \int_0^d \begin{bmatrix} 0 & -Z \\ -Y & 0 \end{bmatrix} dz \right\} \begin{bmatrix} \bar{V}(0) \\ \bar{I}(0) \end{bmatrix}. \quad (10)$$

For regular-placed cables, the  $T_k$  of different segments is equal since each segment has the same p.u.l. parameter matrix. The electromagnetic matrix formula can be expressed as:

$$\int_0^d \begin{bmatrix} 0 & -Z \\ -Y & 0 \end{bmatrix} dz = d * \begin{bmatrix} 0 & -Z \\ -Y & 0 \end{bmatrix}. \quad (11)$$

Similar with the electromagnetic matrix formula (11) of the regular cable above, the equivalent electromagnetic matrix  $Z_d$ ,  $Y_d$  and  $T_d$  of coplanar irregular-placed cables can be expressed as:

$$Z_d = \int_0^d Z dz / d, \quad (12)$$

$$Y_d = \int_0^d Y dz / d, \quad (13)$$

$$T_d = \begin{bmatrix} 0 & Z_d \\ Y_d & 0 \end{bmatrix} = \int_0^d \begin{bmatrix} 0 & Z \\ Y & 0 \end{bmatrix} dz / d. \quad (14)$$

It is noteworthy that the integral equation can be solved more accurately when the equivalent electromagnetic matrix  $Z_d$  and  $Y_d$  are calculated by the function method. Therefore, the solution of the crosstalk of coplanar irregular-placed cables can be divided into two steps. The first step is to calculate the equivalent electromagnetic parameter matrix to make coplanar irregular-placed cables equivalent to regular cables. The second step is to predict the crosstalk of coplanar irregular-placed cables by using the method of crosstalk prediction for regular cables under ideal conditions.

### III. COPLANAR IRREGULAR-PLACED CABLES PARAMETER MATRIX AND CROSSTALK INFLUENCING FACTORS

#### A. Calculation of coplanar irregular-placed cables parameter matrix based on cubic spline interpolation

In the crosstalk study of MTL, the resistance and conductance values of the transmission line are usually negligible relative to the terminal load resistance value. The inductance depends on the permeability of the surrounding medium and is independent of the dielectric constant of the medium [10]. In practical applications, the transmission line is usually laid on materials such as aluminum, copper and PCB (usually FR-4) with almost constant magnetic permeability. The inductance parameter matrix  $L$  of the  $n$  cores MTL on the return surface can be expressed as:

$$L = \begin{bmatrix} l_{11} & l_{12} & \cdots & l_{1n} \\ l_{21} & l_{22} & \cdots & l_{2n} \\ \vdots & \vdots & \ddots & \vdots \\ l_{n1} & l_{n2} & \cdots & l_{nn} \end{bmatrix}, \quad (15)$$

$$l_{ii} = \frac{\mu}{2\pi} \ln \left( \frac{2h_i}{r_{wi}} \right), \quad (16)$$

$$l_{ij} = \frac{\mu}{2\pi} \ln \left( 1 + \frac{4h_i h_j}{s_{ij}^2} \right), \quad (17)$$

where  $i$  and  $j$  are positive integer, and  $i, j \in [1, n]$ . The permeability of the medium is represented by  $\mu$ . The heights of the  $i$ -th and  $j$ -th conductors from the ground are represented by  $h_i$  and  $h_j$ , respectively. The distance between the  $i$ -th and  $j$ -th conductor is denoted by  $s_{ij}$ . The radius of the  $i$ -th conductor is indicated by  $r_{wi}$ .

Observing (14), the solution of the equivalent electromagnetic parameter matrix can be transformed into the integral calculation of the electromagnetic parameter matrix.

The inductance parameter matrix is easy to solve its integral in the form of an analytical form, specifically:

$$\mathbf{L}_d = \int_0^d \mathbf{L} dz = j\omega \int_0^d \begin{bmatrix} l_{11} & l_{12} & \cdots & l_{1n} \\ l_{21} & l_{22} & \cdots & l_{2n} \\ \vdots & \vdots & \ddots & \vdots \\ l_{n1} & l_{n2} & \cdots & l_{nn} \end{bmatrix} dz, \quad (18)$$

where  $\mathbf{L}_d$  equivalent inductance matrix.

However, the capacitance parameter matrix  $\mathbf{C}$  is sensitive to the dielectric constant and is difficult to express with an analytical expression. Therefore, it is impossible to directly solve the integral of capacitance matrix  $\mathbf{C}$  of each differential segment by using a function method similar to the inductance matrix, such as (19):

$$\mathbf{C}_d = \int_0^d \mathbf{C} dz = j\omega \int_0^d \begin{bmatrix} c_{11} & c_{12} & \cdots & c_{1n} \\ c_{21} & c_{22} & \cdots & c_{2n} \\ \vdots & \vdots & \ddots & \vdots \\ c_{n1} & c_{n2} & \cdots & c_{nn} \end{bmatrix} dz, \quad (19)$$

where  $\mathbf{C}_d$  is the capacitance matrix.

The capacitance matrix of each differential segment can be solved by ANSYS Q3D based on the finite element method (FEM), but only the equivalent capacitance matrix at some specific points on the coplanar irregular-placed cables can be obtained. Therefore, this paper combines the cubic spline interpolation under the condition of no twist to solve the capacitance matrix integral.

Take the element  $c_{11}$  in the capacitance matrix as an example. The distance from the midpoint of each segment to the starting point is recorded as  $[z_1, z_2, \dots, z_k, z_{k+1}, \dots, z_{m-1}, z_m]$ , and use the FEM method to solve the corresponding  $c_{11}$ . The continuous function  $G(z)$  on parameter  $c_{11}$  is established,  $G(z) = c_{11}(z)$  can be expressed as:

$$G(z) = G_1(z) + G_2(z) + \cdots + G_m(z), \quad (20)$$

$$G_k(z) = a_k z^3 + b_k z^2 + c_k z + d_k, \quad z \in [z_k, z_{k+1}], \quad (21)$$

where  $k$  is a positive integer,  $k \in [0, m]$ . The parameters  $a_k$ ,  $b_k$ ,  $c_k$  and  $d_k$  stand for the coefficients corresponding to the third to zero terms.

Similar to  $c_{11}$ , other elements in the capacitance parameter matrix  $\mathbf{C}$  are treated by this method. The capacitance parameter matrix  $\mathbf{C}$  of the cables can be easily solved by using (19).

## B. Orthogonal experiment on the influencing factors of the crosstalk

As shown in Table 1, the orthogonal experimental method is used to qualitatively compare the main influencing factors of crosstalk (distance between cables, length of cables, the height of cables from ground and the terminal load of cables), and add frequency as the contrast factor. The above factors are divided into four levels, each of which corresponds to different values, in which frequency is divided by its order of magnitude (logarithm).

Table 1: Orthogonal experimental factors

Levels	1	2	3	4
Length/cm	50	100	150	200
Height from the ground/cm	1.25	2.5	3.75	5
Distance between cables/cm	1.25	2.5	3.75	5
Load/ $\Omega$	25	50	75	100
Frequency logarithm	6	7	8	9

The 16 sets of crosstalk under the regular-placed cables model are calculated, and the data obtained are put into the orthogonal table specially used for orthogonal experiment method. The results are shown in Table 2.

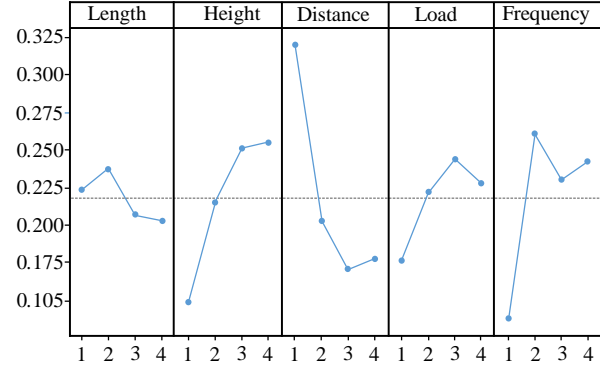


Fig. 3. Main effect diagram of orthogonal experiments.

From the main effect diagram Fig. 4, it can be seen that in the physical condition of the cable in this paper, the distance between cables has the greatest influence on crosstalk, followed by the height, frequency, load, length, etc. Therefore, the sampling points with large distance variation between cables should be selected as much as possible, followed by the height from the ground.

## VI. VERIFICATION AND ANALYSIS

In order to describe the convenience of the new

method, two long straight coplanar irregular-placed cables on the return surface is taken as an example to verify the effectiveness of this method. The relevant parameters of cables are shown in Table 3. The frequency band for solving crosstalk is 1MHz - 1GHz.

Table 2: The orthogonal experiment scheme

No.	Factors					Crosstalk
	Length/ cm	Height/ cm	Distance/ cm	Load/ Ω	Frequency Logarithm	
1	50	1.25	1.25	25	6	-39.834
2	50	2.5	2.5	50	7	-27.416
3	50	3.75	3.75	75	8	-27.871
4	50	5	5	100	9	-27.305
5	100	1.25	2.5	75	9	-31.663
6	100	2.5	1.25	100	8	-20.452
7	100	3.75	5	25	7	-29.243
8	100	5	3.75	50	6	-37.589
9	150	1.25	3.75	100	7	-38.561
10	150	2.5	5	75	6	-44.325
11	150	3.75	1.25	50	9	-19.866
12	150	5	2.5	25	8	-32.028
13	200	1.25	5	50	8	-44.025
14	200	2.5	3.75	25	9	-39.620
15	200	3.75	2.5	100	6	-37.597
16	200	5	1.25	75	7	-17.816

Table 3: Physical parameters of cables

Parameters	Values
Cable diameter	1mm
Thickness of insulation layer	0.65mm
The height from the ground	50mm
Length of harness	1m
Minimum distance between cables	25mm
Maximum distance between conductors	50mm
Relative permittivity of insulation lay	3.5
Relative permeability of conductor	1.0

The important electromagnetic matrices in this paper include the inductance matrix and the capacitance matrix. Since the inductance parameter is independent of the insulation layer, each parameter of the inductance matrix can be calculated according to the (16) and (17). However, the capacitance parameter matrix mentioned in the previous section cannot be directly calculated by the analytical formula.

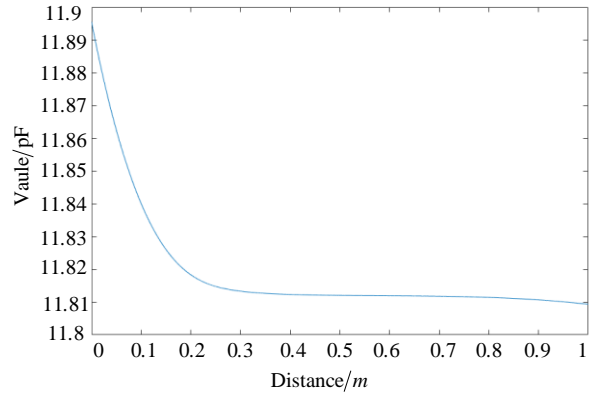


Fig. 5. The self-capacitance ( $c_{11}$  or  $c_{22}$ ).

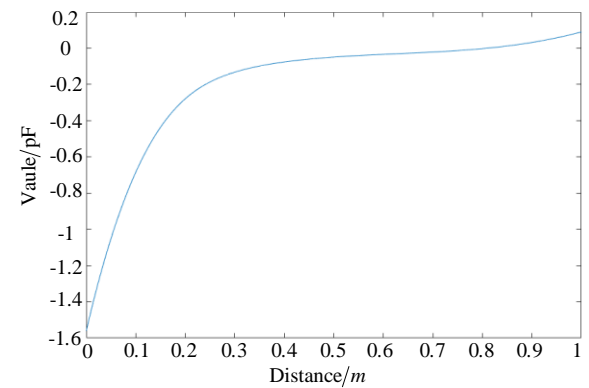


Fig. 6. The mutual capacitance ( $c_{12}$  or  $c_{21}$ ).

The processing of the capacitance parameter matrix is as follows. Firstly, the FEM method is used to solve the capacitance matrix  $C$  of different transmission line distance, and the solution points are 50 points of equal distance on the transmission line. Then, the self-capacitance elements  $c_{11}$  and  $c_{22}$  and the mutual capacitance elements  $c_{12}$  and  $c_{21}$  in the capacitance matrix are fitted by cubic spline interpolation method. The fitting results are shown in Fig. 5 and Fig. 6. Among them, the physical parameters of the cables are the same, so  $c_{11}=c_{22}$ . And the parameter matrix  $C$  is a symmetric matrix, so  $c_{12}=c_{21}$ .

The calculated equivalent inductance matrix  $L_d$  and the capacitance matrix  $C_d$  based on the electromagnetic parameters of all sampling points are:

$$L_d = \begin{bmatrix} 1059.7 & 25.138 \\ 25.138 & 1059.7 \end{bmatrix} nH \quad C_d = \begin{bmatrix} 11.813 & -0.098 \\ -0.098 & 11.813 \end{bmatrix} pF \quad (22)$$

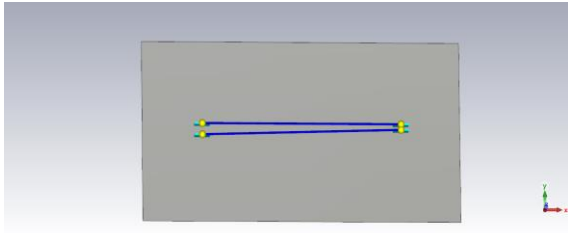


Fig. 7. CST model of coplanar irregular-placed cables.

The full wave simulation of the CST Cable Studio<sup>®</sup> commercial software - the transmission line matrix (TLM) method, an electromagnetic field numerical method based on the Huygens wave propagation model, is used to solve the crosstalk results as a reference standard in this paper. The simulation model of CST are shown in Fig. 7.

In order to verify the effectiveness of the algorithm, the experimental bench is set as shown in Fig. 8 and Fig. 9. The experimental equipment mainly includes R&S ZVL3 Vector Network Analyzer (VNA), a return plane of a tin-plated copper sheet and two boards for fixing wires.



Fig. 8. Photo of experiment.

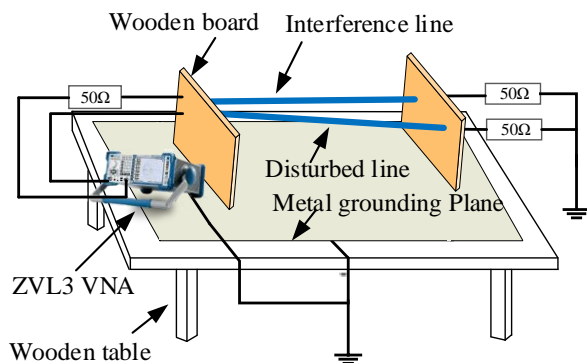


Fig. 9. Experimental configuration diagram.

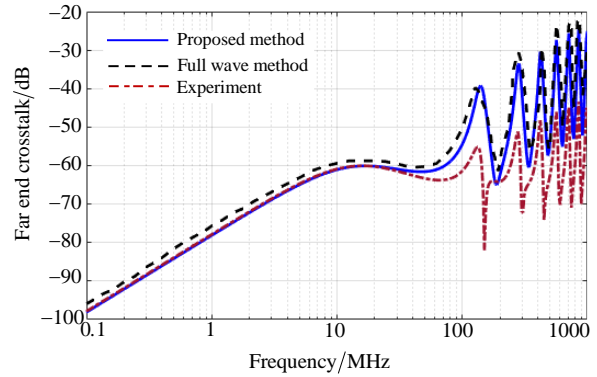


Fig. 10. Far end crosstalk of coplanar irregular-placed cables.

The crosstalk results solved by different methods are shown in Fig. 10. The error of some frequency points are shown in Table 4. In the frequency band of 0.1 MHz - 30 MHz, the error between the new method and the experimental results is much smaller than the error between the full wave method and the experimental results. The maximum error between the new method and the experiment is -0.58dB. In the frequency band of 30 MHz - 100 MHz, the error of the new method is larger than the error of the new method in the low frequency band, but the result of the new method still has higher precision than the full wave method. In the frequency band of 100 MHz - 1000 MHz, the new method and the full wave method are consistent with the trend of the experimental results, but the error is significantly increased. In conclusion, the new method has a higher accuracy for the far end cross of coplanar irregular-placed cables, especially in the low frequency range.

Table 4: Error solving by different methods

Frequency/ MHz	Experiment	Full Wave Method		Proposed Method	
	Value/dB	Value/dB	Error/dB	Value/dB	Error/dB
0.1	-97.53	-95.91	-1.62	-96.95	-0.58
1	-77.95	-75.46	-2.49	-77.81	-0.14
10	-60.84	-59.43	-1.41	-60.54	-0.30
100	-61.76	-50.20	-11.56	-54.85	-6.91
1000	-45.10	-28.41	-16.69	-28.34	16.76

In the high frequency band, the error accuracy of the new method and the full wave method is significantly increased because of the non-ideality of the experimental conditions, such as the transmission line (the transmission line may not be completely coplanar due to gravity), the terminal resistance, VNA. Although each factor alone has little effect on the value of the far



end crosstalk, the effect of all factors on the actual crosstalk cannot be neglected.

## V. CONCLUSION

A new method for predicting crosstalk of coplanar irregular-placed cables is presented in this paper. The crosstalk prediction method of coplanar irregular-placed cables based on the theory of cascade transmission line and the cubic spline interpolation algorithm is studied with the research method of regular-placed cables as a reference. And the orthogonal experiment method is used to compare and analyze the factors affecting the crosstalk of the transmission line. The analysis results show that the distance between the transmission lines has the greatest influence on crosstalk, followed by the height from the current return plane, frequency, load, length. In this paper, the far end crosstalk of coplanar irregular-placed cables is verified and analyzed by the new method, full wave method and experiment. Compared with the full wave method, the new method has better solution accuracy. Specifically, the maximum errors between the new method and experiment are -0.58 dB and -6.91 dB in the frequency band of 0.1 MHz - 30 MHz and 30 MHz - 100 MHz, respectively.

## ACKNOWLEDGMENT

This work was supported by the National Natural Science Foundation of China under Grant 51475246; National Natural Science Foundation of Jiangsu Province under Grant BK20161019; and Aviation Science Foundation under Grant 20172552017. The paper is supported by the Aviation Science Foundation under Grant 20172552017; Key Project of Social Development in Jiangsu Province under Grant BE2019716; and Nanjing International Industrial Technology R&D Cooperation Project under Grant 201911.

## REFERENCES

- [1] C. Stagner, D. G. Beetner, and S. L. Grant, "A comparison of algorithms for detecting synchronous digital devices using their unintended electromagnetic emissions," *IEEE Trans. Electromagn. Compat.*, vol. 56, no. 6, pp. 1304-1312, Dec. 2014.
- [2] C. R. Paul, *Introduction to Electromagnetic Compatibility (EMC)*. New York, USA: John Wiley & Sons, 2006.
- [3] F. M. Tesche, "On the analysis of a transmission line with nonlinear terminations using the time dependent BLT equation," *IEEE Trans. Electromagn. Compat.*, vol. 49, no. 2, pp. 427-433, May 2007.
- [4] F. M. Tesche, "Development and use of the BLT equation in the time domain as applied to a coaxial cable," *IEEE Trans. Electromagn. Compat.*, vol. 49, no. 1, pp. 3-11, Feb. 2007.
- [5] C. Taylor, R. Satterwhite, and C. Harrison, "The response of a terminated two-wire transmission line excited by a nonuniform electromagnetic field," *IEEE Trans. Antennas. Propagation*, vol. 13, no. 6, pp. 987-989, Nov. 1965.
- [6] M. Jensen and Y. Rahmat Samii, "Performance analysis of antennas for hand-held transceivers using FDTD," *IEEE Trans. Antennas. Propagation*, vol. 42, no. 8, pp. 1106-1113, Aug. 1994.
- [7] L. Dou and J. Dou, "Sensitivity analysis of lossy non-uniform multiconductor transmission lines based on the Lax-Wendroff technique," *IEEE Trans. Advanced Packaging.*, vol. 33, no. 2, pp. 492-497, May 2010.
- [8] S. Ohtsu, K. Nagase, and T. Yamagajou, "Analysis of radiation caused by LSI package crosstalk and cable by using the time-domain moment method," *IEEE EMC Europe Symp.*, Minneapolis, USA, pp. 268-272, Nov. 2002.
- [9] L. L. Liu, Z. Li, and J. Yan, "Simplification method for modeling crosstalk of multicoaxial cable bundles," *Progress in Electromagnetics Research-Pier*, 135, pp. 281-296, 2013.
- [10] C. R. Paul, *Analysis of Multiconductor Transmission Lines*. (2nd ed), New York, USA: John Wiley & Sons, 1994.
- [11] Y. X. Sun, Q. H. Jiang, W. H. Yu, Q. K. Zhuo, and Q. Li, "Approximation through common and differential modes for twist wire pair crosstalk model," *Applied Computational Electromagnetics Society Journal*, vol. 29, no. 12, pp. 1124-1132, Dec. 2014.
- [12] M. Shiota, M. Itsumi, A. Takeuchi, K. Imada, A. Yokomizo, and H. Kuruma, "Crosstalk between epithelial-mesenchymal transition and castration resistance mediated by twist1/AR signaling in prostate cancer," *The Journal of Urology*, vol. 195, no. 4, pp. 820-821, Apr. 2015.
- [13] D. Bellan and S. A. Pignari, "Efficient estimation of crosstalk statistics in random wire bundles with lacing cords," *IEEE Trans. Electromagn. Compat.*, vol. 53, no. 1, pp. 209-218, Feb. 2011.
- [14] F. A. Smit, R. V. Liere, and B. Froehlich, "Non-uniform crosstalk reduction for dynamic scenes," *IEEE Virtual Reality Conference*, Charlotte, USA, pp. 4433-4445, Mar. 2007.
- [15] Z. Li, L. L. Liu, J. Ding, M. H. Cao, and Z. Y. Niu, "A new simplification scheme for crosstalk prediction of complex cable bundles within a cylindrical cavity," *IEEE Trans. Electromagn. Compat.*, vol. 54, no. 4, pp. 940-943, Aug. 2012.
- [16] G. Andrieu, A. Reineix, X. Bunlon, J. P. Parmantier, and D. Bernard, "Extension of the "equivalent cable bundle method" for modeling electromagnetic emissions of complex cable bundles," *IEEE Trans. Electromagn. Compat.*, vol. 51, no. 1, pp. 108-118, Feb. 2009.
- [17] S. Venuturumilli, F. Berg, L. Prisse, M. Zhang, and

- W. Yuan, "DC line to line short-circuit fault management in a turbo-electric aircraft propulsion system using superconducting devices," *IEEE Trans. Applied. Superconductivity*, vol. 29, no. 5, pp. 1-6, Aug. 2019.
- [18] A. Sano, H. Takara, T. Kobayashi, and Y. Miyamoto, "Crosstalk-managed high capacity long haul multicore fiber transmission with propagation-direction interleaving," *Journal of Lightwave Technology*, vol. 32, no. 16, pp. 2771-2779, Aug. 2014.
- [19] C. Jullien, P. Besnier, M. Dunand, and I. Junqua, "Crosstalk analysis in complex aeronautical bundle," in *IEEE. EMC Symp.*, Brugge, Belgium, pp. 253-258, Sep. 2013.
- [20] X. D. He, Y. H. Wen, J. B. Zhang, and L. S. Feng, "Analysis of crosstalk between cables on board in high speed EMUs," *IEEE 6th International Symposium on Microwave, Antenna, Propagation, and EMC Technologies (MAPE)*, Shanghai, China, pp. 454-457, Oct. 2016.
- [21] F. Dai, G. Bao, and D. L. Su, "Crosstalk prediction in non-uniform cable bundles based on neural network," *IEEE Proceedings of the 9th International Symposium on Antennas, Propagation and EM Theory*, Guangzhou, China, pp. 1043-1046, Dec. 2010.
- [22] W. Lee, G. Heo, and K. You, "Neural network compensation for frequency crosstalk in laser interferometry," *Ieice Transactions on Fundamentals of Electronics Communications & Computer Sciences*, 92, pp. 681-684, 2009.

# W-band Electronic Focus-Scanning by a Reconfigurable Transmitarray for Millimeter-Wave Imaging Applications

Xiaotian Pan, Fan Yang, Shenheng Xu, and Maokun Li

Department of Electrical Engineering  
Tsinghua University, Beijing, 100084, China  
fan\_yang@tsinghua.edu.cn

**Abstract**— A w-band electronic focus-scanning function, which is desired for high-resolution fast-speed millimeter-wave imaging systems, is realized by a reconfigurable transmitarray antenna (RTA). As a two-layer structure, each RTA element is integrated with two packaged PIN diodes symmetrically within a limited area ( $1.6 \times 1.6 \text{ mm}^2$ ). When a linearly polarized electromagnetic wave incidents on this reconfigurable element, an orthogonally polarized transmission wave is generated, with the ability of 1-bit phase adjustment ( $0^\circ/180^\circ$ ). Using this element, a  $32 \times 2$  reconfigurable transmitarray is designed and fabricated to realize 1-D steerable focal points in a near-distance focal plane. The measured focal points agree well with the design, illustrating the feasibility of the proposed RTA for w-band microwave imaging systems.

**Index Terms** — Antennas, PIN diode, reconfigurable, transmitarray, W-band.

## I. INTRODUCTION

W-band microwave imaging systems have advantages of good penetrability and high resolution, especially suitable for applications of security checking [1]. For this type of near-distance imaging applications, the image resolution and scanning rate are two important objectives. As a core component, a high-performance low-cost w-band electronically-scanning antenna remains challenging [2].

By integrating electrically tunable components into transmitarray element, steerable beams are realized by RTAs [3]. The low-cost and low-profile features of RTAs make these antennas promising alternatives for conventional phased arrays. At w band, liquid crystal (LC) and micro electro mechanical system (MEMS) have been applied in reconfigurable antennas [4-5]. However, the switching time, material loss, and complicated fabrication process are still concerns. Meanwhile, PIN diode [6], as a common electrical component, has been applied for RTAs in Ka band [7-8], and shows promising potential in higher frequency band. Furthermore, the switching time at nanosecond

level of PIN diode guarantees fast beam-switching speed, especially suitable for high-speed imaging applications.

In this work, a 1-D PIN-controlled RTA is designed for focus scanning at 96.5GHz. A two-layer RTA element with switchable resonance structure integrated with two packaged PIN diodes is proposed to realize a  $180^\circ$  phase shift. This symmetrical structure can generate an orthogonally polarized transmission wave with 1-bit phase shift precisely, overcoming the adverse effects from uncertain parasitic parameters of PIN diode and fabrication error of PCB at such high frequency band. A  $32 \times 2$  RTA prototype has been fabricated for steerable focal points at near distance. Measured focal points match well with calculated results. This antenna shows a low-cost solution for microwave imaging systems with high-resolution and high scanning rate.

## II. ANTENNA DESCRIPTION

The antenna consists of three parts: an open-end waveguide (WR10), a parallel-plate waveguide, and a 1-D arrays of two-row RTA elements, as shown in Fig. 1. The waveguides support an incident y-polarization wave. Each element receives the incident wave, changes the phase, and then radiates for the x-polarized scanning focuses. The phase of the transmitted wave can be adjusted to be  $0^\circ$  or  $180^\circ$  electronically by the RTA. The element design and the phase distribution for the focus scanning are presented in this section in detail.

### A. Element design and working principle

Traditional RTA elements usually have three or more layers to achieve enough reconfigurability of transmission phase [7]. However, these designs require accurate alignment during assembling layers, which is challenging at w band. To solve this problem, a novel RTA element is designed as a two-layer structure that can be directly printed on opposite sides of one substrate, as shown in Fig. 2. Being a coupling layer, the first layer of the element is a rectangular slot. This layer couples a y-polarized incident electromagnetic wave to a U-shaped

microstrip resonance structure on the second layer. Two PIN diodes are integrated on the U-shaped microstrip line for reconfigurability.

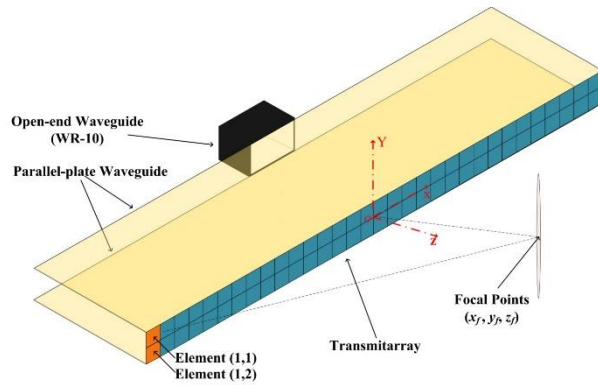


Fig. 1. W-band transmitarray design with 1-D steerable focal points.

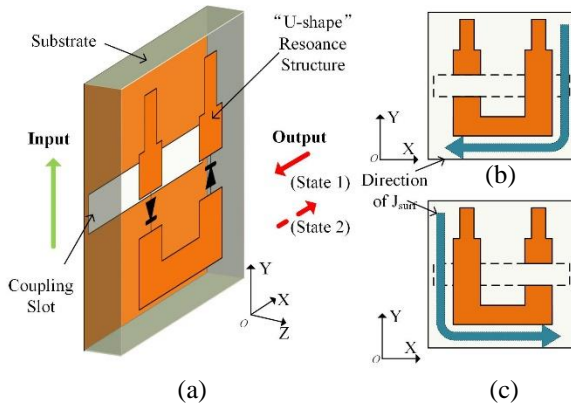


Fig. 2. Schematic and operation principle of the RTA element: (a) Geometry of element; (b) Ideal case 1; (c) Ideal case 2.

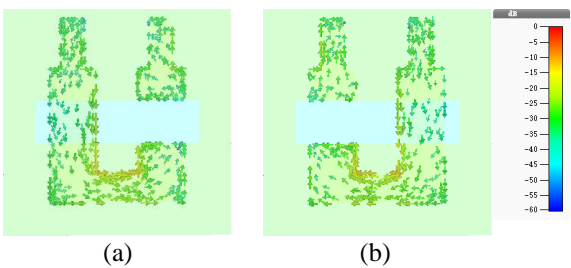


Fig. 3. Current distributions on the ideal element under two states: (a) State 1 and (b) State 2.

At state 1, the left PIN diode is at “ON” condition, and the right one is at “OFF” condition. For state 2, working conditions of two PIN diodes are opposite to

state 1. Under different states of PIN diodes, one side of the U-shaped structure is cut off. Two ideal cases can be used to illustrate working principle of the RTA element. Current distributions of the element under two states are shown as Fig. 3. Two symmetrical L-shaped resonance structures are formed, and generate symmetrically surface current  $J_{surf}$  on the resonators. The element will produce output waves with both y-polarization and x-polarization. It is worthy to mention that, when the states of PIN diodes change, the y-polarized wave remains the same, but the x-polarized wave has an  $180^\circ$  phase difference due to the opposite current direction as shown before. Hence, the x-polarized wave with the phase tuning capability is used for focusing and scanning in this paper, and the y-polarized wave cannot. The transmission coefficients  $T_{xy}$  for the x-polarized output wave under two cases follow the equation as below:

$$\arg(T_{xy})|_{\text{State 2}} - \arg(T_{xy})|_{\text{State 1}} = \pi. \quad (1)$$

## B. Element simulation and optimization

The element is designed on Rogers 5880 dielectric substrate with the thickness of  $h_p=0.508\text{mm}$ ,  $\epsilon_r=2.2$  and  $\tan\delta=0.0009$ . The period of the element is  $p_c=1.6\text{mm}$ . A mm-wave PIN diode (MA4AGFCP910) is chosen as the w-band switch component because of its highest cut-off frequency compared with other commercially available PIN diodes [9]. The bias structure is designed for supplying controlling voltages for these PIN diodes, as shown in Fig. 4. Electromagnetic simulation software CST is used to analyze these elements by setting periodic boundary conditions. Series RLC model is used to describe the RF impedance characteristic of PIN diode [10]. In CST, the series RLC model of PIN diode is set according to the online datasheet:  $R_{on}=4\Omega$ ,  $L_{on}=10\text{pH}$ ;  $R_{off}=3\Omega$ ,  $L_{off}=10\text{pH}$ ,  $C_{off}=18\text{fF}$ .

In order to acquire the optimum magnitude of  $T_{xy}$  at working frequency, parameters of the element are studied through EM simulations. For the receiving layer, the working frequency decreases with the increasing length of  $s_x$ , which mainly affects the working mode of the slot, as shown in Fig. 5. For the second layer, the effective current path of the working mode increases with the lengths of both the x-direction part and the y-direction part in the L-shaped resonance structures. As a result, the working frequency is expected to decrease with larger sizes:  $g_x$ ,  $b_u$ , as shown in Figs. 6 & 7. Other parameters of the L-shaped structure are defined by the standard sizes of soldering pad for the PIN diode [9]. After optimizing these antenna parameters through EM simulations, a practical 1-bit RTA at w band is achieved. Detailed sizes of the RTA element are shown in the caption of Fig. 4, as well as the biasing structure.

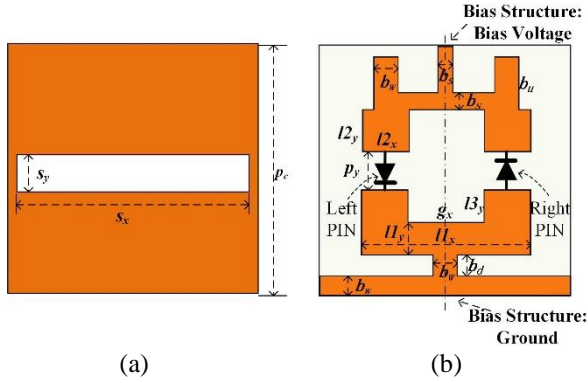


Fig. 4. Detailed sizes of RTA element with a bias structure: (a) first layer of the reconfigurable element; (b) second layer of the reconfigurable element. ( $s_x=1.15$ ,  $s_y=0.3$ ,  $b_w=0.15$ ,  $b_u=0.35$ ,  $b_s=0.1$ ,  $p_y=0.33$ ,  $b_w=0.15$ ,  $b_u=0.135$ ,  $b_x=0.185$ ,  $l1_x=0.93$ ,  $l1_y=0.2$ ,  $l2_x=0.31$ ,  $l2_y=0.2$ ,  $l3_y=0.2$ ,  $g_x=0.31$ . Unit: mm).

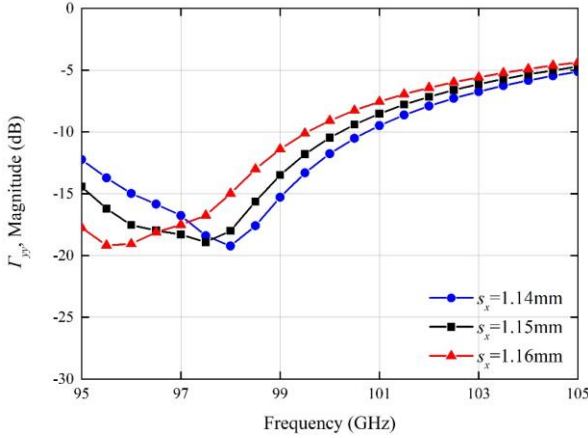


Fig. 5. Magnitude of  $\Gamma_{yy}$  versus different values of  $s_x$ .

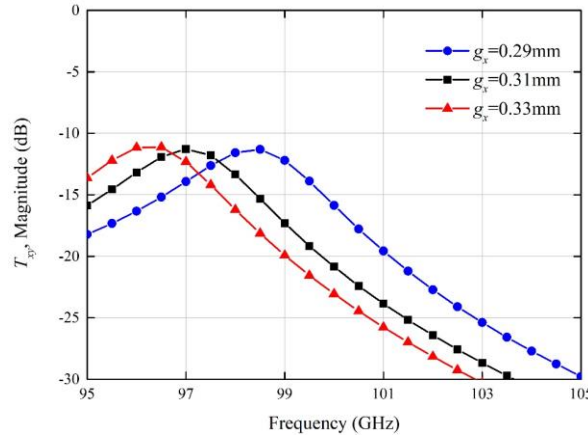


Fig. 6. Magnitude of  $T_{xy}$  versus different values of  $g_x$ .

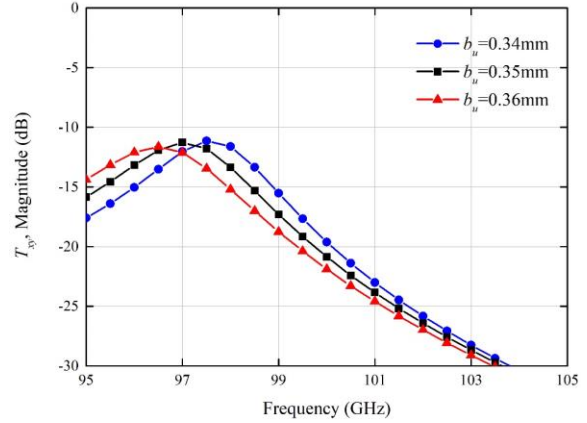


Fig. 7. Magnitude of  $T_{xy}$  versus different values of  $b_u$ .

The transmission phases of the ideal case and the practical PIN case are different due to the practical diode model and the existence of the biasing circuit. However, the phase difference between states 1 & 2 remains to be  $180^\circ$  due to the symmetrical element design, as shown in Figs. 8 & 9. Hence, the proposed element can guarantee the precise  $180^\circ$  phase shift, regardless of the PIN model and the biasing effect.

In contrast, the magnitude of transmission coefficient  $T_{xy}$  of the RTA element is dependent on the PIN model. For the ideal case, the maximum of  $T_{xy}$  is  $-3.1\text{dB}$  at  $101.5\text{GHz}$ , as shown in Fig. 10. Meanwhile, the corresponding  $T_{yy}$  value is  $-3.5\text{dB}$ , which shows that the proposed element converts more energy into the cross-polarized wave than that in the co-polarized wave. For the practical PIN model, the maximum of  $T_{xy}$  is  $-11.1\text{dB}$  at  $97\text{GHz}$ . The distinct difference between the two models is the value of  $C_{off}$ , which controls the polarization conversion efficiency ( $T_{xy}$ ) of the antenna. To study influence of the capacitance  $C_{off}$ , different reconfigurable elements with the increasing value of capacitance  $C_{off}$ , have been simulated. Magnitudes of the simulated transmission coefficients of RTA element, are shown in Fig. 11. As a result, with the value of  $C_{off}$  decreasing, magnitude of the transmission coefficient  $T_{xy}$  increases, leading to a better element performance.

Another reason is the biasing circuit effect. In the ideal design, high-impedance microstrip lines with large resistance value are needed to reduce the influence of outer biasing structure [11]. However, limited by the PCB fabrication technology (minimum width of the bias line is  $0.1\text{mm}$ ), the width of the biasing line is close to that of the resonance structure, and does affect the performance of the RTA element. After adding the biasing structure, the new shape is more like a split-ring resonator. The parameters are optimized to get an acceptable polarization conversion efficiency.

In summary, the proposed RTA element has a relatively large insertion loss due to the limitations of available PIN diode (large  $C_{off}$  value) and fabrication process (0.1 mm line width). However, it is worth noting that precise 1-bit phase shift can be guaranteed even under these two adverse effects, which is critical for high-resolution applications.

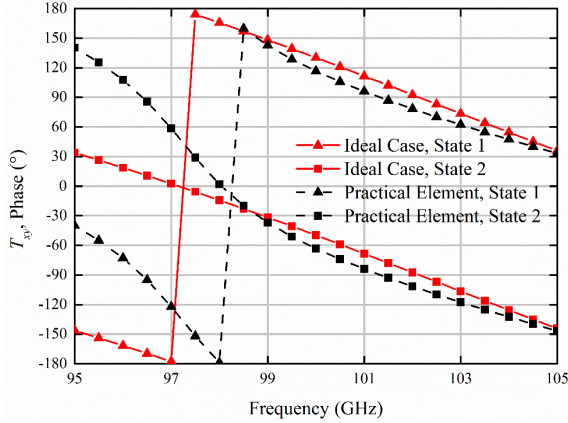


Fig. 8. Simulated results of  $T_{xy}$  phase under different element models.

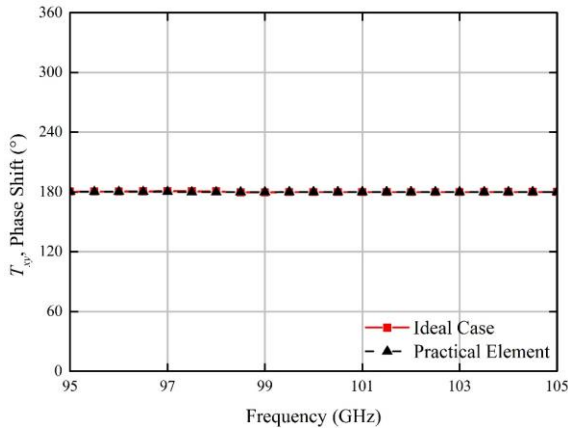


Fig. 9. Simulated results of phase shift under different element models.

### C. Transmitarray with 1-D steerable focal points

1-D steerable focal points on a focal plane can be used for near-field imaging system. A  $32 \times 2$  reconfigurable transmitarray antenna (RTA) is designed for this purpose. An open-end waveguide generates the electromagnetic wave of  $TE_{10}$  mode and radiates it to the RTA located at the end of a parallel-plate waveguide, as shown in Fig. 1. The length of the parallel-plate waveguide along z-direction is 27.5mm. Incident phase distribution and magnitude distribution on the RTA aperture are measured. The measured illumination taper

at the edge of the array is -11.9dB.

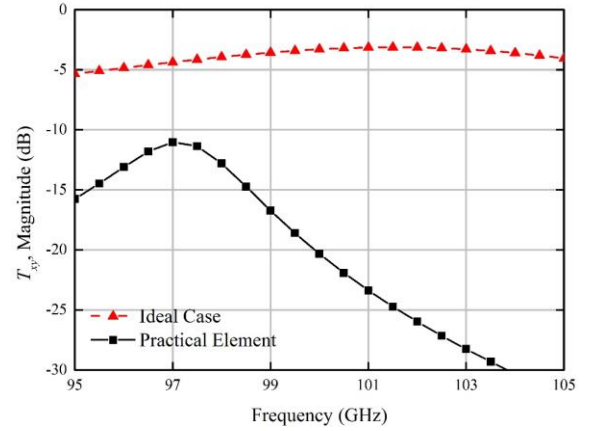


Fig. 10. Simulated results of  $T_{xy}$  magnitude under different element models.

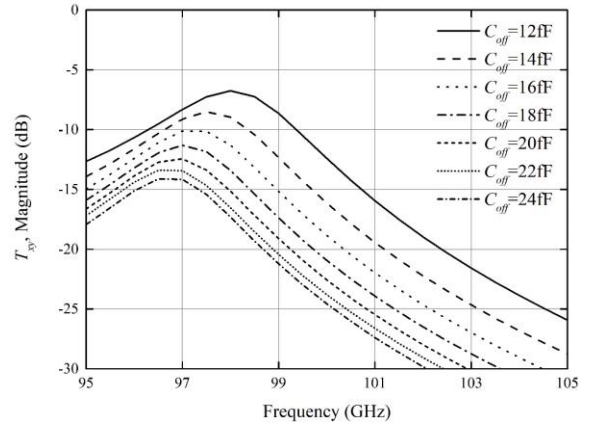


Fig. 11. Magnitude of  $T_{xy}$  versus different values of capacitances  $C_{off}$ . (The other parameters are defined as the commercially available PIN diode, MA4AGFCP910.)

The output equal phase point is designed at the focal point  $(x_f, y_f, z_f)$ . The transmitarray is designed to provide phase compensation, which includes two parts: the incident phase of the illumination wave, and the phase delay from each element to the focal point. Thus, the phase distribution of each element can be calculated according to the equations below:

$$\varphi_{element}(m, n) = -\varphi_{inc}(m, n) + kr_{fmn} + \Delta\varphi, \quad (2)$$

$$r_{fmn} = \sqrt{(x_f - x_{mn})^2 + (y_f - y_{mn})^2 + (z_f - z_{mn})^2}. \quad (3)$$

where  $\varphi_{inc}$  is the measured phase distribution of incident wave, and  $r_{fmn}$  is the distance from each element  $(x_{mn}, y_{mn}, z_{mn})$  to the focal point. In these equations,  $m$  is chosen as 1, 2, ..., 32, and  $n$  is chosen as 1, 2. For the 1-bit reconfigurable transmitarray, each element generates only two phase states,  $0^\circ$  and  $180^\circ$ . Hence, a phase

quantization process is applied after Eq. (2). Figure 12 shows the compensated phase distributions for two focal points:  $(x_f=0\text{mm}, y_f=0\text{mm}, z_f=80\text{mm})$  and  $(x_f=-30\text{mm}, y_f=0\text{mm}, z_f=80\text{mm})$ .

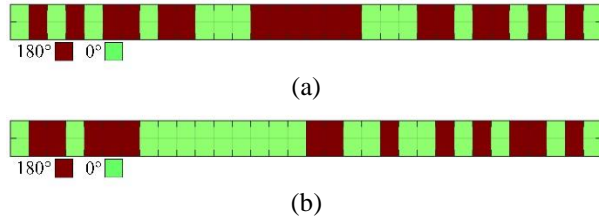


Fig. 12. Phase distribution for the reconfigurable transmitarray: (a)  $x_f=0\text{mm}, y_f=0\text{mm}, z_f=80\text{mm}$ ; (b)  $x_f=-30\text{mm}, y_f=0\text{mm}, z_f=80\text{mm}$ .

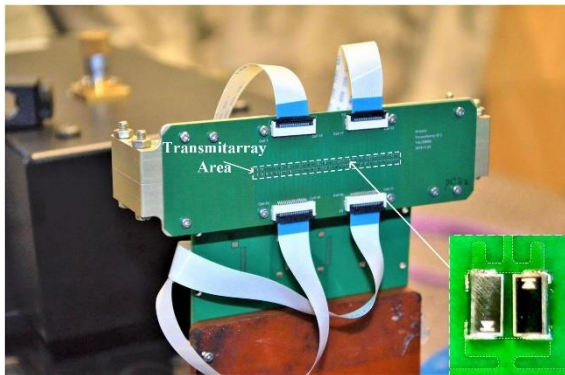


Fig. 13. Prototype of the w-band focus-scanning antenna.

### III. EXPERIMENT AND DISCUSSION

A prototype of the 1-bit transmitarray has been fabricated. Prototype of the antenna is shown in Fig. 13. Size of the total antenna structure is  $110 \times 34\text{mm}^2$ , containing the total transmitarray of  $51.2 \times 3.2\text{mm}^2$  in the middle. The front layer of arrays, including resonance structures and bias structures, are all printed in the rectangular area. It should be noted that the upper elements and the lower elements are inverted in  $y$ -direction for the purpose of easy biasing. Polarity of the diodes are also symmetrically inverted for these two kinds of elements. Thus, ground lines are all combined. The upper bias voltages and lower bias voltages are inverted to generate the same state for upper and lower elements. The bias lines are extended to 4 connectors with 20 pins at upper and lower edges of the transmitarray, and finally connected to a control board and power supply. At the back layer, the transmitarray is also covered by printed metal, except the rectangular slots as designed.

A w-band probe connected with a VDI frequency converter, which is installed on a scanner, is used to

measure XY-plane field distribution at the position of focal points at 96.5GHz. Area of the 2-D plane is  $174 \times 174\text{mm}^2$ . Measured result of the focal point at broadside is shown in Fig. 14. Detailed comparison of measured result and calculated result along the  $x$ -axis is shown in Fig. 15. The measured half power beam width (HPBW) along  $x$ -direction is 6mm, compared to the calculated results of 6mm.

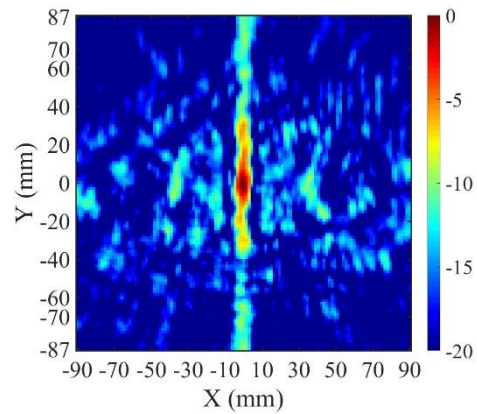


Fig. 14. Measured 2-D result of focal point at  $x_f=0\text{mm}, y_f=0\text{mm}, z_f=80\text{mm}$ . (Unit: dB).

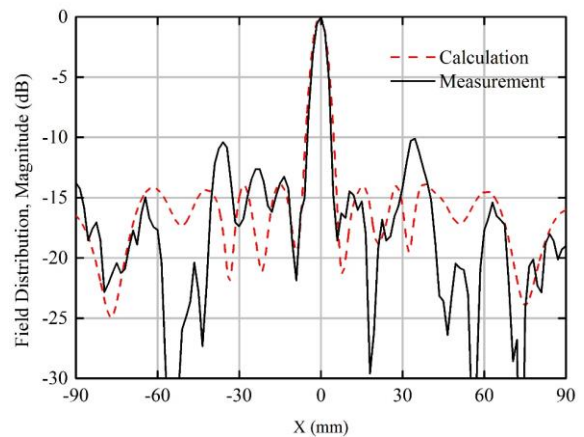


Fig. 15. Comparison between the measured result and the calculated result along  $x$ -direction for the focal point at  $x_f=0\text{mm}, y_f=0\text{mm}, z_f=80\text{mm}$ .

1-D steered focal points of the reconfigurable transmitarray along  $x$ -direction are also measured. Figure 16 shows measured steered focal points from  $x_f=0\text{mm}$  to  $x_f=-30\text{mm}$ . The location of measured focal plane keeps the same at  $z_f=80\text{mm}$ . Measured results of focal points also show that steered focal points keep stable. The location of measured focal point keeps in accordance with the design from  $x_f=0\text{mm}$  to  $x_f=-30\text{mm}$ . The half power beam width keeps under 6mm, which is

in accordance with the calculated result. This small HPBW shows promising applications for high-resolution imaging applications.

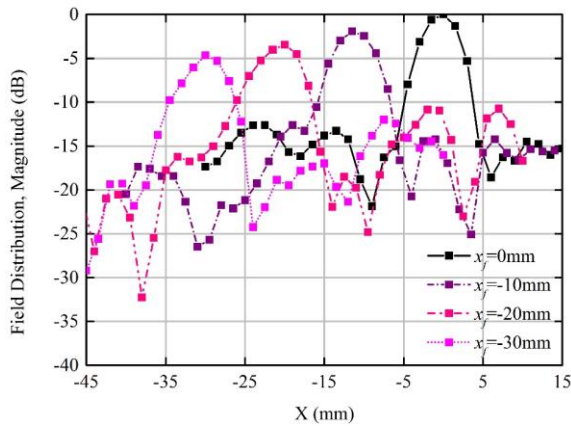


Fig. 16. Magnitude distribution for the 1-D steered focal points along x-direction.

#### IV. CONCLUSION

A w-band focus-scanning method based on PIN-diode RTA is proposed. The 1-bit phase accommodation is designed for scanning focal points. Based on PIN diode, the beam switching can be conducted in a very short time. Under the switchable states of two PIN diodes, a two-layer symmetrically resonance structure is formed. This design can generate the x-polarization output waves with opposite directions, and guarantee the precise phase shift of  $180^\circ$ . A transmitarray with  $32 \times 2$  elements is finally fabricated for verification of steerable focal points. Measured results show good agreement with the calculated results. Scanning focal points at x-direction are also measured, which verify the functionality of the RTA design. The proposed method shows notable advantages in weight, size and cost. These features make this antenna suitable for w-band high-resolution fast-speed imaging applications, especially for security checking.

#### REFERENCES

- [1] R. Appleby, "The history of passive millimetre-wave imaging at QinetiQ," in *Proc. of SPIE*, vol. 7117, p. 711702, 2008.
- [2] D. M. Sheen, D. L. McMakin, and T. E. Hall, "Combined illumination cylindrical millimeter-wave imaging technique for concealed weapon detection," in *Proc. AeroSense*, pp. 52-60, 2000.
- [3] S. V. Hum and J. Perruisseau-Carrier, "Reconfigurable reflectarrays and array lenses for dynamic antenna beam control: A review," *IEEE*

*Trans. Antennas Propag.*, vol. 62, no. 1, pp. 183-198, 2014.

- [4] G. Perez-Palomino, P. Baine, R. Dickie, M. Bain, J. A. Encinar, R. Cahill, M. Barba, and G. Toso, "Design and experimental validation of liquid crystal-based reconfigurable reflectarray elements with improved bandwidth in F-band," *IEEE Trans. Antennas Propag.*, vol. 61, no. 4, pp. 1704-1713, 2013.
- [5] S. Montori, E. Chiuppesi, P. Farinelli, L. Marcaccioli, R. V. Gatti, and R. Sorrentino, "W-band beam-steerable MEMS-based reflectarray," *Int. J. Microw. Wireless Tech.*, vol. 3, no. 5, pp. 521-532, 2011.
- [6] N. Ojaroudi, Y. Ojaroudi, S. Ojaroudi, Y. Ebazadeh, and M. Shirgir, "Small reconfigurable monopole antenna integrated with PIN diodes for multimode wireless communications," *Applied Computational Electromagnetics Society (ACES) Journal*, vol. 29, no. 7, pp. 541-546, 2014.
- [7] M. Wang, S. Xu, F. Yang, and M. Li, "Design and measurement of a 1-bit reconfigurable transmitarray with subwavelength H-shaped coupling slot elements," *IEEE Trans. Antennas Propag.*, vol. 67, no. 5, pp. 3500-3504, 2019.
- [8] L. Di Palma, A. Clemente, L. Dussopt, R. Sauleau, P. Potier, and P. Pouliguen, "1-Bit reconfigurable unit cell for Ka-band transmitarrays," *IEEE Antennas Wireless Propag. Lett.*, vol. 15, pp. 560-563, 2016.
- [9] <https://www.macom.com/products/product-detail/MA4AGFCP910>.
- [10] X. Pan, F. Yang, S. Xu, and M. Li, "Mode analysis of 1-Bit reflectarray element using p-i-n diode at W-band," in *IEEE Int. Symp. Antennas Propag. Soc.*, San Diego, U.S., pp. 2055-2056, 2017.
- [11] A. Khidre, F. Yang, and A. Z. Elsherbeni, "Reconfigurable microstrip antenna with tunable radiation beamwidth," in *IEEE Int. Symp. Antennas Propag. Soc.*, Florida, U.S., pp. 1444-1445, 2013.



**Xiaotian Pan** received the B.S. degree from Zhengzhou University in 2013, and the M.S. degree from Beihang University in 2016. He is currently pursuing the Ph.D. degree with the Department of Electronic Engineering in Tsinghua University. His current research interests include reconfigurable reflectarray, reconfigurable transmitarray, and the imaging applications.





**Fan Yang** (Fellow, IEEE) received the B.S. and M.S. degrees from Tsinghua University, Beijing, China, in 1997 and 1999, respectively, and the Ph.D. degree from the University of California at Los Angeles (UCLA) in 2002. From 1994 to 1999, he was a Research Assistant at the State Key Laboratory of Microwave and Digital Communications, Tsinghua University. From 1999 to 2002, he was a Graduate Student Researcher at the Antenna Laboratory, UCLA. From 2002 to 2004, he was a Post-Doctoral Research Engineer and Instructor at the Electrical Engineering Department, UCLA. In 2004, he joined the Electrical Engineering Department, The University of Mississippi, as an Assistant Professor, and was promoted to the post of an Associate Professor in 2009. In 2011, he joined the Electronic Engineering Department, Tsinghua University, as a Professor, and has served as the Director of the Microwave and Antenna Institute since then.

His research interests include antennas, surface

electromagnetics, computational electromagnetics, and applied electromagnetic systems. He has published over 300 journal articles and conference papers, six book chapters, and five books. Yang is a fellow of the ACES. He has been a recipient of several prestigious awards and recognitions, including the Young Scientist Award of the 2005 URSI General Assembly and of the 2007 International Symposium on Electromagnetic Theory, the 2008 Junior Faculty Research Award of the University of Mississippi, the 2009 inaugural IEEE Donald G. Dudley Jr. Undergraduate Teaching Award, and the 2011 Recipient of Global Experts Program of China. He was the Technical Program Committee (TPC) Chair of the 2014 IEEE International Symposium on Antennas and Propagation and USNC-URSI Radio Science Meeting. He has served as an Associate Editor for the IEEE Transactions on Antennas and Propagation (2010–2013) and an Associate Editor-in-Chief of the Applied Computational Electromagnetics Society (ACES) Journal (2008–2014). He is also an IEEE APS Distinguished Lecturer (2018–2020).

## Protective Role of Vitamin C in Wi-Fi Induced Oxidative Stress in MC3T3-E1 Cells in Vitro

Mengxi Wang<sup>1,2</sup>, Guohui Yang<sup>1</sup>, Yu Li<sup>3</sup>, Qun Wu<sup>1,\*</sup>, and Yingsong Li<sup>4</sup>

<sup>1</sup> School of Electronic and Information Engineering, Harbin Institute of Technology, Harbin 150001, China

<sup>2</sup> The Fourth Affiliated Hospital of Harbin Medical University, Harbin 150001, China

<sup>3</sup> Department of Life Science and Engineering, Harbin Institute of Technology, Harbin 150001, China

<sup>4</sup> College of Information and Communication Engineering, Harbin Engineering University, Harbin 150001, China  
\*qwu@hit.edu.cn

**Abstract** — The increasing convenience and benefits provided by wireless technology innovations may also affect the human health because of Wi-Fi electromagnetic radiation. The effects of 2.45 GHz Wi-Fi on oxidative stress (OS) in MC3T3-E1 cells and the protective role of vitamin C are presented and analyzed in this paper. MC3T3-E1 cells were exposed to 100 mW and 500 mW 2.45 GHz Wi-Fi signals at specific absorption rates (SARs) of 0.1671 W/kg and 0.8356 W/kg, referred to as SARa and SARb, respectively, for 0-180 minutes to determine the optimal irradiation time by testing reactive oxygen species (ROS) and glutathione (GSH). Following irradiation for the optimal irradiation time, ROS levels were assayed for 0-120 min after each irradiation. Additional vitamin C is added to the medium to investigate the effect on ROS and GSH. A FDTD simulation showed that the cell layer temperature increased by 0.1°C and 0.5°C after being exposed in the SARa and SARb for the optimal irradiation time (90 min). Ninety min of Wi-Fi irradiation provoked an obvious increment in ROS and GSH on the first day, and the ROS level returned to the initial level 30 min after the irradiation; however, on the third day, it took 90-120 min for ROS to return to baseline. Vitamin C significantly reduced ROS levels and recovery times. In conclusion, 2.45 GHz Wi-Fi radiation triggered oxidative stress in osteoblasts 3cm from the source antenna. Vitamin C effectively reduced the ROS levels stimulated by nonthermal effects of Wi-Fi irradiation.

**Index Terms** — FDTD, in vitro, osteoblast, oxidative stress, temperature.

### I. INTRODUCTION

Wi-Fi, a wireless network technique that emits radiation mostly at 2.45 GHz in the radio frequency (RF) range, affects the human body mainly through

nonthermal effects [1]. However, several reports have addressed the problem of temperature measurements, since some researchers continue to believe that the biological effects of Wi-Fi irradiation can be attributed to increases in temperature [2]. The determination of whether the biological effects of Wi-Fi being caused by thermal or nonthermal effects requires a clear understanding of the temperature increase in biological tissue.

Bone is a metabolically active organ that continuously renews itself throughout life through a dynamic equilibrium dominated by three major types of bone cells: osteoclasts, osteoblasts and osteocytes [3]. Bone homeostasis can be disturbed by a variety of endogenous and exogenous factors, such as inflammation [4], loading [5], diabetes [6] and electromagnetic fields (EMFs) [7]. OS as a consequence of an oxidant-antioxidant imbalance favoring oxidants is the most direct response to a variety of adverse stimuli [8]. EMFs have been reported to increase the production or longer presence of free radicals which are the endogenous mechanism responsible for OS [9]. OS induced by Wi-Fi irradiation has been confirmed in the brain [10], liver [11], laryngotracheal mucosa [12] and uterus [13] in vivo experiments, and Çiğ B [14] found that the electromagnetic radiation (EMR) from Wi-Fi devices and mobile phones placed within 10 cm of cells induced OS in MCF-7 cells in vitro. In addition, vitamin C, an important free-radical scavenger, is considered to be an important inhibitor of Wi-Fi-related OS in the rat liver [11]. Thus, it is reasonable to presume that OS induced by Wi-Fi in osteoblasts might also be suppressed by vitamin C.

In this paper, the effects of 2.45 GHz Wi-Fi on OS in MC3T3-E1 cells and the protective role of vitamin C are presented and analyzed in detail. The contribution of this paper can be outlined as follows. (1) The specific

absorption rates in the cell's were calculated in the 2.45 GHz Wi-Fi environment. (2) The temperature difference in the cell layer was analyzed. (3) Wi-Fi induced ROS and GSH changes were found. (4) The role of vitamin C in reducing OS was confirmed.

## II. MATERIALS AND METHODS

### A. Wi-Fi exposure settings

A laptop computer with Wi-Fi antenna, 60-mm cell culture dishes containing 4 mL of culture medium and a Wi-Fi router were placed in a Forma Series II 3110 Water Jacketed CO<sub>2</sub> Incubator (Thermo Fisher Scientific Inc., Waltham, USA) with 5% CO<sub>2</sub> at 37°C, as illustrated in Fig. 1. In the control group, the Wi-Fi router and computer were placed in the cell incubator in an open position without data transmission. The distance between culture dishes and router antennas is approximately 3 cm.

### B. Thermal simulation

The FDTD method (Lumerica Solutions Inc., Vancouver, Canada) was employed to assess the SAR distribution in the cell monolayer. In the research of [15] the temperature of cells was carefully calculated with Debye's parameters of the cornea and aqueous humor by FDTD. However, it was confirmed by [16] that the effect of cell layers on the power delivery or heating of liquid is negligible. Consequently, the model in this research was simplified and the last layer (0.1 mm) of the culture medium was considered as the cell monolayer. The detailed steps and methods of FDTD was describe in [17] and [18]. The determination inside biological solution is expressed in terms of the specific absorption rate:

$$SAR = \frac{\sigma}{2\rho} |\vec{E}|^2. \quad (1)$$

Where E is the root-mean-square local electric field strength (V/m),  $\sigma$  is the electric conductivity (S/m), and  $\rho$  is the sample density (kg/m<sup>3</sup>). If the electric field components of a point (i, j, k) in an organism are Ex, Ey and Ez respectively, the distributional SAR can be calculated by the following formula (2), expressed in SAR( $\vec{r}$ ), which is defined as the electromagnetic power absorbed per unit mass of a biological tissue at a distance  $\vec{r}$  adjacent to at any point:

$$SAR(\vec{r}) = \frac{1}{2\rho(i,j,k)} [\sigma_x(i,j,k)E_x^2(i,j,k) + \sigma_y(i,j,k)E_y^2(i,j,k) + \sigma_z(i,j,k)E_z^2(i,j,k)]. \quad (2)$$

The dielectric and material thermal parameters at 37°C and 2.45 GHz are given in Table 1. The temperature of the surrounding atmosphere was assumed to be stable at 37°C. The voxel size was 0.1 mm, and the time step was 0.1 seconds. The last layer (height 0.1 mm) of the culture medium was considered the cell monolayer. The specific absorption rates are 0.1671 W/kg and 0.8356 W/kg for 100 mW and 500 mW Wi-Fi radiation, referred to as SARa and SARb, respectively.

The thermodynamics equation was used to determine the temperature increase in the cell monolayer at the bottom of the culture dishes. The thermodynamics equation is as follows [20]:

$$C\rho \frac{dT}{dt} = KV^2T + \rho(SAR) - BT. \quad (3)$$

Where T is the temperature (K), C is the specific heat capacity (J.K<sup>-1</sup>.kg<sup>-1</sup>), K is the thermal conductivity (W.m<sup>-1</sup>.K<sup>-1</sup>), B is a parameters related to blood flow.

The boundary condition is:

$$H \cdot (T_s - T_c) = -K \frac{\partial T}{\partial n}. \quad (4)$$

Where H is Convection coefficient, T<sub>s</sub> is surface temperature, and T<sub>c</sub> is air temperature.

For the spatial continuity function F(x,y,z,t), the discrete form of its time step at m can be written as follows:

$$F^m(i, j, k) = F(i\delta x, j\delta y, k\delta z, m\delta t). \quad (5)$$

Where  $\delta$  is the space step,  $\delta t$  is the time step.

(3) and (4) come to:

$$T^{m+1}(i, j, k) = T^m(i, j, k) + \frac{\delta t}{C\rho(i, j, k)} SAR(i, j, k) - \frac{\delta t \cdot b(i, j, k)}{\rho(i, j, k)C\rho(i, j, k)} * [T^m(i, j, k) - T_b] + \frac{\delta t \cdot K(i, j, k)}{\rho(i, j, k)C\rho(i, j, k)\delta^2} * [T^m(i+1, j, k) + T^m(i, j+1, k) + T^m(i, j, k+1) + T^m(i-1, j, k) + T^m(i, j-1, k) + T^m(i, j, k-1) - 6T^m(i, j, k)], \quad (6)$$

$$T^{m+1}(i_{min}, j, k) = \frac{KT(i_{min+1}, j, k)}{K+h\delta} + \frac{T_{ah}\delta}{K+h\delta}, \quad (7)$$

$\delta t$  satisfies the condition:

$$\delta t \leq \frac{2\rho C\rho\delta^2}{12K+b\delta^2}. \quad (8)$$

Figure 2 (a) shows a temperature comparison for Wi-Fi EMF radiation powers of 100 mW and 500 mW after 90 min of irradiation in the cell layer. The mean temperature increases under the 100 mW mode and 500 mW mode were approximately 0.1°C and 0.5°C respectively at 90 min (Fig. 2).

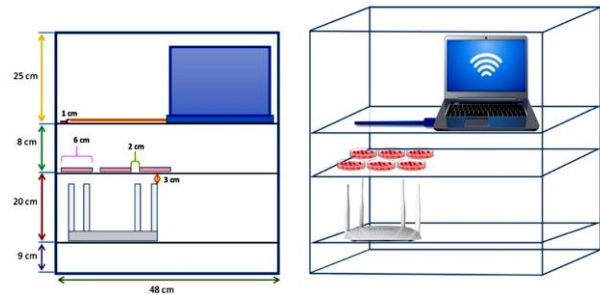


Fig. 1. Layout of cell dishes, the Wi-Fi router and the laptop computer in the cell incubator.

### C. Cell culture

MC3T3-E1 cells (iCell Bioscience Inc., Shanghai, China) of the clone-14 preosteoblastic murine cell line were cultured in  $\alpha$ -MEM containing 10% newborn bovine

serum, 100 IU/mL penicillin and 100  $\mu\text{g}/\text{mL}$  streptomycin under saturating humidity, 5%  $\text{CO}_2$  and  $37^\circ\text{C}$ . The medium was changed every 48 h. When the cells reached approximately 80% confluence, they were digested with 0.25% trypsin (Gibco Inc., Grand Island, USA), diluted and then subcultured at a 1:3 ratio.

#### D. In vitro differentiation

For this step, 10 mmol/L  $\beta$ -phospho-glycerol,  $10^{-8}$  mol/L dexamethasone and 50  $\mu\text{g}/\text{mL}$  ascorbic acid (vitamin C) were added to the above culture medium to

make osteogenic medium which was changed every 48 h.

#### E. Experimental groups

To select the optimum daily irradiation time, the cells were exposed to radiation after 72 h of induced differentiation, and each group contained at least three samples. The cells were divided into six groups: (i) 0 min, (ii) 30 min, (iii) 60 min, (iv) 90 min, (v) 120 min, and (vi) 180 min. These groups were further subdivided into sham, SARa 2.45 GHz Wi-Fi, and SARb 2.45 GHz Wi-Fi groups.

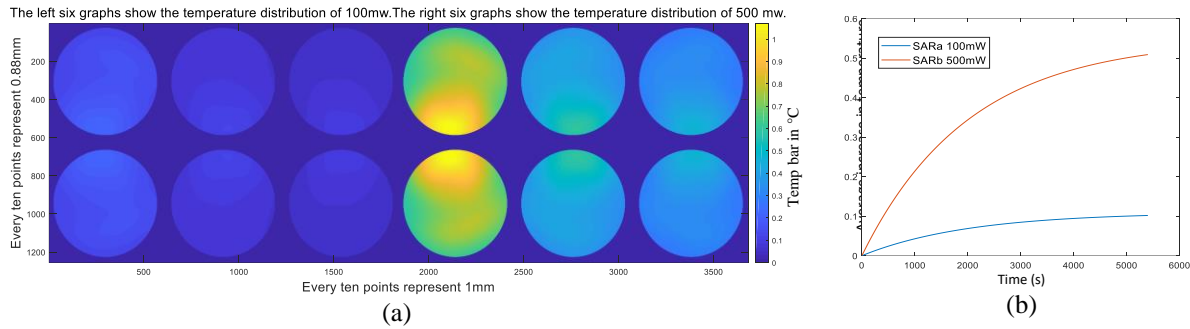


Fig. 2. The simulation result of temperature in the cell layer: (a) temperature difference after 90 min of irradiation in the cell layer, and (b) temperature dynamics within a cell monolayer.

Table 1: Electrical properties and thermal parameters of materials at  $37^\circ\text{C}$  2.45 GHz [15-16], [19]

	$\epsilon_r$	$\sigma$ ( $\text{Sm}^{-1}$ )	C ( $\text{kJ}(\text{kg}^\circ\text{C})^{-1}$ )	K ( $\text{W}(\text{km})^{-1}$ )	$\rho$ ( $\text{kgm}^{-3}$ )
Medium	71	2.5	4.2	0.6	1000
Petri dish	2.5	0.001	0.12	L2	1100

To measure GSH/ROS after radiation, the cells were exposed to Wi-Fi radiation for the optimum irradiation time each day for 1 to 3 days in 3 groups: (i) sham, (ii) SARa 2.45 GHz Wi-Fi, and (iii) SARb 2.45 GHz Wi-Fi. Tests were performed at 0 min, 15 min, 30 min, 45 min, 60 min, 90 min, and 120 min after Wi-Fi irradiation.

#### F. ROS

After 72 h of induction in osteogenic medium, the cells were digested with 0.25% trypsin-0.53 mM EDTA and then seeded into a 96-well plate at a density of  $5 \times 10^3$  cells/mL in 100  $\mu\text{L}$  of osteogenic medium, which was changed every 48 h. 2',7'-Dichlorofluorescein diacetate (KeyGen Biotech Co., NanJing, China) was added to each well according to the instructions. After 45 min of incubation in the dark, the cells were exposed to Wi-Fi radiation. ROS levels were determined by measuring the fluorescence intensity at 518-nm excitation and 605-nm emission using a spectrophotometer plate reader (Spectra Max M3, Molecular Devices, California, USA).

#### G. GSH

Cells were seeded in 60-mm culture dishes at a density of  $5 \times 10^4$  cells/mL in 4 mL of osteogenic medium,

which was changed every 48 h. Seventy-two hours later, the cells were exposed to Wi-Fi radiation. Then, the cells were digested with 0.25% trypsin-0.53 mM EDTA. After centrifugation (3500 g, 10 min), the cell supernatant was added to a 96-well culture plate. Cellular GSH was determined using a GSH assay kit (KeyGen Biotech Co.) according to the manufacturer's instructions. The optical absorbance values were measured with a microplate reader at 405 nm (SpectraMax M3).

#### H. Statistical analysis

The data are expressed as the mean  $\pm$  standard deviation (SD) of three or more independent experiments. Significant differences were determined through factorial analysis of variance (ANOVA). Statistical analysis was performed using SPSS 13.0 software (SPSS Inc., Chicago, USA). A P-value  $< 0.05$  was considered statistically significant.

### III. RESULTS

#### A. Determining the optimum irradiation time for further experiments (Fig. 3)

The cells were exposed to Wi-Fi radiation for 0-180 min after being induced for 72 h in osteogenic medium,

and ROS and GSH levels were measured immediately after irradiation. ROS levels in both the SARa group and SARb group were largely unaltered in the first 60 min. Although an upward trend was observed from 30 to 60 min, the changes at the 30th and 60th minutes were not significantly different in either the SARa or SARb group compared with the control group. From the 60<sup>th</sup> minute onward, the ROS level increased rapidly, peaked at the 90<sup>th</sup> minute, and then began to decrease but remained higher than in the control group at the 180<sup>th</sup> minute. ROS levels in the SARb group were significantly higher than in the SARa group at the 90<sup>th</sup> min but not at the other times. The peak GSH level was recorded at the 120<sup>th</sup> min. Significant differences between the SARa and SARb groups were detected at the 60<sup>th</sup>, 90<sup>th</sup> and 120<sup>th</sup> minutes, and the GSH levels of the SARa group were higher than those of the SARb group, except at the 60<sup>th</sup> minute. Unlike the GSH level in the SARb group, the GSH level in the SARa group increased significantly as early as the 60<sup>th</sup> minute. At the 180<sup>th</sup> minute, the GSH and ROS levels were still much higher than the original levels. We chose 90 min as the daily optimum irradiation time for the subsequent experiments since the ROS levels in both the SARa and SARb groups were highest at the 90<sup>th</sup> minute. In addition, both ROS and GSH levels differed significantly between the SARa and SARb groups, between the SARa and control groups, and between the SARb and control groups at the 90<sup>th</sup> minute.

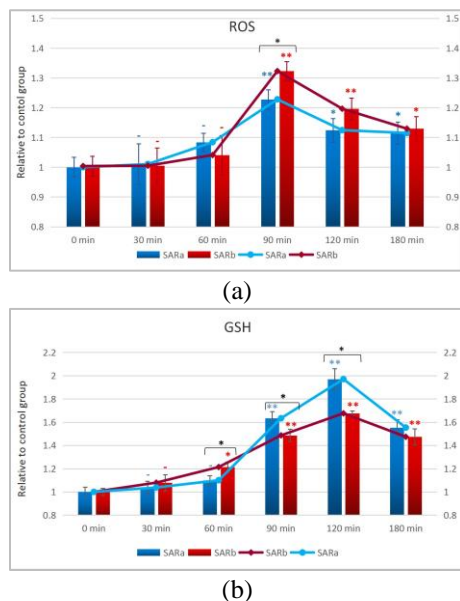


Fig. 3. ROS and GSH levels during Wi-Fi exposure: (a) relative ROS levels at 0/30/60/90/120/180 min of Wi-Fi exposure, and (b) relative GSH levels at 0/30/60/90/120/180 min of Wi-Fi exposure ( $P \geq 0.05$  -,  $P < 0.05$  \*,  $P < 0.01$  \*\*).

### B. Changes in ROS 0-30 min after Wi-Fi irradiation for the optimum irradiation time (Fig. 4 (a))

MC3T3-E1 cells were exposed to Wi-Fi radiation for 90 min after 72 h of differentiation. ROS were measured 0-30 min after irradiation was completed. The measurement taken immediately after irradiation was defined as 0 min. ROS levels began to decrease at the time at which irradiation stopped and took 30 min to return to the original level. ROS levels in the SARb group were significantly higher than those in the SARa group at 0 and 15 min. Even though the ROS level at 30 min after irradiation did not completely recover in either the SARa or SARb group, this difference can be ignored because these levels were not significantly different from the control level.

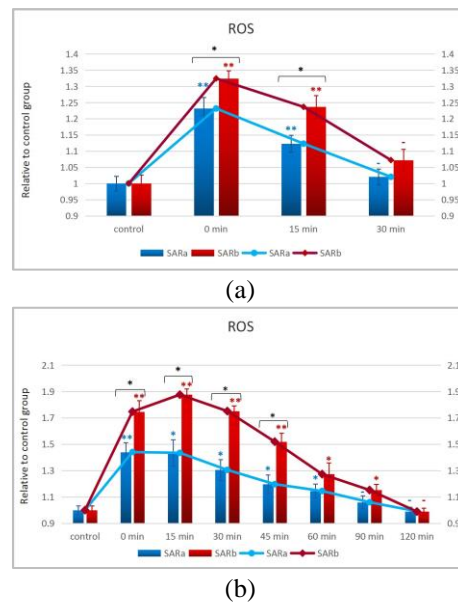


Fig. 4. ROS levels after Wi-Fi exposure: (a) relative ROS levels after Wi-Fi exposure for 90 min, and (b) relative ROS levels after Wi-Fi exposure for 90 min/day for 3 days ( $P \geq 0.05$  -,  $P < 0.05$  \*,  $P < 0.01$  \*\*).

### C. Changes in ROS after Wi-Fi irradiation for the optimum irradiation time every day for 3 days (Fig. 4 (b))

After 72 h of differentiation, MC3T3-E1 cells were exposed to 90 min of Wi-Fi radiation for 3 days. ROS were measured after the 3<sup>rd</sup> day of irradiation. The time point immediately after irradiation was defined as 0 min. ROS levels increased slightly after irradiation was stopped and took 120 min or 90 min to decrease to control levels in the SARb and SARa groups, respectively. The ROS levels of the SARb group were significantly higher than those of the SARa group at 0 min, 15 min, 30 min and 45 min after Wi-Fi irradiation.

#### D. Determining the optimum concentration of vitamin C by repeating experiment 1 in the SARb group with extra vitamin C in the induction culture medium (Fig. 5)

The results of experiments A, B and C show that the peak ROS level was higher in the SARb group than in the SARa group and that recovery was slower in the SARb group than in the SARa group. Thus, our subsequent studies were performed under the SARb conditions. We adjusted the concentration of vitamin C in the induction medium from 50  $\mu\text{g/mL}$  to 55  $\mu\text{g/mL}$ , 60  $\mu\text{g/mL}$  or 65  $\mu\text{g/mL}$  and then repeated experiment 1 to examine ROS and GSH in the SARb group. After 60 min of irradiation, ROS levels increased in all vitamin C groups, peaked at the 90th minute, and then decreased to basal levels. The ROS level at the 90th minute was inversely proportional to the vitamin C concentration (50  $\mu\text{g/mL}$  to 60  $\mu\text{g/mL}$ ) and was significantly different from the level in the control group. However, the ROS level in the presence of 65  $\mu\text{g/mL}$  vitamin C was lower than in the presence of 60  $\mu\text{g/mL}$  vitamin C at the 90th minute, but the difference was not significant. At the 90th minute, GSH levels in the 60  $\mu\text{g/mL}$  group were also higher than those in the other groups. Therefore, we adopted 60  $\mu\text{g/mL}$  as the optimum concentration of vitamin C.

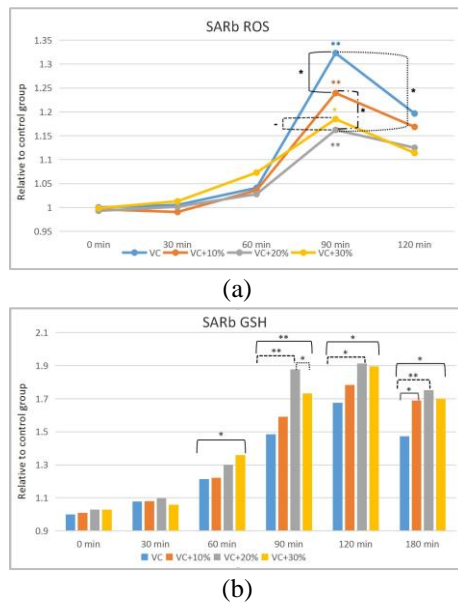


Fig. 5. ROS and GSH levels in the SARb group during Wi-Fi irradiation with extra vitamin C in the induction medium: (a) relative ROS levels in the SARb group at 0/30/60/90/120 min of Wi-Fi exposure with 10-30% extra vitamin C in the induction medium, and (b) relative GSH levels in the SARb group at 0/30/60/90/120/180 min of Wi-Fi exposure with 10-30% extra vitamin C in the induction medium ( $P \geq 0.05$  -,  $P < 0.05$  \*,  $P < 0.01$  \*\*).

#### E. Changes in ROS in the SARb group 0-30 min after Wi-Fi irradiation for the optimum irradiation time with the optimum concentration of vitamin C in the induction medium (Fig. 6 (a))

Experiment B was repeated with 60  $\mu\text{g/mL}$  vitamin C in the induction medium to measure the ROS in the SARb group. The measurement performed immediately after 90 min of Wi-Fi exposure was considered 0 min. The ROS levels in the vitamin C and vitamin C+20% control groups were not significantly different, but the ROS levels in the 50  $\mu\text{g/mL}$  vitamin C experimental group were significantly higher than those in the 60  $\mu\text{g/mL}$  vitamin C experimental group at both 0 and 15 min.

#### F. Changes in ROS in the SARb group 0-120 min after Wi-Fi irradiation for the optimum irradiation time for 3 days with the optimum concentration of vitamin C in the induction medium (Fig. 6 (b))

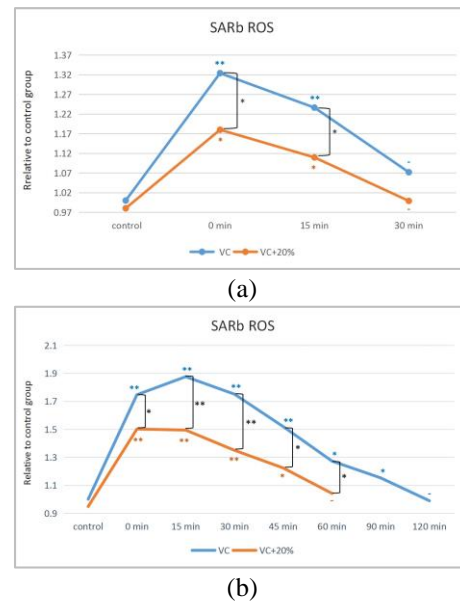


Fig. 6. ROS levels in the SARb group after Wi-Fi exposure with 20% extra vitamin C in the induction medium: (a) relative ROS levels in the SARb group after 90 min/day of Wi-Fi exposure with 20% extra vitamin C in the induction medium, and (b) relative ROS levels in the SARb group after 90 min/day of Wi-Fi exposure for 3 days with 20% extra vitamin C in the induction medium. ( $P \geq 0.05$  -,  $P < 0.05$  \*,  $P < 0.01$  \*\*).

Experiment C was repeated with 60  $\mu\text{g/mL}$  vitamin C in the induction medium to measure ROS in the SARb groups. The time point immediately after 90 min of Wi-Fi exposure was considered 0 min. ROS levels in the vitamin C+20% experimental groups at 0 min, 15 min, 30 min and 45 min were higher than those in the vitamin

C+20% control group, while the ROS levels in the vitamin C experimental groups at 0 min, 15 min, 30 min, 45 min, 60 min and 90 min were higher than those in the vitamin C control group. The ROS levels of the 50  $\mu\text{g/mL}$  vitamin C group at 0 min, 15 min, 30 min, 45 min and 60 min were significantly higher than those of the 60  $\mu\text{g/mL}$  vitamin C group. Therefore, the ROS recovery time in the 60  $\mu\text{g/mL}$  vitamin C groups was half that in the 50  $\mu\text{g/mL}$  vitamin C groups.

#### IV. DISCUSSIONS

The safety standard of non ionizing radiation was set mainly focusing on whether it exerts obvious thermal effects on the human body over a certain period of time [21], but without considering nonthermal or cumulative effects. Thus, even within the recommended values, adverse effects of Wi-Fi radiation on certain types of cells or organs have been verified [13]. Non ionizing EMR can alter the energy level and spin orientation of electrons and, consequently, increase the activity, concentration and lifetime of ROS [14]. OS stimulated by Wi-Fi irradiation for a period from 5 days [11] to 6 months [22] has been found in some important organs deep in rats' body. In the vitro experiment, [14] set 6 tubes of MCF-7 breast cancer cells at different distances (0 cm, 1 cm, 5 cm, 10 cm, 20 cm and 25 cm) from a radiant for 1 h. The mean SAR of the 6 tubes was  $0.36 \pm 0.02$  W/kg under 900 MHz exposure at  $12 \mu\text{W/cm}^2$ . Çiğ B found that cytosolic ROS production,  $\text{Ca}^{2+}$  concentrations, apoptosis, and caspase-3 and caspase-9 levels were higher in all the mobile phone and 2.45 GHz Wi-Fi groups at distances of less than 10 cm. An increase in ROS in a osteoblasts monolayer exposed to Wi-Fi radiation (3 cm from router antennas) was also found in our work, and Wi-Fi radiation was clearly shown to be an exogenous OS stimulus. Our main concern is the duration of ROS generation and the return of ROS to baseline levels. ROS did not increase until 90 min after the initial exposure to Wi-Fi, which may be attributed to "window effects" [23]. Even with continuing irradiation, ROS did not increase and instead decreased from 90 to 180 min because of the increase in GSH which, as an antioxidant, serves as a natural defense mechanism to restore the dynamic balance between ROS generation and elimination in cells [24].

ROS levels in the SARb group were higher than those in the SARa group in experiments 1, 2 and 3 and showed an SAR-dependent pattern similar to that found in other studies [25]. The ROS level returned to baseline within 30 min of the initial exposure to Wi-Fi; however, after the third day of radiation, this return took 90 min in the SARa group and 120 min in the SARb group, which could be interpreted as a "cumulative effect" [26]. Prolonged exposure times and increased exposure doses may reasonably be concluded to make it increasingly difficult to restore ROS levels to normal. The mechanism

by which EMFs increase ROS is partly attributing to the decreased efficiency of antioxidant mechanisms [27]. However, in our study, GSH rapidly increased even before ROS levels changed, which might play an important part in ROS regulation during Wi-Fi exposure. Similarly, in a study by [28], V79 fibroblast cells were exposed 1800 MHz RF (SAR 1.6 W/kg) generated in a gigahertz transverse electromagnetic mode (GTEM) cell, and GSH levels were found to increase immediately after 10 min of exposure, but ROS increased only after 60 min of exposure. Cermak AMM suggested that short-term RF exposure resulted in a transient oxidation-reduction imbalance in fibroblast cells following adaptation to the applied experimental conditions. [29] also found that ROS increased in osteoblasts after a single exposure to extremely low-frequency pulsed electromagnetic fields (ELF-PEMFs) and that GSH did not decrease; these changes essentially represented an antioxidant defense mechanism in which ELF-PEMF stimulated the cells to produce a small amount of harmless ROS to improve osteoblast function and activity. Hence, the ROS and GSH increases observed in our study may similarly be a protective mechanism elicited by Wi-Fi irradiation.

If Wi-Fi exposure is inevitable, then it is particularly important to explore ways to reduce ROS and minimize the risk of side effects. Various antioxidant mechanisms have been confirmed to neutralize the harmful effects of ROS in cells, among which vitamin C, a free-radical scavenger in extracellular fluids, is considered to be an important inhibitor of Wi-Fi-related OS in rats [11]. The original culture medium for osteoblasts contains vitamin C, which may be another factor that reduces ROS and/or accelerates the reduction of ROS levels. High levels of GSH might be related to the fact that vitamin C can reduce oxidized GSH (GSSG) into GSH. Accordingly, we added different concentrations of extra vitamin C to the culture medium and found that 60  $\mu\text{g/mL}$  was the most appropriate concentration for limiting ROS and upregulating GSH. This optimum concentration of vitamin C significantly reduced ROS levels and shortened the recovery time by half (from 120 to 60 min) after the 3rd day of Wi-Fi irradiation. Furthermore, the ROS levels of the different vitamin C groups were inversely proportional to the GSH level of the same groups, further supporting a mechanism whereby GSH plays an important role in ROS regulation during Wi-Fi exposure and is upregulated by vitamin C.

#### V. CONCLUSIONS

The long-term and close-range Wi-Fi EMF radiation slightly increases the temperature in a cell monolayer, however the temperature variation (no more than  $1^\circ\text{C}$ ) is too small to induce the cell biological reaction. Hence, it is believed that the effect of Wi-Fi irradiation on cells would be stimulated by nonthermal effects.

The SARs of Wi-Fi EMF is far below the safety

standard of non ionizing radiation, but still elevates ROS in cells after long-term exposure. Therefore, Wi-Fi EMF could be an exogenous OS stimulus and affect bone homeostasis. Furthermore, the longer the irradiation time and the stronger the radiation, the more obvious the effect on osteoblasts. However, short-term exposure (less than 60 min) can neither change the level of ROS nor GSH owing to “window effects”.

ROS induced by Wi-Fi EMF radiation can be eliminated by endogenous or Wi-Fi induced GSH, which acts as a protective mechanism of osteoblasts. Nevertheless, it takes longer times for osteoblasts to eliminated ROS with the increase of exposure doses due to the “cumulative effect”.

Vitamin C effectively reduces ROS levels and recovery times by increasing GSH, and its effect shows a concentration-dependent pattern at low concentrations.

Due to the limited experimental conditions, the radiation distance setting is an extreme case (a cell layer 3cm from the source antenna), and the influence of distance change on the result needs further study. In the future, we will consider the MIMO antenna and circular polarization antenna [30-34] and arrays [35] in the experiment and use the adaptive filtering [36-41] to suppress the noises and improve the performance.

#### ACKNOWLEDGMENTS

This study was funded by the National Natural Science Foundation of China (61571155); the Natural Science Foundation of Heilongjiang Province, China (QC2015124), and the Fundamental Research Funds for the Central Universities (3072020CFT0802).

#### REFERENCES

- [1] M. B. Salah, H. Abdelmelek, and M. Abderraba, “Wifi and health: Perspectives and risks,” no. 1, pp. 012-022, 2017.
- [2] S. S. Lee, H. R. Kim, M. S. Kim, et al., “Influence of smartphone Wi-Fi signals on adipose-derived stem cells,” *J. Craniofac Surg.*, vol. 25, no. 5, pp. 1902-1907, 2014.
- [3] V. Domazetovic, G. Marcucci, T. Iantomasi, et al., “Oxidative stress in bone remodeling: Role of antioxidants,” *Clin. Cases Miner. Bone Metab.*, vol. 14, no. 2, pp. 209-216, 2017.
- [4] W. Razawy, M. van Driel, and E. Lubberts, “The role of IL-23 receptor signaling in inflammation-mediated erosive autoimmune arthritis and bone remodeling,” *Eur. J. Immunol.*, vol. 48, no. 2, pp. 220-229, 2018.
- [5] S. A. Murshid, “The role of osteocytes during experimental orthodontic tooth movement: A review,” *Arch. Oral Biol.*, vol. 73, pp. 25-33, 2017.
- [6] A. G. D. Vianna, C. P. Sanches, and F. C. Barreto, “Effects of type 2 diabetes therapies on bone metabolism,” *Diabetol. Metab. Syndr.*, vol. 9, no. 1, 2017.
- [7] M. Zhai, D. Jing, S. Tong, et al., “Pulsed electromagnetic fields promote in vitro osteoblastogenesis through a Wnt/ $\beta$ -catenin signaling-associated mechanism,” *Bioelectromagnetics*, vol. 37, no. 3, pp. 152-162, 2016.
- [8] V. Selvaraju, M. Joshi, S. Suresh, et al., “Diabetes, oxidative stress, molecular mechanism, and cardiovascular disease—An overview,” *Toxicol. Mech. Methods*, vol. 22, no. 5, pp. 330-335, 2012.
- [9] M. Simko, “EMF and the redox homeostasis: The link to cell activation processes,” *Toxicology Letters*, ID:280 S32, 2017.
- [10] H. Othman, M. Ammari, K. Rtibi, et al., “Postnatal development and behavior effects of in-utero exposure of rats to radiofrequency waves emitted from conventional WiFi devices,” *Environ. Toxicol. Pharmacol.*, vol. 52, pp. 239-247, 2017.
- [11] F. Shekoohi-Shooli, S. M. J. Mortazavi, M. B. Shojaei-Fard, et al., “Evaluation of the protective role of vitamin c on the metabolic and enzymatic activities of the liver in the male rats after exposure to 2.45 GHz of Wi-Fi routers,” *J. Biomed. Phys. Eng.*, vol. 6, no. 3, ID:157, 2016.
- [12] G. Aynali, M. Nazırođlu, Ö. Çelik, et al., “Modulation of wireless (2.45 GHz)-induced oxidative toxicity in laryngotracheal mucosa of rat by melatonin,” *Eur. Arch. Oto-rhino-L.*, vol. 270, no. 5, pp. 1695-1700, 2013.
- [13] M. Yüksel, M. Nazırođlu, M. O. Özkaya, “Long-term exposure to electromagnetic radiation from mobile phones and Wi-Fi devices decreases plasma prolactin, progesterone, and estrogen levels but increases uterine oxidative stress in pregnant rats and their offspring,” *Endocrine*, vol. 52, no. 2, pp. 352-362, 2015.
- [14] B. Çiđ and M. Nazırođlu, “Investigation of the effects of distance from sources on apoptosis, oxidative stress and cytosolic calcium accumulation via TRPV1 channels induced by mobile phones and Wi-Fi in breast cancer cells,” *BBA-Biomembranes*, vol. 1848, no. 10, pp. 2756-2765, 2015.
- [15] J. Zhao, “In vitro dosimetry and temperature evaluations of a typical millimeter-wave aperture-field exposure setup,” *IEEE Transactions on Microwave Theory and Techniques*, vol. 60, no. 11, pp. 3608-3622, 2012.
- [16] M. Zhadobov, S. I. Alekseev, R. Sauleau, et al., “Microscale temperature and SAR measurements in cell monolayer models exposed to millimeter waves,” *Bioelectromagnetics*, vol. 38, no. 1, pp. 11-21, 2016.
- [17] A. Collin, M. Cueille, A. Perrin, et al., “Electromagnetic dosimetry and thermal analysis of a new exposure setup for in vitro studies on a large frequency band,” *Microwave Symposium, IEEE/MTT-S International*, pp. 2221-2224, 2017.



- [18] A. Paffi, M. Liberti, F. Apollonio, et al., "In vitro exposure: Linear and non-linear thermodynamic events in Petri dishes," *Bioelectromagnetics*, vol. 36, no. 7, pp. 527-537, 2015.
- [19] M. Zhadobov, R. Augustine, R. Sauleau, et al., "Complex permittivity of representative biological solutions in the 2–67 GHz range," *Bioelectromagnetics*, vol. 33, no. 4, pp. 346-355, 2016.
- [20] A. Hirata and T. Shiozawa, "Correlation of maximum temperature increase and peak SAR in the human head due to handset antennas," *IEEE Transactions on Microwave Theory and Techniques*, vol. 51, no. 7, pp. 1834-1841, 2003.
- [21] ICNIRP, International Commission of Non-Ionizing Radiation Protection. Guidelines for limiting exposure to time-varying electric, magnetic and electromagnetic fields, URL: <http://www.icnirp.de/documents/emfgdl.pdf>
- [22] A. Özorak, M. Naziroğlu, Ö. Çelik, et al., "Wi-Fi (2.45 GHz)-and mobile phone (900 and 1800 MHz)-induced risks on oxidative stress and elements in kidney and testis of rats during pregnancy and the development of offspring," *Biol. Trace Elem. Res.*, vol. 156, no. 1-3, pp. 221-229, 2013.
- [23] J. Zhou, L. G. Ming, B. F. Ge, et al., "Effects of 50 Hz sinusoidal electromagnetic fields of different intensities on proliferation, differentiation and mineralization potentials of rat osteoblasts," *Bone*, vol. 49, no. 4, pp. 753-761, 2014.
- [24] H. Wang and X. Zhang, "Magnetic fields and reactive oxygen species," *Int. J. Mol. Sci.*, vol. 18, no. 10, 2017.
- [25] G. N. De Iulii, R. J. Newey, B. V. King, et al., "Mobile phone radiation induces reactive oxygen species production and DNA damage in human spermatozoa in vitro," *PLOS ONE*, vol. 4, no. 7, 2009.
- [26] H. S. Kim, J. S. Park, Y. B. Jin, et al., "Effects of exposure to electromagnetic field from 915 MHz radiofrequency identification system on circulating blood cells in the healthy adult rat," *Bioelectromagnetics*, vol. 39, no. 1, pp. 68-76, 2018.
- [27] J. Espino, I. Bejarano, S. D. Paredes, et al., "Protective effect of melatonin against human leukocyte apoptosis induced by intracellular calcium overload: Relation with its antioxidant actions," *J. Pineal. Res.*, vol. 51, no. 2, pp. 195-206, 2011.
- [28] A. M. M. Cermak, I. Pavicic, B. T. Lovakovic, et al., "In vitro non-thermal oxidative stress response after 1800 MHz radiofrequency radiation," *GEN Physiol. Biophys.*, vol. 36, no. 4, pp. 407-414, 2017.
- [29] S. Ehnert, A. K. Fentz, A. Schreiner, et al., "Extremely low frequency pulsed electromagnetic fields cause antioxidative defense mechanisms in human osteoblasts via induction of  $O_2^-$  and  $H_2O_2$ ," *Sci. Rep.*, vol. 7, no. 1, ID: 14544, 2017.
- [30] K. Yu, Y. Li, and X. Liu, "Mutual coupling reduction of a MIMO antenna array using 3-D novel meta-material structures," *Appl. Comput. Electromagn. Soc. J.*, vol. 33, no. 7, pp. 758-763, 2018.
- [31] J. Jiang, Y. Xia, and Y. Li, "High isolated X-band MIMO array using novel wheel-like metamaterial decoupling structure," *Appl. Comput. Electromagn. Soc. J.*, vol. 34, no. 12, pp. 1829-1836, 2019.
- [32] S. Luo, Y. Li, Y. Xia, and L. Zhang, "A low mutual coupling antenna array with gain enhancement using metamaterial loading and neutralization line structure," *Applied Computational Electromagnetics Society Journal*, vol. 34, no. 3, pp. 411-418, 2019.
- [33] S. Luo, Y. Li, Y. Xia, et al., "Mutual coupling reduction of a dual-band antenna array using dual-frequency metamaterial structure," *Applied Computational Electromagnetics Society Journal*, vol. 34, no. 3, pp. 403-410, 2019.
- [34] K. L. Chuang, X. Yan, Y. Li, and Y. Li, "A Jia-shaped artistic patch antenna for dual-band circular polarization," *AEÜ - International Journal of Electronics and Communications*, vol. 120,10.1016/j.aeue.2020.153207.
- [35] X. Zhang, T. Jiang, and Y. Li, "A novel block sparse reconstruction method for DOA estimation with unknown mutual coupling," *IEEE Communications Letters*, vol. 23, no. 10, pp. 1845-1848, 2019.
- [36] T. Jiang, T. Jiao, and Y. Li, "A low mutual coupling MIMO antenna using periodic multi-layered electromagnetic band gap structures," *Applied Computational Electromagnetics Society Journal*, vol. 33, no. 3, 2018.
- [37] Y. Li, Z. Jiang, O. M. Omer-Osman, et al., "Mixed norm constrained sparse APA algorithm for satellite and network echo channel estimation," *IEEE Access*, vol. 6, pp. 65901-65908, 2018.
- [38] Y. Li, Y. Wang, and T. Jiang, "Sparse-aware set-membership NLMS algorithms and their application for sparse channel estimation and echo cancelation," *AEU - International Journal of Electronics and Communications*, vol. 70, no. 7, pp. 895-902, 2016.
- [39] Q. Wu, Y. Li, Y. V. Zakharov, et al., "A kernel affine projection-like algorithm in reproducing kernel hilbert space," *IEEE Transactions on Circuits and Systems II: Express Briefs*, 10.1109/TCSII.2019.2947317.
- [40] B. Chen, Z. Li, Y. Li, and P. Ren, "Asymmetric correntropy for robust adaptive filtering," *IEEE Signal Processing Letters*, arXiv preprint arXiv: 1911.11855.
- [41] W. Shi, Y. Li, and B. Chen, "A Separable maximum correntropy adaptive algorithm," *IEEE Transactions on Circuits and Systems II: Express Briefs*, 10.1109/TCSII.2020.2977608.